

Washington University in St. Louis
Washington University Open Scholarship

Engineering and Applied Science Theses &
Dissertations


McKelvey School of Engineering

Summer 8-15-2018

Development and Evaluation of Biocompatible Engineered Nanoparticles for Use in Ophthalmology

Bedia Begum Karakocak
Washington University in St. Louis

Follow this and additional works at: https://openscholarship.wustl.edu/eng_etds

 Part of the [Biomedical Engineering and Bioengineering Commons](#), [Nanoscience and Nanotechnology Commons](#), and the [Toxicology Commons](#)

Recommended Citation

Karakocak, Bedia Begum, "Development and Evaluation of Biocompatible Engineered Nanoparticles for Use in Ophthalmology" (2018). *Engineering and Applied Science Theses & Dissertations*. 368.
https://openscholarship.wustl.edu/eng_etds/368

This Dissertation is brought to you for free and open access by the McKelvey School of Engineering at Washington University Open Scholarship. It has been accepted for inclusion in Engineering and Applied Science Theses & Dissertations by an authorized administrator of Washington University Open Scholarship. For more information, please contact digital@wumail.wustl.edu.

WASHINGTON UNIVERSITY IN ST. LOUIS
School of Engineering and Applied Science
Department of Energy, Environmental and Chemical Engineering

Dissertation Examination Committee:

Nathan Ravi, Chair
Pratim Biswas, Co-chair
Rajendra S. Apte
Palghat Ramachandran
Fuzhong Zhang

Development and Evaluation of Biocompatible Engineered Nanoparticles for
Use in Ophthalmology
by
Bedia Begüm Karakoçak

A dissertation presented to
The Graduate School
of Washington University in
partial fulfillment of the
requirements for the degree
of Doctor of Philosophy

August 2018
St. Louis, Missouri

© 2018, Bedia Begüm Karakoçak

Table of Contents

List of Figures	vii
List of Tables	xiv
Acknowledgments.....	xv
Abstract of The Dissertation	xviii
Chapter 1: Introduction	1
1.1 Background and Motivation.....	2
1.1.1 Ophthalmic uses of engineered nanoparticles: Opportunities and roadblocks.....	3
1.1.2 Engineering nanoparticles to reduce their toxicity, overcome ocular drug delivery barriers, and facilitate imaging.....	7
1.2 Dissertation Outline.....	10
1.3. References	11
Chapter 2: Biocompatibility of Gold Nanoparticles in Retinal Pigment Epithelial Cell Line.	19
Abstract	20
2.1 Introduction	21
2.2 Materials and Methods	23
2.2.1 Synthesis of gold nanoparticles.....	23
2.2.2 Characterization of nanoparticles and exposure to ARPE-19 cell line	23
2.2.3 Biocompatibility assessment of the Au NPs with the ARPE-19 cell line	23
2.3 Results and Discussion.....	27
2.3.1 Characterization of synthesized NPs.....	27
2.3.2 Biocompatibility assessment of the Au NPs with the ARPE-19 cell line	29
2.4 Discussion	34
2.5 Conclusions	39
2.6 References	40
Chapter 3: Hyaluronate Coating as a Solution to Toxicity of Gold Nanoparticles	44
Abstract	45
3.1 Introduction	46
3.2 Materials and Methods	48
3.2.1 Reagents	48
3.2.2 Synthesis of Au NPs	48
3.2.3 Preparation of end-thiol modified HA (HS-HA)	49

3.2.4	Conjugation of HS-HA with Au NPs and quantification of the coating.....	49
3.2.5	Investigation of the internalization of NPs.....	50
3.2.6	<i>In-vitro</i> toxicity measurements on ARPE-19 cells with MTT, ApoTox-Glo™, and ROS-Glo™ H ₂ O ₂ assays.....	50
3.2.7	Confocal microscopy analysis.....	51
3.2.8	Cell attachment measurements by electrical impedance spectrometry (ECIS).....	51
3.2.9	Statistical analysis.....	52
3.3	Results and Discussion.....	52
3.3.1	Synthesis of end-thiolated hyaluronic acid (HS-HA).....	52
3.3.2	Synthesis of Au NPs conjugated with HS-HA and confirmation of the presence of the coating.....	55
3.3.3	Characterization of HS-HA conjugated Au NPs.....	56
3.3.4	Cellular uptake of nascent and coated Au NPs.....	57
3.3.5	The fate of nascent and coated Au NPs in the cells.....	59
3.3.6	Biocompatibility assessment of HS-HA-coated Au NPs with ARPE-19 cells.....	61
3.3.6	Cell attachment behavior with ECIS measurements in response to Au NPs.....	64
3.4	Conclusions.....	64
3.5	Acknowledgements.....	65
3.6	References.....	66
Chapter 4: Nitrogen-doped Carbon Dots as a Biocompatible Alternative for Bioimaging.....		70
	Abstract.....	71
4.1	Introduction.....	72
4.2	Methods.....	74
4.2.1	Materials.....	74
4.2.2	Synthesis of nCDs.....	74
4.2.3	Physico-chemical characterization of nCDs.....	75
4.2.4	<i>In-vitro</i> Cytotoxicity measurements on Retinal Pigment Epithelial (ARPE-19), lens epithelial, and Chinese Hamster Ovary (CHO) Cells with MTT, Apotox-Glo™, and ROS-Glo™ H ₂ O ₂ assays.....	77
4.2.5	<i>In-vitro</i> Imaging of Cells Treated with nCDs.....	77
4.3	Results and Discussion.....	78
4.3.1	Effects of synthesis conditions on short and long-wavelength emission abilities.....	78
4.3.2	Maximization of nCD red fluorescence intensity.....	81
4.3.3	Characterization of long wavelength nCDs.....	85
4.3.4	Cytotoxicity evaluation of nCDs.....	89
4.3.5	<i>In-vitro</i> imaging of nCDs.....	90

4.4	Conclusions	92
4.5	Acknowledgements	92
4.6	References	93
Chapter 5: Hyaluronate Conjugated Nitrogen-doped Carbon Quantum Dots for Use in Bioimaging.....		96
	Abstract	97
5.1	Introduction	98
5.2	Methods.....	99
5.2.1	Materials	99
5.2.2	Central-composite response surface design for synthesizing nCQDs with desired properties	100
5.2.3	Conjugation of nCQDs with hyaluronic acid.....	101
5.2.4	Characterization of nCQDs and HA-CQDs	101
5.2.5	Hydrodynamic size and zeta potential measurements with dynamic light scattering analysis	102
5.2.6	<i>In-vitro</i> cytotoxicity measurements on Retinal Pigment Epithelial (ARPE-19), NIH 3T3, and Chinese Hamster Ovary (CHO) cells with MTT, ApoTox-Glo™, and ROS-Glo™ H ₂ O ₂ assays	102
5.2.7	<i>In-vitro</i> imaging of nCQDs and HA-nCQDs.	102
5.2.8	<i>Ex-vivo</i> and <i>post-mortem</i> imaging of nCQDs and HA-nCQDs.	103
5.3	Results and Discussion.....	104
5.3.1	Conjugation of hyaluronic acid with carbon quantum dots	104
5.3.2	<i>In-vitro</i> imaging of nCQDs and HA-nCQDs	107
5.3.3	Cytotoxicity evaluation of nCQDs and HA-nCQDs.....	109
5.3.4	<i>Ex-vivo</i> and <i>post-mortem</i> imaging of nCQDs and HA-nCQDs	110
5.4	Conclusions	112
5.5	Acknowledgements	113
5.6	References	114
Chapter 6: Assessing the Nanoparticle Transport through the Biological Barriers in the Eye		116
	Abstract	117
6.1	Introduction	118
6.2	Materials and Methods	123
6.2.1	Animals	123
6.2.2	Mimicking the blood-retinal barrier: Cell inserts.....	124
6.2.3	Intravitreal and intravenous injections of Au NPs and CDs	124

6.3	Results and Discussion.....	127
6.3.1	Demonstration of 20 nm Au NPs crossing the tight junctions of retinal pigment epithelial (RPE) <i>in-vitro</i>	127
6.3.2	Distribution of intravitreally injected HA-coated and uncoated Au NPs in the cornea.....	129
6.3.3	Distribution of intravenously injected uncoated and HA-coated Au NPs in the eye.....	132
6.3.4	Post-mortem imaging of CDs.....	143
6.3.5	Electroretinogram analysis of intravenously injected uncoated and HA-coated Au NPs in the eye.....	144
6.3.6	Histology staining and imaging of eye tissue sections with uncoated Au NPs and HA-S-Au NPs.....	147
6.4	Conclusions.....	147
6.5	References.....	149
Chapter 7: Conclusions and Suggestions for Future Work.....		153
7.1	Conclusions.....	154
7.1.1	Assessing the biocompatibility of Au NPs with retinal cells and providing a solution for their toxicity (Chapters 2 and 3).....	154
7.1.2	Creating biocompatible red-emissive carbon dots for use in ophthalmology (Chapters 4 and 5).....	155
7.1.3	Demonstration of the usefulness of gold nanoparticles and carbon dots <i>in-vivo</i> (Chapter 6).....	156
7.2	Suggestions for Future Work.....	158
7.2.1	Selecting a disease model to demonstrate the usefulness of the Au NPs as targeted drug delivery agents.....	158
7.2.2	Controlled dose-dependent <i>in-vivo</i> studies.....	159
7.2.3	Long-term toxicity analysis of engineered gold nanoparticles as a prerequisite to clinical trials.....	160
7.2.4	Synthesis of red-emissive carbon dots with ultrahigh quantum yield.....	161
7.3.	References.....	163
Appendix I. Supporting Materials for Chapter 2.....		166
Appendix II. Supporting Materials for Chapter 3.....		180
Appendix III. Supporting Materials for Chapter 4.....		216
Appendix IV.....		232
Post Intravenous Injection Histology Analysis for Uncoated and Coated Au NPs.....		232
Appendix V.....		239
A Highly Sensitive Non-enzymatic Glucose Sensor based on Cu/Cu ₂ O/CuO Ternary Composite Hollow Spheres Prepared in a Furnace Aerosol Reactor.....		239
Appendix VI.....		279

Investigating the Effects of Stove Emissions on Ocular and Cancer Cells	279
Appendix VII. Curriculum Vitae	307

List of Figures

Figure 1.1 The structure of the “Eye”.....	4
Figure 1.2 Structural features of the eye. Many barriers impede delivery to the retina. Selected agents, such as NPs loaded with drugs cannot be efficiently delivered to the retina by topical administration, for example, by using eye drops, because of tear drainage and choroidal blood flow. Systemically administered large NPs enter the retina with great difficulty because of the strict blood-aqueous barrier and the inner and outer blood-retinal barriers. Copyright 2018, Bedia Begüm Karakoçak and Naci Köksal.	5
Figure 2.1 Transmission electron micrographs of synthesized NPS: (a) Au 5-nm sphere, (b) Au 10-nm sphere, (c) Au 20-nm sphere, (d) Au 30-nm sphere, (e) Au 50-nm sphere, (f) Au 100-nm sphere, (g) Au 50-nm cube, and (h) Au 10×90 nm rod.	28
Figure 2.2 (a) Percentage biocompatibility of ARPE-19 cells exposed to Au NPs (Data is represented in log scale for x axis). (b) ARPE-19 cells’ biocompatibility with Au NPs as a function of surface area and particle diameter, with biocompatibility (%) as a function of surface area concentration (cm ² /ml) (Data is represented in log scale for x axis). (c) The critical surface area concentration (LD _{50,A}) for spherical Au NPs was 23 cm ² /ml. The data is normalized using both negative and positive controls. Values are expressed in mean ± for each condition, three independent experiments were done with eight replicates (n=24, *P<0.05 vs controls).	29
Figure 2.3 Electrical cell-substrate impedance sensing measurements for ARPE-19 cells exposed to (a) 5-nm Au spheres, (b) 10-nm Au spheres, (c) 20-nm Au spheres, and (d) 30-nm Au spheres when, at critical concentrations previously detected in MTT assay results, cells started to detach from the culture plate. (e) 50-nm Au spheres with cell detachment unhindered; however, the measured resistance is decreasing as the exposure concentration increases. (f) 100-nm Au spheres with no occurrence of cytotoxic effect. Values are expressed in mean ± SEM with each condition tested at least in triplicate (n=24, **P<0.001 vs. controls).....	31
Figure 2.4 3D Confocal microscopic images of nanoparticles inside cells after 72 h of exposure. (a) cells without nanoparticle exposure, (b) ARPE-19 cells exposed to 5-nm Au sphere (LD _{50,M} : 0.030 mg/ml) with green dots representing Au NPs inside cells in the vicinity of the nucleus and voids (exact areas are shown with white arrows) representing loss of cytoplasm on the observed layer. (c) ARPE-19 cells exposed to 10-nm Au spheres (LD _{50,M} : 0.057 mg/ml, with particles inside cells and nuclei. (d) ARPE-19 cells exposed to 20 nm Au spheres at a critical concentration of LD _{50,M} : 0.113 mg/ml; the presence of particles inside cells and nuclei is confirmed. (e) ARPE-19 cells exposed to 0.129 mg/ml of 30-nm Au spheres. (f) LD _{50,M} :0.050 mg/ml of 10×90 nm Au nanorods inside cells and nuclei. (g) 0.129 mg/ml of 50- nm Au spheres. (h) 0.129 mg/ml of 100-nm Au spheres. Internalization of 50- and 100-nm Au spheres may be hindered by their large size. The available surface area per unit volume, the key metric for biocompatibility, is much less for 50- and 100-nm Au spheres	

compared than for ARPE-19 cells exposed to smaller Au nanospheres. (i) 0.129 mg/ml of Au nanocubes.....33

Figure 2.5 The mechanism of NPs' mediated cytotoxicity is illustrated here by (a) NP exposure to ARPE-19 cell growing in DMEM. (b) Dynamic bi-polymer layer (nano-biointerface) (thick and loose blue color coating) that forms when NPs are mixed with DMEM), creating a superficial surface exposed to the cell membrane. (c-d) NP internalization by endocytosis in which the pH of the endocytic vesicle is same as cell's physiological pH. (e) Fusion of endocytic vesicle with lysosome where pH of lysosome is acidic, (f) Internalized NP in lysosome, where the protein coating, the nano-biointerface, disappears because of degradation of protein by the hydrolytic mechanism of the acid hydrolases enzyme of lysosome. (g) NP can cross a single membrane of lysosome and may penetrate the mitochondrial intermembrane space where the apoptosis signal is initiated. (h) Cytoplasmically accumulated NPs cause cell death by activating subcellular downstream signaling for apoptosis, initializing cell shrinkage, cytoplasm decrease, and the beginning of subcellular fragmentation. For ease of visualizing, the structure of NP and cell is not according to size scale.34

Figure 2.6 The surface area concentration required to affect 50% of the cells ($LD_{50,A}$) is independent from particle size, as is ROS generation. (a) LD_{50} based on surface area concentration (cm^2/ml) versus particle size for two different data sets in which the biocompatibility of Au NPs was tested on different cells. Pan et al. 2005, tested the biocompatibility of Au NPs with HeLa cells whereas we exposed retinal cells to Au NPs. The critical surface area concentration for retinal cells was $23 cm^2/ml$; the $LD_{50,A}$ amount for HeLa cells was $83 cm^2/ml$. (b) Misawa et al. (2011) measured ROS generation for different sizes of Au NPs at different concentrations. The ROS generation is plotted as a function of surface area concentration. (Data is represented in log scale for x axis).37

Figure 3.1 HS-HA synthesis chemistry. In the presence of borate buffer at pH 9, the terminal cyclic hemiacetal ring opens and changes to a linear aldehyde form. A Schiff base forms with cystamine. Thus, the terminal saccharide reverses between two states to reach the final form. The Amadori compound, sodium cyanoborohydride ($NaBH_3CN$), is added, and then Dithiothreitol (DTT) is added to reduce the disulfide and produce HS-HAs.53

Figure 3.2 Illustration of coated Au NPs with end-thiolated HA (HS-HA), where the thiol group at the end of each HA chain is attracted to the Au NP surface.....54

Figure 3.3 Thermal gravimetric analysis plot for the HS-HA coated Au NPs. HA decomposition occurs at around $280 ^\circ C$, and Au NPs melt approximately at $500 ^\circ C$. Au NP grafting density (the number of HA molecules/ nm^2) determined by TOC and TGA measurements. Errors provided reflect standard deviation of the replicate error in repeated measurements of the sample. At least two measurements were taken for each analysis technique.55

Figure 3.4 (A) Cellular uptake of Au NPs of different sizes, with and without HS-HA coating by ARPE-19 cells. (B) 50 nm Au NPs (0.11 mg/ml) exposed to ARPE-19, NIH 3T3, and CHO cells with and without pretreatment with 10x HS-HA. CD44 receptor density of NIH

3T3 cells is significantly less than that of ARPE-19 cells; therefore, blocking the CD44 receptors of NIH 3T3 cells did not significantly affect internalization of HA-S-Au NPs, unlike the results for ARPE-19 and CHO cells. Overall, cells like ARPE-19 and CHO cells, which express high enough number of CD44 receptors and meet the threshold for HA binding, internalize more coated NPs than NIH 3T3 cells. ARPE-19 cells exposed to HA-S-Au NPs, Nascent Au NPs, ARPE-19 cells treated with 10x HS-HA, and then exposed to HA-S-Au NPs.58

Figure 3.5 3D Confocal microscopy images of Au NPs with ARPE-19 cells. The red staining corresponds to actin, the nucleus is blue, and Au NPs are green. ARPE-19 cells exposed to (A) no particles, the negative control. 50-nm (B) nascent Au NPs (C) HA-S-Au NPs (D) ARPE-19 cells pretreated with 10x HS-HA and then exposed to 50-nm HA-S-Au NPs. The HS-HA coating significantly enhanced the intracellular concentration of Au NPs, whereas when the same particles were exposed to the retinal cells after blocking the CD44 receptors, the amount internalized is significantly decreased. The exposure concentration was selected as 0.11 mg/ml. Scale bars are 20 μ m.60

Figure 3.6 Biocompatibility results of (A) nascent Au NPs and (B) HA-S-Au NPs. HS-HA coating significantly increased the compatibility of NPs with ARPE-19 cells. Values are expressed in mean \pm SEM for each condition; three independent experiments were done with eight replicates (n = 24; Student's t-test, *P < 0.05 versus controls). The results were compared to each other using two-factor ANOVA analysis. For nascent particles, in terms of both particle size and exposure concentration, the results were significantly different from each other (*P < 0.05). For coated particles, the results were found to be independent of the exposure concentration (**P > 0.05) but statistically different among each nanoparticle size tested (P* < 0.05).....62

Figure 3.7 Measurement of apoptotic cells amounts using the Apo Tox-GloTM assay when the cells are exposed to (A) nascent Au NPs and (B) HA-S-Au NPs. Measurement of ROS levels using the ROS GloTM H₂O₂ assay, when the cells are exposed to (C) nascent Au NPs and (D) HA-S-Au NPs. The HS-HA coating prevented both apoptosis and ROS generation in ARPE-19 cells for all particle sizes tested. (n = 24; Student's t-test, *P < 0.05 versus controls). The results were compared to each other using two-factor ANOVA analysis. In both measurements, for nascent particles, in terms of both particle size and exposure concentration, the results were significantly different from each other (*P < 0.05). For coated particles, the results were found to be independent of the exposure concentration (**P > 0.05) but statistically different among each nanoparticle size tested (*P < 0.05).....63

Figure 4.1 Schematic CCD-RSM design responses. (A) λ_{ex} = 350 nm, λ_{em} = 460 nm. (B) λ_{ex} = 540 nm, λ_{em} = 600 nm.80

Figure 4.2 (A) Absorbance and (B) PL emission intensities of nCDs at different concentrations with varied amine to acid ratios.....82

Figure 4.3 Fluorescence excitation-emission spectroscopy of nCDs with amine/acid ratios of (A) 0.25, (B) 0.50, (C) 1.00, (D) 1.50, (E) 2.00. The peak for excitation and emission shifts towards near infrared region as the amine to acid ratio increases. All spectra were corrected

for the lamp intensity. The insets of each figures represents synthesized nCDs in DI water, from left to right, the NH ₂ /COOH ratio is increasing from 0.25 to 2.00.	84
Figure 4.4 (A) HR-TEM image of nCDs with amine/acid ratio of 2.0. The particle size distribution is determined to be 4.05±0.46 nm. The lattice spacing is found to be 0.15 nm. (B) AFM images of nCDs with amine/acid ratio of 2.0. The diameter of nCDs is less than 5 nm. (C) Size distribution of nCDs which was determined by measuring the height of 50 single carbon dots observed under AFM.....	86
Figure 4.5 Dynamic light scattering analysis of nCDs with NH ₂ /COOH of 0.25, 0.75, 1.00, 1.50, and 2.00: (A) Hydrodynamic particle size measurement results. (B) Zeta potential measurement results.....	86
Figure 4.6 High-resolution C1s XPS analysis results of nCDs with amine/acid ratios of (A) 0.25, (B) 0.50, (C) 1.00, (D) 1.50, (E) 2.00. Increasing NH ₂ /COOH ratio resulted in an apparent C–N bond formation. (F) Proposed formation mechanism for a possible product (N,N'-substituted-pyrrolo[2,3-b]pyrrole) contributing to red-emissivity of nCDs	88
Figure 4.7 Confocal microscopy images of nCDs excited at four different wavelengths: 405, 488, 532, 635 nm, exposed to (a) retinal pigment epithelial, (b) lens epithelial, (c) CHO cells.	91
Figure 5.1. HA-CQD conjugation chemistry	104
Figure 5.2. A comparison of the ¹ H NMR spectra of (A) HA, (B) CQDs, and (C) HA-CQD conjugate confirms the presence of HA and CQD peaks in the HA-CQD conjugate.	105
Figure 5.3 PL emission spectra of CQDs with an amine to acid ratio of (A) 0.5 and (B) 2.0 and their HA-CQD conjugates when excited at 540 nm.....	106
Figure 5.4 Confocal microscopy images of retinal pigment epithelial cells exposed to 0.6 mg/ml CQDs with and without HA conjugation.	108
Figure 5.5 Biocompatibility results of nCQDs and HA-nCQDs with ARPE-19 cells. (A) % Viability (B) ROS generation (C) Apoptotic cell percentage measurement results after incubation with nCQDs for 24 h at concentrations up to 0.6 mg/mL. Data are expressed as mean ± SD from three independent experiments (*P < 0.05).....	110
Figure 5.6 Ex-vivo pig eyes images of 50 µl intravitreal injections of nascent and HA-coated CQDs. Excitation: 470 nm, Emission: 600 nm. (A) Control, no particle injection. (B) Post-injection of nascent CQDs at 2 minutes. (C) Post-injection of HA-CQDs at 2 minutes.	111
Figure 5.7 Post-mortem mouse images of 100 µl subcutaneous injections of nascent and HA-coated CQDs. Excitation: 685 nm, Emission: 720 nm. (A) Control, no particle injection. (B) Post-injection of nascent CQDs at 2 minutes. (C) Post-injection of HA-CQDs at 2 minutes.	112
Figure 6.1 Structure of Blood Retina Barrier (BRB) and Blood Brain Barrier (BBB) (Adapted from (London et al. 2013)).	121

Figure 6.2 Detailed structure of the Blood Retina Barrier (BRB) and thicknesses of each section. The NP has to travel at least 11 μm while passing at least two layers of cells with tight junctions having an opening of 60 nm..... 122

Figure 6.3 ICP-MS quantification results for the Au NPs that could cross both the tight junctions formed in between the RPE cells and the insert membrane. The amount that is detected in the bottom chamber of the inserts is denoted as % of NPs that can cross the BRB, as this in-vitro experimental design is a widely expected in-vitro model as proof of concept for the NPs crossing the BRB. 128

Figure 6.4 H&E stained optical microscopy images of the eye. (A) The whole cross-section. (B) 40X magnification of the front of the eye, where the cornea is present. (C) 40X magnification of the back of the eye, where the retina is located. The parts of the cornea and retina are labeled. 129

Figure 6.5 Optical microscopy images of a paraffined section of an 8-week old C57BL/6 mouse eye. The main eye sections – cornea, lens, retina, along with RPE cells are labeled. Following the intravitreal injection of Au NPs, the retina was detached. 130

Figure 6.6 Confocal microscopy images of the cornea of an 8-week-old C57BL/6 mouse 24 hours post-injection of (A) nascent Au NPs, (B) HA-S-Au NPs. The nucleus is stained with DAPI and blue in color, and Au NPs are green. There are more HA-coated Au NPs detected in all sections of the cornea. (C) ImageJ analysis quantified the amounts of Au NPs in each section. 131

Figure 6.7 The red staining corresponds to cadherin, a tight junction protein; the nucleus is stained with DAPI and blue, and Au NPs are green. The fourth image in each time point is a merged version of the previous three images. The amount of Au NPs that reached the cornea peaked at 15 minutes post injection, as can be seen. Scale bars are 50 μm 133

Figure 6.8 Au NP quantification results in the cornea. (A) The amount of Au NPs accumulated in each main section of the cornea: endothelium, stroma, and epithelium. (B) The results plotted as a function of time. (C) The cumulative amount of NPs found in the cornea as a function of time. It took more than 5 minutes, and less than 10 minutes for NPs to reach the cornea. The delivered amount of NPs reaching the cornea peaks at minute 15. After minute 25, the amount remaining in the cornea significantly decreases. By the end of 24 hours, only 3.74% of the peak Au NP concentration remains in the cornea. 134

Figure 6.9 The red staining corresponds to cadherin, a tight junction protein, the nucleus is stained with DAPI and blue; and Au NPs are green. The fourth image in each time point is the merged version of all three previous images. The intensity of the signal coming from the second channel is proportional to the amount Au NPs present. The amount of Au NPs that reached the cornea peaked at 60 minutes post injection, as it can be clearly seen. Scale bars are 50 μm 136

Figure 6.10 HA-S-Au NP quantification results in the cornea. (A) The amounts of Au NPs accumulated in each section of the cornea: endothelium, stroma, and epithelium. (B) The precise amounts in each section of the cornea are plotted as a function of time. (C) The

cumulative amount of NPs found in the cornea as a function of time. It took the first NPs less than 5 minutes to reach the cornea. The amount of HA-S-Au NPs reaching the cornea peaks at minute 60. After minute 60, the amount left in the cornea significantly decreases. By the end of 24 hours, 17.10 % of the peak HA-S-Au NP concentration remains in the cornea.... 137

Figure. 6.11 The red staining corresponds to cadherin, a tight junction protein, the nucleus is stained with DAPI and blue; and Au NPs are green. The fourth image in each time point is the merged version of all three previous images. The intensity of the signal coming from the second channel is proportional to the amount of Au NPs present. The amount of Au NPs that reached the retina was peaked at 20 minutes post injection, as it can be clearly distinguished from the images. Scale bars are 50 μm 138

Figure 6.12 Au NP quantification results in the retina. (A) The amount of Au NPs accumulated in each main section of the retina: retinal epithelium, the outer retina, and the inner retina. The outer retina consists of the outer plexiform layer and outer nuclear layer, whereas the inner retina is composed of the inner plexiform layer, inner nuclear layer and the extension of the ganglion cells. (B) The results are plotted as a function of time for each central section of the retina. (C) The cumulative amount of NPs found in the retina as a function of time. The amount of Au NPs reaching the cornea peaks at minute 20. After the end of one hour, the amount remaining in the retina significantly decreases. By the end of 24 hours, 8.55% of the peak Au NP concentration remains in the retina. 139

Figure 6.13 The red staining corresponds to cadherin, a tight junction protein, the nucleus is stained with DAPI and blue; and Au NPs are green. The fourth image in each time point is the merged version of all three previous images. The intensity of the signal coming from the second channel is proportional to the NPs present. The amount of HA-S-Au NPs that reached the retina was peaked at 25 minutes post injection, as it can be clearly distinguished from the images. Scale bars are 50 μm 141

Figure 6.14 HA-S-Au NP quantification results in the retina. (A) The amount of HA-S-Au NPs accumulated in each main section of the retina: retinal epithelium, the outer retina, and the inner retina. The outer retina consists of the outer plexiform layer and outer nuclear layer, whereas the inner retina is composed of the inner plexiform layer, inner nuclear layer and the extension of the ganglion cells. (B) The results are plotted as a function of time for each main section of the retina. (C) The cumulative amount of NPs found in the retina as a function of time. The amount reaches the retina peaks at minute 25. After 24 minutes, the amount remains in the retina significantly decreases. By the end of 24 hours, 12.06% of the peak Au NP concentration remains in the retina. 142

Figure 6.15. Ex-vivo ocular globe images obtained with a small animal imager (excitation $\lambda_{\text{ex}} = 650 \text{ nm}$, $\lambda_{\text{em}} = 700 \text{ nm}$). Porcine ocular globes with nCDs injections. (A) No injection of CDs, control. (B) Post-injection at 6 minutes. (C) Post-injection at 30 minutes..... 143

Figure 6.16. Post-mortem images of mice with nCDs obtained with the small animal imager, Bruker spectral FX. (A) No injection of CDs, control. $\lambda_{\text{ex}} = 550 \text{ nm}$, $\lambda_{\text{em}} = 600 \text{ nm}$. With nCD injections (B) After first injection, $\lambda_{\text{ex}} = 550 \text{ nm}$, $\lambda_{\text{em}} = 600 \text{ nm}$. (C) After second

injection, $\lambda_{ex} = 550 \text{ nm}$, $\lambda_{em} = 600 \text{ nm}$. (D) $\lambda_{ex} = 550 \text{ nm}$, $\lambda_{em} = 700 \text{ nm}$. (E) $\lambda_{ex} = 600 \text{ nm}$, $\lambda_{em} = 750 \text{ nm}$ 144

Figure 6.17. ERG analysis of nascent and HA-S-Au NPs: 1-day post-injection (A) scotopic a-wave (B) scotopic b-wave (C) photopic b-wave and 1-week post-injection (D) scotopic a-wave (E) scotopic b-wave (F) photopic b-wave. The results showed no significant difference among all the measurements obtained. 146

List of Tables

Table 3.1 Gel permeation chromatography results for HS-HA	54
Table 5.1 Experimental conditions (factors) of each synthesis of nCQDs using CCD-RSM design	100

Acknowledgments

I would like to express my deepest and most sincere gratitude to Professors Nathan Ravi and Pratim Biswas, my PhD advisors, for their wise guidance and continuous support of my scientific research. Dr. Ravi introduced me to the amazing world of ophthalmology and visual sciences, while Dr. Biswas introduced me to the marvelous world of aerosol science, and they both shared with me their excitement and knowledge of these two fascinating fields. I am sure that my entire life will benefit greatly from their guidance in both research and conduct.

I thank Professors Rajendra S. Apte, Palghat Ramachandran, and Fuzhong Zhang for serving on my dissertation committee, and providing valuable suggestions to improve this dissertation and my career plan. They are, and will always be, my career role models.

I would like to thank my previous advisors, Professors. Orhan Yenigün (Boğaziçi University) and Dr. John D. Fortner (WUStL) for their patience, endless support, and understanding.

I also thank the colleagues in the Ravi Lab, especially Mr. Paul Hamilton, Jessica Struckhoff, and Sruthi Santhanam, and in the Aerosol & Air Quality Research Laboratory (AAQRL) for providing their help and assistance. The Ravi lab has been a home for me, and all the past and present members have been a huge help. In the AAQRL, we are a big family with a glorious history and bright future, and we are all working hard to make the AAQRL “the world’s best aerosol group”.

In particular, I want to thank Drs. Josh Davis, Jue Liang, and Liang-Yi Lin for their valuable help and guidance on my research, and Drs. Sameer Patel, Anna Leavey, Yao Nie, and Ramesh Raliya for their collaboration on our projects. Many thanks also go to my friends Agnes Terenyi, Drs. Alireza Faghaninia, Chelsea Neil, and Jessica Ray and the staff in the

EECE Department and the School of Engineering and Applied Science. I also would like to thank Dr. Huafang Li, from the Institute of Materials Science and Engineering, for her patience and hands-on instrument training. I am also sincerely thankful to Professor James Ballard from the Engineering Communication Center for helping me edit my manuscripts and dissertation.

For funding, I gratefully acknowledge, the National Institute of Health, the National Eye Institute, a Lacey and Nelson grant, a core grant from the Association for the Prevention of Blindness, and a Veteran Affairs Merit review grant. In addition, I would like to thank the Veteran Affairs Office of Research and Development for a grant to Kelle H. Moley in support of confocal imaging. Partial support from the McDonnell Academy Global Energy and Environment Partnership (MAGEEP) and the Lopata Endowment are also gratefully acknowledged.

Finally, I do want to express my special gratitude to my best friend and lab mate, Shalinee Kavadiya, who was always there for me during my worst and best days. I also would like to thank my colleague Necip Berker Üner for always being there for me whenever I needed help. My dearest uncle, Naci Köksal, has always supported me, and he also provided the outstanding illustrations in this dissertation. Last but not least, countless thanks go to my parents, Nesrin and Muzaffer Karakoçak, and my brother, Barış Can Karakoçak, for their tremendous support and encouragement during my PhD studies.

Bedia Begüm Karakoçak

Washington University in St. Louis

August 2018

Dedicated to Nesrin and Muzaffer Karakoçak

Abstract of The Dissertation

Development and Evaluation of Biocompatible Engineered Nanoparticles for Use in

Ophthalmology

by

Bedia Begüm Karakoçak

Doctor of Philosophy in Energy, Environmental, and Chemical Engineering

School of Engineering and Applied Science

Washington University in St. Louis, 2018

Professor Nathan Ravi, Chair

Professor Pratim Biswas, Co-chair

The synthesis and design of biocompatible nanoparticles for targeted drug delivery and bioimaging requires knowledge of both their potential toxicity and their transport. For both practical and ethical reasons, evaluating exposure via cell studies is a logical precursor to *in vivo* tests. As a step towards clinical trials, this work extensively investigated the toxicity of gold nanoparticles (Au NPs) and carbon dot (CD) nanoparticles as a prelude to their *in vivo* application, focusing specifically on ocular cells. As a further step, it also evaluated their whole-body transport in mice. The research pursued two approaches in assessing the toxicity of engineered nanoparticles and the suitability of their use in targeted delivery and bioimaging applications: (1) *In vitro* (using retinal pigment epithelial, corneal, and lens epithelial cells) (2) *In vivo* (mouse whole body studies).

Part. 1. In the *in vitro* assessments of Part 1, the biocompatibilities of spherical, rod, and cubic shaped Au NPs were compared for different exposure concentrations. Spherical Au NPs were evaluated in particular detail, and a possible toxicity mechanism was proposed, based on the findings of a colorimetric assay, electrical impedance measurements, and

confocal imaging analysis. The assay measured the activity of succinate hydrogenase, a mitochondrial enzyme, while electrical impedance spectroscopy quantified the strength of cell-cell and cell-substrate attachment, a proxy of viability. Finally, confocal imaging analysis verified that the NPs were internalized and confirmed the degree of their toxicity.

Collectively, the data indicated that surface area concentration was the critical toxicity parameter. Subsequently, to create biocompatible Au NPs, a unique end-thiolation of hyaluronic acid was adapted to create homogeneously coated Au NPs. The end-thiolated hyaluronate (HS-HA) coating not only improved the biocompatibility of the Au NPs but also enhanced the internalization rate of the larger Au NPs, which could not enter the cells otherwise.

The first part of this research also studied the synthesis of biocompatible deep red-emissive CDs for bioimaging applications. For this purpose, a central-composite design response surface methodology (CCD-RSM) was utilized. A scalable isolation-free microwave pyrolysis method for synthesizing deep red-emissive nitrogen-doped carbon dots (nCDs) from citric acid and ethylenediamine was successfully developed and optimized. The formation of C–N and the presence of pyrrolic N content proved to be keys to creating red-emissive nCDs. Confocal images demonstrated that the nanoparticles could enter healthy corneal, retinal, and lens epithelial ocular cells, as well as cancerous Chinese Hamster Ovary cells.

Part 2. Building on the results of *in-vitro* testing of the engineered Au NPs and nCDs, in Part 2 we developed protocols for injecting both types of NPs *in-vivo*. Prior to any intravenous or intravitreal injections, a preliminary study tested the ability of Au NPs to cross the tight junctions between retinal pigment epithelial cells. Transwell® permeable supports were used to simulate the blood-retinal barrier (BRB). The results showed that 20 nm Au NPs

successfully crossed the permeable supports covered with confluent retinal pigment epithelial cells. Based on this finding, both intravitreal and intravenous injections of nascent and HS-HA coated Au NPs were tested. The intravitreal injections caused retinal detachment, very probably due to the mechanical intrusion of the injection needle and the volume, albeit small, of the injected NPs. Far more significant and encouraging, intravenously injected coated and uncoated NPs successfully crossed the BRB. As a result of the intravenous injections, it was observed that both coated and uncoated Au NPs were able to cross the blood-retinal barrier. As expected, the numbers of HS-HA-coated Au NPs were significantly higher in specific parts of the retina that contain more CD44 expressing cells, which have cell surface receptors for internalizing HA. Finally, based on the confocal imaging analysis, the NP concentration in each retinal layer was quantified as a function of time, post-injection. The NPs reached the retina in less than 5 minutes and reached a maximum concentration within approximately 20 minutes. Due to the enhanced retention and permeability effect of NPs, 8.5% of the uncoated and 12.1% of the HA-coated NPs that reach the retina remained after 24 hours.

Next, nCDs with and without the HA coating were injected subcutaneously into *post-mortem* mouse and porcine eye globes. *Ex-vivo* porcine eye images showed that intravitreally injected nCDs had effectively diffused through the vitreous to the cornea, and *post-mortem* whole-body mouse images also demonstrated that the nCDs are suitable for bioimaging, excitable in the NIR region with the sensitivity of 15%.

Cumulatively, our observations indicate that HA coated NPs could potentially deliver other payloads such as DNAs, mRNAs, proteins, siRNAs, and drugs into the cells which overexpress CD44 receptors, for example, cancerous and inflammatory cells, thus providing a platform for targeted treatment and imaging of many severe vision-threatening diseases and degenerative conditions.

Chapter 1: Introduction

The results of this chapter have been partially compiled in Karakoçak, B. B., Biswas, P., and Ravi N. (2018). Applications of Gold Nanoparticles in Ophthalmology. Prog. Retin. Eye Res. In preparation.

1.1 Background and Motivation

During the past three decades, nanomaterials have received tremendous attention for their distinctive mechanic, thermal, acoustic, magnetic, electrical, and optical characteristics. At nanometer scale, materials have a high surface area to mass ratio, which gives them novel properties that differ markedly from the same properties exhibited at bulk scale. Worldwide, the nanotechnology sector has achieved a multi-billion US\$ market (Markets 2018).

According to a recent study, from 2014 to 2019 the global market for nanoparticles in the pharmaceutical and biotechnology sectors is expected to increase from \$30 to 80 billion by 2019, with a compound annual growth rate of 22.0% (J. 2014). The annual production of engineered nanoparticles is in the millions of tons, valued at over \$15 billion/year (Li et al. 2016).

Recent advances in the synthesis and biomolecular functionalization of engineered nanoparticles have dramatically expanded their current and potential biomedical applications, including their use as nanoprobes (Leduc et al. 2013) and nanosensors (Swierczewska et al. 2012). Engineered nanoparticles now play significant roles in bioimaging (Koide et al. 1986, McKechnie et al. 1986, Grant et al. 1996, Ruiz-Ederra et al. 2005, Chang 2012), photothermal therapy (Ryu et al. 2012), gene therapy (Shestopalov et al. 2002, Raju et al. 2011), targeted drug delivery, and tissue engineering (Karthikeyan et al. 2010, Parveen et al. 2012, Kompella et al. 2013, Naha et al. 2015).

Specific engineered nanoparticle types are prominent in biomedical applications. Gold nanoparticles (Au NPs) in particular have attractive intrinsic properties, such as high chemical stability (Gao et al. 2012), convenient surface functionalization (Adokoh et al. 2014), unique surface plasmon properties (Diebold and Calonge 2010, Parveen et al. 2012) and anti-angiogenic properties (Arvizo et al. 2010, Jo et al. 2014).

The synthesis of Au NPs is well studied, with established protocols for creating different shapes and sizes (Turkevich et al. 1951, Kimling et al. 2006, Grzelczak et al. 2008, Tyagi et al. 2016). However, their toxic potential is debated, and the toxicity mechanism is still an enigma (Goodman et al. 2004, Alkilany and Murphy 2010, Albanese and Chan 2011, Choi et al. 2012, Fraga et al. 2014).

As another example, carbon dots (CDs), measuring less than 5 nm in diameter, are the subject of several recent studies in bioimaging (Luo et al. 2013, Berezin 2014, Cherukula et al. 2016, Gan et al. 2016). They are particularly interesting for their wavelength dependent excitation/emission behavior (Jiang et al. 2015, Ding et al. 2016), long fluorescence lifetime (Dong et al. 2015), good photostability (Zhang et al. 2015), and relatively high biocompatibility (Tao et al. 2012). With these unique properties, CDs have demonstrated promise for bioimaging applications. (Hola et al. 2014, Choi et al. 2016, Zhang et al. 2016). Especially for bioimaging applications, high quantum yield and near-infrared excitability are key properties for CDs to be worthy of exploring. Up to date, numerous synthesis methods have been developed for synthesis of CDs such as laser ablation, pyrolysis, electrochemical oxidation, hydrothermal reactions, and microwave treatment (Zhu et al. 2009, Zhu et al. 2013, Wang et al. 2014, Wang and Hu 2014, Ding et al. 2016). However, the lack of a facile synthesis method to create red-emissive CDs with high quantum yield has limited their widespread biomedical application.

1.1.1 Ophthalmic uses of engineered nanoparticles: Opportunities and roadblocks

The eye, considered the most complex organ (Fig. 1.1) after the brain, is the window to the colors of life. The retina is an extension of the central nervous system (CNS) because the axons of the retinal ganglion cells originate from the optic nerve. Thus, the eye is also considered to be a part of the central nervous system (London et al. 2013). Eye transplantation

has not been achieved yet due to the complexity of the optic nerve, which has more than 1.2 million nerve fibers (Sanchez et al. 1986, Sivak et al. 2016). Therefore, curing eye diseases is crucial as the eye is the most important sensory organ and has a direct effect on the quality of life.

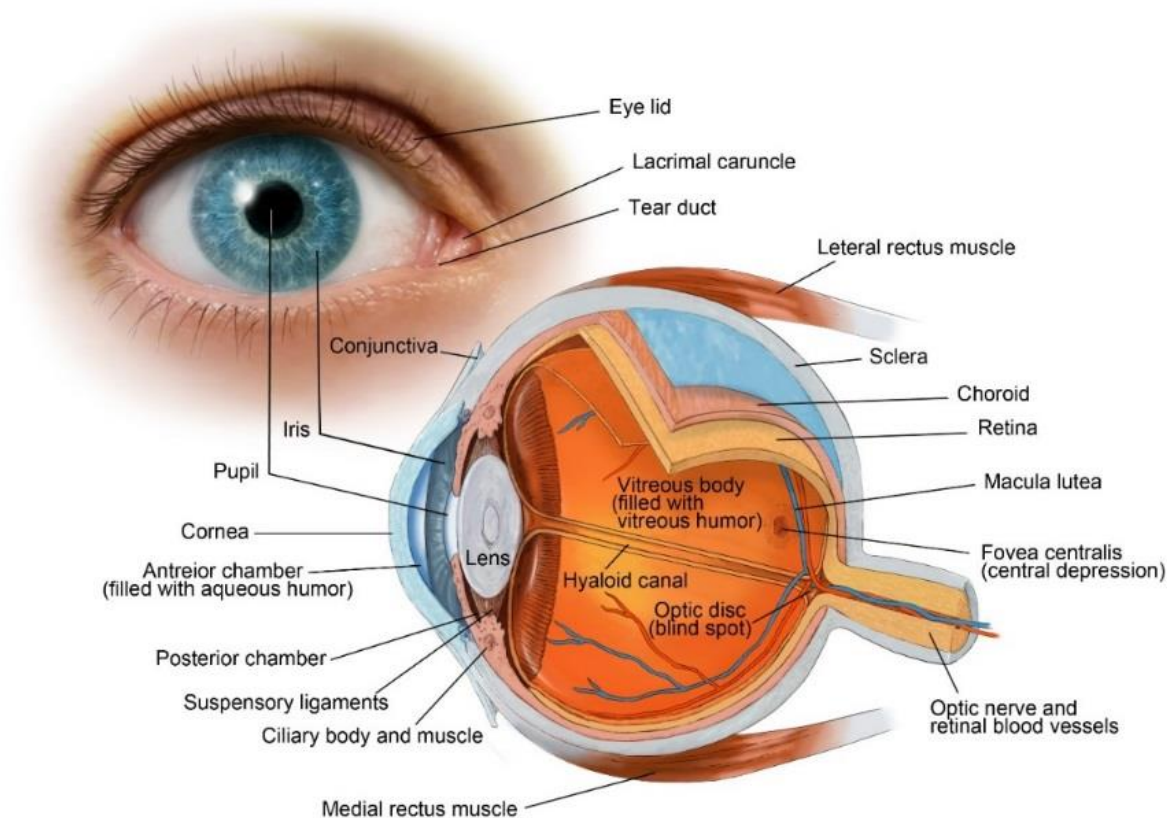


Figure 1.1 The structure of the “Eye”.
Copyright 2018, Bedia Begüm Karakoçak and Naci Köksal

Nanoparticles can serve as a platform both for ocular drug delivery and for imaging. Since the 1985 study of Wood et al. showing the intrinsic capacity of NPs to adhere to the ocular surface and interact with the epithelium, nanotechnological agents to treat eye problems have been sought. NPs can deliver ocular drugs to specific target sites and promise to revolutionize the therapy for many eye diseases (Barar et al. 2008, Diebold and Calonge 2010, Jo et al. 2011, Gonzalez et al. 2013). Numerous reports to date strongly suggest that ocular medicine will benefit greatly from the use of nanotechnology (Diebold et al. 2007, Cai et al. 2008, Conley and Naash 2010, Fischer et al. 2011, Jin Hyung et al. 2011).

In treating the eye, intravenous delivery of nanoparticles is challenged by the first pass losses through the liver and kidneys, and the presence of the blood-retinal barrier. When agents are administered topically, the ocular surface epithelium and tear film, labeled in Fig. 1.2, form external barriers (Barar et al. 2008, Boisselier and Astruc 2009, Choonara et al. 2010, Cunha-Vaz et al. 2011, Honda et al. 2013, Barua and Mitragotri 2014). Due to these barriers, intraocular injections are currently the most common route of administration (Abu El-Asrar and Al-Mezaine 2010, Choonara et al. 2010, Bochot and Fattal 2012, Christoforidis et al. 2012). Topical application remains as an optional route for delivering drugs (Del Amo and Urtti 2008, Chen et al. 2011, Chantalat et al. 2012, Butler et al. 2013, Cho et al. 2015).

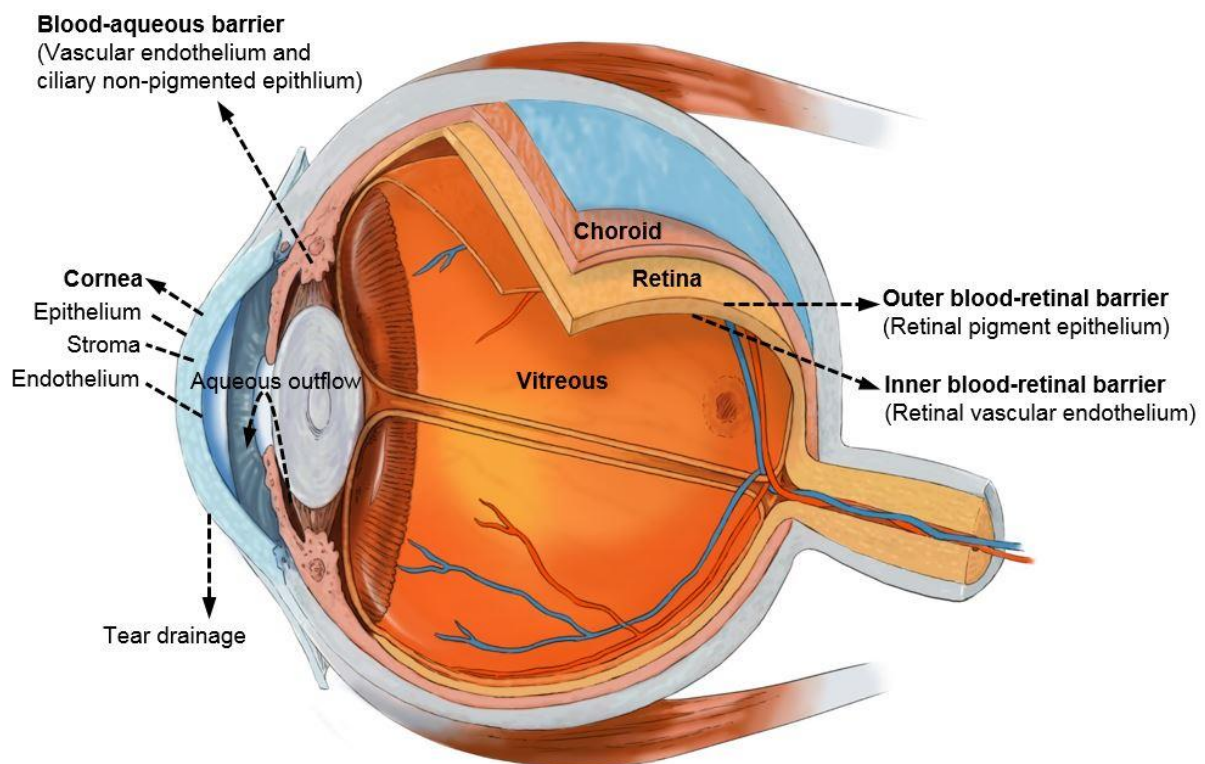


Figure 1.2 Structural features of the eye. Many barriers impede delivery to the retina. Selected agents, such as NPs loaded with drugs cannot be efficiently delivered to the retina by topical administration, for example, by using eye drops, because of tear drainage and choroidal blood flow. Systemically administered large NPs enter the retina with great difficulty because of the strict blood-aqueous barrier and the inner and outer blood-retinal barriers. Copyright 2018, Bedia Begüm Karakoçak and Naci Köksal.

Direct drug administration using either of these two routes can fail to achieve a therapeutic dose, or the dose may not be bioavailable (Avitabile et al. 2001, Duvvuri et al. 2003, Barar et al. 2008, Diebold and Calonge 2010, Gaudana et al. 2010, Kompella et al. 2010). Untargeted delivery of drugs may have side effects, and repeated uncomfortable treatments are not well tolerated by patients. In short, achieving therapeutic drug levels with currently preferred administration routes is difficult. In this regard, the high surface area to volume ratio of nanoparticles is of special interest, particularly where the desired therapeutic drug levels can be achieved without repeated untargeted injections (Diebold et al. 2007, Diebold and Calonge 2010, Kompella et al. 2010, Kompella et al. 2013, Zhou et al. 2013, Azharuddin et al. 2014). Moreover, for topical administration, nanoparticles may provide improved topical passage of large and poorly water-soluble molecules (Poon et al. 2001, Atluri and Mitra 2003, Xiong et al. 2008, Shah et al. 2011).

If the current delivery barriers could be surmounted, ocular disorders such as age-related macular degeneration, glaucoma, and retinal ischemia be potentially treated (Gaudana et al. 2009, Conley and Naash 2010, Fischer et al. 2011, Gonzalez et al. 2013). Conventionally developed drugs elicit a limited response due to rapid removal from the eye by local circulation and eventual systemic absorption. For example, dipivalylepinephrine, flurbiprofen, and timolol have systemic circulation losses of 65%, 74%, and 80%, respectively (Weisse et al. 1995). As a result, these drugs, although FDA approved, mostly fail to effectively treat the target disease (Saettone 2002). Engineering nanoparticles to overcome the current barriers and increase the delivered drug dose can truly promote the effectiveness of curative treatments and potentially introduce alternative treatments for most eye diseases (Jo et al. 2013, Luo et al. 2013, Zhou et al. 2013). Finally, NPs offer the possibility of targeted and controlled drug release, especially for poorly water-soluble drugs, that defeats the ocular barriers and effectively reaches the target. In addition to improving the delivery of poorly water-soluble

drugs, inherently biocompatible nanoparticle systems can potentially reduce toxicity compared to the free drug (Diebold and Calonge 2010).

1.1.2 Engineering nanoparticles to reduce their toxicity, overcome ocular drug delivery barriers, and facilitate imaging

To make full use of nanoparticles, a thorough understanding of their toxic potential is crucial. Classical approaches to predict the toxicity of nanoparticles take into account the level of nanoparticle exposure (mass and number concentration), as well as their size, shape, and coating (Pan et al. 2007, Johnston et al. 2010, Tarantola et al. 2011, Moghadam et al. 2012, Sabella et al. 2014). It has also been shown that nanoparticle toxicity is dependent on the cell type (Coulter et al. 2012, Manshian et al. 2015, Schlinkert et al. 2015). Among these toxicity factors, the incipient nanoparticle exposure concentration, especially given the traditional concentration metrics for assessing toxicity, remains problematic due to the complex interactions of nanoparticles with their environment (Biswas and Wu 2005, Suttiponparnit et al. 2011).

Au NPs have been widely explored in medicine as delivery agents for biopharmaceuticals (Kim et al. 2011, Kumar et al. 2015). Although Au NPs are usually more biocompatible than other metal or metal oxide nanoparticles, their positively charged surface disrupts the negatively charged cell membrane, and their labile surface electrons are involved in reactions that typically produce reactive oxygen species (ROS), causing cytotoxicity (Moghadam et al. 2012). Moreover, plasma proteins can spontaneously adsorb to nascent Au NPs, affecting the surface properties of the particles and influencing their interaction with cells (Nel et al. 2009). As a result, surface modification has been pursued as an essentially ideal way to prevent protein adsorption (Larson et al. 2012) and nonspecific delivery of Au NPs (Rana et al. 2012), to decrease their opsonization by the immune system (Papasani et al. 2012), and finally to mitigate their toxicity.

Ocular imaging is critical in diagnosing, treating, and monitoring the progress of many eye diseases (Nadler et al. 2012). Fluorescence-based methods such as indocyanine green (ICG) angiography remain the gold standard for detecting abnormalities of the choroid vasculature in healthy and diseased eyes. Optical coherence tomography (OCT), typically employing a near-infrared wavelength, is a well-established optical imaging technique. It is non-invasive, non-destructive, and capable of providing micron-scale axial resolution via low-coherence interferometry (Lavers and Zambarakji 2014). The relatively long wavelength light penetrates deep into scattering tissue and media. OCT is used in such fields as dermatology, cardiology, otolaryngology, ophthalmology, and oncology to acquire cross-sectional images of dermal lesions, cardiac vessels, and the retina. In OCT, imaging agents which fluoresce with a high quantum yield at near infrared wavelengths are desired. Carbon-based nanoparticles have been considered as bioimaging agents (Yanai et al. 2012, Saghiri et al. 2015, Saghiri et al. 2015); however, most show intense emission only in the blue-green region following excitation with ultraviolet or blue light which has a relatively shallow penetration depth (Bourlinos et al. 2008, Peng and Travas-Sejdic 2009, Wang et al. 2010, Bourlinos et al. 2012, Zhu et al. 2013, Yang et al. 2015, Qu et al. 2017). A technique to create highly efficient red-emissive carbon dots would significantly extend the reach of ophthalmic imaging. Finally, for ocular imaging applications, targeted delivery may also be desirable depending on the disease to be treated, in other words, the type of cells of interest.

Hyaluronic Acid as a Biocompatible Surface Coating for Targeted Delivery of NPs

Many coating conjugates, ranging from synthetic ligands to natural biomolecules have been used to improve the stability of particles and the efficiency of their delivery to specific cells or tissues (Manson et al. 2011, Lowe et al. 2015, Yilmaz et al. 2016, Lin et al. 2017). Examples include polyethylene glycol, polycarboxybetaine, poly(hydroxy functional acrylates), poly(2-oxazoline)s, poly(vinylpyrrolidone), and poly(glycerol). However, these coating conjugates

suffer from unspecific protein binding and are not specific to cell types, thus making them unsuitable for targeted drug delivery. In this study, we chose hyaluronic acid (HA) as a coating material, because it can prevent adsorption of proteins on the surfaces of biomaterials (Hans and Lowman 2002) and has an antifouling effect that arises from its hydrophilic and polyanionic characteristics (Lee et al. 2008, Santhanam et al. 2015). HA also scavenges free radicals and chelates pro-oxidant metals (Glucksam-Galnoy et al. 2012). It exhibits many desirable physiological properties: For example, it can be either anti-inflammatory or pro-inflammatory, depending on its molecular weight.

HA plays an essential physiological role as a ligand for several cell-surface receptors. Its interaction with cluster of differentiation 44 (CD44), a transmembrane receptor (Jaggupilli and Elkord 2012), is the most well studied. It is present on, for example, the lymphatic vessel endothelial HA receptor (LYVE-1) (Chen et al. 2005), the receptor for hyaluronate-mediated motility (RHAMM) (Nedvetzki et al. 2005), and the HA receptor for endocytosis (HARE) (Pandey and Weigel 2014). Proliferating cells, certain types of epithelial and particularly cancer cells, express CD44 receptors; therefore, HA-conjugated NPs can be selectively delivered to these cells while ensuring that the NPs are biocompatible with the target cell.

Low molecular weight HA (~2500 Da) was shown to disrupt endothelial cell barriers (Lennon et al. 2014). It was also demonstrated that HA aided NPs in passing the BRB transcellularly, via CD44-receptor-mediated endocytosis (Santiago-Tirado et al. 2017), as well as by increasing the permeability of tight paracellular junctions (Kirschner et al. 2010). Because the internalization is based only on the HA coating and not its payload, the HA coating is expected to act as a Trojan horse for delivering NPs into ocular cells without causing additional toxicity.

1.2 Dissertation Outline

This dissertation has two main objectives:

- 1) To evaluate *in vitro* toxicity and create biocompatible-engineered gold nanoparticles and red-emissive carbon dots for targeted delivery and bioimaging applications, respectively.
- 2) To investigate Au NPs' and CDs' effectiveness as delivery and bioimaging agents *in-vivo*.

Each of the five chapters of the dissertation is self-contained, with an introduction, experimental section, results, discussion, and conclusions. Chapters 2 and 3 describe respectively the systematic toxicity assessment of Au NPs and how to overcome this drawback with an end-thiolated hyaluronate coating. These studies identified the potential toxicity of Au NPs with ocular tissue, while offering a representative metric for their toxicity assessment and providing a way to use of Au NPs as delivery agents in ophthalmology. In Chapter 4, we optimize an isolation-free method for synthesizing red-emissive CDs (red-CDs with deep red to NIR fluorescence) as bioimaging agents. This work highlights the use a powerful statistical tool, central-composite design response surface methodology, in constructing experiments which involve multiple parameters. The tool successfully identified the critical parameters in the creation of red emissive CDs. Next, in Chapter 5, we create HA-conjugated CDs and evaluate their internalization rate as well as their biocompatibility with ocular cells. Finally, Chapter 6 investigates the fate and transport of Au NPs in the eye, *in vivo*, following intravitreal and intravenous injections. It also demonstrates the effectiveness of CDs as bioimaging agents in *ex-vivo* porcine eye globes and a *post mortem* mouse model.

1.3. References

1. Abu El-Asrar, A. M. and H. S. Al-Mezaine (2010). "Advances in the treatment of diabetic retinopathy." Discovery Medicine **47**: 363-373.
2. Adokoh, C. K., S. Quan, M. Hitt, J. Darkwa, P. Kumar and R. Narain (2014). "Synthesis and evaluation of glycopolymeric decorated gold nanoparticles functionalized with gold-triphenyl phosphine as anti-cancer agents." Biomacromolecules **15**(10): 3802-3810.
3. Albanese, A. and W. C. W. Chan (2011). "Effect of gold nanoparticle aggregation on cell uptake and toxicity." ACS Nano **5**(7): 5478-5489.
4. Alkilany, A. M. and C. J. Murphy (2010). "Toxicity and cellular uptake of gold nanoparticles: What we have learned so far?" Journal of Nanoparticle Research **12**(7): 2313-2333.
5. Arvizo, R. R., O. R. Miranda, R. Bhattacharya, V. M. Rotello and P. Mukherjee (2010). "Antiangiogenic properties of gold nanoparticles: Effect of size and surface charge." Abstracts of Papers of the American Chemical Society **240**: 1.
6. Atluri, H. and A. K. Mitra (2003). "Disposition of short-chain aliphatic alcohols in rabbit vitreous by ocular microdialysis." Experimental Eye Research **76**(3): 315-320.
7. Avitabile, T., F. Marano, F. Castiglione, C. Bucolo, M. Cro, L. Ambrosio, C. Ferrauto and A. Reibaldi (2001). "Biocompatibility and biodegradation of intravitreal hyaluronan implants in rabbits." Biomaterials **22**(3): 195-200.
8. Azharuddin, M., S. Sahana, H. Datta and A. Dasgupta (2014). "Corneal penetration of gold nanoparticles-therapeutic implications." Journal of Nanoscience and Nanotechnology **14**(8): 5669-5675.
9. Barar, J., A. R. Javadzadeh and Y. Omid (2008). "Ocular novel drug delivery: Impacts of membranes and barriers." Expert Opinion on Drug Delivery **5**(5): 567-581.
10. Barua, S. and S. Mitragotri (2014). "Challenges associated with penetration of nanoparticles across cell and tissue barriers: A review of current status and future prospects." Nano Today **9**(2): 223-243.
11. Berezin, M. Y. (2014). Nanotechnology for Biomedical Imaging and Diagnostics: from Nanoparticle Design to Clinical Applications, John Wiley & Sons.
12. Biswas, P. and C. Y. Wu (2005). "Nanoparticles and the environment." Journal of the Air & Waste Management Association **55**(6): 708-746.
13. Bochot, A. and E. Fattal (2012). "Liposomes for intravitreal drug delivery: A state of the art." Journal of Controlled Release **161**(2): 628-634.
14. Boisselier, E. and D. Astruc (2009). "Gold nanoparticles in nanomedicine: Preparations, imaging, diagnostics, therapies and toxicity." Chemical Society Reviews **38**(6): 1759-1782.
15. Bourlinos, A. B., A. Stassinopoulos, D. Anglos, R. Zboril, V. Georgakilas and E. P. Giannelis (2008). "Photoluminescent carbogenic dots." Chemistry of Materials **20**(14): 4539-4541.
16. Bourlinos, A. B., R. Zboril, J. Petr, A. Bakandritsos, M. Krysmann and E. P. Giannelis (2012). "Luminescent surface quaternized carbon dots." Chemistry of Materials **24**(1): 6-8.
17. Butler, M. R., C. M. Prospero Ponce, Y. E. Weinstock, S. Orengo-Nania, P. Chevez-Barrios and B. J. Frankfort (2013). "Topical silver nanoparticles result in improved bleb function by increasing filtration and reducing fibrosis in a rabbit model of filtration surgery." Investigative Ophthalmology & Visual Science **54**(7): 4982-4990.
18. Cai, X., S. Conley and M. Naash (2008). "Nanoparticle applications in ocular gene therapy." Vision Research **48**(3): 319-324.

19. Chang, H. T., and Chau, L. K. (2012). "From bioimaging to biosensors: Noble metal nanoparticles in biodetection." CRC Press: 322-332.
20. Chantalat, J., E. Bruning, Y. Sun and J. C. Liu (2012). "Application of a topical biomimetic electrical signaling technology to photo-aging: A randomized, double-blind, placebo-controlled trial of a galvanic zinc-copper complex." Journal of Drugs in Dermatology **11**(1): 30-37.
21. Chen, L., C. Cursiefen, S. Barabino, Q. Zhang and M. R. Dana (2005). "Novel expression and characterization of lymphatic vessel endothelial hyaluronate receptor 1 (lyve-1) by conjunctival cells." Investigative Ophthalmology & Visual Science **46**(12): 4536-4540.
22. Chen, W., Z. Li, J. Hu, Z. Zhang, L. Chen, Y. Chen and Z. Liu (2011). "Corneal alternations induced by topical application of benzalkonium chloride in rabbit." PLoS One **6**(10): e26103.
23. Cherukula, K., K. M. Lekshmi, S. Uthaman, K. Cho, C.-S. Cho and I.-K. Park (2016). "Multifunctional inorganic nanoparticles: Recent progress in thermal therapy and imaging." Nanomaterials **6**(4).
24. Cho, W. K., S. Kang, H. Choi and C. R. Rho (2015). "Topically administered gold nanoparticles inhibit experimental corneal neovascularization in mice." Cornea **34**(4): 456-459.
25. Choi, S. Y., S. Jeong, S. H. Jang, J. Park, J. H. Park, K. S. Ock, S. Y. Lee and S. W. Joo (2012). "In vitro toxicity of serum protein-adsorbed citrate-reduced gold nanoparticles in human lung adenocarcinoma cells." Toxicology in Vitro **26**(2): 229-237.
26. Choi, Y., B. Kang, J. Lee, S. Kim, G. T. Kim, H. Kang, B. R. Lee, H. Kim, S. H. Shim, G. Lee, O. H. Kwon and B. S. Kim (2016). "Integrative approach toward uncovering the origin of photoluminescence in dual heteroatom-doped carbon nanodots." Chemistry of Materials **28**(19): 6840-6847.
27. Choonara, Y. E., V. Pillay, M. P. Danckwerts, T. R. Carmichael and L. C. du Toit (2010). "A review of implantable intravitreal drug delivery technologies for the treatment of posterior segment eye diseases." Journal of Pharmaceutical Sciences **99**(5): 2219-2239.
28. Christoforidis, J. B., S. Chang, A. Jiang, J. Wang and C. M. Cebulla (2012). "Intravitreal devices for the treatment of vitreous inflammation." Mediators of Inflammation **2012**: 126463.
29. Conley, S. M. and M. I. Naash (2010). "Nanoparticles for retinal gene therapy." Progress in Retinal Eye Research **29**(5): 376-397.
30. Coulter, J. A., S. Jain, K. T. Butterworth, L. E. Taggart, G. R. Dickson, S. J. McMahon, W. B. Hyland, M. F. Muir, C. Trainor, A. R. Hounsell, J. M. O'Sullivan, G. Schettino, F. J. Currell, D. G. Hirst and K. M. Prise (2012). "Cell type-dependent uptake, localization, and cytotoxicity of 1.9 nm gold nanoparticles." International Journal of Nanomedicine **7**: 2673-2685.
31. Cunha-Vaz, J., R. Bernardes and C. Lobo (2011). "Blood-retinal barrier." European Journal of Ophthalmology **21-6**: 3-9.
32. Del Amo, E. M. and A. Urtti (2008). "Current and future ophthalmic drug delivery systems. A shift to the posterior segment." Drug Discovery Today **13**(3-4): 135-143.
33. Diebold, Y. and M. Calonge (2010). "Applications of nanoparticles in ophthalmology." Progress in Retinal and Eye Research **29**(6): 596-609.
34. Diebold, Y. and M. Calonge (2010). "Applications of nanoparticles in ophthalmology." Progress in Retinal Eye Research **29**(6): 596-609.
35. Diebold, Y., M. Jarrin, V. Saez, E. L. Carvalho, M. Orea, M. Calonge, B. Seijo and M. J. Alonso (2007). "Ocular drug delivery by liposome-chitosan nanoparticle complexes (lcs-*np*)." Biomaterials **28**(8): 1553-1564.

36. Ding, H., S.-B. Yu, J.-S. Wei and H.-M. Xiong (2016). "Full-color light-emitting carbon dots with a surface-state-controlled luminescence mechanism." ACS Nano **10**(1): 484-491.
37. Dong, X. W., L. M. Wei, Y. J. Su, Z. L. Li, H. J. Geng, C. Yang and Y. F. Zhang (2015). "Efficient long lifetime room temperature phosphorescence of carbon dots in a potash alum matrix." Journal of Materials Chemistry C **3**(12): 2798-2801.
38. Duvvuri, S., S. Majumdar and A. K. Mitra (2003). "Drug delivery to the retina: Challenges and opportunities." Expert Opinion on Biological Therapy **3**(1): 45-56.
39. Fischer, N., R. Narayanan, A. Loewenstein and B. D. Kuppermann (2011). "Drug delivery to the posterior segment of the eye." European Journal of Ophthalmology **21-6**: 20-26.
40. Fraga, S., A. Brandao, M. E. Soares, T. Morais, J. A. Duarte, L. Pereira, L. Soares, C. Neves, E. Pereira, M. D. Bastos and H. Carmo (2014). "Short- and long-term distribution and toxicity of gold nanoparticles in the rat after a single-dose intravenous administration." Nanomedicine-Nanotechnology Biology and Medicine **10**(8): 1757-1766.
41. Gan, Z. X., H. Xu and Y. L. Hao (2016). "Mechanism for excitation-dependent photoluminescence from graphene quantum dots and other graphene oxide derivatives: Consensus, debates and challenges." Nanoscale **8**(15): 7794-7807.
42. Gao, J., X. Y. Huang, H. Liu, F. Zan and J. C. Ren (2012). "Colloidal stability of gold nanoparticles modified with thiol compounds: Bioconjugation and application in cancer cell imaging." Langmuir **28**(9): 4464-4471.
43. Gaudana, R., H. K. Ananthula, A. Parenky and A. K. Mitra (2010). "Ocular drug delivery." American Association of Pharmaceutical Scientists **12**(3): 348-360.
44. Gaudana, R., J. Jwala, S. H. Boddu and A. K. Mitra (2009). "Recent perspectives in ocular drug delivery." Pharmaceutical Research **26**(5): 1197-1216.
45. Glucksam-Galnoy, Y., T. Zor and R. Margalit (2012). "Hyaluronan-modified and regular multilamellar liposomes provide sub-cellular targeting to macrophages, without eliciting a pro-inflammatory response." Journal of Controlled Release **160**(2): 388-393.
46. Gonzalez, L., R. J. Loza, K. Y. Han, S. Sunoqrot, C. Cunningham, P. Purta, J. Drake, S. Jain, S. Hong and J. H. Chang (2013). "Nanotechnology in corneal neovascularization therapy--a review." Journal of Ocular Pharmacology and Therapeutics **29**(2): 124-134.
47. Goodman, C. M., C. D. McCusker, T. Yilmaz and V. M. Rotello (2004). "Toxicity of gold nanoparticles functionalized with cationic and anionic side chains." Bioconjugate Chemistry **15**(4): 897-900.
48. Grant, M. B., E. A. Ellis, S. Caballero and R. N. Mames (1996). "Plasminogen activator inhibitor-1 overexpression in nonproliferative diabetic retinopathy." Experimental Eye Research **63**(3): 233-244.
49. Grzelczak, M., J. Perez-Juste, P. Mulvaney and L. M. Liz-Marzan (2008). "Shape control in gold nanoparticle synthesis." Chemical Society Reviews **37**(9): 1783-1791.
50. Hans, M. L. and A. M. Lowman (2002). "Biodegradable nanoparticles for drug delivery and targeting." Current Opinion in Solid State & Materials Science **6**(4): 319-327.
51. Hola, K., Y. Zhang, Y. Wang, E. P. Giannelis, R. Zboril and A. L. Rogach (2014). "Carbon dots-emerging light emitters for bioimaging, cancer therapy and optoelectronics." Nano Today **9**(5): 590-603.
52. Honda, M., T. Asai, N. Oku, Y. Araki, M. Tanaka and N. Ebihara (2013). "Liposomes and nanotechnology in drug development: Focus on ocular targets." International Journal of Nanomedicine **8**: 495-504.
53. J., H. (2014). "Nanoparticles in biotechnology, drug development & drug delivery."
54. Jaggupilli, A. and E. Elkord (2012). "Significance of CD44 and CD24 as cancer stem cell markers: An enduring ambiguity." Clinical & Developmental Immunology: 11-21.

55. Jiang, K., S. Sun, L. Zhang, Y. Lu, A. G. Wu, C. Z. Cai and H. W. Lin (2015). "Red, green, and blue luminescence by carbon dots: Full-color emission tuning and multicolor cellular imaging." Angewandte Chemie-International Edition **54**(18): 5360-5363.
56. Jin Hyoung, K., K. Myung Hun, J. Dong Hyun, Y. Young Suk, L. Tae Geol and K. Jeong Hun (2011). "The inhibition of retinal neovascularization by gold nanoparticles via suppression of vegfr-2 activation." Biomaterials **32**(7): 1865-1871.
57. Jo, D. H., J. H. Kim, T. G. Lee and J. H. Kim (2013). "Nanoparticles in the treatment of angiogenesis-related blindness." Journal of Ocular Pharmacology and Therapeutics **29**(2): 135-142.
58. Jo, D. H., J. H. Kim, J. G. Son, Y. Piao and T. G. Lee (2014). "Inhibitory activity of gold and silica nanospheres to vascular endothelial growth factor (vegf)-mediated angiogenesis is determined by their sizes." Nano Research **7**(6): 844-852.
59. Jo, D. H., T. G. Lee and J. H. Kim (2011). "Nanotechnology and nanotoxicology in retinopathy." International Journal of Molecular Sciences **12**(11): 8288-8301.
60. Johnston, H. J., G. Hutchison, F. M. Christensen, S. Peters, S. Hankin and V. Stone (2010). "A review of the in vivo and in vitro toxicity of silver and gold particulates: Particle attributes and biological mechanisms responsible for the observed toxicity." Critical Reviews in Toxicology **40**(4): 328-346.
61. Karthikeyan, B., K. Kalishwaralal, S. Sheikpranbabu, V. Deepak, R. Haribalaganesh and S. Gurunathan (2010). "Gold nanoparticles downregulate vegf-and il-1 beta-induced cell proliferation through src kinase in retinal pigment epithelial cells." Experimental Eye Research **91**(5): 769-778.
62. Kim, J. H., M. H. Kim, D. H. Jo, Y. S. Yu and T. G. Lee (2011). "The inhibition of retinal neovascularization by gold nanoparticles via suppression of VEGFR-2 activation." Biomaterials **32**(7): 1865-1871.
63. Kimling, J., M. Maier, B. Okenve, V. Kotaidis, H. Ballot and A. Plech (2006). "Turkevich method for gold nanoparticle synthesis revisited." Journal of Physical Chemistry B **110**(32): 15700-15707.
64. Kirschner, N., M. Haftek, C. M. Niessen, M. J. Behne, I. Moll and J. M. Brandner (2010). "CD44 regulates tight junction assembly and barrier function." Experimental Dermatology **19**(2): 214-214.
65. Koide, H., T. Sukanuma, F. Murata and N. Ohba (1986). "Ultrastructural-localization of lectin receptors in the monkey retinal photoreceptors and pigment-epithelium - application of lectin gold complexes on thin-sections." Experimental Eye Research **43**(3): 343-354.
66. Kompella, U. B., A. C. Amrite, R. Pacha Ravi and S. A. Durazo (2013). "Nanomedicines for back of the eye drug delivery, gene delivery, and imaging." Progress in Retinal Eye Research.
67. Kompella, U. B., A. C. Amrite, R. P. Ravi and S. A. Durazo (2013). "Nanomedicines for back of the eye drug delivery, gene delivery, and imaging." Progress in Retinal and Eye Research **36**: 172-198.
68. Kompella, U. B., R. S. Kadam and V. H. Lee (2010). "Recent advances in ophthalmic drug delivery." Therapeutic Delivery **1**(3): 435-456.
69. Kumar, C. S., M. D. Raja, D. S. Sundar, M. G. Antoniraj and K. Ruckmani (2015). "Hyaluronic acid co-functionalized gold nanoparticle complex for the targeted delivery of metformin in the treatment of liver cancer (hepg2 cells)." Carbohydrate Polymers **128**: 63-74.
70. Larson, T. A., P. R. Joshi and K. Sokolov (2012). "Preventing protein adsorption and macrophage uptake of gold nanoparticles via a hydrophobic shield." ACS Nano **6**(10): 9182-9190.

71. Lavers, H. and H. Zambarakji (2014). "Enhanced depth imaging-oct of the choroid: A review of the current literature." Graefes Archive for Clinical and Experimental Ophthalmology **252**(12): 1871-1883.
72. Leduc, C., S. Si, J. Gautier, M. Soto-Ribeiro, B. Wehrle-Haller, A. Gautreau, G. Giannone, L. Cognet and B. Lounis (2013). "A highly specific gold nanoprobe for live-cell single-molecule imaging." Nano Letters **13**(4): 1489-1494.
73. Lee, H., K. Lee, I. K. Kim and T. G. Park (2008). "Synthesis, characterization, and in vivo diagnostic applications of hyaluronic acid immobilized gold nanoprobe." Biomaterials **29**(35): 4709-4718.
74. Lennon, F. E., T. Mirzapioazova, N. Mambetsariev, B. Mambetsariev, R. Salgia and P. A. Singleton (2014). "Transactivation of the receptor-tyrosine kinase ephrin receptor a2 is required for the low molecular weight hyaluronan-mediated angiogenesis that is implicated in tumor progression." Journal of Biological Chemistry **289**(35): 24043-24058.
75. Li, S. Q., Y. H. Ren, P. Biswas and S. D. Tse (2016). "Flame aerosol synthesis of nanostructured materials and functional devices: Processing, modeling, and diagnostics." Progress in Energy and Combustion Science **55**: 1-59.
76. Lin, W. J., W.-C. Lee and M.-J. Shieh (2017). "Hyaluronic acid conjugated micelles possessing cd44 targeting potential for gene delivery." Carbohydrate Polymers **155**: 101-108.
77. London, A., I. Benhar and M. Schwartz (2013). "The retina as a window to the brain-from eye research to cns disorders." Nature Reviews Neurology **9**(1): 44-53.
78. Lowe, S., N. M. O'Brien-Simpson and L. A. Connal (2015). "Antibiofouling polymer interfaces: Poly(ethylene glycol) and other promising candidates." Polymer Chemistry **6**(2): 198-212.
79. Luo, L., X. Zhang, Y. Hirano, P. Tyagi, P. Barabas, H. Uehara, T. R. Miya, N. Singh, B. Archer, Y. Qazi, K. Jackman, S. K. Das, T. Olsen, S. R. Chennamaneni, B. C. Stagg, F. Ahmed, L. Emerson, K. Zygmunt, R. Whitaker, C. Mamalis, W. Huang, G. Gao, S. P. Srinivas, D. Krizaj, J. Baffi, J. Ambati, U. B. Kompella and B. K. Ambati (2013). "Targeted intrareceptor nanoparticle therapy reduces angiogenesis and fibrosis in primate and murine macular degeneration." ACS Nano **7**(4): 3264-3275.
80. Luo, P. G., S. Sahu, S.-T. Yang, S. K. Sonkar, J. Wang, H. Wang, G. E. LeCroy, L. Cao and Y.-P. Sun (2013). "Carbon "quantum" dots for optical bioimaging." Journal of Materials Chemistry B **1**(16): 2116-2127.
81. Manshian, B. B., S. J. Soenen, A. Al-Ali, A. Brown, N. Hondow, J. Wills, G. J. S. Jenkins and S. H. Doak (2015). "Cell type-dependent changes in cdse/zns quantum dot uptake and toxic endpoints." Toxicological Sciences **144**(2): 246-258.
82. Manson, J., D. Kumar, B. J. Meenan and D. Dixon (2011). "Polyethylene glycol functionalized gold nanoparticles: The influence of capping density on stability in various media." Gold Bulletin **44**(2): 99-105.
83. Markets, R. a. (2018). "Nanotechnology market outlook 2020."
84. McKechnie, N. M., S. Almahdawi, G. Dutton and J. V. Forrester (1986). "Ultrastructural-localization of retinal s-antigen in the human retina." Experimental Eye Research **42**(5): 479-487.
85. Moghadam, B. Y., W. C. Hou, C. Corredor, P. Westerhoff and J. D. Posner (2012). "Role of nanoparticle surface functionality in the disruption of model cell membranes." Langmuir **28**(47): 16318-16326.
86. Nadler, Z., G. Wollstein, H. Ishikawa and J. S. Schuman (2012). "Clinical application of ocular imaging." Optometry and Vision Science **89**(5): E543-553.
87. Naha, P. C., P. Chhour and D. P. Cormode (2015). "Systematic in vitro toxicological screening of gold nanoparticles designed for nanomedicine applications." Toxicology in Vitro **29**(7): 1445-1453.

88. Nedvetzki, S., E. Gonen, N. Assayag, R. Reich, R. O. Williams, R. L. Thurmond, J. F. Huang, B. A. Neudecker, F. S. Wang, E. A. Turley and D. Naor (2005). "Rhamm, a receptor for hyaluronan-mediated motility, compensates for CD44 in inflamed CD44-knockout mice: A different interpretation of redundancy (vol 101, pg 18081, 2004)." Proceedings of the National Academy of Sciences of the United States of America **102**(4): 1263-1263.
89. Nel, A. E., L. Madler, D. Velegol, T. Xia, E. M. V. Hoek, P. Somasundaran, F. Klaessig, V. Castranova and M. Thompson (2009). "Understanding biophysicochemical interactions at the nano-bio interface." Nature Materials **8**(7): 543-557.
90. Pan, Y., S. Neuss, A. Leifert, M. Fischler, F. Wen, U. Simon, G. Schmid, W. Brandau and W. Jahnen-Dechent (2007). "Size-dependent cytotoxicity of gold nanoparticles." Small **3**(11): 1941-1949.
91. Pandey, M. S. and P. H. Weigel (2014). "Hyaluronic acid receptor for endocytosis (hare)-mediated endocytosis of hyaluronan, heparin, dermatan sulfate, and acetylated low density lipoprotein (acldl), but not chondroitin sulfate types a, c, d, or e, activates nf-kappa b-regulated gene expression." Journal of Biological Chemistry **289**(3): 1756-1767.
92. Papasani, M. R., G. K. Wang and R. A. Hill (2012). "Gold nanoparticles: The importance of physiological principles to devise strategies for targeted drug delivery." Nanomedicine-Nanotechnology Biology and Medicine **8**(6): 804-814.
93. Parveen, S., R. Misra and S. K. Sahoo (2012). "Nanoparticles: A boon to drug delivery, therapeutics, diagnostics and imaging." Nanomedicine-Nanotechnology Biology and Medicine **8**(2): 147-166.
94. Peng, H. and J. Travas-Sejdic (2009). "Simple aqueous solution route to luminescent carbogenic dots from carbohydrates." Chemistry of Materials **21**(23): 5563-5565.
95. Poon, A. C., G. Geerling, J. K. Dart, G. E. Fraenkel and J. T. Daniels (2001). "Autologous serum eyedrops for dry eyes and epithelial defects: Clinical and in vitro toxicity studies." British Journal of Ophthalmology **85**(10): 1188-1197.
96. Qu, D., X. Miao, X. Wang, C. Nie, Y. Li, L. Luo and Z. Sun (2017). "Se & n co-doped carbon dots for high-performance fluorescence imaging agent of angiography." Journal of Materials Chemistry B **5**(25): 4988-4992.
97. Raju, H. B., Y. Hu, A. Vedula, S. R. Dubovy and J. L. Goldberg (2011). "Evaluation of magnetic micro- and nanoparticle toxicity to ocular tissues." Plos One **6**(5): e17452.
98. Rana, S., A. Bajaj, R. Mout and V. M. Rotello (2012). "Monolayer coated gold nanoparticles for delivery applications." Advanced Drug Delivery Reviews **64**(2): 200-216.
99. Ruiz-Ederra, J., M. Garcia, M. Hernandez, H. Urcola, E. Hernandez-Barbachana, J. Araiz and E. Vecino (2005). "The pig eye as a novel model of glaucoma." Experimental Eye Research **81**(5): 561-569.
100. Ryu, J. H., H. Koo, I. C. Sun, S. H. Yuk, K. Choi, K. Kim and I. C. Kwon (2012). "Tumor-targeting multi-functional nanoparticles for theragnosis: New paradigm for cancer therapy." Advanced Drug Delivery Reviews **64**(13): 1447-1458.
101. Sabella, S., R. P. Carney, V. Brunetti, M. A. Malvindi, N. Al-Juffali, G. Vecchio, S. M. Janes, O. M. Bakr, R. Cingolani, F. Stellacci and P. P. Pompa (2014). "A general mechanism for intracellular toxicity of metal-containing nanoparticles." Nanoscale **6**(12): 7052-7061.
102. Saettone, M. F. (2002). "Progress and problems in ophthalmic drug delivery." Business Briefing: Pharmatech **1**: 167-171.
103. Saghiri, M. A., A. Asatourian, J. Orangi, C. M. Sorenson and N. Sheibani (2015). "Functional role of inorganic trace elements in angiogenesis--part I: N, Fe, Se, P, Au, and Ca." Critical Reviews in Oncology and Hematology **96**(1): 129-142.

104. Saghiri, M. A., A. Asatourian, J. Orangi, C. M. Sorenson and N. Sheibani (2015). "Functional role of inorganic trace elements in angiogenesis-part II: Cr, Si, Zn, Cu, and S." Critical Reviews in Oncology and Hematology **96**(1): 143-155.
105. Sanchez, R. M., G. R. Dunkelberger and H. A. Quigley (1986). "The number and diameter distribution of axons in the monkey optic-nerve." Investigative Ophthalmology & Visual Science **27**(9): 1342-1350.
106. Santhanam, S., J. Liang, R. Baid and N. Ravi (2015). "Investigating thiol-modification on hyaluronan via carbodiimide chemistry using response surface methodology." Journal of Biomedical Materials Research Part A **103**(7): 2300-2308.
107. Santiago-Tirado, F. H., M. D. Onken, J. A. Cooper, R. S. Klein and T. L. Doering (2017). "Trojan horse transit contributes to blood-brain barrier crossing of a eukaryotic pathogen." American Society for Microbiology **8**(1): 16-23.
108. Schlinkert, P., E. Casals, M. Boyles, U. Tischler, E. Hornig, N. Tran, J. Y. Zhao, M. Himly, M. Riediker, G. J. Oostingh, V. Puentes and A. Duschl (2015). "The oxidative potential of differently charged silver and gold nanoparticles on three human lung epithelial cell types." Journal of Nanobiotechnology **13**: 18.
109. Shah, H. K., J. A. Conkie, R. C. Tait, J. R. Johnson and C. G. Wilson (2011). "A novel, biodegradable and reversible polyelectrolyte platform for topical-colonic delivery of pentosan polysulphate." International Journal of Pharmaceutics **404**(1-2): 124-132.
110. Shestopalov, V. I., H. Missey and S. Bassnett (2002). "Delivery of genes and fluorescent dyes into cells of the intact lens by particle bombardment." Experimental Eye Research **74**(5): 639-649.
111. Sivak, W. N., E. H. Davidson, C. Komatsu, Y. Li, M. R. Miller, J. S. Schuman, M. G. Solari, G. Magill and K. M. Washington (2016). "Ethical considerations of whole-eye transplantation." The Journal of Clinical Ethics **27**(1): 64-67.
112. Suttiponparnit, K., J. Jiang, M. Sahu, S. Suvachittanont, T. Charinpanitkul and P. Biswas (2011). "Role of surface area, primary particle size, and crystal phase on titanium dioxide nanoparticle dispersion properties." Nanoscale Research Letters **6**.
113. Swierczewska, M., G. Liu, S. Lee and X. Y. Chen (2012). "High-sensitivity nanosensors for biomarker detection." Chemical Society Reviews **41**(7): 2641-2655.
114. Tao, H. Q., K. Yang, Z. Ma, J. M. Wan, Y. J. Zhang, Z. H. Kang and Z. Liu (2012). "In vivo nir fluorescence imaging, biodistribution, and toxicology of photoluminescent carbon dots produced from carbon nanotubes and graphite." Small **8**(2): 281-290.
115. Tarantola, M., A. Pietuch, D. Schneider, J. Rother, E. Sunnick, C. Rosman, S. Pierrat, C. Sonnichsen, J. Wegener and A. Janshoff (2011). "Toxicity of gold-nanoparticles: Synergistic effects of shape and surface functionalization on micromotility of epithelial cells." Nanotoxicology **5**(2): 254-268.
116. Turkevich, J., P. C. Stevenson and J. Hillier (1951). "A study of the nucleation and growth processes in the synthesis of colloidal gold." Discussions of the Faraday Society (11): 55-&.
117. Tyagi, H., A. Kushwaha, A. Kumar and M. Aslam (2016). "A facile ph controlled citrate-based reduction method for gold nanoparticle synthesis at room temperature." Nanoscale Research Letters **11**(1): 362.
118. Wang, F., S. P. Pang, L. Wang, Q. Li, M. Kreiter and C. Y. Liu (2010). "One-step synthesis of highly luminescent carbon dots in noncoordinating solvents." Chemistry of Materials **22**(16): 4528-4530.
119. Wang, T., L. X. Wang, D. L. Wu, W. Xia, H. Y. Zhao and D. Z. Jia (2014). "Hydrothermal synthesis of nitrogen-doped graphene hydrogels using amino acids with different acidities as doping agents." Journal of Materials Chemistry A **2**(22): 8352-8361.

120. Wang, Y. F. and A. G. Hu (2014). "Carbon quantum dots: Synthesis, properties and applications." Journal of Materials Chemistry C **2**(34): 6921-6939.
121. Weisse, I., O. Hockwin, K. Gree and R. C. Tripathi (1995). Ocular Toxicology, Springer.
122. Xiong, C., D. Chen, J. Liu, B. Liu, N. Li, Y. Zhou, X. Liang, P. Ma, C. Ye, J. Ge and Z. Wang (2008). "A rabbit dry eye model induced by topical medication of a preservative benzalkonium chloride." Investigative Ophthalmology & Visual Sciences **49**(5): 1850-1856.
123. Yanai, A., U. O. Hafeli, A. L. Metcalfe, P. Soema, L. Addo, C. Y. Gregory-Evans, K. Po, X. H. Shan, O. L. Moritz and K. Gregory-Evans (2012). "Focused magnetic stem cell targeting to the retina using superparamagnetic iron oxide nanoparticles." Cell Transplantation **21**(6): 1137-1148.
124. Yang, Y. M., W. Q. Kong, H. Li, J. Liu, M. M. Yang, H. Huang, Y. Liu, Z. Y. Wang, Z. Q. Wang, T. K. Sham, J. Zhong, C. Wang, Z. Liu, S. T. Lee and Z. H. Kang (2015). "Fluorescent n-doped carbon dots as in vitro and in vivo nanothermometer." ACS Applied Materials & Interfaces **7**(49): 27324-27330.
125. Yilmaz, G., B. Demir, S. Timur and C. R. Becer (2016). "Poly(methacrylic acid)-coated gold nanoparticles: Functional platforms for theranostic applications." Biomacromolecules **17**(9): 2901-2911.
126. Zhang, J. X., M. Zheng, F. L. Zhang, B. Xu, W. J. Tian and Z. G. Xie (2016). "Supramolecular hybrids of aiegen with carbon dots for noninvasive long-term bioimaging." Chemistry of Materials **28**(23): 8825-8833.
127. Zhang, Y., Y. J. Shen, X. Y. Teng, M. Q. Yan, H. Bi and P. C. Morais (2015). "Mitochondria-targeting nanoplatfrom with fluorescent carbon dots for long time imaging and magnetic field-enhanced cellular uptake." ACS Applied Materials & Interfaces **7**(19): 10201-10212.
128. Zhou, H. Y., J. L. Hao, S. Wang, Y. Zheng and W. S. Zhang (2013). "Nanoparticles in the ocular drug delivery." International Journal of Ophthalmology **6**(3): 390-396.
129. Zhu, H., X. L. Wang, Y. L. Li, Z. J. Wang, F. Yang and X. R. Yang (2009). "Microwave synthesis of fluorescent carbon nanoparticles with electrochemiluminescence properties." Chemical Communications(34): 5118-5120.
130. Zhu, S. J., Q. N. Meng, L. Wang, J. H. Zhang, Y. B. Song, H. Jin, K. Zhang, H. C. Sun, H. Y. Wang and B. Yang (2013). "Highly photoluminescent carbon dots for multicolor patterning, sensors, and bioimaging." Angewandte Chemie-International Edition **52**(14): 3953-3957.

Chapter 2: Biocompatibility of Gold Nanoparticles in Retinal Pigment Epithelial Cell Line

The results of this chapter have been reprinted with permission from Karakoçak, B. B., Raliya, R., Davis J. T., Chavalmane S., Wang, W.-N., Ravi, N., Biswas, P. (2016). Biocompatibility of Gold Nanoparticles in Retinal Pigment Epithelial Cell Line. Toxicol. In Vitro. 37:61-69. Copyright 2016 Elsevier

Supplementary information along with figures and tables are available in Appendix I

Abstract

Gold nanoparticles (Au NPs) have been tested as targeted delivery agents because of their high chemical stability and surface plasmon properties. Here, we investigated the biocompatibility of Au spheres (5-, 10-, 20-, 30-, 50- and 100-nm), cubes (50-nm), and rods (10×90nm) on a retinal pigment epithelial (ARPE-19) cell line. The lethal dose for killing 50% of the cells (LD_{50}) was evaluated using an MTT (3-[4, 5 dimethyl-thiazoly-2-yl] 2-5 diphenyl tetrazolium bromide) assay. At and above LD_{50} , based on mass concentrations, the confluent cell layer began to detach, as shown by real-time measurements of electric impedance. We found that the biocompatibility of spheres improved with increasing nanoparticle size. The Au rods were less biocompatible than 10-nm spheres. Confocal microscopy showed that cubic (50-nm) and spherical NPs (50- and 100-nm) neither had cytotoxic effects nor entered cells. Lethal doses for internalized spherical NPs, which were toxic, were recalculated based on surface area ($LD_{50,A}$) concentrations. Indeed, when biocompatibility was expressed as the surface area concentration of NPs, the curve was independent of size. The $LD_{50,A}$ of Au nanospheres was $23 \text{ cm}^2/\text{ml}$. Our findings demonstrate that the sole modulation of the surface area would make it possible to use Au NPs for therapeutic purposes.

2.1 Introduction

Materials at the nanometer scale have a large surface area to mass ratio, which gives them novel properties that differ markedly from those of other material properties with corresponding bulk sizes. Recent advances in the synthesis and biomolecular functionalization of engineered nanoparticles have led to a dramatic expansion of their potential biomedical applications, including their use as nanoprobe (Leduc et al. 2013), nanosensors (Swierczewska et al. 2012) and in bioimaging (Ruiz-Ederra et al. 2005, Peng et al. 2006), photothermal therapy (Ryu et al. 2012), gene therapy (Shestopalov et al. 2002, Raju et al. 2011), targeted drug delivery, and tissue engineering (Parveen et al. 2012, Kompella et al. 2013, Austin et al. 2015, Naha et al. 2015). Specifically, gold nanoparticles (Au NPs) are being used because of their intrinsic characteristics, such as high chemical stability, suitable surface functionalization, and unique surface plasmon properties (Diebold and Calonge 2010, Parveen et al. 2012).

Researchers have attempted nanoparticle-mediated drug and gene delivery to tissues of the eye, including the retina, to treat major eye diseases such as age-related macular degeneration and diabetes-related retinopathy (Jin Hyoung et al. 2011, Li et al. 2012, Ngwa et al. 2012, Ngwa et al. 2012, Joris et al. 2013). Moreover, intravitreal injection of Au NPs has been investigated for retinal imaging and inhibition of angiogenesis to prevent macular degeneration (Jeong Hun et al. 2009, Farjo and Ma 2010). Au NPs have been shown to be promising agents for enhanced delivery of anti-VEGF antibody or other antiangiogenic agents to specific sites in the eye (Hayashi et al. 2009, Jeong Hun et al. 2009, Diebold and Calonge 2010). Currently, intravitreal and topical routes are most commonly used (Hayashi et al. 2009).

The use of intravitreal injection of nanoparticles depends on the safety of the particles (Biswas and Wu 2005, Diebold and Calonge 2010, Kompella et al. 2013). Therefore, safety concerns necessitate a better understanding of the potential toxicity hazards of novel materials. One method of measuring toxicity is to examine cellular viability (Abe and Saito 1999) by determining the lethal dose concentration (LD_{50}), the dose required to kill 50% of the cells. Lethal doses of selected nanoparticles will provide guidance as to safe levels of use for nanomedicine applications.

In this chapter, we report on the *in-vitro* biocompatibility of Au NPs with spontaneously arising retinal pigment epithelial (ARPE-19) cells. This cell line is an acceptable alternative to repeated isolation and standardization of primary RPE cells (Dunn et al., 1996; Pfeffer and Philp, 2014), provided that its detailed physicochemical characterization is closely similar to that of primary cells for toxicity evaluation. Although important research has been done on Au NPs (Bakri et al., 2008b, a; Cho et al., 2011; Pan et al., 2007b; Soderstjerna et al., 2014) on various cell lines, no studies have correlated the size, shape, and surface area of the administered Au NPs while reporting biocompatibility with the RPE cells. In the present study, we provided a comprehensive picture of physico-chemical characteristics of NPs and correlated these characteristics to their biocompatibility because it is crucial to predict the response of the targeted retinal cells to the Au NP exposure.

The effect of Au NP shape (spherical, cubic, and rod; size 5-100 nm), and concentration (up to 5 mg/ml) on toxicity was assessed by MTT (3-[4, 5 dimethyl-thiazoly-2-yl] 2-5 diphenyl tetrazolium bromide) assay. In our study, the exposure period was a minimum of 72 h, which is long enough for gold nanoparticles to reach the cells (Bejjani et al. 2005, Cohen et al. 2014) for biocompatibility assessment. To better understand the effect of Au NP on cell toxicity, the electrical impedance of the cells was monitored continuously for 96 h. Furthermore, the presence or absence of NPs inside the cell was verified using plasmonic imaging by confocal

microscopy. The correlation was developed for LD₅₀ of Au NPs regarding the mass and surface area concentration to toxicity. A mechanistic description of NP toxicity interactions with ARPE-19 cells is presented, along with a simple universal toxicity curve that may apply to all cell types.

2.2 Materials and Methods

The experimental setup for particle generation and measurement (Figure 2.1), methods for data inversion, and the experimental plan are described as follows.

2.2.1 Synthesis of gold nanoparticles

Au nanoparticles shaped as spheres, cubes, or rods at sizes from 5 to 100 nm were synthesized using a seed-mediated approach (Jana et al. 2001, Wu et al. 2010). Details are provided in the supplementary information.

2.2.2 Characterization of nanoparticles and exposure to ARPE-19 cell line

Synthesized NPs were characterized by their size, shape, and agglomeration state by transmission electron microscopy (TEM). To confirm the size and the morphology of the Au NPs, micrographs were taken using an FEI Spirit TEM (Hillsboro, OR, USA) operated at 120 kV. The hydrodynamic diameter and zeta potential of NPs in solution before and after their exposure to cell culture medium was measured using dynamic light scattering (DLS). Batch mode measurements were done using a Malvern Zetasizer Nano ZS (Malvern Instruments, Westborough MA). Quantitative determination of gold (Au) concentrations in stock solutions and aliquots before confocal imaging was done with an inductively coupled plasma spectrophotometer, ICP-MS (Elan DRC II, Perkin Elmer, Norwalk, CT).

2.2.3 Biocompatibility assessment of the Au NPs with the ARPE-19 cell line

Since animal cell culture is sensitive to microbial contamination, Au NP solutions were checked for microbial growth before cell exposure. Tests for bacterial and fungal

contamination, respectively, were performed on nutrient agar and potato dextrose agar plates both at room temperature and 37°C.

In a flat-bottom, 96-well plates, 150 μL volumes (1.2×10^4 cells per well) of cells were incubated (37°C, 5% CO_2) until confluent (supplementary information, Fig. S1), then exposed to different concentrations of NPs. Physically characterized particles were dispersed in cell culture medium containing Dulbecco's Modified Eagle Medium/Ham's F-12 (DMEM/F-12), 10% fetal calf serum (FCS), and antibiotics (C-DMEM/F12) to be used for cell exposure. For each shape and size of Au NPs, concentrations of the exposed solutions were 0.01, 0.05, 0.1, 0.25, 0.5, 0.75, 1, 2.5, and 5 mg/ml. The upper limit of exposure concentration was determined by NP's toxic potential reported in the literature (Pan et al. 2007, Hayashi et al. 2009, Jin Hyoung et al. 2011, Choi et al. 2012, Naha et al. 2015). Nanoparticle exposure duration was a minimum of 72 h.

The viability of ARPE-19 cells, defined as their ability to maintain its growth, was evaluated using the MTT assay, which is widely used for *in-vitro* nanotoxicity assessment (Dumortier et al. 2006, Sayes et al. 2007, Warheit et al. 2007, Conde et al. 2014). This technique, while requires the acquisition of optical density at a single wavelength has advantages over other toxicity assays because it requires minimal physical manipulation of ARPE-19 cells and yields quick, reproducible results. Following the exposure of NPs, 100 μL of MTT (1 mg/mL in growth medium) was added to each well, after which the plate was further incubated for 5 h at 37°C in 5% CO_2 . The resulting blue component, produced by the reduction of tetrazolium salt of MTT by mitochondrial dehydrogenase enzyme, was dissolved in 100 μL dimethyl sulfoxide (DMSO). The optical density of the colored product was read photometrically using a spectrophotometer at 540 nm. Possible interactions between the nanoparticles and the formazan crystals, which form as a result of the reduction of MTT dye, can be minimized by selection of the proper dissolution solvent, DMSO, and adjusting the dye concentration as

well as the volume added to each well (Kong et al. 2011, Sylvester 2011). On the other hand, the spectrophotometer plate readings for both positive controls where the ARPE-19 cells were not exposed to Au NPs, and negative controls where the cells were exposed to Au NPs but not treated with MTT were also taken. The results were normalized based on both positive and negative controls. The percentage viability of ARPE-19 cells was calculated using the following formula:

$$\text{Biocompatibility (Cell Viability)} = \left(\frac{\text{Mean optical density of the sample}}{\text{Control optical density}} \right) \times 100 \quad (2.1)$$

The lethal dose is typically reported as the mass concentration of NPs at which the biocompatibility is 50%. LD₅₀ values, based on mass concentration, were calculated by using a four-parameter logistic equation. Data were plotted as sigmoidal dose-response curves using Systat SigmaPlot 11.0 software. LD_{50,M} values were derived from three independent experiments in which eight-well replicate measurements were done. In this work, LD₅₀ values are defined based on both mass concentration (LD_{50,M}) and surface area concentration (LD_{50,A}).

The cellular characteristics were also analyzed using electric cell-substrate impedance sensing (ECIS), a noninvasive technique that continuously measures the impedance across gold electrodes present at the bottom of tissue culture wells using various frequencies of alternating current (Wegener et al. 2000, Arndt et al. 2004). As the cell morphology and attachment via adhesion proteins (Hall et al. 1987, Borradori and Sonnenberg 1999) to the electrodes in the bottom of the well changes, the resistance across the electrodes also changes. The change in resistance at different frequencies from 400 to 64,000 Hz can be measured over time. The impedance at low frequency (less than 4,000 Hz) represents paths around the cells and, hence, the layer's cell-to-cell barrier functions (Arndt et al. 2004). At a frequency of 4,000 Hz, the contribution of resistance through the cells was dominant and, at much higher frequencies

(8,000 to 64,000 Hz), the contribution is primarily from Au NPs with medium (Kandasamy et al. 2010). Hence, a frequency of 4,000 Hz was chosen to monitor cell growth characteristics.

Cells were studied at high density and in confluence to closely mimic the natural structure and physiology of the retinal pigmented epithelial cell monolayer. Before the addition of nanoparticles, the confluency was confirmed by ECIS (supporting information, Fig. S1). Cells were plated in a 96-well ECIS array identical to those plated for the MTT assay. The resistance of cells was monitored for 24 h to ensure confluency before the addition of Au NPs. The Au NP solution was introduced on top of the cells at room temperature under sterile conditions.

All tissue culture data (both MTT and ECIS) were expressed as the mean \pm standard error of the mean (SEM) values of at least three independent culture experiments. Eight replicates were performed for each independent cell culture experiment. Statistical significance was evaluated using ANOVA (analysis of variance) to compare with the respective positive (untreated cells) and negative (NPs without the cells) control groups. $P^* < 0.05$, $P^{**} < 0.001$, the significance level, was statistically acceptable.

To confirm the presence of NPs inside cells, we investigated the distribution of the Au NPs at their critical mass concentrations ($LD_{50, M}$) using a nanoplasmonic confocal laser scanning microscope (LEICA TCS-SP8). The gold nanoparticles have surface plasmon resonance property (SPR). For the size range of 5-100 nm, for gold nanoparticles, the SPR wavelength is around 520 nm (Huang et al. 2008) depending on the size of the nanoparticles as also confirmed by our UV-Vis measurements (Supplementary information Fig. S2). Three lasers were used during Confocal imaging (405, 532, and 635 nm). Thus, the detection range is 405-635 nm which is a wide enough range to detect all sizes of Au NPs in this study.

ARPE19 cells were seeded in CELLview™ plates at 5×10^4 cells/well for 24 h. After 72 h of NP exposure, the cells were fixed and washed with PBS three times before imaging (supplementary information). During confocal imaging, 45 images were taken through different optical sections by collecting Z-stacks with a thickness of 100 nm. A control sample was prepared with and without cells in the absence of nanoparticles.

To identify the difference between the administered and delivered doses, the amount of nanoparticles that failed to enter the cell was quantified in the aliquot obtained from the PBS washes prior to confocal imaging. Using ICP-MS, the aliquot was tested for the presence of Au NPs. The results were presented in supplementary information Fig. S4. The internalization efficiency of 5-, 10-, 20-, and 30- nm was found to be 96.1 ± 7.92 , 86.3 ± 11.5 , 95.88 ± 0.7 , 86.81 ± 2.28 , respectively. The concentration of Au in the aliquots were found to be much lower than the administered dose (the LD₅₀ concentration of each NP) for 5-, 10-, 20-, and 30- nm Au NPs proving that after a minimum of 72 h of exposure to Au NPs, the difference between the administered dose and the delivered dose (intracellular concentration of gold) was negligible, as has also been reported elsewhere (Bejjani et al. 2005). On the other hand, it was found that only 9.9 ± 5.1 of 50- and 1.5 ± 0.1 of 100- Au NPs were internalized (supplementary information Fig S4).

2.3 Results and Discussion

2.3.1 Characterization of synthesized NPs

Size and morphology characterization by TEM and UV-Vis analysis

Dimensions and morphology of NPs were analyzed by TEM. The mean diameters of Au sphere nanoparticles (Au S) were approximately 5, 10, 20, 30, 50, and 100 nm. Cubes (Au C) were 50 nm, and rod-shaped NPs (Au R) were 90 nm in length and 10 nm in diameter (Fig. 2.1). These sizes of gold nanorods and nanocubes were selected to compare their

biocompatibility to gold nanospheres of similar sizes. Standard deviations of the sizes are reported in the supplementary information, Table S2.

Au NPs showed strong interactions at specific wavelengths of light as a function of their size; for example, the UV-Vis analysis showed a shift in the absorption peaks that qualitatively confirmed the measured particle sizes (supplementary information, Fig. S2). As a result, a range of varying NPs with strict control of size was successfully synthesized for biocompatibility assessment.

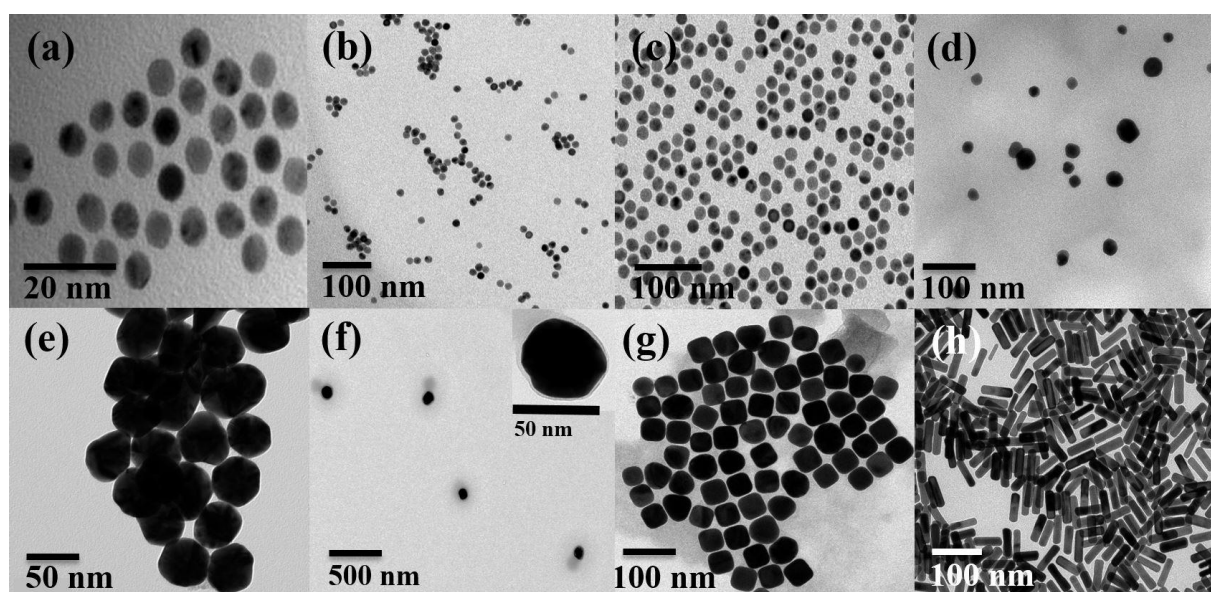


Figure 2.1 Transmission electron micrographs of synthesized NPS: (a) Au 5-nm sphere, (b) Au 10-nm sphere, (c) Au 20-nm sphere, (d) Au 30-nm sphere, (e) Au 50-nm sphere, (f) Au 100-nm sphere, (g) Au 50-nm cube, and (h) Au 10x90 nm rod.

Hydrodynamic diameter measurements by DLS

The hydrodynamic sizes of all the Au NPs as measured by DLS were larger than their physical size as determined by TEM measurements due to the adhered solvent molecules on the particle surface. Also, the hydrodynamic size increased when Au NPs were dispersed in cell culture medium rather than water.

Surface zeta potential

Zeta potential is one of the crucial parameters for the measure of particles' stability. To test the stability of NPs and measure their surface charge, the zeta potential was measured using a

dielectric cell. Nanoparticles with zeta potentials greater than 20 mV or less than -20 mV have strong electrostatic repulsion and thus remain stable in solution. Results indicated that when Au NPs were dispersed in cell culture medium, their zeta potential significantly decreased, possibly to a new protein corona formation, increasing the possibility of aggregation. No aggregation was observed after particles had been dispersed for 96 h in both C-DMEM/F12 and DI water (supplementary information, Table S2). No microbial growth was detected after 72 h of incubation.

2.3.2 Biocompatibility assessment of the Au NPs with the ARPE-19 cell line

MTT assay measurements

The MTT assay was used to investigate how the shape and size of Au NPs affect the internalization and viability of ARPE-19 cells. Results clearly showed that Au nanospheres with diameters of 5, 10, 20, and 30 nm and nanorods of 10×90 nm, even at the low concentration of 0.05 mg/ml, adversely affected cellular viability (Figure 2.2)

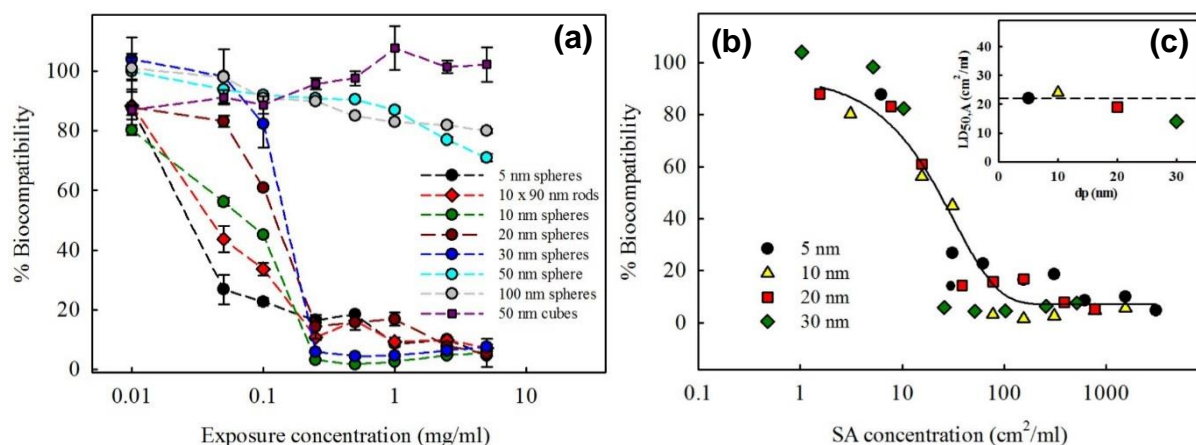


Figure 2.2 (a) Percentage biocompatibility of ARPE-19 cells exposed to Au NPs (Data is represented in log scale for x axis). (b) ARPE-19 cells' biocompatibility with Au NPs as a function of surface area and particle diameter, with biocompatibility (%) as a function of surface area concentration (cm²/ml) (Data is represented in log scale for x axis). (c) The critical surface area concentration (LD_{50,A}) for spherical Au NPs was 23 cm²/ml. The data is normalized using both negative and positive controls. Values are expressed in mean ± for each condition, three independent experiments were done with eight replicates (n=24, *P<0.05 vs controls).

ECIS measurements

Cell attachment behavior was monitored in the presence of spherical Au NPs having diameters ranging between 5 and 30 nm. Fig. 2.3a to f, respectively, show the resistance at 4,000 Hz over time after the addition of Au NPs of the six different sizes (5, 10, 20, 30, 50, and 100 nm). The exposure concentration range was narrowed down to 0.01–0.50 mg/ml based on the MTT assay findings. According to the cell attachment measurements, it can be inferred that the cells become confluent by the end of the 23rd h (Fig. 2.3a-f). ARPE-19 cells show no change in resistance compared to control cells in the presence of all concentrations of the 50 and 100 nm Au NPs (Fig. 2.3e, f).

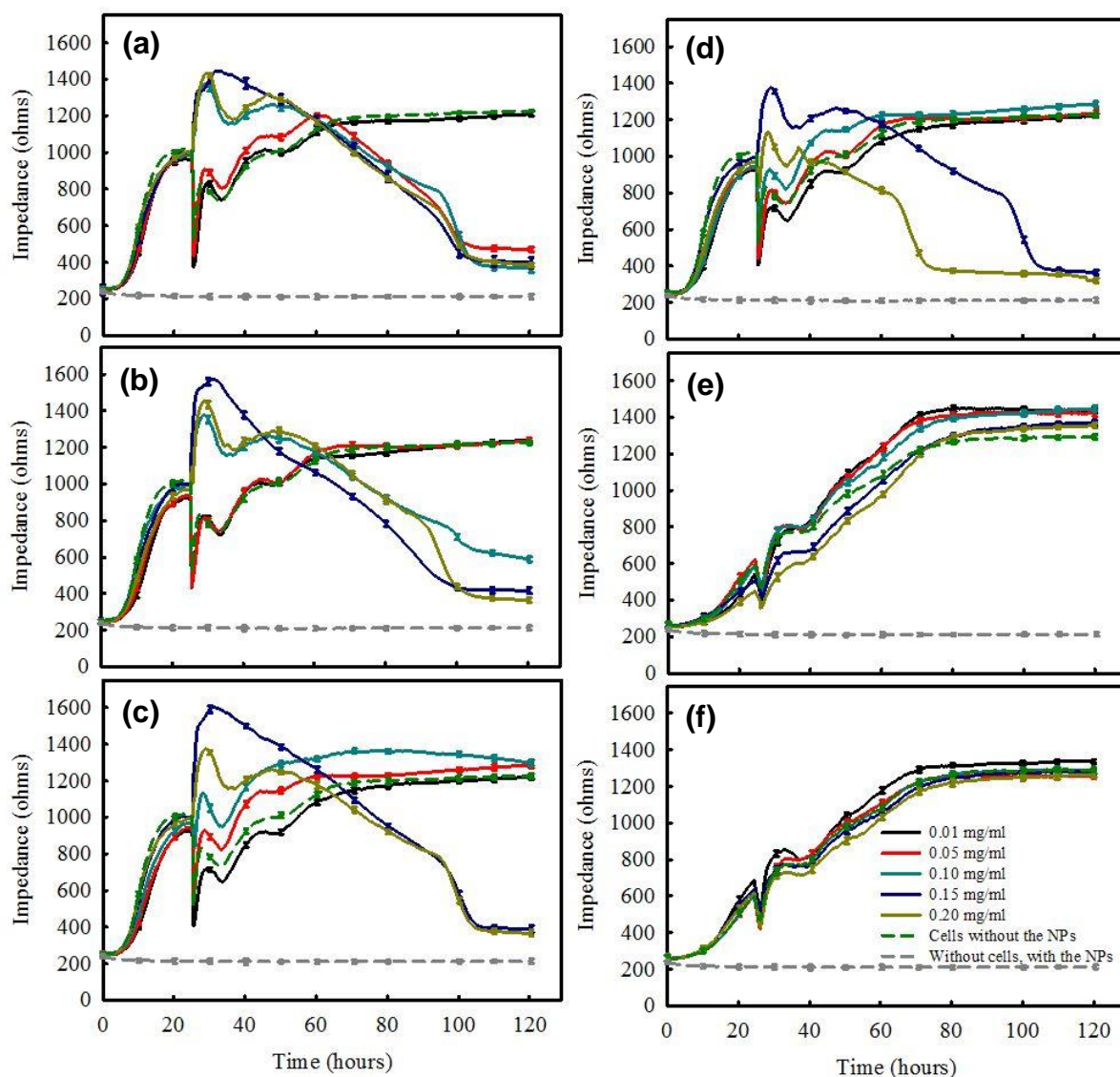


Figure 2.3 Electrical cell-substrate impedance sensing measurements for ARPE-19 cells exposed to (a) 5-nm Au spheres, (b) 10-nm Au spheres, (c) 20-nm Au spheres, and (d) 30-nm Au spheres when, at critical concentrations previously detected in MTT assay results, cells started to detach from the culture plate. (e) 50-nm Au spheres with cell detachment unhindered; however, the measured resistance is decreasing as the exposure concentration increases. (f) 100-nm Au spheres with no occurrence of cytotoxic effect. Values are expressed in mean \pm SEM with each condition tested at least in triplicate ($n=24$, $**P<0.001$ vs. controls).

The cells that were exposed to 5 nm Au NPs at 0.030 mg/ml (Fig. 2.3a) and 10 nm Au NPs at 0.057 mg/ml (Fig. 2.3b) followed the same pattern of change in impedance as did the positive control. However, the impedance of cells in contact with higher concentrations of 5 and 10 nm Au NPs showed a significant decrease after 32 h of exposure (Fig. 2.3a and 2.3b).

Similarly, when the exposure concentration reached the critical $LD_{50,M}$ value of the selected

nanoparticle, the impedance steadily dropped to baseline over 72-76 h, indicating that the cells started to round up and detach from the plate soon after NP introduction.

For particles of all sizes, the cells started to detach at their critical exposure concentration, and the death phase started approximately after the 32nd h of particle addition. This finding indicated that the MTT assay results, which were measured after 72 h of exposure, were representative and covered the entire time span of cell death.

Confirmation of internalization of Au NPs inside ARPE-19 cells

Au NPs were tracked inside cells using confocal microscopy. The nanoparticles that could not enter cells and floated outside of them were quantified as explained in the supplementary information. Both 2D and 3D confocal images were collected. Due to the space limitation, the 3D images are presented in supplementary information (supplementary information Fig. S3). According to ICP-MS results (supplementary information Fig. S4) for Au nanorods (10×90 nm) and Au nanospheres with diameters of 5, 10, 20, and 30 nm confirmed that almost all particles were able to enter cells at their critical LD_{50,M} concentration (Fig. 2.4b-f). We found that at their critical LD_{50,M} concentration, Au nanospheres with diameters of 50 and 100 nm and nanocubes of 50 nm were not able to penetrate through the cell membrane. This was confirmed by both ICP-MS measurements of free-floating NPs in the exposure medium and confocal microscopy images (Fig. 2.4g, h).

On the other hand, for spherical Au NPs, which were able to cross the cell membrane, we observed that as NP size increased, their presence inside the nucleus decreased significantly (Fig. 2.4b-e). Images taken at 60x magnification showed that cells exposed to 5-nm Au spheres had large vacuole-like structures throughout the cell, which can be attributed to regional cytoplasm loss (Fig. 2.4b and supplementary information Fig. S3c). Confocal images supported the results of MTT assays and ECIS measurements, showing that the 50- and 100-nm Au spheres, as well as 50-nm nanocubes, did not enter cells. This may explain why 50-

and 100-nm sizes did not exert a cytotoxic effect, even up to a 5 mg/ml exposure concentration.

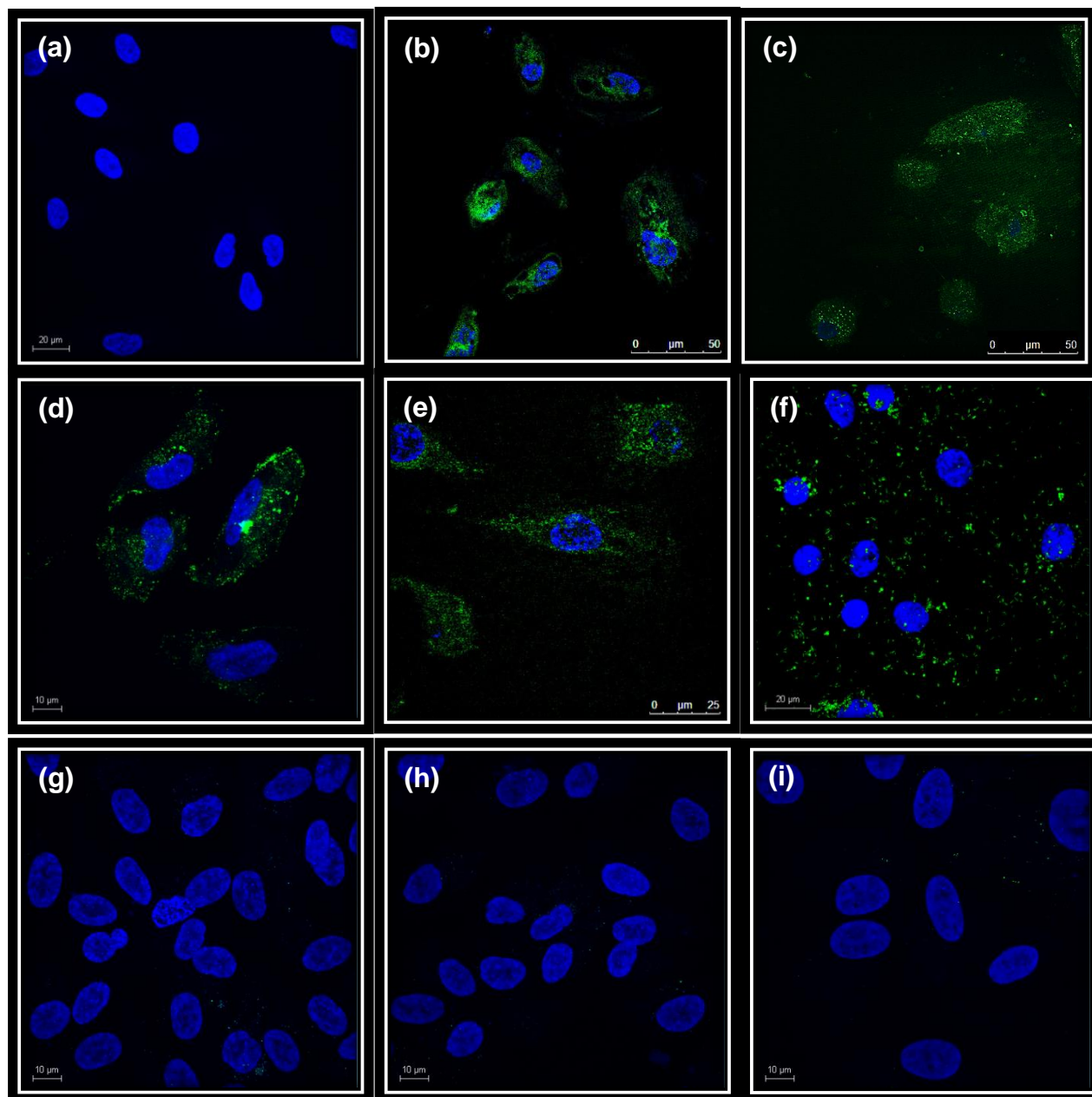


Figure 2.4 3D Confocal microscopic images of nanoparticles inside cells after 72 h of exposure. (a) cells without nanoparticle exposure, (b) ARPE-19 cells exposed to 5-nm Au sphere ($LD_{50,M}$: 0.030 mg/ml) with green dots representing Au NPs inside cells in the vicinity of the nucleus and voids (exact areas are shown with white arrows) representing loss of cytoplasm on the observed layer. (c) ARPE-19 cells exposed to 10-nm Au spheres ($LD_{50,M}$: 0.057 mg/ml, with particles inside cells and nuclei. (d) ARPE-19 cells exposed to 20 nm Au spheres at a critical concentration of $LD_{50,M}$: 0.113 mg/ml; the presence of particles inside cells and nuclei is confirmed. (e) ARPE-19 cells exposed to 0.129 mg/ml of 30-nm Au spheres. (f) $LD_{50,M}$:0.050 mg/ml of 10×90 nm Au nanorods inside cells and nuclei. (g) 0.129 mg/ml of 50- nm Au spheres. (h) 0.129 mg/ml of 100-nm Au spheres. Internalization of 50- and 100-nm Au spheres may be hindered by their large size. The available surface area per unit volume, the key metric for biocompatibility, is much less for 50- and 100-nm Au spheres compared than for ARPE-19 cells exposed to smaller Au nanospheres. (i) 0.129 mg/ml of Au nanocubes.

2.4 Discussion

The primary objective of this study was to elucidate the relationship between the structure (shape and size) and biocompatibility or toxicity of Au NPs with regard to ARPE-19 cells.

Based on our findings, a possible mechanistic description of NP interactions with internalization into RPE cells is hypothesized (Fig. 2.5).

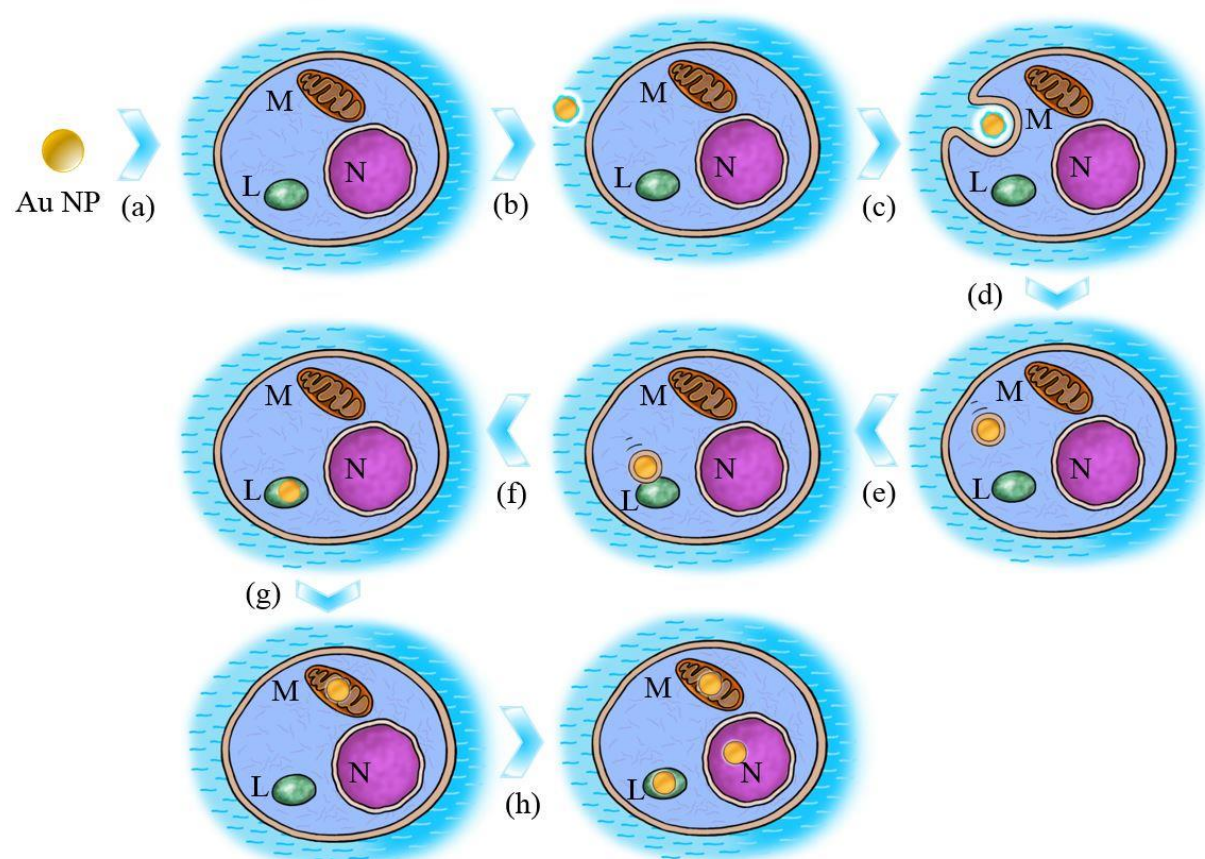


Figure 2.5 The mechanism of NPs' mediated cytotoxicity is illustrated here by (a) NP exposure to ARPE-19 cell growing in DMEM. (b) Dynamic bi-polymer layer (nano-biointerface) (thick and loose blue color coating) that forms when NPs are mixed with DMEM), creating a superficial surface exposed to the cell membrane. (c-d) NP internalization by endocytosis in which the pH of the endocytic vesicle is same as cell's physiological pH. (e) Fusion of endocytic vesicle with lysosome where pH of lysosome is acidic, (f) Internalized NP in lysosome, where the protein coating, the nano-biointerface, disappears because of degradation of protein by the hydrolytic mechanism of the acid hydrolases enzyme of lysosome. (g) NP can cross a single membrane of lysosome and may penetrate the mitochondrial intermembrane space where the apoptosis signal is initiated. (h) Cytoplasmically accumulated NPs cause cell death by activating subcellular downstream signaling for apoptosis, initializing cell shrinkage, cytoplasm decrease, and the beginning of subcellular fragmentation. For ease of visualizing, the structure of NP and cell is not according to size scale.

The Au NPs were first suspended in C-DMEM/F12 and exposed to ARPE-19 cells (Fig. 2.5a, b). The pristine NPs were coated with a layered nanostructure in which a protein corona, consisting of a dynamic biopolymer layer (nano-biointerface), formed on the NP surface. The hydrodynamic sizes of all studied Au NPs dispersed in DI water were larger than their physical sizes as determined by TEM and DLS measurements. That size was further increased when NPs were dispersed in DMEM cell culture medium (supplementary information, Table S2). The latter finding demonstrates that the increase in size was probably the result of serum protein adsorption on the NP surface, as illustrated in Fig. 2.5b. This finding is consistent with the results of a study by Tarantola et al. (2011) in which spectral shifting and changes in hydrodynamic diameter changed with solvent type. The change in zeta potential of the pristine Au NPs, when exposed to cell culture medium, provides further confirmation of the presence of an outer layer.

Cell membrane receptors recognize Au NPs and signal the beginning of an internalization process (Fig. 2.5c, d). The interaction of NPs with the external surface of the cell membrane depends on surface properties such as charge (zeta potential) and coating by components of C-DMEM/F12. As also reported in previous studies (Dykman and Khlebtsov 2011, Dykman and Khlebtsov 2012), our results indicate that a possible pathway of internalization maybe receptor-mediated endocytosis, in which the protein-coated Au NPs are recognized by a membrane receptor and then internalized.

An interesting shape effect is observed on internalization. Internalization efficiency depends mainly on the local mean curvature of the particle, the contact angle, and the available area of contact between particles and cell membrane receptors (Li et al. 2012, Li et al. 2015). Cubic Au NPs have small local mean curvatures, at which the cell membrane is less strongly bent compared to spherical Au NPs. Therefore, their internalization into ARPE-19 cells may be hindered (Li et al. 2015). Au nanospheres with diameters less than 30 nm and rod-shaped (10

$\times 90\text{nm}$) Au NPs are internalized, as shown by their lower biocompatibility (Fig. 2.2a) and confocal images (Fig. 2.4). Gold nanorods with a particle diameter of 10 nm were found to be less biocompatible than gold nanospheres of similar size (Fig. 2.2a). The lower biocompatibility of gold nanorods than nanospheres may be attributable to the disruption of lipid membranes, leading to loss of cytoplasmic substance and culminating in cell death (Gratton et al. 2008, Nangia and Sureshkumar 2012). Internalization of NPs depends on cell-surface receptors (Chithrani et al. 2006) and occurs by direct penetration or passive density gradient diffusion. Both internalization mechanisms are specific to particle dimensions while the cell membrane receptors and lipid bilayer barriers are specific to cell type.

Inside the cell, Au NPs fuse with the lysosome (Fig. 2.5e, f). The low pH (4.5) in the lysosome, where the digestive protease enzymes are active, results in degradation of the protein layer, but not the nanoparticle core (Luzio et al. 2007, Sabella et al. 2014). The resulting Au NP, stripped of its protein corona, leaves the lysosome with a new lysosomal corona and penetrates the mitochondrial membrane (Fig. 2.5g). Mitochondria are the central coordinators of cell death and affect metabolic activity. This is the basis of our MTT assay measurements of the enzymatic activity in mitochondria (Fig. 2.2a).

We also investigated the effect of size (5 to 100 nm) of spherical Au NPs. Our data (Fig. 2.2a) indicates that for the same mass concentration of Au NP, the biocompatibility is higher as size increases (in the range of 5 to 30 nm). At the same mass concentration of different sizes, the number of NPs and the total surface area concentration is different. To better elucidate the results, we plotted the biocompatibility data as a function of the surface area concentration for all the Au spheres that exerted significant toxicity (Fig. 2.2b). As can be seen, the data collapses into a single curve irrespective of sphere size. As long as the surface area concentration was similar, the biocompatibility values were the same for NPs of different sizes ($23\text{ cm}^2/\text{ml}$).

Although our detailed search of the literature identified no studies of ocular cells, we found studies in which the biocompatibility of different sizes of Au NPs was reported with different cell types. For example, Pan et al. (Pan et al. 2007) studied the biocompatibility of different sizes of Au NPs with HeLa cells. We plotted their biocompatibility data as a function of the surface area concentration of the Au NPs and found a similar trend (Fig. 2.6a). In another case, (Misawa and Takahashi 2011) reported a similar surface area dependence with the ROS (reactive oxygen species) generation by different sizes of Au NPs (Fig. 2.6b). These authors also emphasized that the key parameter should be the surface area concentration rather than the mass concentration of NPs. These findings indicate that the surface area concentration is the determinant metric of biocompatibility in the range of particle sizes studied. The observed toxicity was a result of the surface interactions inside the cell, which is directly correlated to the surface area concentration of the pristine NPs.

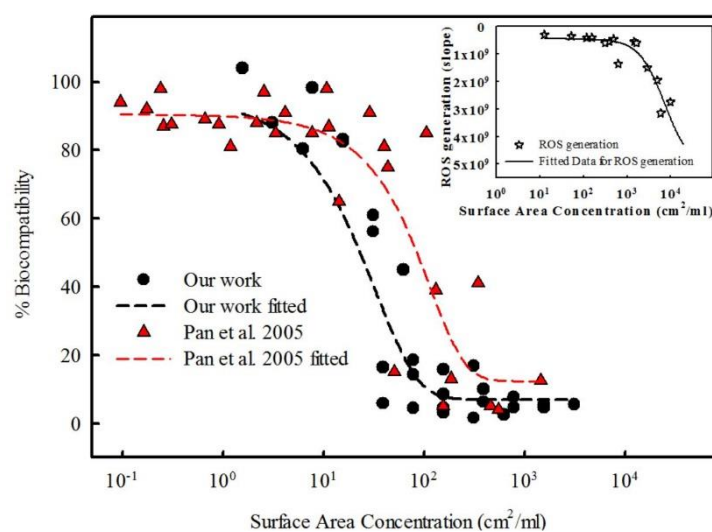


Figure 2.6 The surface area concentration required to affect 50% of the cells ($LD_{50,A}$) is independent from particle size, as is ROS generation. (a) LD_{50} based on surface area concentration (cm^2/ml) versus particle size for two different data sets in which the biocompatibility of Au NPs was tested on different cells. Pan et al. 2005, tested the biocompatibility of Au NPs with HeLa cells whereas we exposed retinal cells to Au NPs. The critical surface area concentration for retinal cells was $23 cm^2/ml$; the $LD_{50,A}$ amount for HeLa cells was $83 cm^2/ml$. (b) Misawa et al. (2011) measured ROS generation for different sizes of Au NPs at different concentrations. The ROS generation is plotted as a function of surface area concentration. (Data is represented in log scale for x axis).

Au nanospheres found to be nonbiocompatible were further tested by ECIS, so that cell adhesion was monitored in real time (Fig. 2.3). Most biocompatibility assays are end-point assays in which cell viability is measured by the end of a certain exposure period; with ECIS measurements, however, cell attachment behavior was recorded throughout the entire exposure period without terminating the experiment (Yun et al. 2010, Kling et al. 2014, Liang et al. 2016). Cell attachment behavior is crucial for biocompatibility assessment because it provides a direct measure of cellular activity. When a cell enters the apoptosis phase, the integrity of the cell structure cannot be maintained, and the adhesion proteins start losing their functionality (Borradori and Sonnenberg 1999). At critical exposure concentrations, which were determined via MTT assay measurements, the cells started to detach from the plate, resulting in a decrease in impedance (Fig. 2.3). The ECIS measurements were in perfect agreement with the MTT assay findings.

The particles tend to escape from intracellular trafficking when they are a part of endocytic vesicles (Shang et al. 2014). Once they escape from these vesicles, they can cause damage to the nucleus (Fig. 2.5h), which is consistent with our findings since the particles were inside nuclei (Fig. 2.4b, c, d, e). It is hypothesized that they activate cell-induced apoptosis (programmed cell death) signals, which lead to cell death (Kim et al. 2009, Shang et al. 2014). Larger Au spheres were subjected to retarded internalization and, upon entering the cytosol, could not enter mitochondria or nuclei because of their larger sizes (Fig. 2.5g and 2.5h). This led to higher biocompatibility results.

2.5 Conclusions

Use of Au NPs is being explored for treatment or imaging of the retina. However, there has been no detailed study on the biocompatibility of Au NPs with retinal cells. In this study, we report the *in-vitro* biocompatibility of Au NPs exposed to cells of the retinal pigment epithelium. The results indicate that NP biocompatibility depends on both the shape and the size of nanoparticles. Cubic Au nanoparticles with a size of 50 nm and spherical Au nanoparticles with diameters of 50 and 100 nm were found to be biocompatible up to an exposure concentration of 5 mg/ml. Au spheres with diameters of 5-30 nm and rod-shaped Au NPs of 10×90nm exert toxicity in concentration ranges from 0.01 to 0.2 mg/ml. Size-dependent biocompatibility trends were also found for spherical Au NPs with diameters of 5 to 30 nm. At the same mass concentration, the compatibility of Au NPs decreased with decreasing particle size.

The key observation, however, is that when the concentration is expressed as a function of surface area per unit volume, the effect of size is no longer relevant. For similar surface area concentrations, Au NPs in the range of 5–30 nm had almost the same biocompatibility. Similar surface area dependence has been observed in other cited works. We recommend that to use Au NPs intracellularly for therapeutic purposes; it may be necessary only to modulate the surface area. The overall assessment and generalization of cytotoxicity is, however, more complex and depends on the various parameters and factors we have discussed here. The reported critical doses for specific shapes and sizes of Au NPs and the proposed possible toxicity mechanism can serve as a guide when Au NPs will potentially be used in ophthalmic studies, especially when targeted to retinal cells.

2.6 References

1. Abe, K. and H. Saito (1999). "Both oxidative stress-dependent and independent effects of amyloid beta protein are detected by 3-(4,5-dimethylthiazol-2-yl)-2,5-diphenyltetrazolium bromide (mtt) reduction assay." Brain Research **830**(1): 146-154.
2. Arndt, S., J. Seebach, K. Psathaki, H. J. Galla and J. Wegener (2004). "Bioelectrical impedance assay to monitor changes in cell shape during apoptosis." Biosensors and Bioelectronics **19**(6): 583-594.
3. Austin, L. A., S. Ahmad, B. Kang, K. R. Rommel, M. Mahmoud, M. E. Peek and M. A. El-Sayed (2015). "Cytotoxic effects of cytoplasmic-targeted and nuclear-targeted gold and silver nanoparticles in hsc-3 cells - a mechanistic study." Toxicology in Vitro **29**(4): 694-705.
4. Bejjani, R., D. BenEzra, H. Cohen, J. Rieger, C. Andrieu, J. C. Jeanny, G. Gollomb and F. Behar-Cohen (2005). "Nanoparticles for gene delivery to retinal pigment epithelial cells." Molecular Vision **11**(14): 124-132.
5. Biswas, P. and C. Y. Wu (2005). "2005 critical review: Nanoparticles and the environment." Journal of the Air & Waste Management Association **55**(6): 708-746.
6. Borradori, L. and A. Sonnenberg (1999). "Structure and function of hemidesmosomes: More than simple adhesion complexes." Journal of Investigative Dermatology **112**(4): 411-418.
7. Chithrani, B. D., A. A. Ghazani and W. C. W. Chan (2006). "Determining the size and shape dependence of gold nanoparticle uptake into mammalian cells." Nano Letters **6**(4): 662-668.
8. Choi, S. Y., S. Jeong, S. H. Jang, J. Park, J. H. Park, K. S. Ock, S. Y. Lee and S. W. Joo (2012). "In vitro toxicity of serum protein-adsorbed citrate-reduced gold nanoparticles in human lung adenocarcinoma cells." Toxicology in Vitro **26**(2): 229-237.
9. Cohen, J. M., J. G. Teeguarden and P. Demokritou (2014). "An integrated approach for the in vitro dosimetry of engineered nanomaterials." Particle and Fibre Toxicology **11**.
10. Conde, J., M. Larginho, A. Cordeiro, L. R. Raposo, P. M. Costa, S. Santos, M. S. Diniz, A. R. Fernandes and P. V. Baptista (2014). "Gold-nanobeacons for gene therapy: Evaluation of genotoxicity, cell toxicity and proteome profiling analysis." Nanotoxicology **8**(5): 521-532.
11. Diebold, Y. and M. Calonge (2010). "Applications of nanoparticles in ophthalmology." Progress in Retinal and Eye Research **29**(6): 596-609.
12. Dumortier, H., S. Lacotte, G. Pastorin, R. Marega, W. Wu, D. Bonifazi, J. P. Briand, M. Prato, S. Muller and A. Bianco (2006). "Functionalized carbon nanotubes are non-cytotoxic and preserve the functionality of primary immune cells." Nano Letters **6**(7): 1522-1528.
13. Dykman, L. and N. Khlebtsov (2012). "Gold nanoparticles in biomedical applications: Recent advances and perspectives." Chemical Society Reviews **41**(6): 2256-2282.
14. Dykman, L. A. and N. G. Khlebtsov (2011). "Gold nanoparticles in biology and medicine: Recent advances and prospects." Acta Naturae **3**(2): 34-55.
15. Farjo, K. M. and J. Ma (2010). "The potential of nanomedicine therapies to treat neovascular disease in the retina." Journal of Angiogenesis Research **2**: 21.
16. Gratton, S. E. A., P. A. Ropp, P. D. Pohlhaus, J. C. Luft, V. J. Madden, M. E. Napier and J. M. DeSimone (2008). "The effect of particle design on cellular internalization pathways." Proceedings of the National Academy of Sciences of the United States of America **105**(33): 11613-11618.

17. Hall, D. E., K. M. Neugebauer and L. F. Reichardt (1987). "Embryonic neural retinal cell response to extracellular-matrix proteins - developmental-changes and effects of the cell substratum attachment antibody." Journal of Cell Biology **104**(3): 623-634.
18. Hayashi, A., A. Naseri, M. E. Pennesi and E. de Juan, Jr. (2009). "Subretinal delivery of immunoglobulin g with gold nanoparticles in the rabbit eye." Japanese Journal of Ophthalmology **53**(3): 249-256.
20. Huang, X. H., P. K. Jain, I. H. El-Sayed and M. A. El-Sayed (2008). "Plasmonic photothermal therapy (PPTT) using gold nanoparticles." Lasers in Medical Science **23**(3): 217-228.
21. Jana, N. R., L. Gearheart and C. J. Murphy (2001). "Seed-mediated growth approach for shape-controlled synthesis of spheroidal and rod-like gold nanoparticles using a surfactant template." Advanced Materials **13**(18): 1389-1393.
22. Jeong Hun, K., K. Jin Hyoung, K. Kyu-Won, K. Myung Hun and Y. Young Suk (2009). "Intravenously administered gold nanoparticles pass through the blood-retinal barrier depending on the particle size, and induce no retinal toxicity." Nanotechnology **20**(50): 505101-50510.
23. Jin Hyoung, K., K. Myung Hun, J. Dong Hyun, Y. Young Suk, L. Tae Geol and K. Jeong Hun (2011). "The inhibition of retinal neovascularization by gold nanoparticles via suppression of VEGFR-2 activation." Biomaterials **32**(7): 1865-1871.
24. Joris, F., B. B. Manshian, K. Peynshaert, S. C. De Smedt, K. Braeckmans and S. J. Soenen (2013). "Assessing nanoparticle toxicity in cell-based assays: Influence of cell culture parameters and optimized models for bridging the in vitro-in vivo gap." Chemical Society Reviews **42**(21): 8339-8359.
25. Kandasamy, K., C. S. Choi and S. Kim (2010). "An efficient analysis of nanomaterial cytotoxicity based on bioimpedance." Nanotechnology **21**(37): 10.
26. Kim, S., J. E. Choi, J. Choi, K. H. Chung, K. Park, J. Yi and D. Y. Ryu (2009). "Oxidative stress-dependent toxicity of silver nanoparticles in human hepatoma cells." Toxicology in Vitro **23**(6): 1076-1084.
27. Kling, B., D. Bucherl, P. Palatzky, F. M. Matysik, M. Decker, J. Wegener and J. Heilmann (2014). "Flavonoids, flavonoid metabolites, and phenolic acids inhibit oxidative stress in the neuronal cell line HT-22 monitored by ecis and mtt assay: A comparative study." Journal of Natural Products **77**(3): 446-454.
28. Kompella, U., A. Amrite, R. Ravi and S. Durazo (2013). "Nanomedicines for back of the eye drug delivery, gene delivery, and imaging." Progress in Retinal and Eye Research **36**: 172-198.
29. Kong, B., J. H. Seog, L. M. Graham and S. B. Lee (2011). "Experimental considerations on the cytotoxicity of nanoparticles." Nanomedicine **6**(5): 929-941.
30. Leduc, C., S. Si, J. Gautier, M. Soto-Ribeiro, B. Wehrle-Haller, A. Gautreau, G. Giannone, L. Cognet and B. Lounis (2013). "A highly specific gold nanoprobe for live-cell single-molecule imaging." Nano Letters **13**(4): 1489-1494.
31. Li, F., B. Hurley, Y. Liu, B. Leonard and M. Griffith (2012). "Controlled release of bevacizumab through nanospheres for extended treatment of age-related macular degeneration." The Open Ophthalmology J **6**: 54-58.
32. Li, Y., M. Kroeger and W. K. Liu (2015). "Shape effect in cellular uptake of pegylated nanoparticles: Comparison between sphere, rod, cube and disk." Nanoscale **7**(40): 16631-16646.
33. Li, Y., T. T. Yue, K. Yang and X. R. Zhang (2012). "Molecular modeling of the relationship between nanoparticle shape anisotropy and endocytosis kinetics." Biomaterials **33**(19): 4965-4973.

34. Liang, J., J. J. Struckhoff, H. Du, P. D. Hamilton and N. Ravi (2016). "Synthesis and characterization of in situ forming anionic hydrogel as vitreous substitutes." Journal of Biomedical Materials Research Part B: Applied Biomaterials: 1-12.
35. Luzio, J. P., P. R. Pryor and N. A. Bright (2007). "Lysosomes: Fusion and function." Nature Reviews Molecular Cell Biology **8**(8): 622-632.
36. Misawa, M. and J. Takahashi (2011). "Generation of reactive oxygen species induced by gold nanoparticles under x-ray and uv irradiations." Nanomedicine-Nanotechnology Biology and Medicine **7**(5): 604-614.
37. Naha, P. C., P. Chhour and D. P. Cormode (2015). "Systematic in vitro toxicological screening of gold nanoparticles designed for nanomedicine applications." Toxicology in Vitro **29**(7): 1445-1453.
38. Nangia, S. and R. Sureshkumar (2012). "Effects of nanoparticle charge and shape anisotropy on translocation through cell membranes." Langmuir **28**(51): 17666-17671.
39. Ngwa, W., G. M. Makrigiorgos and R. I. Berbeco (2012). "Gold nanoparticle enhancement of stereotactic radiosurgery for neovascular age-related macular degeneration." Physics in Medicine and Biology **57**(20): 6371-6380.
40. Ngwa, W., M. Makrigiorgos and R. Berbeco (2012). "Enhancing stereotactic radiosurgery for neovascular age-related macular degeneration, using gold nanoparticles." Medical Physics **39**(6): 3798-3798.
41. Pan, Y., S. Neuss, A. Leifert, M. Fischler, F. Wen, U. Simon, G. Schmid, W. Brandau and W. Jahnen-Dechent (2007). "Size-dependent cytotoxicity of gold nanoparticles." Small **3**(11): 1941-1949.
42. Parveen, S., R. Misra and S. K. Sahoo (2012). "Nanoparticles: A boon to drug delivery, therapeutics, diagnostics and imaging." Nanomedicine-Nanotechnology Biology and Medicine **8**(2): 147-166.
43. Peng, T. I., P. R. Yu, J. Y. Chen, H. L. Wang, H. Y. Wu, Y. H. Wei and M. J. Jou (2006). "Visualizing common deletion of mitochondrial DNA-augmented mitochondrial reactive oxygen species generation and apoptosis upon oxidative stress." Biochimica Et Biophysica Acta-Molecular Basis of Disease **1762**(2): 241-255.
44. Raju, H. B., Y. Hu, A. Vedula, S. R. Dubovy and J. L. Goldberg (2011). "Evaluation of magnetic micro- and nanoparticle toxicity to ocular tissues." Plos One **6**(5): e17452.
45. Ruiz-Ederra, J., M. Garcia, M. Hernandez, H. Urcola, E. Hernandez-Barbachana, J. Araiz and E. Vecino (2005). "The pig eye as a novel model of glaucoma." Experimental Eye Research **81**(5): 561-569.
46. Ryu, J. H., H. Koo, I. C. Sun, S. H. Yuk, K. Choi, K. Kim and I. C. Kwon (2012). "Tumor-targeting multi-functional nanoparticles for theragnosis: New paradigm for cancer therapy." Advanced Drug Delivery Reviews **64**(13): 1447-1458.
47. Sabella, S., R. P. Carney, V. Brunetti, M. A. Malvindi, N. Al-Juffali, G. Vecchio, S. M. Janes, O. M. Bakr, R. Cingolani, F. Stellacci and P. P. Pompa (2014). "A general mechanism for intracellular toxicity of metal-containing nanoparticles." Nanoscale **6**(12): 7052-7061.
48. Sayes, C. M., K. L. Reed and D. B. Warheit (2007). "Assessing toxicity of fine and nanoparticles: Comparing in vitro measurements to in vivo pulmonary toxicity profiles." Toxicological Sciences **97**(1): 163-180.
49. Shang, L., K. Nienhaus and G. U. Nienhaus (2014). "Engineered nanoparticles interacting with cells: Size matters." Journal of Nanobiotechnology **12**: 11.
50. Shestopalov, V. I., H. Missey and S. Bassnett (2002). "Delivery of genes and fluorescent dyes into cells of the intact lens by particle bombardment." Experimental Eye Research **74**(5): 639-649.

51. Swierczewska, M., G. Liu, S. Lee and X. Y. Chen (2012). "High-sensitivity nanosensors for biomarker detection." Chemical Society Reviews **41**(7): 2641-2655.
52. Sylvester, P. W. (2011). "Optimization of the tetrazolium dye (MTT) colorimetric assay for cellular growth and viability." Methods in Molecular Biology **716**: 157-168.
53. Warheit, D. B., R. A. Hoke, C. Finlay, E. M. Donner, K. L. Reed and C. M. Sayes (2007). "Development of a base set of toxicity tests using ultrafine tio₂ particles as a component of nanoparticle risk management." Toxicology Letters **171**(3): 99-110.
54. Wegener, J., C. R. Keese and I. Giaever (2000). "Electric cell-substrate impedance sensing (ecis) as a noninvasive means to monitor the kinetics of cell spreading to artificial surfaces." Experimental Cell Research **259**(1): 158-166.
55. Wu, H. L., C. H. Kuo and M. H. Huang (2010). "Seed-mediated synthesis of gold nanocrystals with systematic shape evolution from cubic to trisoctahedral and rhombic dodecahedral structures." Langmuir **26**(14): 12307-12313.
56. Yun, Y. H., Z. Y. Dong, Z. Q. Tan and M. J. Schulz (2010). "Development of an electrode cell impedance method to measure osteoblast cell activity in magnesium-conditioned media." Analytical and Bioanalytical Chemistry **396**(8): 3009-3015.

Chapter 3: Hyaluronate Coating as a Solution to Toxicity of Gold Nanoparticles

The results of this chapter have been reprinted with permission from Karakocak, B. B., Liang, J., Biswas, P., Ravi N. (2018). Hyaluronate Coating Enhances the Delivery and Biocompatibility of Gold Nanoparticles. Carbohydr. Polym. 186:243-251. Copyright 2018 Elsevier

Supplementary information along with figures and tables are available in Appendix II.

Abstract

For targeted delivery with nanoparticles (NPs) as drug carriers, it is imperative that the NPs are internalized into the targeted cell. Surface properties of NPs influence their interactions with cells. We examined the responses of retinal pigment epithelial cells, NIH 3T3 fibroblast cells, and Chinese hamster ovary cells to gold nanoparticles (Au NPs) in their nascent form as well as coated with end-thiolated hyaluronate (HS-HA). The grafting density of (HA-HS) on Au NPs was calculated based on total organic carbon measurements and thermal gravimetric analysis. We imaged the intracellular NPs by 3D confocal microscopy. We quantified viability and generation of reactive oxygen species (ROS) of the cells to Au NPs and monitored cell-surface attachment via electrical cell-substrate impedance sensing. The results confirmed that receptors on cell surfaces, for HA, are critical in internalizing (HA-S-Au NPs), and HA may mitigate ROS pathways known to lead to cell death. The 50- and 100-nm HA-S-Au NPs were able to enter the cells; however, their nascent forms could not. This study shows that the delivery of larger Au NPs is enhanced with HS-HA coating and illustrates the potential of HA-coated NPs as a drug delivery agent for inflamed, proliferating, and cancer cells that express CD44 receptors.

3.1 Introduction

Gold nanoparticles (Au NPs) have been widely explored in medicine as potential delivery agents for various biopharmaceuticals (Kim et al. 2011, Kumar et al. 2015). Although Au NPs are usually more biocompatible than other metal or metal oxide nanoparticles, their inherent positively charged surface disrupts the negatively charged cell membrane, while their production of reactive oxygen species (ROS) causes cytotoxicity (Moghadam et al. 2012). Moreover, plasma proteins can spontaneously adsorb to nascent Au NPs, affecting the surface properties of the particles and their interaction with cells (Nel et al. 2009). As a result, surface modification is essential ideally to prevent protein adsorption (Larson et al. 2012), and nonspecific delivery of Au NPs (Rana et al. 2012), to decrease opsonization by the immune system (Papasani et al. 2012), and finally mitigate their toxicities.

Many coating conjugates, ranging from synthetic ligands to natural biomolecules, have been used to improve the stability of particles and their delivery to specific cells or tissues (Yilmaz et al. 2016, Lin et al. 2017). Our focus is on hyaluronic acid (HA) as a coating material. HA is a bioactive linear polysaccharide that prevents adsorption of proteins on surfaces of biomaterials (Hans and Lowman 2002) and has an antifouling effect that arises from its hydrophilic and polyanionic characteristics (Lee et al. 2008, Santhanam et al. 2015). HA also scavenges free radicals and chelates pro-oxidant metals (Glucksam-Galnoy et al. 2012). HA serves as a ligand for several cell-surface receptors and thereby has an important physiological role. Cluster of differentiation 44 (CD44) is the most well-studied cell membrane receptor (Jaggupilli and Elkord 2012). It is present on, for example, the lymphatic vessel endothelial HA receptor (LYVE-1) (Chen et al. 2005), the receptor for hyaluronate-mediated motility (RHAMM) (Nedvetzki et al. 2005), and the HA receptor for endocytosis (HARE) (Pandey and Weigel 2014). The type of HA receptor on the cell membrane depends on the function of the tissue.

The role of HA receptors in healthy and diseased cells is not well understood. CD44 had been identified during the development, differentiation, and proliferation of cells, for example, the neural retina and in Muller cells (Chaitin and Davis 1995). CD44 has also been found under pathologic conditions, such as inflammation and proliferative vitreoretinopathy, where retinal pigment epithelial (RPE) cells actively proliferate in the subretinal space, on the surface and undersurface of the retina, and in the vitreous cavity. Hence, RPE cells exhibit significantly higher CD44 receptors compared to their quiescent and stationary state (Moysidis et al. 2012). Furthermore, it has been reported that cancer cells also express CD44 receptors and have a significant regulatory role in almost all cancer types (Kesharwani et al. 2015, Wang et al. 2016). It is now well recognized that a threshold of CD44 expression is required before HA binding is observed (Perschl et al. 1995, Tzircotis et al. 2005). Therefore, cells like NIH 3T3, which express relatively less number of CD44 receptors, may lack HA binding while cells like Chinese hamster ovary (CHO) cells with high CD44 receptor density show strong HA binding (Kato et al. 1995, Tzircotis et al. 2005).

In the previous chapter, we have found that for a fixed total surface area, Au NPs (particle diameter, $d_p < 50$ nm) were toxic to retinal pigment epithelial cells, independent from the particle size (Karakocak et al. 2016). The toxicity of Au NPs arises from reactive oxygen species (ROS) activity, which was shown to be correlated to the available total surface area (Pan et al. 2007, Jiang et al. 2008). HA is a known free radical quencher; it is natural and consequently biocompatible (Balogh et al. 2003). Our objective in the current work is to expand the usefulness of Au NPs by mitigating their toxicity via coating them with HA. As expected, we observed that HA coating significantly enhanced the biocompatibility of Au NPs; unexpectedly, the coating also greatly improved the internalization of larger Au NPs, which in their nascent form could not enter the cell. The outcomes of this study could be valuable in treating inflamed, proliferating, or cancer cells that express CD44 receptors.

3.2 Materials and Methods

3.2.1 Reagents

1-Ethyl-3-[3-(dimethylamino)propylcarbodiimide (EDC), sodium citrate, hydrogen tetrachloroaurate (HAuCl₄), cystamine dihydrochloride, sodium cyanoborohydride (NaBH₃CN), Dulbecco's modified Eagles's medium/nutrient mixture F-12 Ham (DMEM/F12), trypsin-ethylenediaminetetraacetic acid (EDTA) solution 10x, and fetal calf serum (FCS), and DAPI for nucleic acid staining were obtained from Sigma-Aldrich (St. Louis, MO). ARPE-19 (Retinal pigment epithelial) (ATCC® CRL-2302™), NIH 3T3 (ATCC® CRL-1658™) and CHO (CCL-61™) cells were purchased from American Type Culture Collection (Manassas, VA). Dithiothreitol (DTT) was obtained from Duchefa Biochemie (Haarlem, Netherlands). HiLyte-Fluor™ 647 amine was purchased from AnaSpec (San Jose, CA). Sodium hyaluronate having a molecular weight of 10,000 Da was obtained from Lifecore (Chaska, MN). The Apo Tox-Glo™ and ROS-Glo™ H₂O₂ assay kits were purchased from Promega Biosciences (San Luis Obispo, CA). All chemicals and reagents were of analytical grade.

3.2.2 Synthesis of Au NPs

We synthesized Au NPs by the citrate reduction method (Frens 1973, Kimling et al. 2006). HAuCl₄ (10 mg) was dissolved in 90 ml of deionized (DI) water, and this solution was heated to boiling. We added sodium citrate solution (250 mM) to the boiling solution in amounts ranging from 400 μl to 900 μl and stirred for 20-30 min until the solution became wine-red. The solution was then left undisturbed in the dark for 24 h at room temperature. Subsequently, Au NP solutions were centrifuged at 10,000 rpm for 20 min and suspended in DI water. We confirmed the final size using transmission electron microscopy (TEM) analysis and dynamic light scattering (DLS) measurements. The detailed procedure for particle size measurements is given as supporting information.

3.2.3 Preparation of end-thiol modified HA (HS-HA)

We prepared HS-HA by reductive amination as described elsewhere (Lee et al. 2012, Kumar et al. 2015). HA (MW: 10,000 Da, 100 mg) and cystamine dichloride (60 mg) were dissolved in 0.1 M borate buffer (10 ml, pH 8.5) with 0.4 M NaCl and stirred for 2 h. NaBH₃CN was added to the solution at a final concentration of 0.2 M and reacted at 50°C for three days. The reaction mixture was then incubated with 0.1 M DTT for 12 h to introduce a free thiol group (Fig. 1). The resulting solution was dialyzed against a large excess of 0.1 M NaCl solution for one day, 25% ethanol for one day, and pure water for one day to remove unreacted chemicals. The efficiency of thiol-end functionalization of HA was higher than 90%, and the ratio of [SH] to [HA repeating units] was 0.025 as determined by Ellman's assay. Physicochemical properties of the HS-HA were obtained using Proton Nuclear Magnetic Resonance (¹H-NMR), Fourier Transform Infrared (FTIR) spectroscopy, and Gel Permeation Chromatography (GPC) analysis. Please refer to supporting information for details of Ellman's assay, ¹H-NMR, FTIR, and GPC analysis.

3.2.4 Conjugation of HS-HA with Au NPs and quantification of the coating

Before initiating the conjugation process, we calculated the average number of HA molecules (MW: 19.69 kDa, 5.42 nm hydrodynamic radius (R_h)) that can bind to one Au NP (particle size based on the TEM and DLS measurements). From that, we calculated the approximate HA to Au NP conjugation mass ratio and ensured that we used at least 1.5x in excess of this amount. HS-HA was added dropwise to the dispersed Au NPs in DI water at room temperature with moderate stirring. The solution was stirred overnight. The HA-Au NP conjugate was further purified by centrifuging it twice at 10,000 rpm for 20 min to remove unbound HA molecules and was finally redispersed in DI water. To take further measurements in the solid phase, the coated nanoparticle solution was lyophilized for two days at -105 °C. We used total organic carbon (TOC) and thermal gravimetric analysis (TGA)

to determine the amount of coating around the nanoparticles. Please refer to supporting information for details of TOC and TGA analysis.

The number of bound HA molecules per unit surface area, grafting density (σ) was calculated based on both TOC (σ_{TOC}) and TGA (σ_{TGA}) measurements as described previously (Benoit et al. 2012). In summary, first, the number of Au NPs in a sample was calculated based on the hydrodynamic diameter of the Au NP and the density of Au. Next, the total available surface area of Au NPs in a sample for HA molecules to bind was determined. The number of HA molecules present in a sample was calculated taking the molecular weight of HA which is determined by GPC analysis. Finally, grafting density was calculated by dividing the number of HA molecules in a sample to the available surface area of Au NPs.

3.2.5 Investigation of the internalization of NPs

The cellular internalization of coated and nascent Au NPs was determined by exposing NPs to ARPE-19, NIH 3T3, and CHO cell lines. This was followed by careful washing to remove NPs that may have reached and been adsorbed on the cell surface (Cho et al. 2011). The intracellular concentrations of Au were quantified with an ELAN DRC II Inductively coupled plasma mass spectrometry (ICP-MS) (Perkin Elmer, Inc., USA). To identify the difference between the administered and delivered doses, the number of nanoparticles that failed to enter the cell, as well as the specific Au NP intracellular concentrations, were quantified in aliquots from the phosphate buffer saline (PBS) washes done before confocal imaging. Using ICP-MS, the aliquots were tested for the presence of Au NPs.

3.2.6 *In-vitro* toxicity measurements on ARPE-19 cells with MTT, ApoTox-Glo™, and ROS-Glo™ H₂O₂ assays

Cell metabolic activity, and hence the viability of retinal cells in the presence of Au NPs, was assessed with MTT (3-[4, 5 dimethyl-thiazoly-2-yl] 2-5 diphenyl tetrazolium bromide). The

relative amount of apoptotic cells and ROS generation were measured, respectively, by ApoTox-Glo™ and ROS Glo™ H₂O₂ assays. See the supporting information for the details

3.2.7 Confocal microscopy analysis

To confirm the presence of NPs inside cells, we investigated the distribution of Au NPs at their critical mass concentrations (LD_{50,M}), determined previously (Karakocak et al. 2016), using a nanoplasmonic confocal laser scanning microscope (Leica TCS-SP8). Au NPs have a surface plasmon resonance property (SPR). For Au NPs in size range of 5-100 nm, the SPR wavelength is around 520 nm (Huang et al. 2008), depending on the sizes of the nanoparticles. See the supporting information for the details.

3.2.8 Cell attachment measurements by electrical impedance spectrometry (ECIS)

We analyzed the biocompatibility of Au NPs as they were exposed to ARPE-19 cells using ECIS, a noninvasive technique that measures the impedance across gold electrodes at the bottom of tissue culture wells, using a range of frequencies of alternating current (Wegener et al. 2000, Arndt et al. 2004). As adhesion proteins changed the cell morphology and attachment to the electrodes in the bottom of wells, the resistance across the electrodes also changed (Borradori and Sonnenberg 1999, Santhanam et al. 2016). The change in resistance at frequencies ranging from 400 to 64,000 Hz was measured over time. Low-frequency impedance can be used to monitor the solution paths around the cells, and hence the layer's cell-to-cell barrier functions (Wegener et al. 2000). The addition of Au NPs complicates the impedance of the system. However, at a frequency of 4,000 Hz, the contribution to resistance from cells was dominant over the contribution to resistance from Au NPs with the medium (Kandasamy et al. 2010). Therefore, we chose a frequency of 4,000 Hz to monitor cell growth and biocompatibility.

3.2.9 Statistical analysis

Results are presented as means \pm standard deviation on the graphs for experiments done at least with three biological replicates per condition or group. First, each test result (viability measurements, the relative amount of apoptotic cells, and ROS generation) was compared with the corresponding negative (untreated cells) and positive (NPs without the cells) control groups with Student's t-test. $P^* < 0.05$, the significance level, was statistically acceptable. Second, Two-Factor ANOVA (analysis of variance) was used to evaluate the results of viability measurements, the relative number of apoptotic cells, and ROS generation. For cell attachment measurements, eight replicates were performed for each independent experiment. Statistical significance was evaluated using ANOVA to compare the results with the respective negative (untreated cells) and positive control (only cell media) groups. $P^* < 0.05$, the significance level, was statistically acceptable.

3.3 Results and Discussion

3.3.1 Synthesis of end-thiolated hyaluronic acid (HS-HA)

HS-HA was synthesized by a previously reported method (Lee et al. 2012), outlined in Fig. 3.1. HA has multiple hydroxyl and carboxyl groups, but only the end six-member ring can open up and form an aldehyde group.

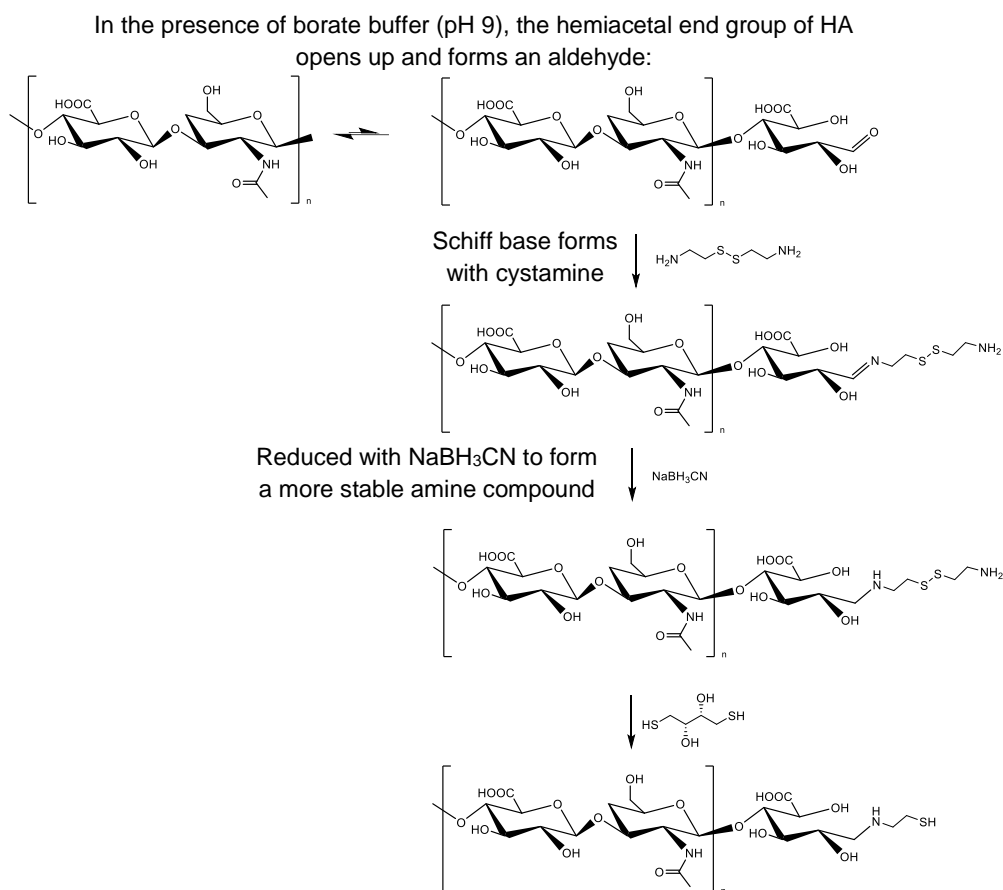


Figure 3.1 HS-HA synthesis chemistry. In the presence of borate buffer at pH 9, the terminal cyclic hemiacetal ring opens and changes to a linear aldehyde form. A Schiff base forms with cystamine. Thus, the terminal saccharide reverses between two states to reach the final form. The Amadori compound, sodium cyanoborohydride (NaBH_3CN), is added, and then Dithiothreitol (DTT) is added to reduce the disulfide and produce HS-HAs.

We took advantage of this lone functional group, modifying it with an amine to introduce an end thiol group and covalently binding it to Au (Fig. 3.2). Ellman's assay results confirmed ~90% of thiolation of HA, and the molar ratio of SH to HA was found to be ~0.025. However, $^1\text{H-NMR}$ and FTIR analysis could not clearly detect the end-thiol content of hyaluronate as $[\text{SH}]/[\text{HA repeating units}]$ is low (Fig. S1 and Fig. S2). On the other hand, based on gel permeation chromatography (GPC) analysis, we determined that the hydrodynamic radius of HS-HA was 5.42 nm. Its number average molecular weight was 15.51 kDa, its polydispersity 1.27, and its intrinsic viscosity was 0.58 dl/g (Table 3.1). The Mark-Houwink constant changes linearly with the logarithm of MW of HA which can correspond to a change in conformation of HA from a random coil to a rigid structure (La Gatta et al. 2010).

The Mark-Houwink constant, based on GPC analysis of the HS-HA, was 0.70, suggesting the presence of a random coil.

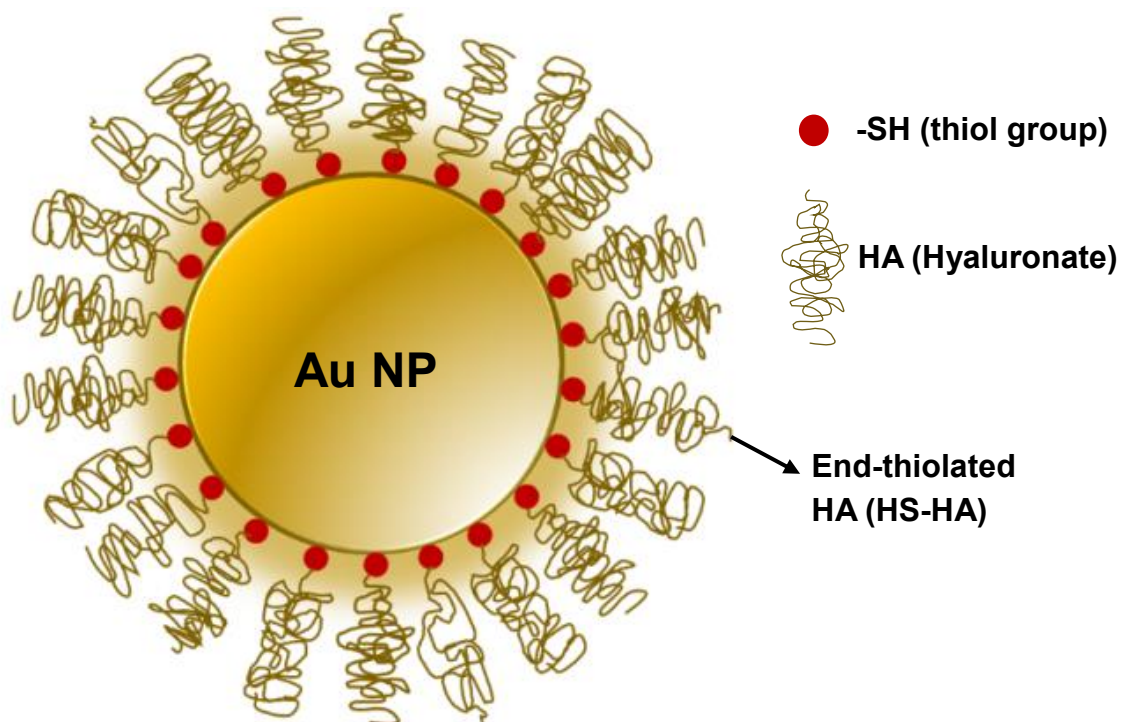


Figure 3.2 Illustration of coated Au NPs with end-thiolated HA (HS-HA), where the thiol group at the end of each HA chain is attracted to the Au NP surface.

Table 3.1 Gel permeation chromatography results for HS-HA

Parameter	Value
Number average molecular weight (Mn)	15.51 kDa
Weight average molecular weight (Mw)	19.69 kDa
Polydispersity	1.27
Hydrodynamic radius	5.42 nm
Intrinsic viscosity	0.58 dl/g
Mark-Houwink constant	0.70

3.3.2 Synthesis of Au NPs conjugated with HS-HA and confirmation of the presence of the coating

We synthesized Au NPs with sizes of 5-, 10-, 20-, 50-, and 100-nm, the sizes most preferred for targeted drug delivery studies (Karthikeyan et al. 2010, Ngwa et al. 2012). The high-resolution TEM (HR-TEM) images of the uncoated Au NPs can be found in supporting information (Fig. S3). The Au NPs were conjugated with HS-HA (see Methods). The amount of coating on Au NPs was determined with TOC analysis and TGA. These two approaches are well suited to probe the content of inorganic and organic compounds on nanoparticle surfaces (Benoit et al. 2012). The presence of the coating was first confirmed and quantified by TOC measurements by determining the extent of organic and inorganic carbon. Because inorganic carbon was negligible, the total carbon content was equivalent to the organic carbon content which was attributed to HA coating. To further confirm and quantify the presence of the coating, we used TGA which records the change in mass as a function of temperature. The peak at ~ 280 °C corresponded to the decomposition of HA (Fig. 3.3). The exact quantity of the coating was determined by calculating the change in mass around the temperature at which HA is known to decompose (Ahire et al. 2016).

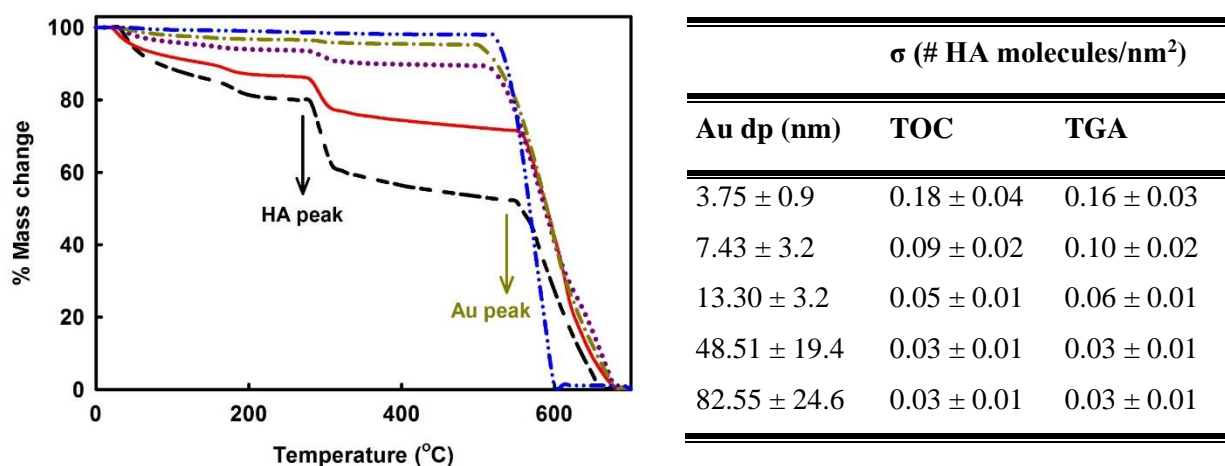


Figure 3.3 Thermal gravimetric analysis plot for the HS-HA coated Au NPs. HA decomposition occurs at around 280 °C, and Au NPs melt approximately at 500 °C. Au NP grafting density (the number of HA molecules/nm²) determined by TOC and TGA measurements. Errors provided reflect standard deviation of the replicate error in repeated measurements of the sample. At least two measurements were taken for each analysis technique.

— 5nm, — 10 nm, 20 nm, -.-.- 50 nm, -.-.- 100 nm

As detailed in a previous study (Benoit et al. 2012), we calculated the grafting density of HA molecules, the number of bound HA per unit surface area (# HA molecules/nm²) based on results of both TOC (σ_{TOC}) and TGA (σ_{TGA}) measurements (Fig. 3.3 and Table S1). The results showed that, for both measurement techniques, the number of HA molecules adsorbed per unit surface area of Au NP decreases as the particle size increases. This trend may be attributed to the HA-HA interactions which could be geometrically minimized due to the increased curvature of the smaller particles (Nasir et al. 2015). One should note that these calculations were based on two main assumptions: Au surface is smooth, even though it is known that the surface of Au has irregularities at the atomic scale (Loskutov et al. 2009) and secondly, end-thiolation allows only a single covalent attachment per HA molecule. We do not have any evidence on the orientation of HA on the surface of Au. However, polymers with a single point attachment to the core nanoparticle generally take on brush-like configuration (Benoit et al. 2012 and Dukes et al. 2010).

3.3.3 Characterization of HS-HA conjugated Au NPs

The hydrodynamic sizes and zeta potential of both nascent and coated Au NPs in DI water and DMEM were measured by dynamic light scattering (DLS) analysis (Figs. S4 and S5). When the nascent particles were dispersed in cell medium, the results indicated a substantial increase in particle size and a decrease in zeta potential. The HS-HA coating also had a major effect on particle size. The increase in size for nascent NPs in cell culture media was attributed to nonspecific protein adsorption on the Au NP. When the Au NPs are coated with HS-HA, and then dispersed in DMEM, the extent of protein adsorption was less, which is consistent with the known property of HA to decrease protein adsorption (Pitarresi et al. 2007).

3.3.4 Cellular uptake of nascent and coated Au NPs

Our uptake studies were based on the measurement of intracellular gold concentration. We had previously determined the critical mass ($LD_{50,M}$) concentration of Au nanoparticles of different sizes and used these critical mass concentrations in the rest of the cellular experiments, including the uptake study (Karakocak et al. 2016). Our earlier study with RPE cells indicated that the $LD_{50,M}$ concentrations of Au NPs with sizes of 5-, 10-, 20-nm were, 0.03 mg/ml, 0.08 mg/ml, and 0.11 mg/ml respectively (Karakocak et al. 2016). Furthermore, Au NPs 50 nm and 100 nm in diameter did not exert any toxic effect up to 5 mg/ml, because they did not enter the cells. Here, we extended our study using two additional different cell lines: ARPE-19 cells and CHO cells with high-density CD44 receptors (Jaggupilli and Elkord 2012) and NIH 3T3 cells with relatively less CD44 receptors (Culty et al. 1992) to investigate the CD44 receptor-mediated internalization of 50-nm Au NPs.

According to the ICP-MS results, the number of NPs internalized by ARPE-19 cells changed with the presence of the coating. Indeed, the coating played a significant role, especially for particles with diameters larger than 50 nm. Nascent particles with a diameter larger than 50 nm were not able to enter cells (Fig. 3.4A). However, when the same particles were coated with HS-HA, their size increased to 58.41 nm in DMEM, and the number of particles internalized by the retinal cells increased considerably (Figs. S4 and S6). Conversely, HS-HA coating increased the size of smaller Au NPs significantly and slightly decreased the number of intracellular Au NPs (Figs. S4 and S6). This difference may be attributed to increase of the coated NP size and the presence of HA coating, therefore the internalization pathway of nanoparticles is predominantly CD44 receptor-mediated endocytosis (Almalik et al. 2013).

To test whether the internalization was CD44 receptor-mediated, nascent (53.81-nm) and coated (58.41-nm) Au NPs in DMEM were exposed to two more cell lines: NIH 3T3 cells, which have significantly fewer CD44 receptors than ARPE-19 cells, and CHO cells which are

also known to express CD44 but a cancer cell line, unlike ARPE-19 cells (Culty et al. 1992). The amount of HA-S-Au NPs internalized by NIH 3T3 cells was significantly less than the amount internalized by ARPE-19 and CHO cells. Therefore, it can be concluded that the internalization of Au NPs coated with HS-HA depends on the density of cell-surface receptors for HA, in this case, CD44 (Fig. 3.4B).

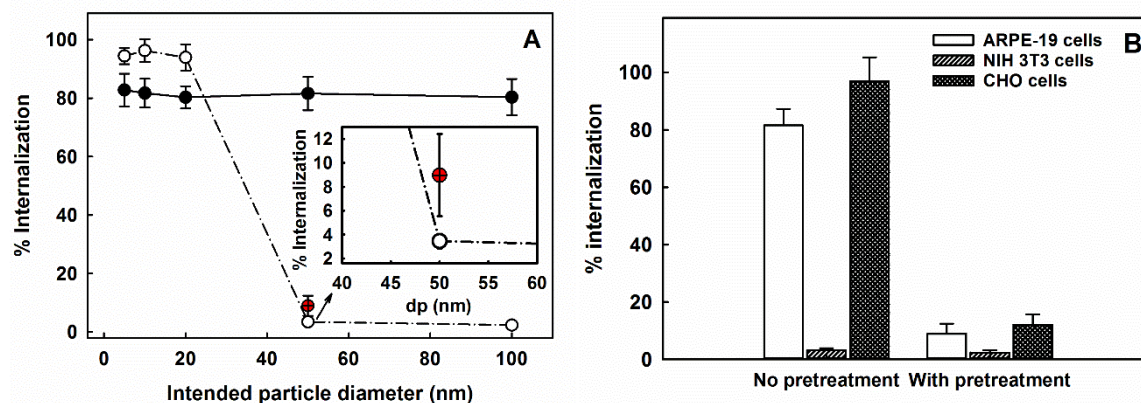


Figure 3.4 (A) Cellular uptake of Au NPs of different sizes, with and without HS-HA coating by ARPE-19 cells. (B) 50 nm Au NPs (0.11 mg/ml) exposed to ARPE-19, NIH 3T3, and CHO cells with and without pretreatment with 10x HS-HA. CD44 receptor density of NIH 3T3 cells is significantly less than that of ARPE-19 cells; therefore, blocking the CD44 receptors of NIH 3T3 cells did not significantly affect internalization of HA-S-Au NPs, unlike the results for ARPE-19 and CHO cells. Overall, cells like ARPE-19 and CHO cells, which express high enough number of CD44 receptors and meet the threshold for HA binding, internalize more coated NPs than NIH 3T3 cells. ARPE-19 cells exposed to ● HA-S-Au NPs, ○ Nascent Au NPs, ⊕ ARPE-19 cells treated with 10x HS-HA, and then exposed to HA-S-Au NPs.

As a step toward confirming this finding, all cells were treated with 10x HS-HA, to saturate the CD44 receptors, and then exposed to 50-nm HA-S-Au NPs. As expected, we found that the number of internalized particles was significantly decreased (Fig. 3.4B). Cell membrane receptors and lipid bilayer barriers are specific to cell type. Because of the presence of CD44 receptors, the amount of internalized HA-S-Au NPs was significantly different in various types of cells. As the size of the nanoparticles decreases, the internalization pathway may involve passive diffusion; however, as particle size increases, receptor-mediated endocytosis may become more prominent (Zhang et al. 2009, Panariti et al. 2012, Gupta and Rai 2017). For smaller particles, there are alternate size-dependent internalization paths that do not involve CD44 receptors. Therefore, the internalized number of coated nanoparticles may

slightly decrease because of the increased size of coated Au NPs (Figs. S5 and S7). For RPE cells, we found that internalization of 5-, 10-, and 20-nm particles was only minimally decreased by the presence of the coating. In contrast, internalization of 50- and 100-nm HS-HA coated Au NPs was significantly increased (Fig. 4A). Furthermore, when we blocked the receptors for HA by adding excess HA to saturate the receptors before administering HA-S-Au, there was less internalization (Fig. 4B). Thus, although several pathways exist for internalization of nanoparticles, CD44-mediated endocytosis is particularly important for larger particles. This finding is noteworthy in that coating with HA provides a “Trojan horse” approach to the delivery of large Au NPs and possibly to other hydrophobic particles into cells with receptors for HA.

3.3.5 The fate of nascent and coated Au NPs in the cells

To confirm the presence of NPs inside cells, we investigated the distribution of Au NPs using a nano-plasmonic confocal laser scanning microscope (Leica TCS-SP8) (see Methods). We first studied the effect of exposure of different sizes of nascent and coated Au NPs to ARPE-19 cells.

Per the 2D and 3D confocal images (Figs S6 and S7, respectively), it can be inferred that for smaller NPs ($d_p < 50$ nm), the presence of an HA coating slightly decreased the number of Au NPs inside retinal cells. Nascent particles with diameters of 50 nm and above could not enter retinal cells (Figs. S6H/S7H and S6J/S7J). However, when these particles were coated with HA, their presence within cells significantly increased (Figs. S6I/S7I and S6K/S7K), as also confirmed by the ICP-MS results shown in Fig. 3.4. In other words, the HA coating enabled NPs larger than 50-nm (58.41 nm in DMEM) to enter retinal cells (Fig. 3.5), even though DLS measurements showed that the size of these particles had significantly increased (Figs S4 and S5). This lends credence to the hypothesis that internalization of larger HS-HA coated Au NPs occurs via the HA receptor-mediated CD44 pathway. Because large HS-HA-coated

particles can enter cells, they can efficiently deliver a greater payload than previously reported targeted drug delivery vehicles (Diebold and Calonge 2010).

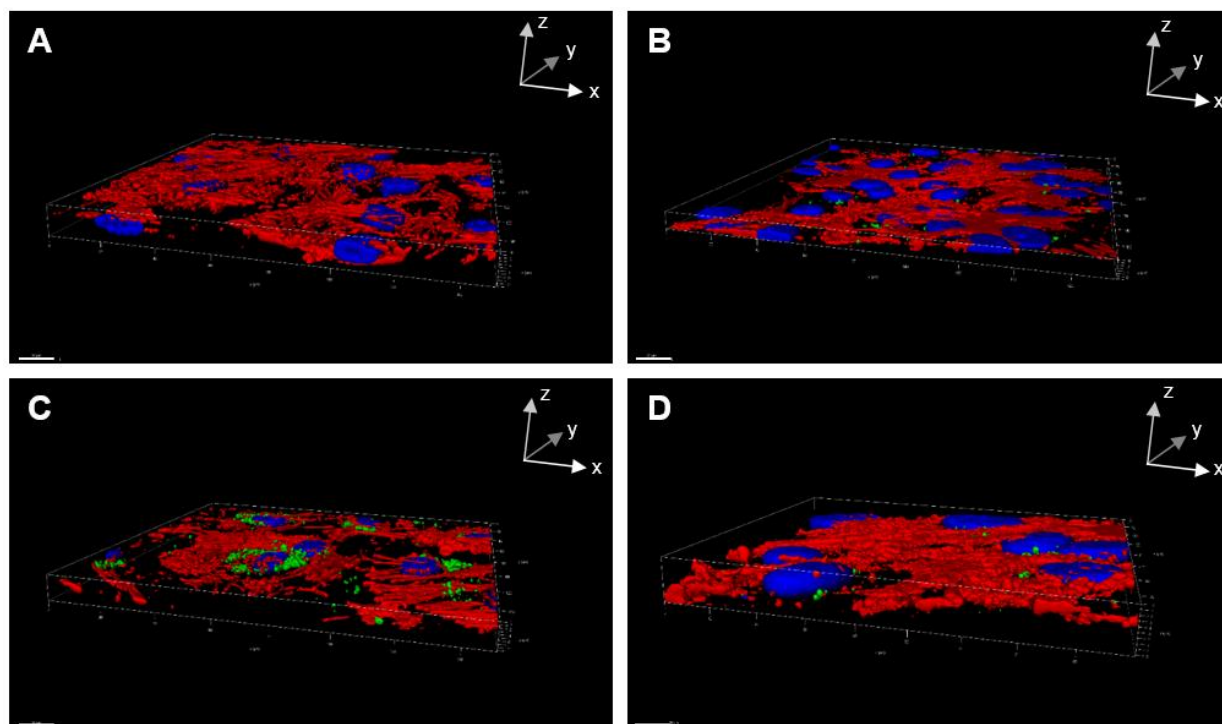


Figure 3.5 3D Confocal microscopy images of Au NPs with ARPE-19 cells. The red staining corresponds to actin, the nucleus is blue, and Au NPs are green. ARPE-19 cells exposed to (A) no particles, the negative control. 50-nm (B) nascent Au NPs (C) HA-S-Au NPs (D) ARPE-19 cells pretreated with 10x HS-HA and then exposed to 50-nm HA-S-Au NPs. The HS-HA coating significantly enhanced the intracellular concentration of Au NPs, whereas when the same particles were exposed to the retinal cells after blocking the CD44 receptors, the amount internalized is significantly decreased. The exposure concentration was selected as 0.11 mg/ml. Scale bars are 20 μm .

Additionally, our observations also extend to non-ocular tissues. Nascent and HS-HA-coated 50-nm Au NPs were administered to NIH 3T3 cells and CHO cells. Both ICP-MS findings (Fig. 3.4B) and 3D confocal microscopy (Figs. S8 and S9) showed that significantly increased number of particles entered NIH 3T3 and CHO cells. This observation confirmed our hypothesis that the number of HA-S-Au NPs internalized is dictated by the presence or absence of the relevant receptors on the cell membrane (in this case, CD44).

3.3.6 Biocompatibility assessment of HS-HA-coated Au NPs with ARPE-19 cells

We next studied the biocompatibility of HS-HA Au NPs with ARPE-19 cells. Three different independent end-point assays were used: viability based on enzymatic activity in mitochondria; the percent of apoptotic cells based on caspase 3/7, and activity ROS generation, which is proportional to luciferase activity (see Methods). The results indicated that nascent Au NPs with diameters smaller than 50 nm were not biocompatible above 0.03 mg/ml (Fig. 3.6A), initiated apoptotic cell death (Fig. 3.7A), and induced ROS generation (Fig. 3.7C). On the other hand, no toxicity was observed for HA-S-Au NPs with a concomitant negligible generation of ROS (Figs. 3.6B, 7B, and 7D). Most of the toxicity of Au originate from ROS production because of its surface chemistry in the cell's cytoplasm (Balogh et al. 2003). Coating with HA significantly decreases the available surface on Au by steric hindrance. In addition, HA and its degradation products (tetrasaccharides) have an exceptional ability to quench free radicals (Balogh et al. 2003). Thus, any ROS formed at the surface of Au NPs has very little opportunity to escape the HA coating, as was confirmed by our ROS GloTM H₂O₂ assay results (Figs. 3.7C and 7D).

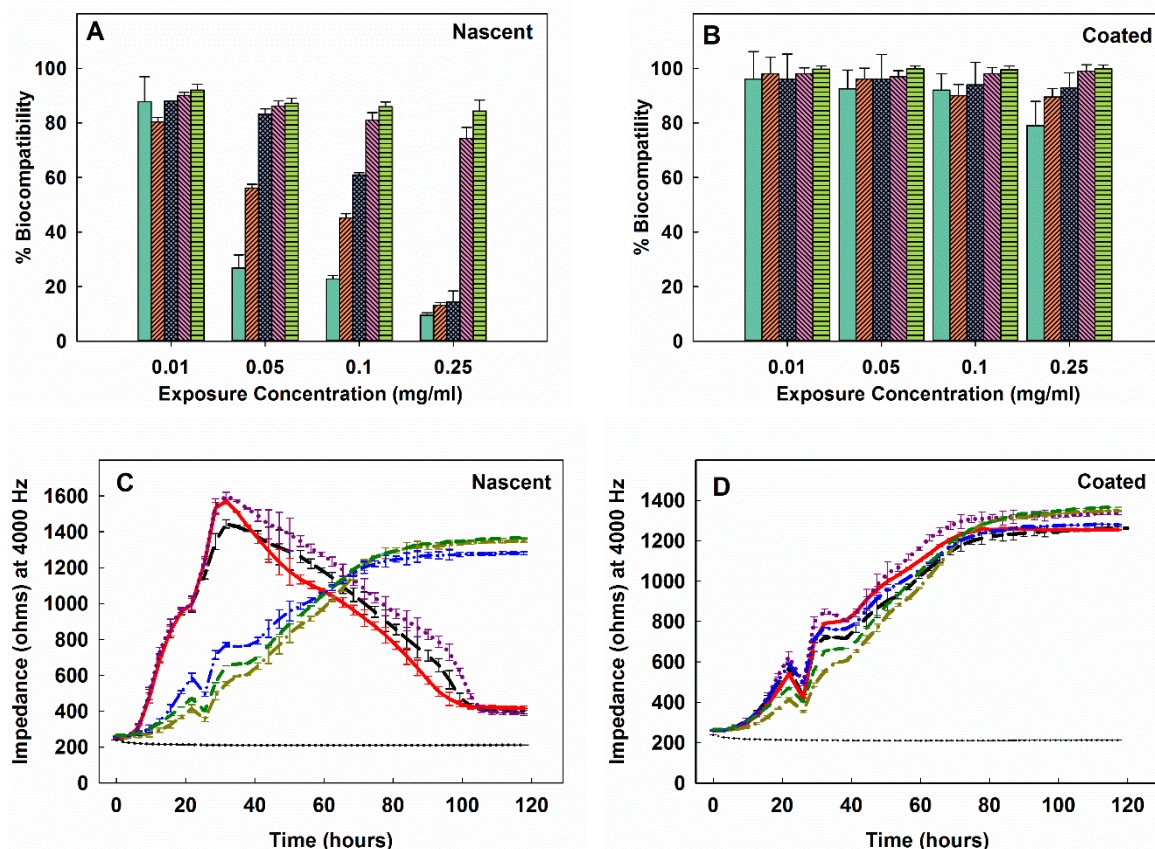


Figure 3.6 Biocompatibility results of (A) nascent Au NPs and (B) HA-S-Au NPs. HS-HA coating significantly increased the compatibility of NPs with ARPE-19 cells. Values are expressed in mean \pm SEM for each condition; three independent experiments were done with eight replicates ($n = 24$; Student's t-test, $*P < 0.05$ versus controls). The results were compared to each other using two-factor ANOVA analysis. For nascent particles, in terms of both particle size and exposure concentration, the results were significantly different from each other ($*P < 0.05$). For coated particles, the results were found to be independent of the exposure concentration ($**P > 0.05$) but statistically different among each nanoparticle size tested ($P* < 0.05$)

5nm,
 10 nm,
 20 nm,
 50 nm,
 100 nm
 5nm,
 10 nm,
 20 nm,
 50 nm,
 100 nm
 untreated cells,
 media (DMEM) only

Cell morphology was observed by 3D confocal microscopy. There was a significant structural change in cytoskeleton fibers (actin) in retinal cells exposed to nascent NPs ($dp < 50$ nm) (Fig. S7). The nuclear morphology was disrupted, and the density of actin significantly decreased (see supporting information, Figs. S7B, S7D, S7F). In a previous study degradation of actin was linked to cell death (Tezel et al. 1999), consistent with our confocal imaging observations.

Cells exposed to HA-S-Au NPs maintained good actin density and intact nuclei (Figs. S7C, S7E, S7G, S7I, S7K). These observations are consistent with our biocompatibility results, which indicated that coated Au NPs are not toxic and do not initiate apoptosis.

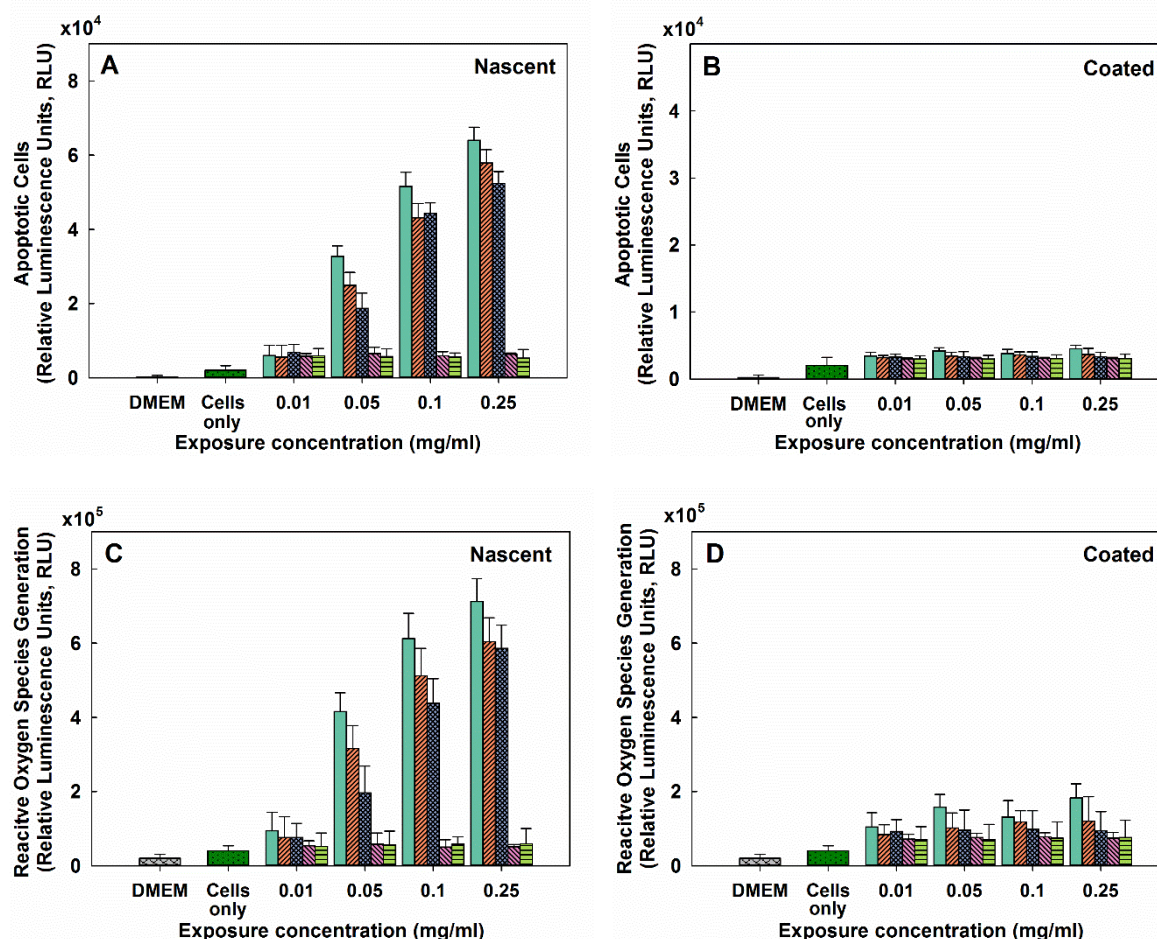


Figure 3.7 Measurement of apoptotic cells amounts using the Apo Tox-Glo™ assay when the cells are exposed to (A) nascent Au NPs and (B) HA-S-Au NPs. Measurement of ROS levels using the ROS Glo™ H₂O₂ assay, when the cells are exposed to (C) nascent Au NPs and (D) HA-S-Au NPs. The HS-HA coating prevented both apoptosis and ROS generation in ARPE-19 cells for all particle sizes tested. (n = 24; Student's t-test, *P < 0.05 versus controls). The results were compared to each other using two-factor ANOVA analysis. In both measurements, for nascent particles, in terms of both particle size and exposure concentration, the results were significantly different from each other (*P < 0.05). For coated particles, the results were found to be independent of the exposure concentration (**P > 0.05) but statistically different among each nanoparticle size tested (*P < 0.05).

5 nm, 10 nm, 20 nm, 50 nm, 100 nm

3.3.6 Cell attachment behavior with ECIS measurements in response to Au NPs

We monitored retinal cells' attachment in the presence of both nascent and coated Au NPs via electrical impedance measurements. Retinal cells exposed to nascent NPs less than 50 nm in diameter, at their critical $LD_{50, M}$ concentrations, almost immediately started to detach from the plate (Fig. 3.6C). On the other hand, cell attachment was not hindered when the ARPE-19 cells were exposed to HA-S-Au NPs (Fig. 3.6D). Following the addition of HA-S-Au NPs, the impedance curves, which show the real-time cellular response, fall in line with the negative control group, in which neither coated nor nascent NPs were exposed to the cells (Fig. 3.6D). The cell attachment behavior is directly correlated to cell viability. Therefore, it can be inferred that cell viability is not compromised in the presence of HA-S-Au NPs. As a result, it is clear that not only HA coating plays a significant role in the internalization of Au NPs, but also that its presence, independent of particle size and the amount of Au NPs inside a cell, protects the cell from ROS damage, does not initiate cell death.

3.4 Conclusions

Our TOC and TGA results indicated that we successfully coated Au NPs with HS-HA. The grafting density varied from 0.18 to 0.03 # of HA molecules/nm² as the size of Au NPs increased from 5 to 100 nm. HS-HA coating decreased Au NPs' toxicity to the cells. The improved biocompatibility is associated with HA's ability to act as a free-radical quencher as revealed by our ROS measurements. The native 50- and 100-nm Au NPs could not enter the cell; however, the HS-HA coating enabled their entry in the cells via CD44 receptors, acting as a Trojan horse for the larger particles. The endocytosis of large particles coated with HS-HA is a significant observation for targeted drug and gene delivery applications.

Internalization was a function of the density of CD44 receptors as evidenced by percent internalization results with three different cell lines: CHO>ARPE-19>NIH 3T3.

In conclusion, we showed that HS-HA coating facilitates entry of Au NPs in size range of 5-100 nm into cells that express CD44 receptors and renders the NPs biocompatible. This observation portends that HS-HA can be used as a biocompatible carrier to deliver larger payloads for treating inflamed, proliferating, and cancer cells that are associated with increased expression of CD44 receptors.

3.5 Acknowledgements

This work was supported by NIH RO1 ECS-0335765, a Lacey and Nelson grant, a Core grant from the Association for the Prevention of Blindness, and a Veteran Affairs Merit review grant. Veteran Affairs Office of Research and Development IO1BX007080 grant to Kelle H. Moley supported confocal imaging. (NR). Partial support from McDonnell Academy Global Energy and Environment Partnership (MAGEEP) and the Lopata Endowment are gratefully acknowledged (PB).

3.6 References

1. Ahire, J. J., D. Robertson, D. P. Neveling, A. J. van Reenen and L. M. T. Dicks (2016). "Hyaluronic acid-coated poly(d,l-lactide) (pdlla) nanofibers prepared by electrospinning and coating." RSC Advances **6**(41): 34791-34796.
2. Almalik, A., S. Karimi, S. Ouasti, R. Donno, C. Wandrey, P. J. Day and N. Tirelli (2013). "Hyaluronic acid (ha) presentation as a tool to modulate and control the receptor-mediated uptake of ha-coated nanoparticles." Biomaterials **34**(21): 5369-5380.
3. Arndt, S., J. Seebach, K. Psathaki, H. J. Galla and J. Wegener (2004). "Bioelectrical impedance assay to monitor changes in cell shape during apoptosis." Biosensors & Bioelectronics **19**(6): 583-594.
4. Balogh, G. T., J. Illes, Z. Szekely, E. Forrai and A. Gere (2003). "Effect of different metal ions on the oxidative damage and antioxidant capacity of hyaluronic acid." Archives of Biochemistry and Biophysics **410**(1): 76-82.
5. Benoit, D. N., H. G. Zhu, M. H. Lillierose, R. A. Verm, N. Ali, A. N. Morrison, J. D. Fortner, C. Ayendano and V. L. Colvin (2012). "Measuring the grafting density of nanoparticles in solution by analytical ultracentrifugation and total organic carbon analysis." Analytical Chemistry **84**(21): 9238-9245.
6. Borradori, L. and A. Sonnenberg (1999). "Structure and function of hemidesmosomes: More than simple adhesion complexes." Journal of Investigative Dermatology **112**(4): 411-418.
7. Chaitin, M. H. and A. A. Davis (1995). "Cd44 in the human retina." Investigative Ophthalmology & Visual Science **36**(4): S279-S279.
8. Chen, L., C. Cursiefen, S. Barabino, Q. Zhang and M. R. Dana (2005). "Novel expression and characterization of lymphatic vessel endothelial hyaluronate receptor 1 (lyve-1) by conjunctival cells." Investigative Ophthalmology & Visual Science **46**(12): 4536-4540.
9. Culty, M., H. A. Nguyen and C. B. Underhill (1992). "The hyaluronan receptor (cd44) participates in the uptake and degradation of hyaluronan." Journal of Cell Biology **116**(4): 1055-1062.
10. Diebold, Y. and M. Calonge (2010). "Applications of nanoparticles in ophthalmology." Progress in Retinal and Eye Research **29**(6): 596-609.
11. Frens, G. (1973). "Controlled nucleation for regulation of particle-size in monodisperse gold suspensions." Nature-Physical Science **241**(105): 20-22.
12. Glucksam-Galnoy, Y., T. Zor and R. Margalit (2012). "Hyaluronan-modified and regular multilamellar liposomes provide sub-cellular targeting to macrophages, without eliciting a pro-inflammatory response." Journal of Controlled Release **160**(2): 388-393.
13. Gupta, R. and B. Rai (2017). "Effect of size and surface charge of gold nanoparticles on their skin permeability: A molecular dynamics study." Scientific Reports **7**:45292.
14. Hans, M. L. and A. M. Lowman (2002). "Biodegradable nanoparticles for drug delivery and targeting." Current Opinion in Solid State & Materials Science **6**(4): 319-327.
15. Huang, X. H., P. K. Jain, I. H. El-Sayed and M. A. El-Sayed (2008). "Plasmonic photothermal therapy (pptt) using gold nanoparticles." Lasers in Medical Science **23**(3): 217-228.
16. Jaggupilli, A. and E. Elkord (2012). "Significance of cd44 and cd24 as cancer stem cell markers: An enduring ambiguity." Clinical & Developmental Immunology: 11.
17. Jiang, J., G. Oberdorster, A. Elder, R. Gelein, P. Mercer and P. Biswas (2008). "Does nanoparticle activity depend upon size and crystal phase?" Nanotoxicology **2**(1): 33-42.
18. Kandasamy, K., C. S. Choi and S. Kim (2010). "An efficient analysis of nanomaterial cytotoxicity based on bioimpedance." Nanotechnology **21**(37): 10.

19. Karakocak, B. B., R. Raliya, J. T. Davis, S. Chavalmane, W.-N. Wang, N. Ravi and P. Biswas (2016). "Biocompatibility of gold nanoparticles in retinal pigment epithelial cell line." Toxicology in Vitro **37**: 61-69.
20. Karthikeyan, B., K. Kalishwaralal, S. Sheikpranbabu, V. Deepak, R. Haribalaganesh and S. Gurunathan (2010). "Gold nanoparticles downregulate vegf-and il-1 beta-induced cell proliferation through src kinase in retinal pigment epithelial cells." Experimental Eye Research **91**(5): 769-778.
21. Katoh, S., Z. Zheng, K. Oritani, T. Shimozato and P. W. Kincade (1995). "Glycosylation of cd44 negatively regulates its recognition of hyaluronan." Journal of Experimental Medicine **182**(2): 419-429.
22. Kesharwani, P., S. Banerjee, S. Padhye, F. H. Sarkar and A. K. Iyer (2015). "Hyaluronic acid engineered nanomicelles loaded with 3,4-difluorobenzylidene curcumin for targeted killing of cd44+stem-like pancreatic cancer cells." Biomacromolecules **16**(9): 3042-3053.
23. Kim, J. H., M. H. Kim, D. H. Jo, Y. S. Yu and T. G. Lee (2011). "The inhibition of retinal neovascularization by gold nanoparticles via suppression of VEGFR-2 activation." Biomaterials **32**(7): 1865-1871.
24. Kimling, J., M. Maier, B. Okenve, V. Kotaidis, H. Ballot and A. Plech (2006). "Turkevich method for gold nanoparticle synthesis revisited." Journal of Physical Chemistry B **110**(32): 15700-15707.
25. Kumar, C. S., M. D. Raja, D. S. Sundar, M. G. Antoniraj and K. Ruckmani (2015). "Hyaluronic acid co-functionalized gold nanoparticle complex for the targeted delivery of metformin in the treatment of liver cancer (hepg2 cells)." Carbohydrate Polymers **128**: 63-74.
26. La Gatta, A., M. De Rosa, I. Marzaioli, T. Busico and C. Schiraldi (2010). "A complete hyaluronan hydrodynamic characterization using a size exclusion chromatography-triple detector array system during in vitro enzymatic degradation." Analytical Biochemistry **404**(1): 21-29.
27. Larson, T. A., P. R. Joshi and K. Sokolov (2012). "Preventing protein adsorption and macrophage uptake of gold nanoparticles via a hydrophobic shield." ACS Nano **6**(10): 9182-9190.
28. Lee, H., K. Lee, I. K. Kim and T. G. Park (2008). "Synthesis, characterization, and in vivo diagnostic applications of hyaluronic acid immobilized gold nanoprobe." Biomaterials **29**(35): 4709-4718.
29. Lee, M. Y., J. A. Yang, H. S. Jung, S. Beack, J. E. Choi, W. Hur, H. Koo, K. Kim, S. K. Yoon and S. K. Hahn (2012). "Hyaluronic acid-gold nanoparticle/interferon alpha complex for targeted treatment of hepatitis c virus infection." ACS Nano **6**(11): 9522-9531.
30. Lin, W. J., W.-C. Lee and M.-J. Shieh (2017). "Hyaluronic acid conjugated micelles possessing cd44 targeting potential for gene delivery." Carbohydrate Polymers **155**: 101-108.
31. Moghadam, B. Y., W. C. Hou, C. Corredor, P. Westerhoff and J. D. Posner (2012). "Role of nanoparticle surface functionality in the disruption of model cell membranes." Langmuir **28**(47): 16318-16326.
32. Moysidis, S. N., A. Thanos and D. G. Vavvas (2012). "Mechanisms of inflammation in proliferative vitreoretinopathy: From bench to bedside." Mediators of Inflammation: 11.
33. Nasir, I., M. Lundqvist and C. Cabaleiro-Lago (2015). "Size and surface chemistry of nanoparticles lead to a variant behavior in the unfolding dynamics of human carbonic anhydrase." Nanoscale **7**(41): 17504-17515.
34. Nedvetzki, S., E. Gonen, N. Assayag, R. Reich, R. O. Williams, R. L. Thurmond, J. F. Huang, B. A. Neudecker, F. S. Wang, E. A. Turley and D. Naor (2005). "Rhamm, a receptor for hyaluronan-mediated motility, compensates for cd44 in inflamed CD44-knockout mice: A

- different interpretation of redundancy (vol 101, pg 18081, 2004)." Proceedings of the National Academy of Sciences of the United States of America **102**(4): 1263-1263.
35. Nel, A. E., L. Madler, D. Velegol, T. Xia, E. M. V. Hoek, P. Somasundaran, F. Klaessig, V. Castranova and M. Thompson (2009). "Understanding biophysicochemical interactions at the nano-bio interface." Nature Materials **8**(7): 543-557.
36. Ngwa, W., M. Makrigiorgos and R. Berbeco (2012). "Enhancing stereotactic radiosurgery for neovascular age-related macular degeneration, using gold nanoparticles." Medical Physics **39**(6): 3798-3798.
37. Pan, Y., S. Neuss, A. Leifert, M. Fischler, F. Wen, U. Simon, G. Schmid, W. Brandau and W. Jahnen-Dechent (2007). "Size-dependent cytotoxicity of gold nanoparticles." Small **3**(11): 1941-1949.
38. Panariti, A., G. Miserocchi and I. Rivolta (2012). "The effect of nanoparticle uptake on cellular behavior: Disrupting or enabling functions?" Nanotechnology, Science and Applications **5**: 87.
39. Pandey, M. S. and P. H. Weigel (2014). "Hyaluronic acid receptor for endocytosis (hare)-mediated endocytosis of hyaluronan, heparin, dermatan sulfate, and acetylated low density lipoprotein (acldl), but not chondroitin sulfate types a, c, d, or e, activates nf-kappa b-regulated gene expression." Journal of Biological Chemistry **289**(3): 1756-1767.
40. Papasani, M. R., G. K. Wang and R. A. Hill (2012). "Gold nanoparticles: The importance of physiological principles to devise strategies for targeted drug delivery." Nanomedicine-Nanotechnology Biology and Medicine **8**(6): 804-814.
41. Perschl, A., J. Lesley, N. English, I. Trowbridge and R. Hyman (1995). "Role of cd44 cytoplasmic domain in hyaluronan-binding." European Journal of Immunology **25**(2): 495-501.
42. Pitarresi, G., E. F. Craparo, F. S. Palumbo, B. Carlisi and G. Giammona (2007). "Composite nanoparticles based on hyaluronic acid chemically cross-linked with alpha,beta-polyaspartylhydrazide." Biomacromolecules **8**(6): 1890-1898.
43. Rana, S., A. Bajaj, R. Mout and V. M. Rotello (2012). "Monolayer coated gold nanoparticles for delivery applications." Advanced Drug Delivery Reviews **64**(2): 200-216.
44. Santhanam, S., J. Liang, R. Baid and N. Ravi (2015). "Investigating thiol-modification on hyaluronan via carbodiimide chemistry using response surface methodology." Journal of Biomedical Materials Research Part A **103**(7): 2300-2308.
45. Santhanam, S., J. Liang, J. Struckhoff, P. D. Hamilton and N. Ravi (2016). "Biomimetic hydrogel with tunable mechanical properties for vitreous substitutes." Acta Biomaterialia **43**: 327-337.
46. Tezel, G., G. M. Seigel and M. B. Wax (1999). "Density-dependent resistance to apoptosis in retinal cells." Current Eye Research **19**(5): 377-388.
47. Tzircotis, G., R. F. Thorne and C. M. Isacke (2005). "Chemotaxis towards hyaluronan is dependent on cd44 expression and modulated by cell type variation in cd44-hyaluronan binding." Journal of Cell Science **118**(21): 5119-5128.
48. Wang, S. J., Y. Tian, W. Tian, J. Sun, S. Zhao, Y. Liu, C. Y. Wang, Y. X. Tang, X. Q. Ma, Z. G. Teng and G. M. Lu (2016). "Selectively sensitizing malignant cells to photothermal therapy using a cd44-targeting heat shock protein 72 depletion nanosystem." ACS Nano **10**(9): 8578-8590.
49. Wegener, J., C. R. Keese and I. Giaever (2000). "Electric cell-substrate impedance sensing (ecis) as a noninvasive means to monitor the kinetics of cell spreading to artificial surfaces." Experimental Cell Research **259**(1): 158-166.
50. Yilmaz, G., B. Demir, S. Timur and C. R. Becer (2016). "Poly(methacrylic acid)-coated gold nanoparticles: Functional platforms for theranostic applications." Biomacromolecules **17**(9): 2901-2911.

51. Zhang, S. L., J. Li, G. Lykotrafitis, G. Bao and S. Suresh (2009). "Size-dependent endocytosis of nanoparticles." Advanced Materials **21**: 419-424.

Chapter 4: Nitrogen-doped Carbon Dots as a Biocompatible Alternative for Bioimaging

The results of this chapter have been reprinted with permission from Karakocak, B. B.; Liang, J.; Kavadiya, S.; Berezin, M. Y.; Biswas, P.; Ravi, N. Optimizing the Synthesis of Red-Emissive Nitrogen-doped Carbon Dots for Use in Bioimaging. ACS Appl. Nano Mater. DOI: 10.1021/acsanm.8b00799. Copyright 2018 American Chemical Society

Supplementary information along with additional figures and tables are available in Appendix III

Abstract

Synthesizing highly efficient red-emissive carbon dots (CDs) is a challenge that still impedes widespread applications of CDs in bioimaging. Herein, we demonstrate a facile, isolation-free synthesis of deep red (600-700 nm) emissive nitrogen-doped CDs (nCDs) based on microwave-assisted pyrolysis of citric acid and ethylenediamine. The duration of pyrolysis, the molar ratio of acid to amine, and the concentration of reactants were optimized by means of Central Composite Design and Response Surface Methodology (CCD-RSM) to yield deep red to near-infrared fluorescence. We demonstrated their applicability on three different cell lines (retinal epithelial, lens epithelial, and Chinese hamster ovary cells (CHO)). We measured the viability, the generation of reactive oxygen species, and percentage of apoptotic cells to determine their level of toxicity in cell culture. Confocal images showed that the nCDs fluoresced at different wavelength depending upon the excitation wavelength and were excitable up to 635 nm. Furthermore, the *ex vivo* imaging of porcine ocular globes and *post-mortem* imaging of a whole mouse exemplified the utility of nCDs.

4.1 Introduction

Carbon dots, a rising star in the bioimaging field (Luo et al. 2013, Berezin 2014, Cherukula et al. 2016, Gan et al. 2016), have attracted considerable attention due to their numerous and unique intrinsic properties such as wavelength dependent excitation/emission (Jiang et al. 2015, Ding et al. 2016) a long fluorescence lifetime (Dong et al. 2015) good photostability (Zhang et al. 2015) and high biocompatibility (Tao et al. 2012). With these unique properties, carbon dots (CDs) have demonstrated promise for bioimaging applications.(Hola et al. 2014, Choi et al. 2016, Zhang et al. 2016) Even though, many kinds of CDs have been reported; most show intense emission only in blue-green regions following excitation with ultraviolet or blue light (Bourlinos et al. 2008, Peng and Travas-Sejdic 2009, Wang et al. 2010, Bourlinos et al. 2012, Zhu et al. 2013, Yang et al. 2015, Qu et al. 2017). The well-known blue autofluorescence of native biological matrix and the severe photodamage caused by ultraviolet excitation further hinder their application. Although, there have been a handful of attempts to create red-emissive CDs (Nie et al. 2014, Ge et al. 2015, Ding et al. 2016, Sun et al. 2016, Feng et al. 2017, Miao et al. 2017), either the excitation was limited to green light or the synthesis method was quite involved. Therefore, it remains highly desirable to achieve red-emissive CDs that can be excited with longer wavelengths, penetrating deep in tissue without causing damage to the target cell/tissue/organ, via a truly facile synthesis method.

Various methods for creating CDs, ranging from relatively simple to rather complex procedures, have been reported (Luo et al. 2013, Nie et al. 2014, Ding et al. 2016, Feng et al. 2016, Feng et al. 2017, Lin et al. 2017, Lin et al. 2018). Certain synthesis methods produce great variety of CDs with a broad distribution of fluorescence emission, and hence necessitate separation (i.e., silica column chromatography (Nie et al. 2014, Ding et al. 2016, Feng et al. 2017), capillary electrophoresis (Hu et al. 2013)) to isolate those nanoparticles with desired optical properties. For clinical applications, it would be ideal to scale up the synthesis,(Wang

and Hu 2014) preferably using a simple method involving commercially available reactants and environmentally friendly techniques (Xu et al. 2014). Among existing methods, microwave pyrolysis has the distinct advantages of shorter reaction times, milder reaction conditions, lower energy consumption, better stability, easy reproducibility, and higher product efficiency (Zhu et al. 2009, Zhai et al. 2012, Hu et al. 2013). Thus, microwave pyrolysis exhibits great promise as opposed to other synthesis methods which are quite involved and require isolation of the desired red-emissive CDs.

In this study, we optimized an isolation-free method of synthesizing red-emissive CDs (red-CDs) with deep red to near-infrared (NIR) fluorescence (600 - 700 nm). Such long-wavelength emitters are highly desired in optical imaging of tissue, due to the decreased interference from tissue autofluorescence at longer wavelengths (Hola et al. 2014, Ostadhossein and Pan 2017). The deep-red emitters were based on nitrogen-doped carbon dots (nCDs) prepared by microwave-assisted pyrolysis of a mixture of citric acid and aliphatic diamines without the need for intensive isolation of the red-emissive nCDs. The duration of pyrolysis, the molar ratio of acid to amine, and the concentration of reactants were optimized to maximize fluorescence efficiency. The biocompatibility of the nCDs was assessed on three different cell lines by measuring cell viability, generation of reactive oxygen species (ROS), and the extent of apoptosis. Confocal microscopy images of the three cell lines showed that the nCDs were excitable also at different wavelengths including the NIR region. Finally, to demonstrate the potential of red-nCDs as bioimaging agents, the nCDs were injected intravitreally into *ex vivo* porcine ocular globes and subcutaneously in euthanized mice, where they are easily detected.

4.2 Methods

4.2.1 Materials

All chemicals were used as received. Ethylenediamine (EDA) (99%, cat# E26266), and Rhodamine 6G (99%, cat# 252433) were purchased from Sigma-Aldrich. Citric acid (CA) was purchased from J.T. Baker Chemical Co. Dulbecco's modified Eagles's medium/nutrient mixture F-12 Ham (DMEM/F12), trypsin-ethylenediaminetetraacetic acid (EDTA) solution 10x, and fetal calf serum (FCS), TritonTM X-100, phosphate buffer saline (PBS), 100x antibiotic-antimycotic solution, and thiazolyl blue tetrazolium bromide (MTT) (98%, cat# M2128) were obtained from Sigma-Aldrich (St. Louis, MO). SlowFade[®] Gold Antifade Mountant with DAPI (cat# S36938) was purchased from Thermo Fisher Scientific (St. Peters, MO). Retinal pigment epithelial (ARPE-19) (ATCC[®] CRL-2302TM), lens epithelial cells (ATCC[®] CRL-11421TM), and CHO (CCL-61TM) cells were purchased from American Type Culture Collection (Manassas, VA). ApoTox-GloTM (cat# G6320) and ROS GloTM H₂O₂ (cat# G8820) assays were purchased from Promega Corporation (Madison, WI).

4.2.2 Synthesis of nCDs

We evaluated the effect of three factors in the synthesis of nCDs – the molar ratio of amine to acid, the duration of pyrolysis (microwave exposure time), and the concentration of the reactants on creating red-nCDs. For this, a Central-Composite Design Response Surface Methodology (CCD-RSM) design was utilized (Stat-Ease, Design-Expert[®] software, version 9.0). Each factor was varied at five levels: amine/acid (molar ratio) = 0.30, 0.48, 0.75, 1.02, and 1.20; microwave exposure time = 70 s, 75 s, 88 s, 95 s, and 100 s; and concentration of citric acid (wt/v %) = 8.0, 8.8, 10.0, 11.2, and 12.0. There were twenty runs of carbon dots synthesis, as tabulated in Table S1.

A stock solution of 12 wt/v % of citric acid was prepared by dissolving 28.39 g of citric acid in 220 mL of water. The desired amount (see Table S1) of this stock solution was added to a

glass beaker (capacity 100 mL), then DI water was added to make the volume up to 10 mL, and then the desired amount of ethylenediamine (see Table S1) was added. The mixture was shaken and heated in a microwave oven (General Electric, 1,100 watts) for a varying durations as listed in Table S1. Products of these 20 different synthesis experiments yielded a brittle solid, whose color varied from yellow to brown. This solid was dissolved in 3 mL of water and transferred to a 20 mL vial. The beaker was rinsed with another 2 mL of water, and the liquids were combined. The solution was dialyzed against water (Molecular weight cut-off (MWCO) = 500 Da, Spectra Por 131084 Biotech-Grade CE dialysis tubing) for 24 hours.

4.2.3 Physico-chemical characterization of nCDs

The morphologies and the size of the synthesized nCDs were examined by high-resolution transmission electron microscopy (HR-TEM, Tecnai TM Spirit, FEI Co.), operated at 200 kV accelerating voltage. Atomic force microscopy (AFM) was carried out using Veeco Dimension 3100 V (Parkafm, Santa Clara, CA). For AFM analysis, the sample was prepared by electrospraying (6 kV) ~5 μ L of nCDs solution (0.625 μ g/mL) on Si wafer to get a clear snapshot of individual nCDs. Dynamic light scattering (DLS) analysis was conducted with a Malvern Zetasizer Nano ZS (Malvern Instruments, Westborough, MA) equipped with a backscattering detector (173°) to measure hydrodynamic sizes and zeta potential of synthesized nCDs. For DLS measurements, the samples were dispersed in water, sonicated for 15 min, filtered through a prerinsed 0.22 μ m polyethersulfone filter. At least three measurements per sample were taken.

UV-Vis absorption spectra were recorded on a Thermo Fisher Biomate 3 UV-Vis spectrophotometer. Fluorescence spectra were measured on a SpectraMax Gemini EM fluorescence reader at ambient conditions. The photoluminescence (PL) emission was determined with a Varian Cary 5000 spectrophotometer. For the measurement of fluorescence homogeneity of the sample and resolving fluorescent impurities, 3D emission-excitation maps

of synthesized nCDs were recorded using a fluorescence excitation-emission spectroscopy method. The measurements were conducted using Vis-NIR (300-1600 nm) spectrofluorometer equipped with an imaging spectrograph iHR320 and a diode array deep-cooled CCD detector Synapse (all from Horiba Jobin Yvon Inc.). Emission spectra acquired at different excitation were corrected for the excitation light intensity. For optical measurements, the samples were diluted until clear and sonicated for 5 minutes before the measurements. At least three measurements per sample were taken.

The quantum yield (Φ_S), the ratio of photons emitted to photons absorbed, of the nCDs in water was determined by a comparative method with Rhodamine 6G as a reference at 540 nm excitation in a 10-mm quartz cuvette. To minimize self-absorption, the absorbance was kept under 0.1 au. Integrated PL intensity in the range of 590-720 nm vs. absorbance was plotted at different concentrations. The Φ_S of the nCD samples was calculated using the following equation(Brouwer 2011):

$$\phi_S = \phi_R \left(\frac{Grad_S}{Grad_R} \right) \left(\frac{\eta_S^2}{\eta_R^2} \right) \quad (Eq. 1)$$

where the subscripts S and R refer to the sample and reference, respectively. $Grad$ is the gradient from the plot of integrated PL intensity against absorbance, and η is the refractive index of the solvent, which is deionized water for both the reference and nCDs solutions.

For molecular weight distribution study, matrix-assisted laser desorption/ionization-time of flight (MALDI-TOF) mass spectrometric analysis of the nCDs was performed with a Bruker UltraFlextreme MALDI-TOF instrument with SmartbeamTM Laser (337 nm) in the positive-ion mode using 2,5 dihydroxybenzoic acid (DHB) as a matrix. The chemical composition of nCDs was determined with X-ray photoelectron spectra (XPS) using a Kratos Axis Ultra spectrometer (DLD, Japan) and a monochromatic Al K α source (1486.6 eV).

4.2.4 *In-vitro* Cytotoxicity measurements on Retinal Pigment Epithelial (ARPE-19), lens epithelial, and Chinese Hamster Ovary (CHO) Cells with MTT, Apotox-Glo™, and ROS-Glo™ H₂O₂ assays.

Cell metabolic activity, and hence the viability of cells in the presence of nCDs (0.01-0.6 mg/ml), was assessed with MTT (3-[4, 5 dimethyl-thiazoly-2-yl] 2-5 diphenyl tetrazolium bromide). The relative amounts of apoptotic cells and reactive oxygen species (ROS) generation were measured by ApoTox-Glo™ and ROS Glo™ H₂O₂ assays, respectively. Each test result (viability measurement, the relative amount of apoptotic cells, and ROS generation) was compared with the corresponding negative (untreated cells) and positive (NPs without the cells) control groups with Student's t-test. $P^* < 0.05$, the significance level, was statistically acceptable. Please refer to the Supplementary Information for further details of the cytotoxicity analysis.

4.2.5 *In-vitro* Imaging of Cells Treated with nCDs

To confirm the presence of nCDs inside cells, we investigated the distribution of nCDs at 0.01-0.6 mg/mL, using a nanoplasmonic confocal laser-scanning microscope (Leica TCS-SP8). Four laser wavelengths (405, 488, 532, and 635 nm) were used during confocal imaging.

Retinal epithelial, lens epithelial, and CHO cells were separately seeded in CELLview™ plates at 5×10^4 cells/well for 24 h. After 24 h of nCD exposure, nCDs that were adsorbed on the cell surface or failed to enter the cells were removed by careful washing with 1x PBS three times. The cells were then fixed by immersion in 4% paraformaldehyde (PFA) as the cross-linking solution for 10 min at room temperature and washed with 1x PBS three times before imaging. For the cell fixation details and preparation for confocal imaging, see the Supplementary Information. A negative control sample (untreated cells) was prepared with cells in the absence of nCDs.

4.3 Results and Discussion

4.3.1 Effects of synthesis conditions on short and long-wavelength emission abilities

Microwave-assisted pyrolysis of organic compounds is a rapid, facile, and cost-effective method for synthesizing CDs (Zhai et al. 2012, Hu et al. 2013, Xu et al. 2014). Generally, a carbon source (a compound containing carbon atoms) and a nitrogen source (a compound containing nitrogen atoms) are dissolved in an aqueous solution, and the mixed solution is heated in a microwave oven. Various types of carbon sources and nitrogen sources have been used in this method, as reported in the literature (Wang and Hu 2014). Among them, using citric acid as the carbon source and a diamine or multi-amine as the nitrogen source has been demonstrated as a successful combination (Zhai et al. 2012). The amine molecules serve as a surface passivating agent and an N-doping precursor. nCDs that were synthesized with this method exhibited excitation-dependent PL (Goh et al. 2012, Zhai et al. 2012). The excitation-dependent emission is due to the heterogeneity of the chemical composition of CDs, in other words, the formation of different functional groups on the surface (Gan et al. 2016, Sharma et al. 2016). Zhai et al. investigated several amine molecules and determined that using 1,2-ethylenediamine led to the highest PL intensity (Zhai et al. 2012). They also varied the amine/acid ratio from 0 to 1.33 and determined that an NH_2/COOH (amine/acid) ratio of 0.67 resulted in the strongest emission. Since then, other groups have also used a similar amine/acid ratio (0.67-0.75) in their research (Zhu et al. 2013, Shi et al. 2014, Jia et al. 2016). However, Zhai's approach was limited to nCDs with a relatively short wavelength optical property with excitation/emission combination ($\lambda_{\text{ex/em}} = 350/460$). For *in vivo* imaging, however, such a short wavelength cannot penetrate through the skin and tissues, and it might be harmful to cells at longer exposure times. (Holla et al. 2014) Therefore, we developed nCDs for long wavelength optical activity with deep red fluorescence ($\lambda_{\text{ex/em}} = 540 \text{ nm}/600 \text{ nm}$)

PL. To optimize the composition of nCDs, we varied three critical factors: amine/acid ratio, citric acid (CA) concentration, and reaction time.

Design of Experiment (DOE) (Liang et al. 2015, Santhanam et al. 2015) (Design Expert® software, version 9.0, Stat-Ease, Minneapolis, MN) was used to outline the optimization space and develop a relationship between the responses of interest and associated factors : the molar ratio of amine to acid, the microwave exposure time, and the concentration of the reactants. In central-composite design we used three factors were varied at five levels, resulting in 20 runs (Table S1). We characterized the PL of the 20 products at both a short wavelength ($\lambda_{ex/em} = 350 \text{ nm}/460 \text{ nm}$) and a long wavelength ($\lambda_{ex/em} = 540 \text{ nm}/600 \text{ nm}$), (Table S1). The details of optimization design and statistical analysis are provided in Supplementary Information.

According to the statistical analysis, the PL at $\lambda_{ex/em} = 350 \text{ nm}/460 \text{ nm}$ could be adjusted by changing the amine/acid ratio and by changing the reaction time; however, changing the concentration of CA within our experimental range did not have a significant effect. Our optimized amine/acid ratio (0.75) is close to the finding from Zhai's work (0.67), this small difference in ratio (0.75-0.67) may be due to their longer microwave exposure time (88 seconds versus 120 seconds) and lower microwave power (1,100 versus 700 W). Using our model, one can precisely predict and control the PL of CDs. Our model also allows changing the value of one factor within a certain range while maintaining the same PL intensity, by changing the other factor on the basis of this equation (Eq. S1). Therefore, the reaction conditions can be tailored to meet specific requirements or limitations.

Furthermore, we determined whether the long wavelength PL follows a similar acid/amine trend to that at a short wavelength as the experimental conditions change (Fig. 4.1A). Our investigation shows it does not, which is a very interesting and valuable result (Fig. 1A vs Fig. 1B). Unlike the PL at short wavelengths, the analysis of the PL at long wavelengths

($\lambda_{ex}/\lambda_{em} = 540 \text{ nm}/600 \text{ nm}$) suggested that the linear model was the most appropriate among all polynomial regression models (Fig. 4.1B). The maximum PL for longer wavelength was observed at amine/acid ratio of 1.20. By using the statistical analysis, we determined that the PL at $\lambda_{ex}/\lambda_{em} = 540 \text{ nm}/600 \text{ nm}$ was mostly affected by the amine/acid ratio. Generally, the emission at 600 nm can be increased by increasing the amine/acid ratio (Eq. S2). The reaction time has a positive effect on the emission at high amine/acid ratio, while it has a negative effect when the amine/acid ratio is low. However, the overall effect of reaction time is much weaker than that of amine/acid ratio. We also determined that the concentration of CA did not have a significant effect.

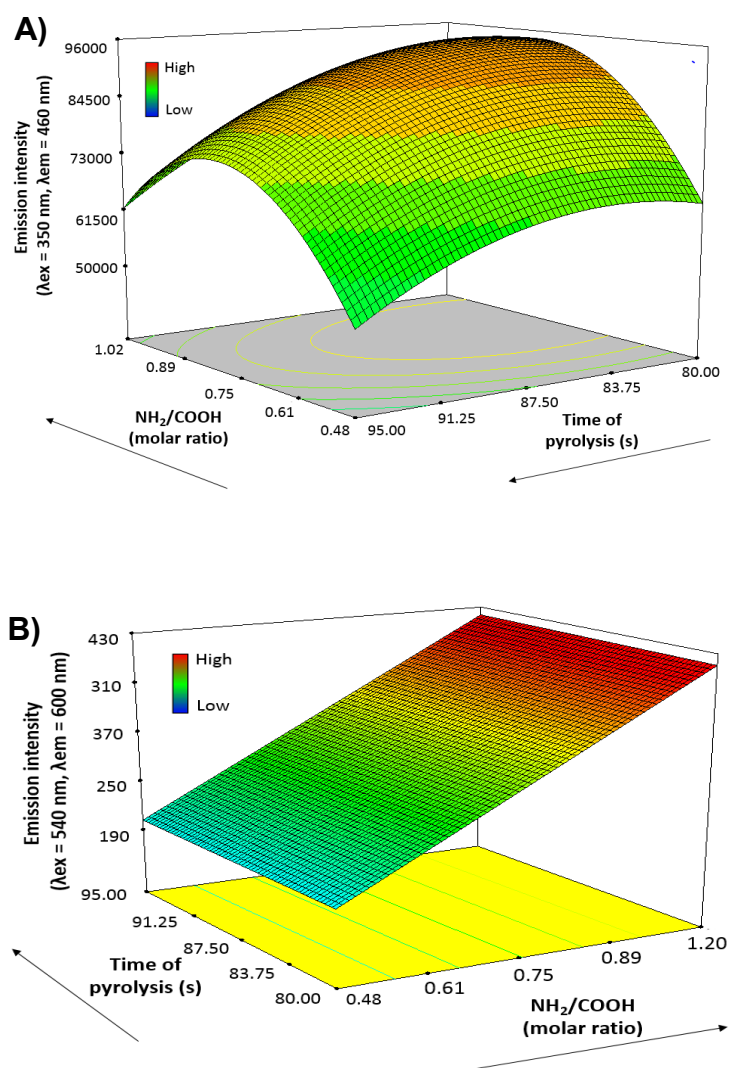


Figure 4.1 Schematic CCD-RSM design responses. (A) $\lambda_{ex} = 350 \text{ nm}$, $\lambda_{em} = 460 \text{ nm}$. (B) $\lambda_{ex} = 540 \text{ nm}$, $\lambda_{em} = 600 \text{ nm}$.

The surface charge of nanoparticles has been shown to be associated with their PL performance (Zhai et al. 2012, Hu et al. 2013, Zhu et al. 2013). Hu et al. utilized a capillary electrophoretic method to characterize the surface charge of CDs synthesized from EDA and CA (Hu et al. 2013). They determined that the amine/acid ratio significantly affected the surface charge of nCDs. When the amine/acid ratio is within 0.25-0.8, positively, neutral, and negatively charged nCDs were generated. According to their results, at higher amine/acid ratio predominantly neutral and positively charged nCDs were formed. They concluded that species with a higher fraction of positively and neutrally charged nCDs exhibited stronger fluorescence than negatively charged nCDs when measured at a wavelength of $\lambda_{ex/em} = 488$ nm/550 nm.

Similar to Hu's results, our findings also indicated that neutral and positively charged nCDs are more likely to be excited at a longer wavelength. The synthesis of nCDs with an amine/acid ratio of 1.20 yielded predominantly neutral and positive emitters, accounting for the strong wavelength emission of our product. The major contribution of our work is that we optimized the synthetic parameters for nCDs that we were able to obtain nCDs with deep-red to NIR emission without their isolation, i.e., by capillary electrophoresis as used by Hu and colleagues.

4.3.2 Maximization of nCD red fluorescence intensity

Since the PL at $\lambda_{ex/em} = 540$ nm/600 nm showed a linear increase when the amine/acid ratio was increased in the range of 0.48 to 1.20, we sought to further increase the PL at long wavelength by extending the range from 0.25 to 3.0. We synthesized another six batches of nCDs with amine/acid ratios of 0.25, 0.5, 1.0, 1.5, 2.0, and 3.0 while keeping the reaction time at 88 seconds and CA% at 10%. However, the batch with amine/acid = 3.0 formed an oily product, which was not completely soluble in water. Thus, amine/acid = 3.0 was eliminated from further study. We determined that the PL at $\lambda_{ex/em} = 540$ nm/600 nm showed a

significant increase with increasing amine/acid ratios in the range of 0.5 to 2.0 (Fig. 4.2). In addition, although the PL intensity showed a linear increase in the range of 0.5-1.0, as demonstrated in the DOE (Fig. 4.1), it approached to a maximum at an amine/acid ratio of 1.20 (Fig. 4.1B). As we found that our synthesis of nCDs with amine/acid ratio of 2.0 yielded longer-wavelength excitable nCDs, which can be explained by the presence of predominantly neutral and positive nCDs, (Hu et al. 2013) accounting for the strong wavelength emission of our product.

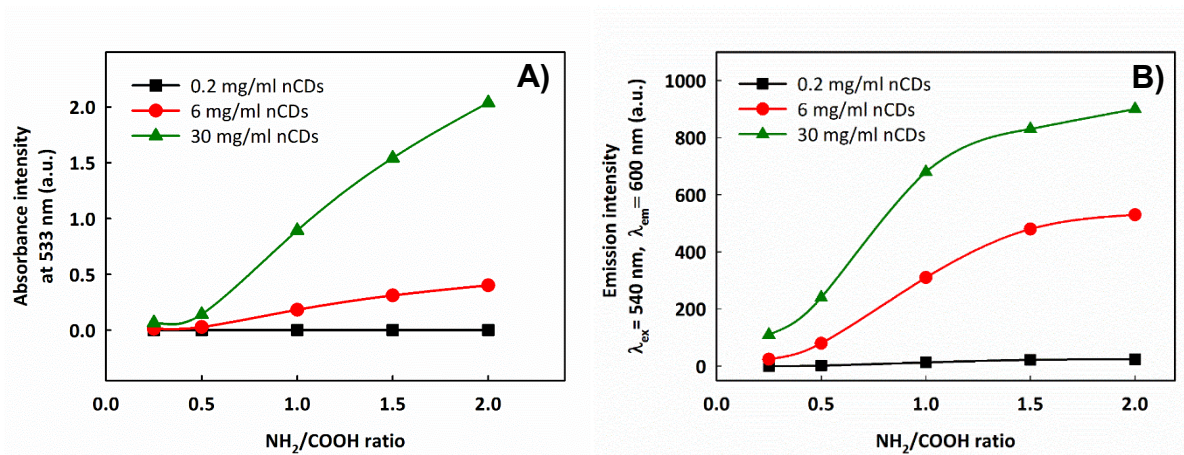


Figure 4.2 (A) Absorbance and (B) PL emission intensities of nCDs at different concentrations with varied amine to acid ratios.

Fluorescence excitation-emission spectroscopy using excitation-emission matrix analysis showed that the nCDs demonstrate characteristic excitation-dependent fluorescence behavior (Fig. 4.3). Such method, in which a series of emission spectra are collected over a range of excitation energies is commonly used to resolve multicomponent fluorescent mixtures (Bachilo et al. 2002, Nevin et al. 2009). The 3D fluorescence spectra revealed the heterogeneity of the emitters at a low amine to acid ratio as indicated by the non-symmetrical and broad shape of the emission. This shape signifies the presence of multiple types of emissive species (i.e., neutral and positively charged) (Fig. 4.3, B-D). The heterogeneity disappears entirely at the high amine to acid ratio = 2.0 (Fig. 4.3E) indicating the formation of a single emitter (i.e., predominantly positively charged). It is worth noting that as the

amine/acid increased, the emission shifts towards NIR region reaching almost 750 nm (Fig. 4.3E). The insets of the figures present nCDs in an aqueous suspension. Changing the NH_2/COOH ratio exhibited different colors of nCDs in an aqueous suspension. The surface characteristics of nCDs have changed leading to a shift in emission as demonstrated by the 3D fluorescence spectra, and the observed colors of the final products are also consistent with this behavior.

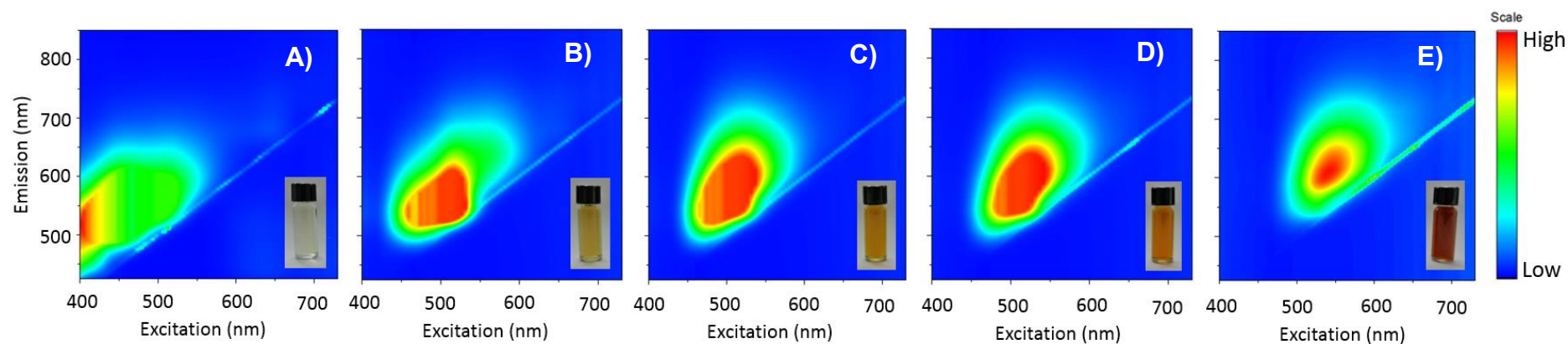
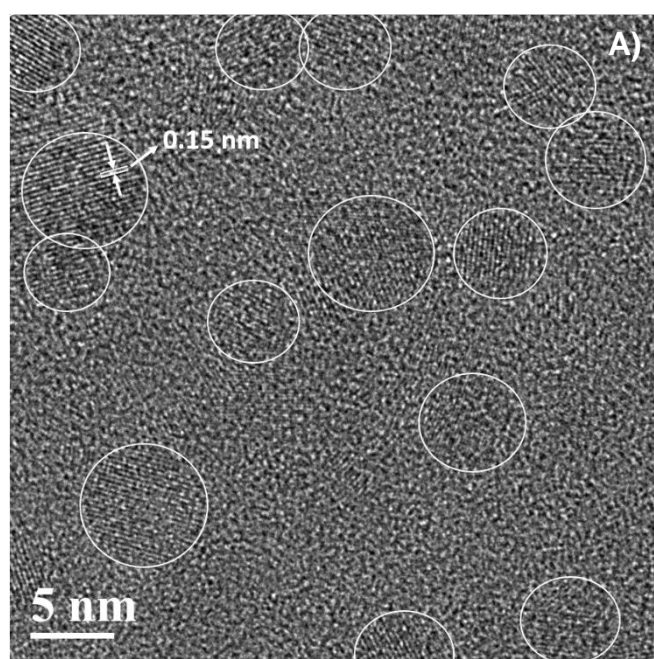


Figure 4.3 Fluorescence excitation-emission spectroscopy of nCDs with amine/acid ratios of (A) 0.25, (B) 0.50, (C) 1.00, (D) 1.50, (E) 2.00. The peak for excitation and emission shifts towards near infrared region as the amine to acid ratio increases. All spectra were corrected for the lamp intensity. The insets of each figures represents synthesized nCDs in DI water, from left to right, the NH₂/COOH ratio is increasing from 0.25 to 2.00.

4.3.3 Characterization of long wavelength nCDs

The HR-TEM images display size distribution 4.05 ± 0.46 nm, and the images reveal that the nCDs have a lattice spacing of 0.15 nm (Fig. 4.4A). This indicates that the nCDs are not amorphous but exhibit long-range ordering. The AFM analysis showed that the particle size of nCDs with amine/acid ratio of 2.0 was less than 5 nm (Fig. 4.4B). Both single carbon dots (marked with white circles) and aggregates of carbon dots were observed in AFM analysis. Fig. 4.4C presents the size distribution of carbon dots, which was determined by measuring the height of 50 single carbon dots observed under AFM. The size distribution suggests the average particle size of 2.99 ± 0.77 nm, with peak size between 2-2.5 nm. On the other hand, according to the DLS analysis, hydrodynamic sizes of the nCDs were found to be ranging from 0.87 ± 0.26 nm to 5.23 ± 1.25 nm in DI water with increasing amine to the acid ratio (Fig. 4.5 and Fig. S1). Furthermore, zeta potential analysis revealed that with increasing amine/acid ratio, the zeta potential of nCDs increased from -4.16 ± 7.76 mV to 45.15 ± 8.05 mV (Fig. 4.5 and Fig. S2). The increase in zeta potential with increasing amine/acid ratio supports the hypothesis that nCDs with high amine/acid ratio yielded neutral and positive nCDs with strong red emission.



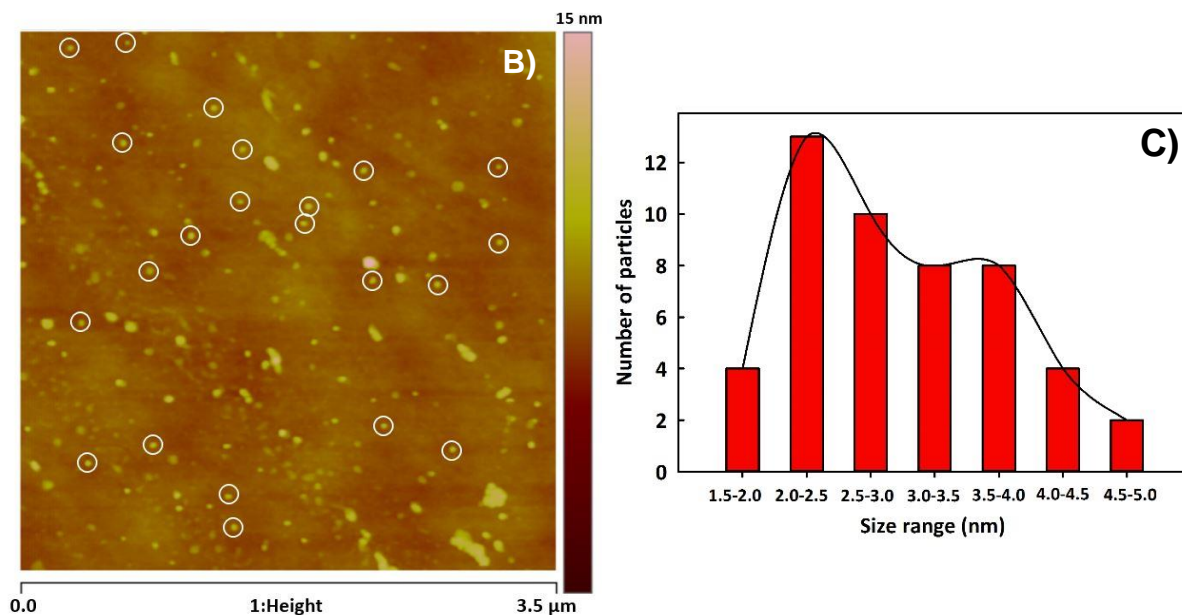


Figure 4.4 (A) HR-TEM image of nCDs with amine/acid ratio of 2.0. The particle size distribution is determined to be 4.05 ± 0.46 nm. The lattice spacing is found to be 0.15 nm. (B) AFM images of nCDs with amine/acid ratio of 2.0. The diameter of nCDs is less than 5 nm. (C) Size distribution of nCDs which was determined by measuring the height of 50 single carbon dots observed under AFM

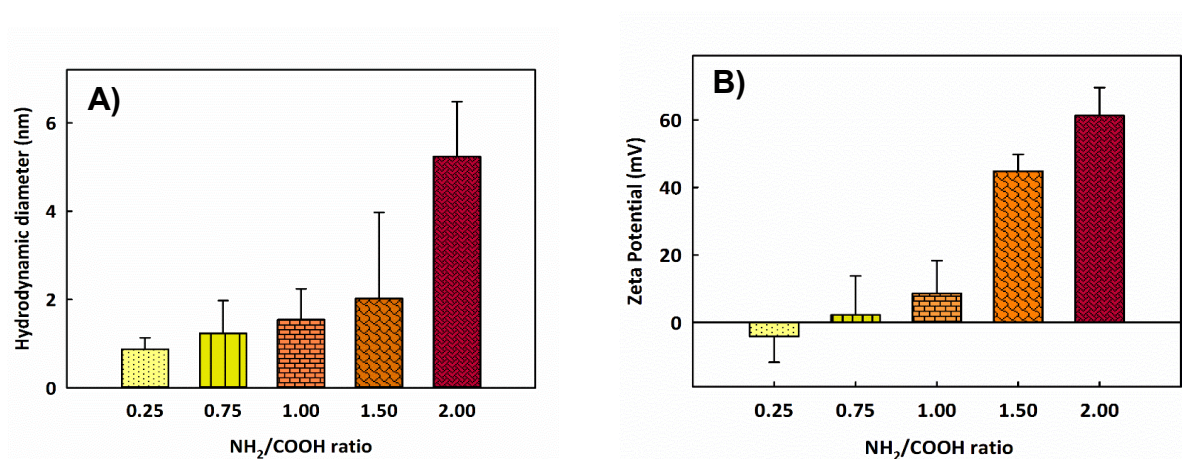


Figure 4.5 Dynamic light scattering analysis of nCDs with NH₂/COOH of 0.25, 0.75, 1.00, 1.50, and 2.00: (A) Hydrodynamic particle size measurement results. (B) Zeta potential measurement results.

Next, we identified the mass of nCDs using MALDI-TOF mass spectroscopy. As shown in Fig. S3, the molecular ions with the highest intensities are $m/z = 799.6$, 1215.0, and 1512.0 for the nCDs with amine/acid ratios of 0.5, 1.0, and 2.0 respectively. The nCD molecular weights determined with MALDI-TOF, increased with increasing amine/acid ratios of 0.5, 1.0, and 2.0, were in accordance with the DLS findings.

The XPS analysis was performed to identify the bonds present on the surface of nCDs. The broad spectrum confirmed the presence of carbon, oxygen, and nitrogen (Fig. S4). Further, high-resolution XPS was performed to identify the type carbon and nitrogen bonds. The high-resolution C1s figures of nCDs with different amine/acid ratio reveal that as the amine to acid ratio increased, different types of bonds were formed on CD surfaces (Fig. 4.6). As shown in Fig. 4.6, the C1s core level peak of the nCDs shows two main peaks at 284.0 ± 0.3 eV (C=C) and 284.5 ± 0.4 eV (C-C), aromatic and aliphatic carbons, respectively. The next peaks at higher binding energy indicate the existence of oxygen groups, including C-O (hydroxyl carbon) at 285.5 ± 0.4 eV, C-O-C (epoxy carbon) at 286.5 ± 0.5 eV, and C=O (carbonyl carbon) at 287.5 ± 0.5 eV (Fig. 6). As the amine/acid was increased, C-O-C bonds (286.5 ± 0.5 eV) disappeared, and starting from amine/acid ratio of 1.00, C-O/C-N bonds (285.5 ± 0.4 eV) were detected. The XPS results clearly indicate that there is a significant change in bonds formed on nCD surfaces as the amine to acid ratio changes. The high-resolution N1s results show that the pyrrolic nitrogen content in nCDs was increased significantly as the amine/acid ratio increased from 0.25 to 2.0 (Fig. S5). It has been shown that specifically cyclic polypyrroles such as pyrrolopyrrole cyanines are fluorescent and emit light beyond 500 nm. (Berezin et al. 2009) It is not possible to provide the exact mechanism of pyrolysis and an accurate molecular structure of the products since pyrolysis is essentially a burning process. However, based on the structure of citric acid, one of the most probable products (or moieties) contributing to deep-red-emissivity of nCDs could be *N,N'*-substituted-pyrrolo[2,3-*b*]pyrrole (Fig. 4.6F). It can be concluded that formation of C-N (Fig. 4.6) and increasing pyrrolic N (Fig. S5) amounts are responsible for red-shifted fluorescence (Fig. 4.3).

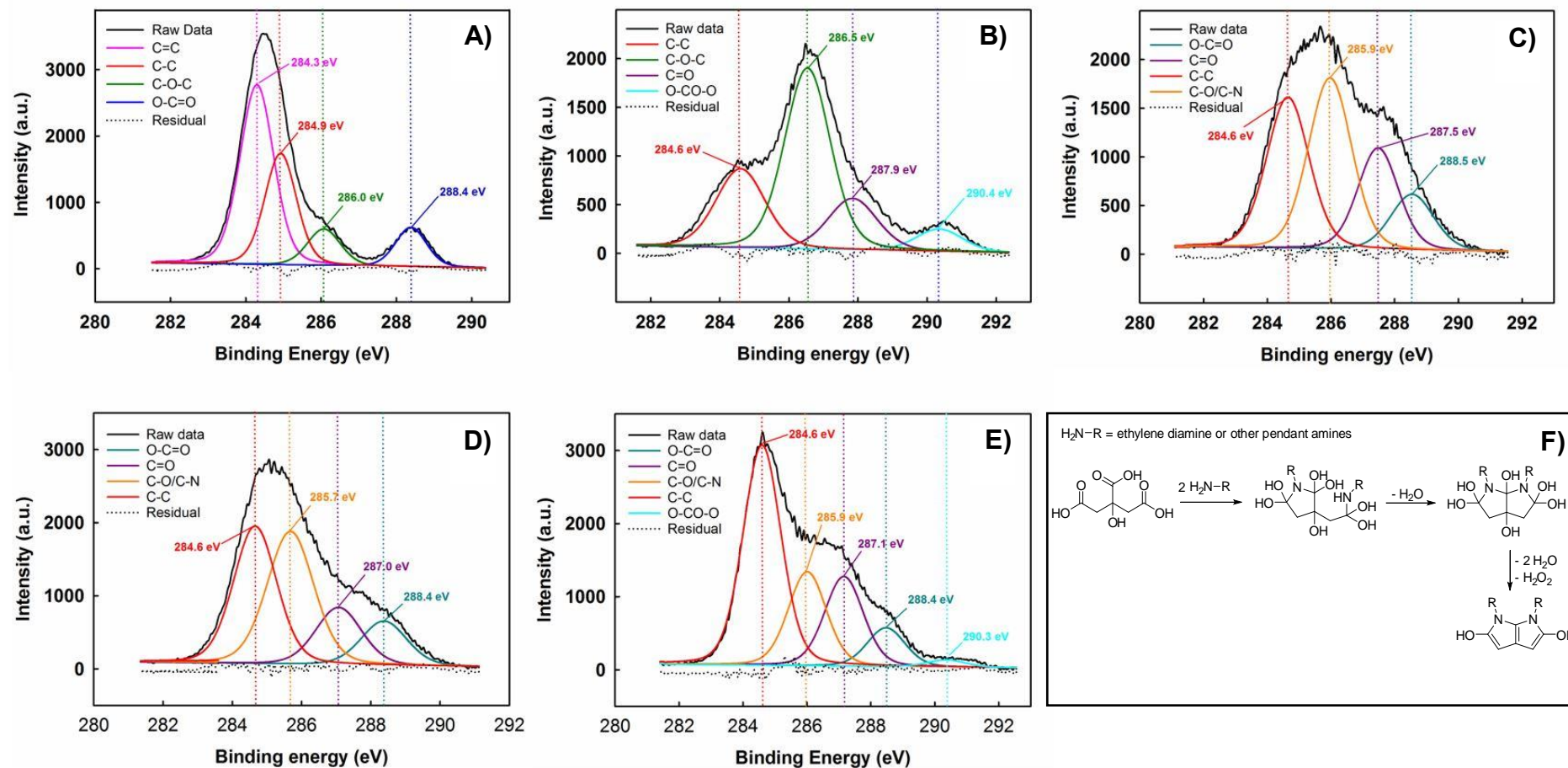


Figure 4.6 High-resolution C1s XPS analysis results of nCDs with amine/acid ratios of (A) 0.25, (B) 0.50, (C) 1.00, (D) 1.50, (E) 2.00. Increasing $NH_2/COOH$ ratio resulted in an apparent C–N bond formation. (F) Proposed formation mechanism for a possible product (N,N'-substituted-pyrrolo[2,3-b]pyrrole) contributing to red-emissivity of nCDs

Table S2. summarizes the effect of molar ratio of reactants to pyrrolic N content and MW of nCDs. Fig. S7A shows the linear relationship between the molar ratio of reactants to pyrrole content ($R^2=0.99$) thereby underscoring that the chemical moieties responsible for red emission is associated with the pyrrole content. MW measurements, based on MALDI-TOF analysis, shows a second order correlation ($R^2=1$) (Fig. S7B) which suggests that increasing the molar ratio of reactants further is not going to increase the MW of nCDs.

The quantum yield of nCDs in the red emission range of 590-720 nm was determined using a comparative quantum yield measurement technique. The red-nCDs quantum yields were found to be in the range of 7%-15% in deionized water (Table S3).

4.3.4 Cytotoxicity evaluation of nCDs

For ocular clinical applications, when the nanoparticles are introduced intravenously, they will have to cross the blood-retinal barrier to reach the ocular tissues (Lavik et al. 2011).

Dysfunction in retinal epithelial cells leads to vascular leakage that could potentially lead to vision-threatening conditions. Lens epithelial cells are associated with cataract formation, the most common visual impairment. We, therefore, investigated the toxicity of nCD to retinal (ARPE-19) and lens epithelial cells. Given the potential application of nCDs in cancer theranostics, we also evaluated the nCDs toxicity to Chinese hamster ovarian (CHO) cells.

For the assessment of toxicity, three different independent end-point assays were used: viability based on enzymatic activity in mitochondria; the percent of apoptotic cells based on caspase 3/7 activity, and ROS generation, which is proportional to luciferase activity (see Methods). The results indicated that for retinal and lens epithelial cells, the lethal dose required to kill 50% of the cells (LD_{50}) of nCDs was approximately 0.6 mg/mL (Fig. S8-9A). Up to this critical concentration, more than 50% of the retinal and lens epithelial cells did not initiate apoptotic cell death (Fig. S8-9B) but induced ROS generation (Fig. S8-9C). On the

other hand, interestingly, CHO cells generated more than twice ROS than ocular epithelial cells; however, their viability was not compromised up to 0.6 mg/ml exposure concentration of nCDs (Fig. S10). Cancer cells, in general, are shown to have increased ROS levels in comparison to normal cells to initiate cell death (Tafani et al. 2016). The increased ROS levels are partly due to an enhanced metabolism and mitochondrial dysfunction in cancer cells (Galadari et al. 2017).

4.3.5 *In-vitro* imaging of nCDs

To confirm the uptake of nCDs by the cells, we investigated the distribution of nCDs after incubation using a nano-plasmonic confocal laser scanning microscope (LEICA TCS-SP8) (see Methods). The above-mentioned cell lines were used for *in vitro* imaging analysis as well. According to the images presented in Fig. 4.7, nCDs have demonstrated successful use of fluorescence imaging *in vitro*, due to their excitability at multiple wavelengths in the visible spectrum. Furthermore, we showed that nCDs could also fluoresce when excited at 635 nm thus minimizing the effect of autofluorescence and increasing the signal to background ratio.

$\lambda_{\text{ex}} = 405 \text{ nm}$
 $\lambda_{\text{em}} = 430\text{-}490 \text{ nm}$

$\lambda_{\text{ex}} = 488 \text{ nm}$
 $\lambda_{\text{em}} = 500\text{-}560 \text{ nm}$

$\lambda_{\text{ex}} = 532 \text{ nm}$
 $\lambda_{\text{em}} = 540\text{-}600 \text{ nm}$

$\lambda_{\text{ex}} = 635 \text{ nm}$
 $\lambda_{\text{em}} = 640\text{-}700 \text{ nm}$

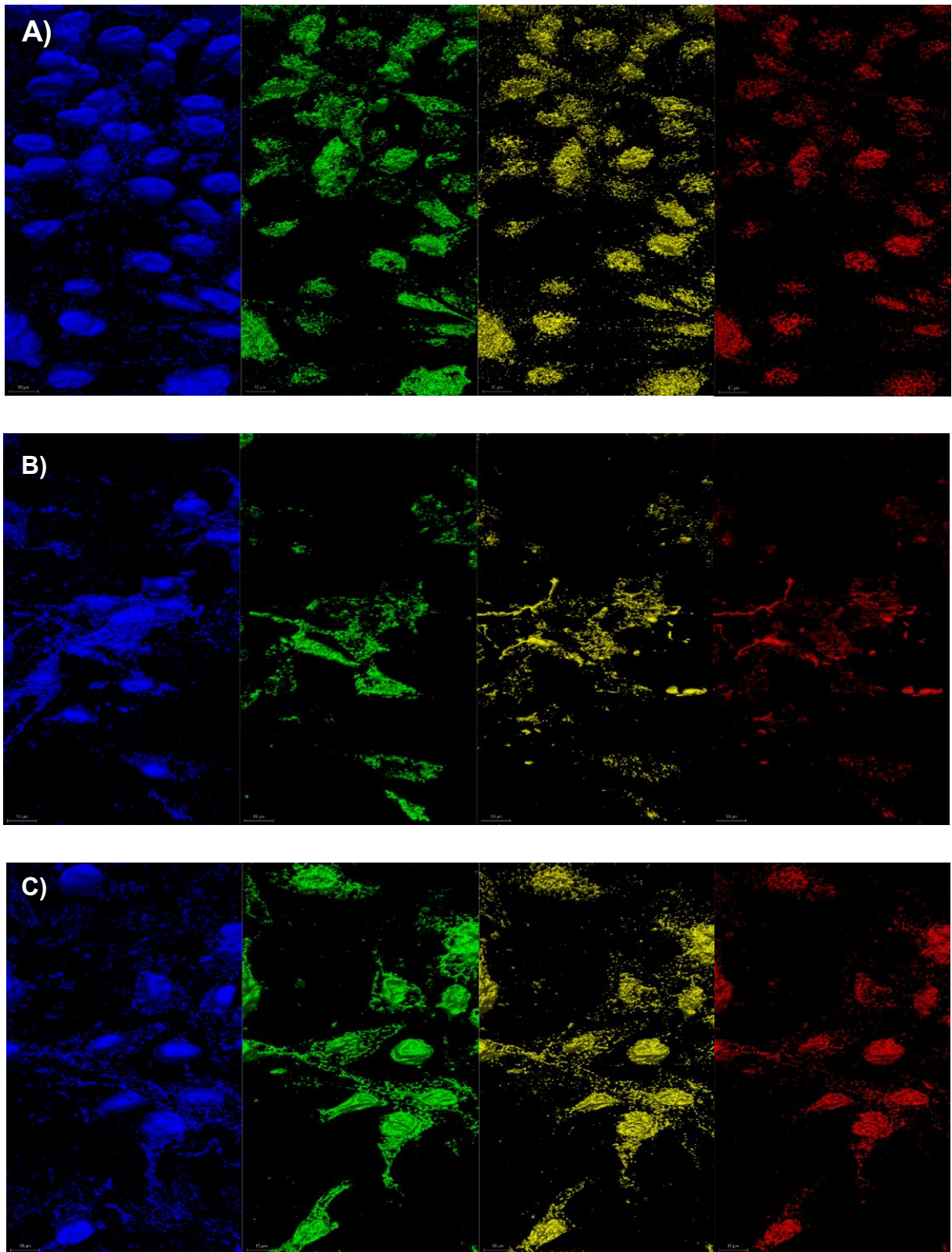


Figure 4.7 Confocal microscopy images of nCDs excited at four different wavelengths: 405, 488, 532, 635 nm, exposed to (a) retinal pigment epithelial, (b) lens epithelial, (c) CHO cells.

4.4 Conclusions

We developed and optimized a scalable isolation-free microwave pyrolysis method for synthesizing deep red-NIR emissive nitrogen-doped carbon dots from citric acid and ethylenediamine. MALDI-TOF and DLS results respectively showed that as the amine to acid ratio increased, both the MW and size of the nCDs increased. Based on the XPS analysis, the formation of C–N and the presence of pyrrolic N content appear to be keys to creating red-emissive nCDs. Both of these critical elements maximized at an amine/acid ratio of 2.0. Confocal images demonstrated that the nanoparticles could enter the cells, including cancer cells. Excellent biocompatibility results support the potential application of nCDs in nanomedicine.

4.5 Acknowledgements

This work was supported by NIH RO1 EY021620, NIH Core Grant P30 EY02687, a Core grant from the Association for the Prevention of Blindness, and a Veteran Affairs Merit review grant (IO1 RX 0000657-01A2). The Veteran Affairs Office of Research and Development IO1BX007080 grant to K.H.M. supported confocal imaging (N.R.). We thank the Alvin J. Siteman Cancer Center at Washington Univ. School of Medicine and Barnes-Jewish Hospital in St. Louis, MO, for the use of the Small Animal Cancer Imaging shared resource, which provided ex vivo and postmortem imaging services, Optical Spectroscopy Core Facility at Washington Univ. (S10RR031621, M.B.) and NIH RO1 CA208623 (M.B.). The Siteman Cancer Center is supported in part by NCI Cancer Center Support Grant No. P30 CA091842. Partial support from the McDonnell Academy Global Energy and Environment Partnership, the Lopata Endowment (P.B.), and NCI RO1 CA208623 (M.B.) are gratefully acknowledged.

4.6 References

1. Bachilo, S. M., M. S. Strano, C. Kittrell, R. H. Hauge, R. E. Smalley and R. B. Weisman (2002). "Structure-assigned optical spectra of single-walled carbon nanotubes." *Science* **298**(5602): 2361-2366.
2. Berezin, M. Y. (2014). *Nanotechnology for Biomedical Imaging and Diagnostics: From Nanoparticle Design to Clinical Applications*, John Wiley & Sons.
3. Berezin, M. Y., W. J. Akers, K. Guo, G. M. Fischer, E. Daltrozzo, A. Zumbusch and S. Achilefu (2009). "Long fluorescence lifetime molecular probes based on near infrared pyrrolopyrrole cyanine fluorophores for in vivo imaging." *Biophysical Journal* **97**(9): L22-L24.
4. Bourlinos, A. B., A. Stassinopoulos, D. Anglos, R. Zboril, V. Georgakilas and E. P. Giannelis (2008). "Photoluminescent carbogenic dots." *Chemistry of Materials* **20**(14): 4539-4541.
5. Bourlinos, A. B., R. Zboril, J. Petr, A. Bakandritsos, M. Krysmann and E. P. Giannelis (2012). "Luminescent surface quaternized carbon dots." *Chemistry of Materials* **24**(1): 6-8.
6. Brouwer, A. M. (2011). "Standards for photoluminescence quantum yield measurements in solution (iupac technical report)." *Pure and Applied Chemistry* **83**(12): 2213-2228.
7. Cherukula, K., K. M. Lekshmi, S. Uthaman, K. Cho, C.-S. Cho and I.-K. Park (2016). "Multifunctional inorganic nanoparticles: Recent progress in thermal therapy and imaging." *Nanomaterials* **6**(4).
8. Choi, Y., B. Kang, J. Lee, S. Kim, G. T. Kim, H. Kang, B. R. Lee, H. Kim, S. H. Shim, G. Lee, O. H. Kwon and B. S. Kim (2016). "Integrative approach toward uncovering the origin of photoluminescence in dual heteroatom-doped carbon nanodots." *Chemistry of Materials* **28**(19): 6840-6847.
9. Ding, H., S.-B. Yu, J.-S. Wei and H.-M. Xiong (2016). "Full-color light-emitting carbon dots with a surface-state-controlled luminescence mechanism." *ACS Nano* **10**(1): 484-491.
10. Dong, X. W., L. M. Wei, Y. J. Su, Z. L. Li, H. J. Geng, C. Yang and Y. F. Zhang (2015). "Efficient long lifetime room temperature phosphorescence of carbon dots in a potash alum matrix." *Journal of Materials Chemistry C* **3**(12): 2798-2801.
11. Feng, L.-L., Y.-X. Wu, D.-L. Zhang, X.-X. Hu, J. Zhang, P. Wang, Z.-L. Song, X.-B. Zhang and W. Tan (2017). "Near infrared graphene quantum dots-based two-photon nanoprobe for direct bioimaging of endogenous ascorbic acid in living cells." *Analytical Chemistry* **89**(7): 4077-4084.
12. Feng, T., X. Z. Ai, H. M. Ong and Y. L. Zhao (2016). "Dual-responsive carbon dots for tumor extracellular microenvironment triggered targeting and enhanced anticancer drug delivery." *ACS Applied Materials & Interfaces* **8**(29): 18732-18740.
13. Galadari, S., A. Rahman, S. Pallichankandy and F. Thayyullathil (2017). "Reactive oxygen species and cancer paradox: To promote or to suppress?" *Free Radical Biology and Medicine* **104**: 144-164.
14. Gan, Z. X., H. Xu and Y. L. Hao (2016). "Mechanism for excitation-dependent photoluminescence from graphene quantum dots and other graphene oxide derivatives: Consensus, debates and challenges." *Nanoscale* **8**(15): 7794-7807.
15. Ge, J., Q. Jia, W. Liu, L. Guo, Q. Liu, M. Lan, H. Zhang, X. Meng and P. Wang (2015). "Red-emissive carbon dots for fluorescent, photoacoustic, and thermal theranostics in living mice." *Advanced Materials* **27**(28): 4169-4177.

16. Goh, E. J., K. S. Kim, Y. R. Kim, H. S. Jung, S. Beack, W. H. Kong, G. Scarcelli, S. H. Yun and S. K. Hahn (2012). "Bioimaging of hyaluronic acid derivatives using nanosized carbon dots." Biomacromolecules **13**(8): 2554-2561.
17. Hola, K., Y. Zhang, Y. Wang, E. P. Giannelis, R. Zboril and A. L. Rogach (2014). "Carbon dots-emerging light emitters for bioimaging, cancer therapy and optoelectronics." Nano Today **9**(5): 590-603.
18. Hu, Q., M. C. Paau, Y. Zhang, W. Chan, X. Gong, L. Zhang and M. M. F. Choi (2013). "Capillary electrophoretic study of amine/carboxylic acid-functionalized carbon nanodots." Journal of Chromatography A **1304**: 234-240.
19. Jia, X., Y. Han, M. L. Pei, X. B. Zhao, K. Tian, T. T. Zhou and P. Liu (2016). "Multi-functionalized hyaluronic acid nanogels crosslinked with carbon dots as dual receptor-mediated targeting tumor theranostics." Carbohydrate Polymers **152**: 391-397.
20. Jiang, K., S. Sun, L. Zhang, Y. Lu, A. G. Wu, C. Z. Cai and H. W. Lin (2015). "Red, green, and blue luminescence by carbon dots: Full-color emission tuning and multicolor cellular imaging." Angewandte Chemie-International Edition **54**(18): 5360-5363.
21. Lavik, E., M. H. Kuehn and Y. H. Kwon (2011). "Novel drug delivery systems for glaucoma." Eye **25**(5): 578-586.
22. Liang, J., L. Cheng, J. J. Struckhoff and N. Ravi (2015). "Investigating triazine-based modification of hyaluronan using statistical designs." Carbohydrate Polymers **132**: 472-480.
23. Lin, L.-Y., S. Kavadiya, B. B. Karakocak, Y. Nie, R. Raliya, S. T. Wang, M. Y. Berezin and P. Biswas (2018). "Zno 1- x/carbon dots composite hollow spheres: Facile aerosol synthesis and superior co 2 photoreduction under uv, visible and near-infrared irradiation." Applied Catalysis B: Environmental.
24. Lin, L.-Y., Y. Nie, S. Kavadiya, T. Soundappan and P. Biswas (2017). "N-doped reduced graphene oxide promoted nano tio 2 as a bifunctional adsorbent/photocatalyst for co 2 photoreduction: Effect of n species." Chemical Engineering Journal **316**: 449-460.
25. Luo, P. G., S. Sahu, S.-T. Yang, S. K. Sonkar, J. Wang, H. Wang, G. E. LeCroy, L. Cao and Y.-P. Sun (2013). "Carbon "quantum" dots for optical bioimaging." Journal of Materials Chemistry B **1**(16): 2116-2127.
26. Miao, X., X. Yan, D. Qu, D. Li, F. F. Tao and Z. Sun (2017). "Red emissive sulfur, nitrogen codoped carbon dots and their application in ion detection and theranostics." Acs Applied Materials & Interfaces **9**(22): 18549-18556.
27. Nevin, A., J.-P. Echard, M. Thoury, D. Comelli, G. Valentini and R. Cubeddu (2009). "Excitation emission and time-resolved fluorescence spectroscopy of selected varnishes used in historical musical instruments." Talanta **80**(1): 286-293.
28. Nie, H., M. J. Li, Q. S. Li, S. J. Liang, Y. Y. Tan, L. Sheng, W. Shi and S. X. A. Zhang (2014). "Carbon dots with continuously tunable full-color emission and their application in ratiometric ph sensing." Chemistry of Materials **26**(10): 3104-3112.
29. Ostadhossein, F. and D. Pan (2017). "Functional carbon nanodots for multiscale imaging and therapy." Wiley Interdisciplinary Reviews-Nanomedicine and Nanobiotechnology **9**(3): 16.
30. Peng, H. and J. Travas-Sejdic (2009). "Simple aqueous solution route to luminescent carbogenic dots from carbohydrates." Chemistry of Materials **21**(23): 5563-5565.
31. Qu, D., X. Miao, X. Wang, C. Nie, Y. Li, L. Luo and Z. Sun (2017). "Se & n co-doped carbon dots for high-performance fluorescence imaging agent of angiography." Journal of Materials Chemistry B **5**(25): 4988-4992.
32. Santhanam, S., J. Liang, R. Baid and N. Ravi (2015). "Investigating thiol-modification on hyaluronan via carbodiimide chemistry using response surface methodology." Journal of Biomedical Materials Research Part A **103**(7): 2300-2308.

33. Sharma, A., T. Gadly, A. Gupta, A. Ballal, S. K. Ghosh and M. Kumbhakar (2016). "Origin of excitation dependent fluorescence in carbon nanodots." The Journal of Physical Chemistry Letters **7**(18): 3695-3702.
34. Shi, Y. P., Y. Pan, H. Zhang, Z. M. Zhang, M. J. Li, C. Q. Yi and M. S. Yang (2014). "A dual-mode nanosensor based on carbon quantum dots and gold nanoparticles for discriminative detection of glutathione in human plasma." Biosensors & Bioelectronics **56**: 39-45.
35. Sun, S., L. Zhang, K. Jiang, A. Wu and H. Lin (2016). "Toward high-efficient red emissive carbon dots: Facile preparation, unique properties, and applications as multifunctional theranostic agents." Chemistry of Materials **28**(23): 8659-8668.
36. Tafani, M., L. Sansone, F. Limana, T. Arcangeli, E. De Santis, M. Polese, M. Fini and M. A. Russo (2016). "The interplay of reactive oxygen species, hypoxia, inflammation, and sirtuins in cancer initiation and progression." Oxidative Medicine and Cellular Longevity: 18.
37. Tao, H. Q., K. Yang, Z. Ma, J. M. Wan, Y. J. Zhang, Z. H. Kang and Z. Liu (2012). "In vivo NIR fluorescence imaging, biodistribution, and toxicology of photoluminescent carbon dots produced from carbon nanotubes and graphite." Small **8**(2): 281-290.
38. Wang, F., S. P. Pang, L. Wang, Q. Li, M. Kreiter and C. Y. Liu (2010). "One-step synthesis of highly luminescent carbon dots in noncoordinating solvents." Chemistry of Materials **22**(16): 4528-4530.
39. Wang, Y. F. and A. G. Hu (2014). "Carbon quantum dots: Synthesis, properties and applications." Journal of Materials Chemistry C **2**(34): 6921-6939.
40. Xu, M., G. He, Z. Li, F. He, F. Gao, Y. Su, L. Zhang, Z. Yang and Y. Zhang (2014). "A green heterogeneous synthesis of n-doped carbon dots and their photoluminescence applications in solid and aqueous states." Nanoscale **6**(17): 10307-10315.
41. Yang, Y. M., W. Q. Kong, H. Li, J. Liu, M. M. Yang, H. Huang, Y. Liu, Z. Y. Wang, Z. Q. Wang, T. K. Sham, J. Zhong, C. Wang, Z. Liu, S. T. Lee and Z. H. Kang (2015). "Fluorescent n-doped carbon dots as in vitro and in vivo nanothermometer." ACS Applied Materials & Interfaces **7**(49): 27324-27330.
42. Zhai, X. Y., P. Zhang, C. J. Liu, T. Bai, W. C. Li, L. M. Dai and W. G. Liu (2012). "Highly luminescent carbon nanodots by microwave-assisted pyrolysis." Chemical Communications **48**(64): 7955-7957.
43. Zhang, J. X., M. Zheng, F. L. Zhang, B. Xu, W. J. Tian and Z. G. Xie (2016). "Supramolecular hybrids of aiegen with carbon dots for noninvasive long-term bioimaging." Chemistry of Materials **28**(23): 8825-8833.
44. Zhang, Y., Y. J. Shen, X. Y. Teng, M. Q. Yan, H. Bi and P. C. Morais (2015). "Mitochondria-targeting nanoplatfrom with fluorescent carbon dots for long time imaging and magnetic field-enhanced cellular uptake." ACS Applied Materials & Interfaces **7**(19): 10201-10212.
45. Zhu, H., X. L. Wang, Y. L. Li, Z. J. Wang, F. Yang and X. R. Yang (2009). "Microwave synthesis of fluorescent carbon nanoparticles with electrochemiluminescence properties." Chemical Communications(34): 5118-5120.
46. Zhu, S. J., Q. N. Meng, L. Wang, J. H. Zhang, Y. B. Song, H. Jin, K. Zhang, H. C. Sun, H. Y. Wang and B. Yang (2013). "Highly photoluminescent carbon dots for multicolor patterning, sensors, and bioimaging." Angewandte Chemie-International Edition **52**(14): 3953-3957.

Chapter 5: Hyaluronate Conjugated Nitrogen-doped Carbon Quantum Dots for Use in Bioimaging

The results of this chapter have been compiled in Karakocak, B. B.; Liang, J.; Biswas, P.; Ravi, N. (2018). Hyaluronate Conjugated Nitrogen-doped Carbon Quantum Dots for Use in Bioimaging. In Preparation.

Abstract

In this work, we demonstrate the application of hyaluronate conjugated nitrogen-doped carbon quantum dots (nCQDs) for bioimaging and their potential use for targeted drug delivery. nCQDs were synthesized by microwave-assisted pyrolysis of citric acid and aliphatic diamines. The time of pyrolysis, the molar ratio of acid to amine, and the concentration of reactants was optimized to yield high fluorescence in the red wavelength range (optimum excitation at 550 nm, emission up to 700 nm). The HA-nCQD conjugate was synthesized by a carbodiimide coupling of the amines on CQDs and the carboxylic acids on HAs. The nCQDs and their conjugates fluoresced variously depending upon the excitation wavelength. Three different cell lines were exposed to nCQDs and HA-nCQDs. Confocal microscopy images showed enhanced internalization of HA-nCQDs, which was facilitated by CD44 receptors. Further, *ex-vivo* (porcine eye globes) and *post-mortem* (mice) images were obtained. Observations demonstrate the use of HA as a carrier for targeted drug delivery into CD44 rich cells, and red emissive nCQDs can be used for both *ex-vivo* and *in-vivo* imaging.

5.1 Introduction

Bioimaging, non-invasive visualization of a cell/tissue/organ is a crucial tool for diagnosis, treatment of various diseases, including cancer. In the last two decades, various nanomaterials were studied (Cherukula et al. 2016), and carbon dots have been shown to be promising for bioimaging applications (Hola et al. 2014, Choi et al. 2016, Zhang et al. 2016). Carbon quantum dots (CQDs) are one of the most promising bioimaging agents due to their unique intrinsic properties such as wavelength dependent excitation/emission (Jiang et al. 2015, Ding et al. 2016), long fluorescence lifetime (Dong et al. 2015), good stability (Zhang et al. 2015), and high biocompatibility (Tao et al. 2012).

Various CQDs synthesis methods ranging from relatively simple to complex have been reported (Hola et al. 2014). For practical applications and mass production, it would be ideal to scale up the synthesis method (Wang and Hu 2014). Therefore, it is desirable to use a simple synthesis method involving commercially available and environmentally friendly reactants (Xu et al. 2014). Among the existing methods, the microwave method has distinct advantages for its shorter reaction times, milder reaction conditions, lower energy consumption, better stability, reproducibility, and higher product efficiency (Zhu et al. 2009, Hu et al. 2013). We have successfully used a domestic microwave oven to synthesize nitrogen doped CQDs (nCQDs) (Zhai et al. 2012, Hu et al. 2013, Xu et al. 2014). The reaction took less than two minutes using citric acid and aliphatic diamines in water as raw materials. This synthetic strategy is facile, fast, convenient, economical, and environmentally friendly.

For CQDs to be used as bioimaging agents, fluorescence emission above 600 nm is desired (Hola et al. 2014, Ostadhossein and Pan 2017). In this study, we optimized a simple yet facile method of synthesizing CQDs to achieve highly efficient red emissive nCQDs. We synthesized nCQDs by microwave-assisted pyrolysis of citric acid and aliphatic diamines.

Time of pyrolysis, the molar ratio of acid to amine, and the concentration of reactants were optimized to yield high fluorescence, specifically above 600 nm. Moreover, we coated nCQDs with hyaluronic acid (HA) to demonstrate receptor-targeted delivery applications. In particular, the cells which express CD44 receptors, that are specific for hyaluronan, showed increased uptake efficiency of HA-coated nCQDs. Finally, the nCQDs were exposed to porcine eye globes and fresh post-mortem mice, respectively. The results showed that the highly efficient red emissive nCQDs could be potentially employed as bioimaging agents and can be functionalized to target cells which express CD44 receptors.

5.2 Methods

5.2.1 Materials

All chemicals were used as received. Sodium hyaluronate (HA) (MW = 200 kDa, cat# HA-200K-1) was purchased from Lifecore Biomedical. *N*-hydroxysuccinimide (98%, cat# 130672), *N*-(3-dimethylaminopropyl)-*N*'-ethyl-carbodiimide hydrochloride (98%, cat# E1769), and ethylenediamine (99%, cat# E26266) were purchased from Sigma-Aldrich. Citric acid was purchased from J.T. Baker Chemical Co. Dulbecco's modified Eagles's medium/nutrient mixture F-12 Ham (DMEM/F12), trypsin-ethylenediaminetetraacetic acid (EDTA) solution 10x, and fetal calf serum (FCS), TritonTM X-100, phosphate buffer saline (PBS) were obtained from Sigma-Aldrich (St. Louis, MO). SlowFade[®] Gold Antifade Mountant with DAPI (cat# S36938) was purchased from Thermo Fisher Scientific (St. Peters, MO). ARPE-19 (Retinal pigment epithelial) (ATCC[®] CRL-2302TM), Lens epithelial cells (ATCC[®] CRL-11421TM), and CHO (CCL-61TM) cells were purchased from American Type Culture Collection (Manassas, VA). ApoTox-GloTM (cat# G6320) and ROS GloTM H₂O₂ (cat# G8820) assays were purchased from Promega Corporation (Madison, WI). All the chemicals were used as received.

5.2.2 Central-composite response surface design for synthesizing nCQDs with desired properties

To investigate the effect of three factors – the molar ratio of amine to acid, the microwave time, and the concentration of the reactants – a Central-Composite Design Response Surface Methodology (CCD-RSM) design was utilized (Stat-Ease, Design-Expert[®] software, version 9.0). Each factor was varied at five levels: amine/COOH = 0.30, 0.48, 0.75, 1.02, and 1.20; microwave time = 75s, 70s, 88s, 95s, and 100s; and concentration of citric acid=8.0%, 8.8%, 10.0%, 11.2%, and 12.0%. There were twenty runs, as tabulated below (Table 5.1):

Table 5.1 Experimental conditions (factors) of each synthesis of nCQDs using CCD-RSM design

Runs	CA wt%	NH₂/COOH	Reaction Time
1	10.0	0.75	88
2	11.2	0.48	80
3	10.0	0.75	100
4	10.0	0.75	88
5	8.8	1.02	95
6	12.0	0.75	88
7	8.8	0.48	80
8	10.0	0.75	75
9	10.0	0.75	88
10	11.2	1.02	95
11	10.0	0.75	88
12	8.0	0.75	88
13	8.8	0.48	95
14	8.8	1.02	80
15	10.0	0.75	88
16	10.0	1.20	88
17	10.0	0.30	88
18	10.0	0.75	88
19	11.2	0.48	95
20	11.2	1.02	80

A stock 12 wt/v % solution of citric acid was made by dissolving 28.39 g of citric acid in 220 mL of water. The desired amount (according to Table 5.1) of this stock solution was added to a 100-mL beaker, then DI water was added to make the volume up to 10 mL, and ethylenediamine was added. The mixture was shaken and heated in a microwave oven (General Electric, 1,100 watts) for one of the times listed in Table 5.1. The result was a solid was obtained, whose color varied from yellow to brown. This solid was dissolved in 3 mL of water and transferred to a 20 mL vial. The beaker was rinsed with another 2 mL of water, and the liquids were combined. The solution was dialyzed against water (Molecular weight cut-off (MWCO) = 500 Da).

5.2.3 Conjugation of nCQDs with hyaluronic acid

An aqueous solution of HA 1 w/v% was prepared by dissolving HA (0.10 g, 0.24 meq of COOH) in 10 mL of water. The pH of the HA solution was adjusted to 4.5. 1-Ethyl-3-(3-dimethylaminopropyl) carbodiimide (EDC: 0.45 g, 2.4 mmol), and N-hydroxysuccinimide (NHS: 0.14 g, 1.2 mmol) was added to the HA solution at 22 °C with stirring for 1 hour. CQD solution (0.10 g, 5 mL) was added to the HA solution, and the reaction mixture was continuously stirred for 18 hours. Thereafter, the reaction was terminated by adjusting the final pH to 8-9. The excess EDC, NHS, and any free CQDs were removed from the reaction mixture by dialysis (MWCO: 12,000-14,000) in H₂O (three times). Then the solution was lyophilized, yielding a powder.

5.2.4 Characterization of nCQDs and HA-CQDs

UltraViolet-Visible (UV-Vis) absorption spectra were recorded on a Thermo Fisher Biomate 3 UV-Vis spectrophotometer. Fluorescent spectra were measured on a SpectraMax Gemini EM fluorescence reader at ambient conditions. Nuclear magnetic resonance spectrum (¹H NMR) spectra were obtained on a Varian Unity Inova 500 MHz (Palo Alto, CA) in D₂O at 25 °C. The PL emission was determined with a Varian Cary 5000 spectrophotometer.

5.2.5 Hydrodynamic size and zeta potential measurements with dynamic light scattering analysis

A Malvern Zetasizer Nano ZS (Malvern Instruments, Westborough MA) equipped with a backscattering detector (173°) was used for hydrodynamic size measurements of synthesized carbon dots. Samples were dispersed in water, then sonicated for 15 min to homogeneously disperse them in the solution, after which they were filtered through a prerinsed 0.22 µm sterile filter, then equilibrated (typically for 5 min) at 25 °C. At least three measurements per sample were taken. The hydrodynamic diameter and zeta potential of nCQDs in solution before their exposure to cell culture medium was measured in batch mode using DLS.

5.2.6 *In-vitro* cytotoxicity measurements on Retinal Pigment Epithelial (ARPE-19), NIH 3T3, and Chinese Hamster Ovary (CHO) cells with MTT, ApoTox-Glo™, and ROS-Glo™ H₂O₂ assays

Cell metabolic activity, and hence the viability of cells in the presence of CQDs (0.01-0.6 mg/ml), was assessed with 3-[4, 5 dimethyl-thiazoly-2-yl] 2-5 diphenyl tetrazolium bromide (MTT) assay. The relative amount of apoptotic cells and reactive oxygen species (ROS) generation were measured, respectively, by ApoTox-Glo™ and ROS Glo™ H₂O₂ assays. In all biological and imaging tests, the cells without NP exposure served as a negative control.

Each test result (viability measurements, the relative amount of apoptotic cells, and ROS generation) was compared with the corresponding negative (untreated cells) and positive (NPs without the cells) control groups with Student's t-test. $P^* < 0.05$, the significance level, was statistically acceptable.

5.2.7 *In-vitro* imaging of nCQDs and HA-nCQDs.

To confirm the presence of CQDs inside cells, we investigated the distribution of CQDs at 0.01-0.6 mg/mL, using a nanoplasmonic confocal laser scanning microscope (Leica TCS-SP8). Three laser wavelengths (405, 532, and 635 nm) were used during confocal imaging. The CQD detection range was 435-700 nm.

ARPE-19, NIH 3T3, and CHO cells were separately seeded in CELLview™ plates at 5×10^4 cells/well for 24 h. After 24 h of CQD exposure, the cells were fixed and washed with PBS three times before imaging. All cells were fixed by immersion in 4% paraformaldehyde (PFA) as the cross-linking solution for 10 min at room temperature. The cells were washed three times with ice-cold 1x phosphate buffered saline (PBS) for 3 min each time. The fixed cells were incubated in ice-cold 1x PBS buffer containing 0.1% Triton (permeabilization agent) for 10 min at room temperature, then washed three times with ice-cold 1x PBS for 5 min each time. The CELLview™ plates were then incubated with blocking buffer for 30 min at room temperature. The cells were subsequently washed three times with ice-cold 1x PBS for 3 min each. To stain the nuclei, SlowFade® Gold Antifade Mountant with DAPI (diluted 1:100 in 1x PBS) was used. The cells were kept at 4 °C overnight. The cells were again washed three times with ice-cold 1x PBS for 5 min each before being transferred to the confocal microscope for visual analyses. The laser wavelengths were 405, 532, and 635 nm for DAPI (nucleus staining) and for CQDs, respectively. During confocal imaging, several different images were taken through different optical sections by collecting Z-stacks with a thickness of 35 nm. Based on the thickness of the cell, the number of images with the same Z-stack thickness varied. A negative control sample (untreated cells) was prepared with cells in the absence of CQDs.

5.2.8 *Ex-vivo* and *post-mortem* imaging of nCQDs and HA-nCQDs.

Fresh porcine ocular globes were obtained from Trenton Processing Center, Trenton, IL. The excessive mass and fat tissue around the eyeballs were cleaned, and the eyeballs were placed in 1% antibiotic-antimycotic in 1x PBS. Intravitreal injections of nCQDs were performed at a dose of 10 mg/ml with an injection volume of 50 μ l. *Ex-vivo* fluorescence imaging was performed on the same day on Bruker Multispectral FX 470/600 for 10 sec exposure, bin 2x2, the field of view (FOV) 50 cm.

Post-mortem mice were shaved prior to nCQD injection and imaging. The nCQDs and HA-nCQDs were injected into dead mice subcutaneously on the left shoulder and upper back, respectively, at a dose of 0.40 mg/kg. Animals (n = 3) were imaged at 2 minutes post-injection using the Pearl Small Animal NIR fluorescence imaging system (LICOR Biosciences, Nebraska), $\lambda_{ex/em}$ 785/820 nm

5.3 Results and Discussion

5.3.1 Conjugation of hyaluronic acid with carbon quantum dots

In the second part of the study, we conjugated CQDs with HA to enable the CQDs to target cells with CD44 receptors. In addition, the HA conjugation was also expected to increase the biocompatibility of the CQDs. (Pomper and Fisher 2014) An EDC-coupling method was used to form amide bonds between the carboxyl groups of HA and the amine groups of CQDs (Figure 5.1). Since CQDs contain both amine and carboxyl groups, amide bonds may also be formed between two CQDs. To minimize crosslinking between CQDs, the carboxyl-activators EDC and NHS were reacted with HA for one hour before adding CQDs.

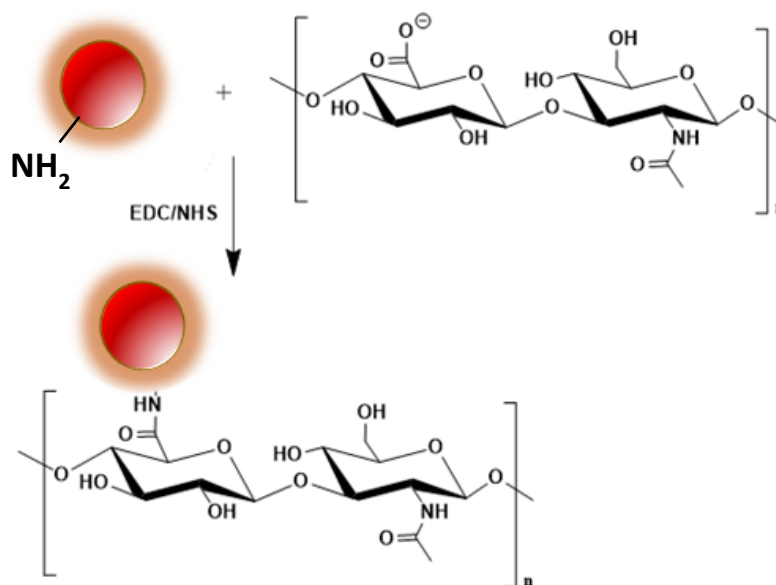


Figure 5.1. HA-CQD conjugation chemistry

We used ^1H NMR spectra of CQDs, HA, and HA-CQD conjugates (Figure 5.2) to demonstrate the conjugation. The peaks at 1.88 ppm and 4.3-4.4 ppm (labeled with asterisks in Figure 5.2A) identify the presence of HA, and the peaks at 4.05 ppm and 5.7-5.9 ppm (marked with triangles in the Figure 5.2B) identify CQDs. In the ^1H NMR spectrum of the HA-CQD conjugate (Figure 5.2C), we were able to detect all the peaks corresponding to HA and CQD. Thus, the ^1H NMR spectra showed successful conjugation of HA and CQDs.

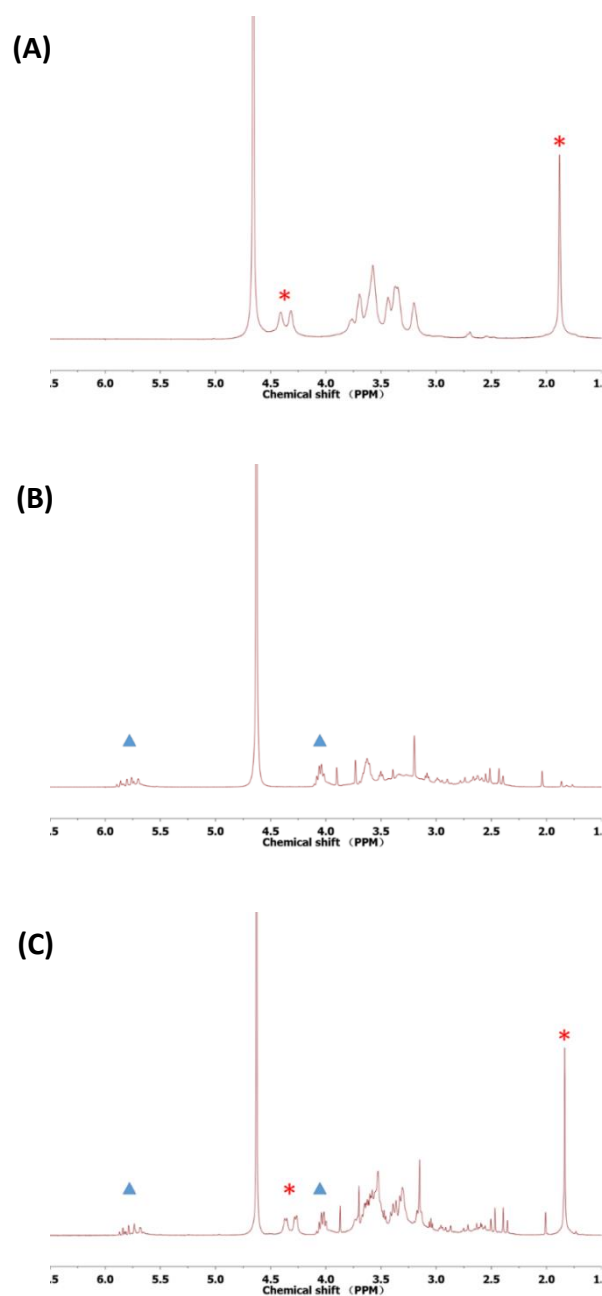


Figure 5.2. A comparison of the ^1H NMR spectra of (A) HA, (B) CQDs, and (C) HA-CQD conjugate confirms the presence of HA and CQD peaks in the HA-CQD conjugate.

We also compared the fluorescence spectra of CQD and HA-CQD conjugates at an excitation wavelength of 540 nm (Figure 5.3). The emission peaks of the HA-CQD conjugates remained at the same wavelength as the CQDs before conjugation, which suggested that the chemical conjugation did not alter the fluorescence property of the CQDs. In addition, the PL intensity of the HA-conjugates was about half of that the native CQDs at the same concentration, which is consistent with 1:1 conjugation ratio of HA and CQD.

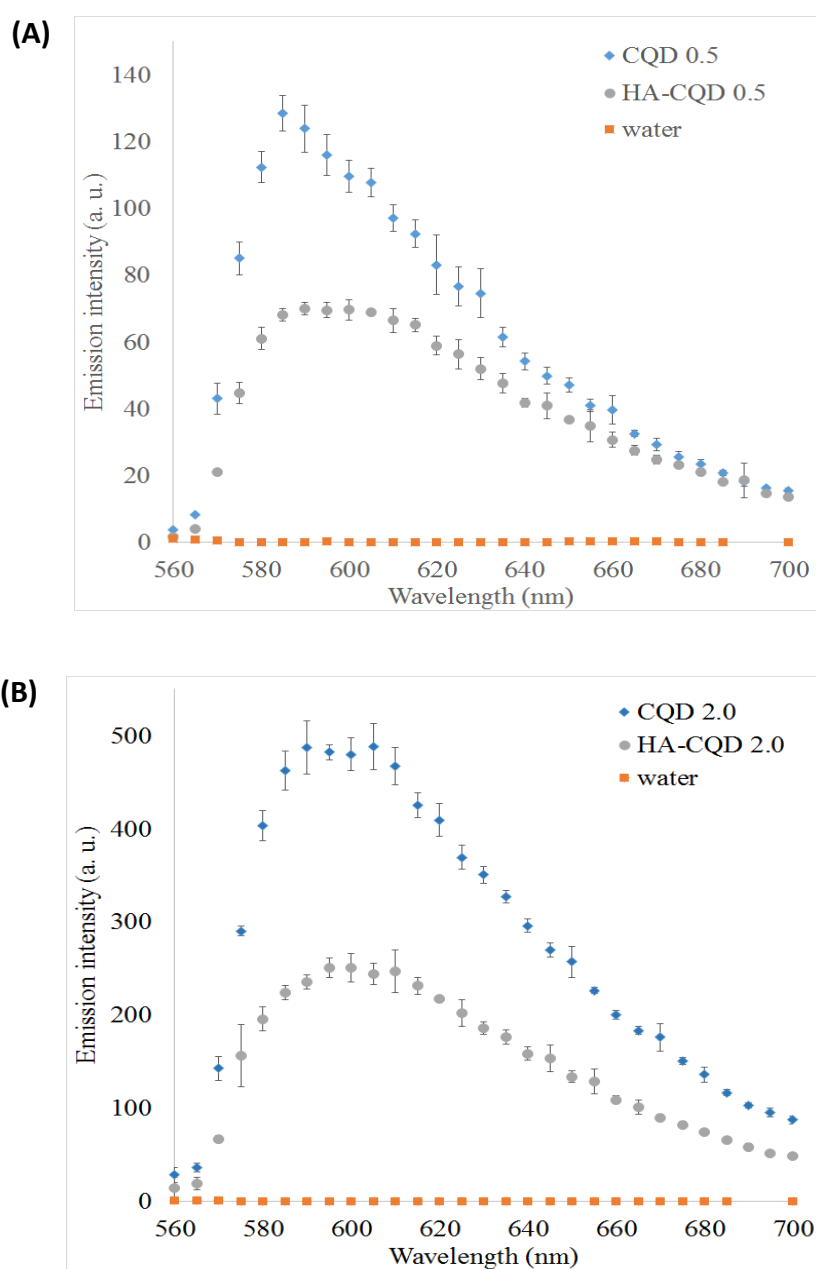


Figure 5.3 PL emission spectra of CQDs with an amine to acid ratio of (A) 0.5 and (B) 2.0 and their HA-CQD conjugates when excited at 540 nm.

5.3.2 *In-vitro* imaging of nCQDs and HA-nCQDs

To confirm the presence of nCQDs inside cells, we investigated the distribution of nCQDs using a nano-plasmonic confocal laser scanning microscope (LEICA TCS-SP8) (see Methods). Three different cell lines were used for *in-vitro* imaging analysis as well: Retinal epithelial cells, NIH 3T3 cells, and CHO cells. According to the results, nCQDs have demonstrated successful use of fluorescence imaging *in vitro*, due to their excitability at multiple wavelengths in the visible spectrum (Figure 5.4B). Furthermore, we showed that nCQDs also fluoresce when excited at 635 nm, unlike previous reports where the exact same synthesis method was used but the nCQDs were excitable up to an excitation wavelength of 488 nm (Zhai et al. 2012, Hu et al. 2013). On the other hand, the HA-CQDs were also excitable up to 635 nm, and no signal loss was observed (Figure 5.4C). The HA conjugation significantly increased the intracellular concentration of nCQDs (Figure 5.4C). Therefore, it can be inferred that HA does not only enable CD44 receptor-targeted delivery but also increased the amount of nCQDs which entered the cells.

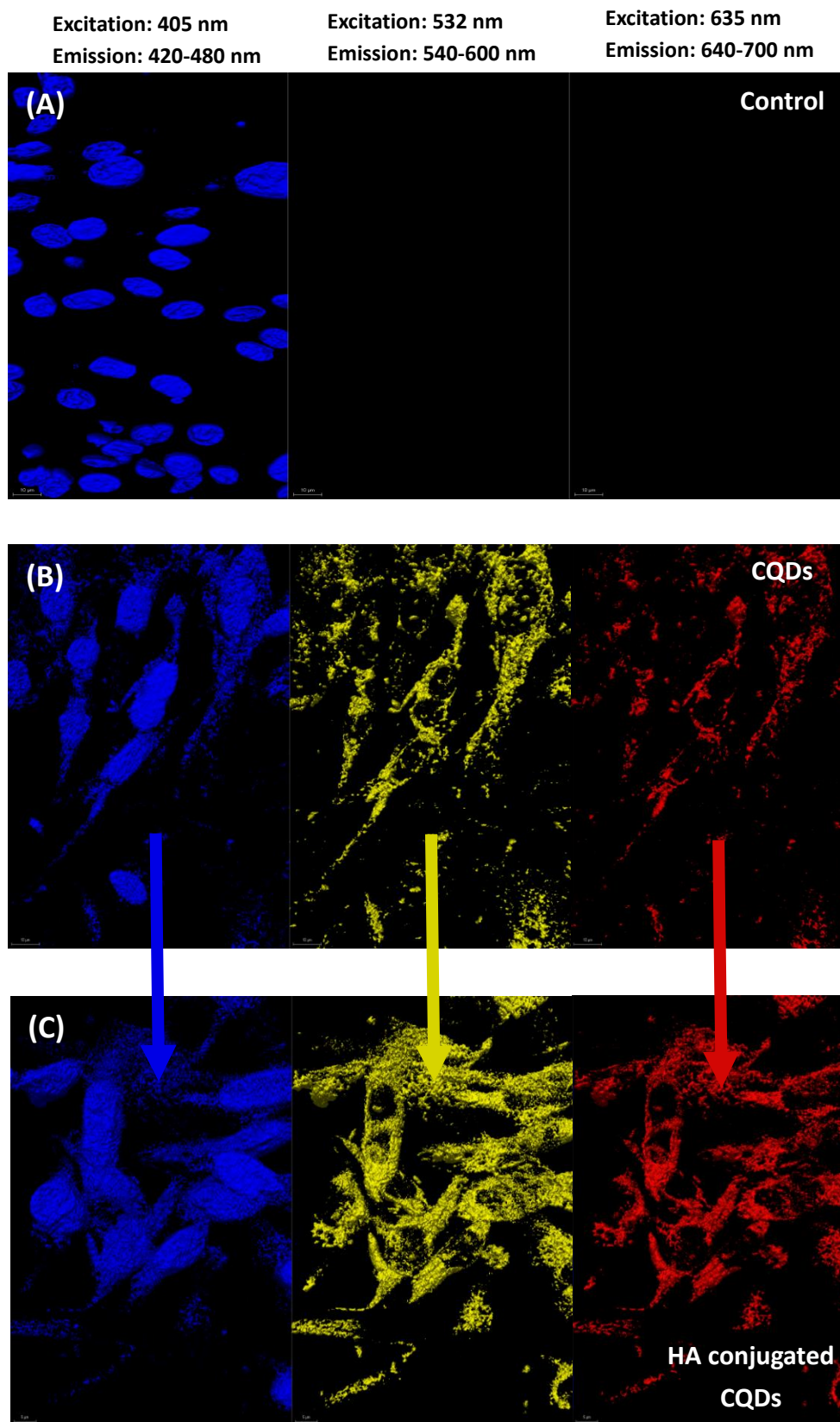
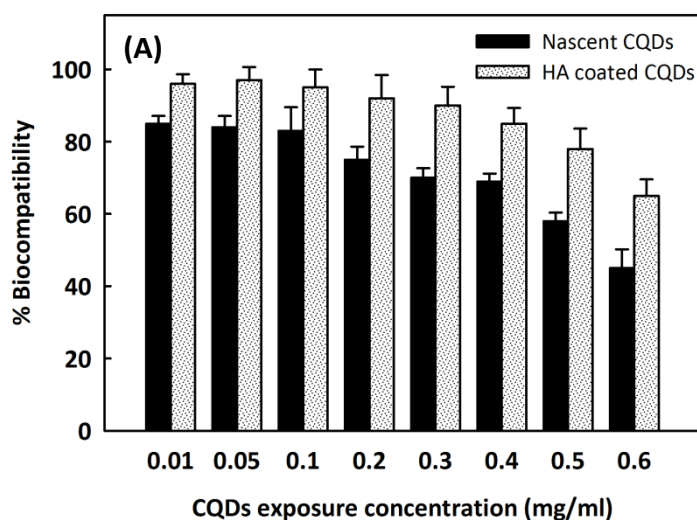


Figure 5.4 Confocal microscopy images of retinal pigment epithelial cells exposed to 0.6 mg/ml CQDs with and without HA conjugation.

5.3.3 Cytotoxicity evaluation of nCQDs and HA-nCQDs

We next studied the biocompatibility of nascent and HA-coated CQDs with retinal pigment epithelial (ARPE-19) cells. Three different independent end-point assays were used: viability based on enzymatic activity in mitochondria; the percent of apoptotic cells based on caspase 3/7, and activity ROS generation, which is proportional to luciferase activity (see Methods). The results indicated that nCQDs were biocompatible up to 0.5 mg/ml (Fig. 5.5A), more than 50% of the cells did not initiate apoptotic cell death (Fig. 5.5B), and induced ROS generation (Fig. 5.5C). However, at 0.6 mg/ml exposure dose, the critical LD₅₀, the lethal dose required to kill 50% of the cells, the level was achieved, and same cells started to show an increased amount of ROS generation which may trigger apoptosis (Al Sulti et al. 2015, Karakocak et al. 2018). Also, the viability results confirmed the increase in cell death. On the other hand, once the particles were conjugated with HA, their biocompatibility with retinal cells significantly increased. HA is known to be a natural antioxidant. When the carbon dots induce ROS generation, the HA acts as a ROS scavenger and reduces the intracellular ROS concentration (Balogh et al. 2003, Rinaudo et al. 2014, Karakocak et al. 2018). This phenomenon is also proven by our ROS measurement results, where HA-CQDs induced significantly less amount of ROS (Figure 5.5C).



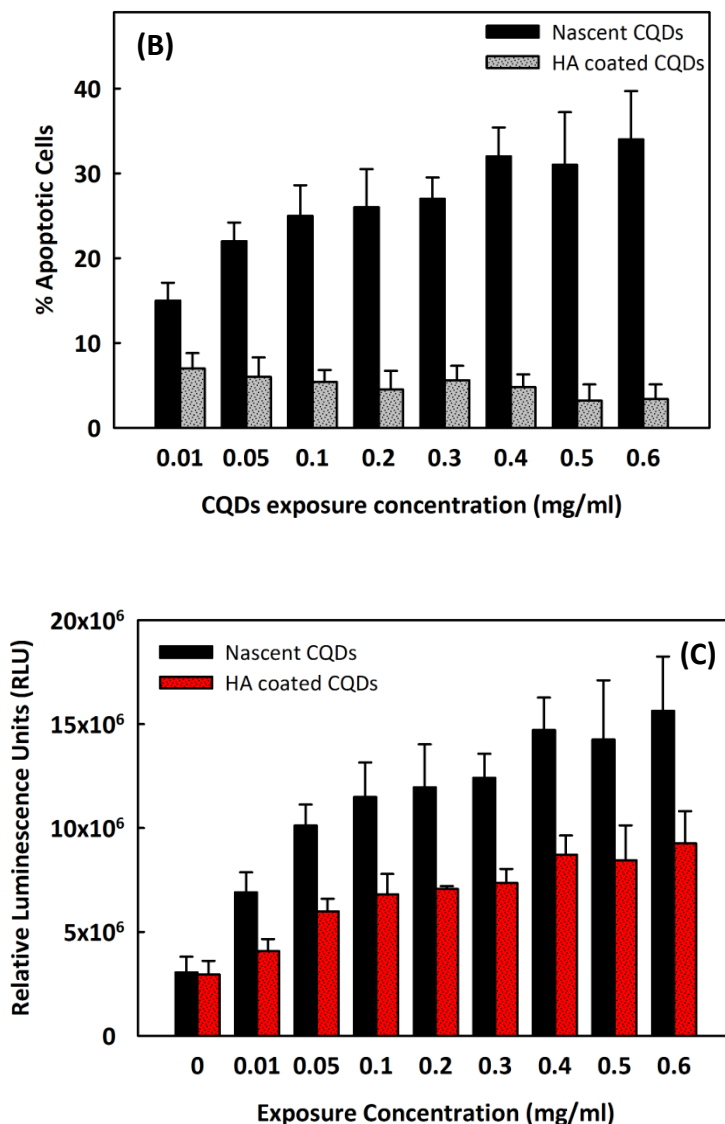


Figure 5.5 Biocompatibility results of nCQDs and HA-nCQDs with ARPE-19 cells. (A) % Viability (B) ROS generation (C) Apoptotic cell percentage measurement results after incubation with nCQDs for 24 h at concentrations up to 0.6 mg/mL. Data are expressed as mean \pm SD from three independent experiments (*P < 0.05).

5.3.4 *Ex-vivo* and *post-mortem* imaging of nCQDs and HA-nCQDs

Ex-vivo fluorescence imaging was performed on the days indicated on Bruker Multispectral FX 470/600 for 10 sec exposure, bin2x2. Post intravitreal injection images of 50 μ l of nCQDs with the highest amine/acid ratio showed that the nCQDs were excitable at 470 nm and emitted light at 600 nm (Figure 5.6). This behavior proves that nCQDs are good candidates for ocular bioimaging applications.

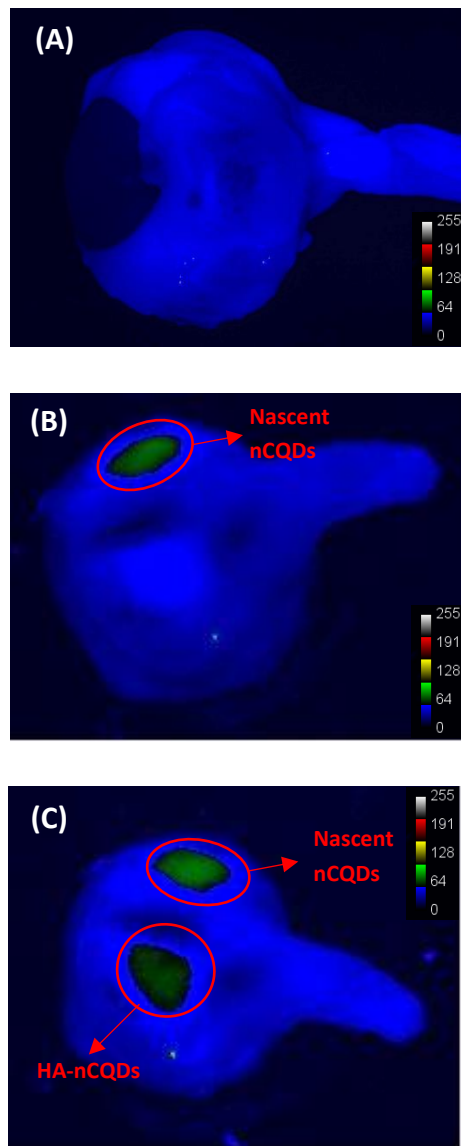


Figure 5.6 Ex-vivo pig eyes images of 50 μ l intravitreal injections of nascent and HA-coated CQDs. Excitation: 470 nm, Emission: 600 nm. (A) Control, no particle injection. (B) Post-injection of nascent CQDs at 2 minutes. (C) Post-injection of HA-CQDs at 2 minutes.

Next, *in-vivo* fluorescence imaging was performed on Pearl Imager (LiCor), excitation: 685 nm, emission: 720 nm for *post-mortem* imaging analysis of nCQDs, a local administration way (subcutaneous injection) was adopted, which is expected to avoid nCQDs entering into the bloodstream. For especially small animal imaging applications, imaging agents which are excitable at near-infrared region are desirable due to the possible interactions of the short-wavelength light with tissue and capability of the light diffusing through multiple tissues. 100 μ l of nCQDs with the highest amine/acid ratio were injected subcutaneously into CD-ICR

mice. It was observed that a fluorescence area was formed around the injection site (Figure 5.7). The images proved that both unconjugated and HA-conjugated nCQDs were excitable at 685 nm and gave an emission signal at 720 nm. Thus both nCQDs and HA-nCQDs can be used for whole animal imaging applications.

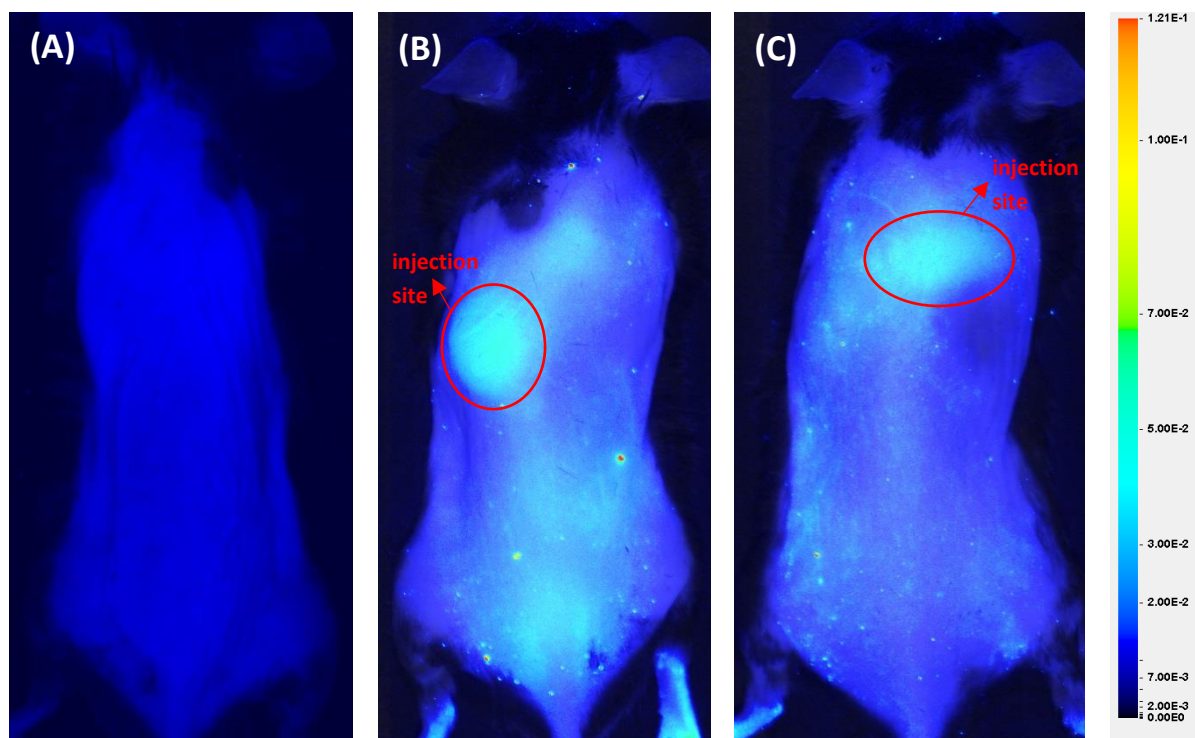


Figure 5.7 Post-mortem mouse images of 100 μ l subcutaneous injections of nascent and HA-coated CQDs. Excitation: 685 nm, Emission: 720 nm. (A) Control, no particle injection. (B) Post-injection of nascent CQDs at 2 minutes. (C) Post-injection of HA-CQDs at 2 minutes.

5.4 Conclusions

We optimized a very simple yet facile method of synthesizing nCQDs to obtain red emissive carbon dots using CCD-RSM. Further, we conjugated nCQDs with HA to target cancer cells and cells which overexpress CD44 receptors. Confocal images proved that the nCQDs could enter the cells, including cancer cells, and the HA conjugation enhanced the intracellular concentration significantly. Nascent nCQDs had fair compatibility up to 0.6 mg/ml; however, once they were conjugated with HA, they showed even better biocompatibility with the tested cells. *Ex-vivo* pig eye images showed that HA-nCQDs could effectively diffuse through

vitreous and *post-mortem* whole-body mouse images also proved that the HA-nCQDs are suitable for bioimaging applications. The results imply the suitable application of HA-nCQDs in nanomedicine both for targeted drug delivery and imaging applications^{4,5}

5.5 Acknowledgements

This work was supported by NIH RO1 EY021620, NIH Core Grant P30 EY02687, a Core grant from the Association for the Prevention of Blindness, and a Veteran Affairs Merit review grant (IO1 RX 0000657-01A2). The Veteran Affairs Office of Research and Development IO1BX007080 grant to K.H.M. supported confocal imaging (N.R.). We thank the Alvin J. Siteman Cancer Center at Washington Univ. School of Medicine and Barnes-Jewish Hospital in St. Louis, MO, for the use of the Small Animal Cancer Imaging shared resource, which provided *ex vivo* and postmortem imaging services, Optical Spectroscopy Core Facility at Washington Univ. (S10RR031621, M.B.) and NIH RO1 CA208623 (M.B.). The Siteman Cancer Center is supported in part by NCI Cancer Center Support Grant No. P30 CA091842. Partial support from the McDonnell Academy Global Energy and Environment Partnership, the Lopata Endowment (P.B.), and NCI RO1 CA208623 (M.B.) are gratefully acknowledged.

5.6 References

1. Al Sulti, Z., R. McDonald, D. Kingsmore, A. Baker and P. Coats (2015). "Mitochondrial dynamics regulation of ros and apoptosis." Heart **101**: A111-A112.
2. Balogh, G. T., J. Illes, Z. Szekely, E. Forrai and A. Gere (2003). "Effect of different metal ions on the oxidative damage and antioxidant capacity of hyaluronic acid." Archives of Biochemistry and Biophysics **410**(1): 76-82.
3. Cherukula, K., K. M. Lekshmi, S. Uthaman, K. Cho, C.-S. Cho and I.-K. Park (2016). "Multifunctional inorganic nanoparticles: Recent progress in thermal therapy and imaging." Nanomaterials **6**(4).
4. Choi, Y., B. Kang, J. Lee, S. Kim, G. T. Kim, H. Kang, B. R. Lee, H. Kim, S. H. Shim, G. Lee, O. H. Kwon and B. S. Kim (2016). "Integrative approach toward uncovering the origin of photoluminescence in dual heteroatom-doped carbon nanodots." Chemistry of Materials **28**(19): 6840-6847.
5. Ding, H., S.-B. Yu, J.-S. Wei and H.-M. Xiong (2016). "Full-color light-emitting carbon dots with a surface-state-controlled luminescence mechanism." ACS Nano **10**(1): 484-491.
6. Dong, X. W., L. M. Wei, Y. J. Su, Z. L. Li, H. J. Geng, C. Yang and Y. F. Zhang (2015). "Efficient long lifetime room temperature phosphorescence of carbon dots in a potash alum matrix." Journal of Materials Chemistry C **3**(12): 2798-2801.
7. Hola, K., Y. Zhang, Y. Wang, E. P. Giannelis, R. Zboril and A. L. Rogach (2014). "Carbon dots-emerging light emitters for bioimaging, cancer therapy and optoelectronics." Nano Today **9**(5): 590-603.
8. Hu, Q., M. C. Paau, Y. Zhang, W. Chan, X. Gong, L. Zhang and M. M. F. Choi (2013). "Capillary electrophoretic study of amine/carboxylic acid-functionalized carbon nanodots." Journal of Chromatography A **1304**: 234-240.
9. Jiang, K., S. Sun, L. Zhang, Y. Lu, A. G. Wu, C. Z. Cai and H. W. Lin (2015). "Red, green, and blue luminescence by carbon dots: Full-color emission tuning and multicolor cellular imaging." Angewandte Chemie-International Edition **54**(18): 5360-5363.
10. Karakocak, B. B., J. Liang, P. Biswas and N. Ravi (2018). "Hyaluronate coating enhances the delivery and biocompatibility of gold nanoparticles." Carbohydrate Polymers **186**: 243-251.
11. Karakocak, B. B., J. Liang, S. Kavadiya, M. Y. Berezin, P. Biswas and N. Ravi (2018). "Optimizing the synthesis of red-emissive nitrogen-doped carbon dots for use in bioimaging." ACS Applied Nano Materials.
12. Ostadhosseini, F. and D. Pan (2017). "Functional carbon nanodots for multiscale imaging and therapy." Wiley Interdisciplinary Reviews-Nanomedicine and Nanobiotechnology **9**(3): 1-16.
13. Pomper, M. G. and P. B. Fisher (2014). Emerging Application of Molecular Imaging to Oncology, Elsevier.
14. Rinaudo, M., B. Lardy, L. Grange and T. Conrozier (2014). "Effect of mannitol on hyaluronic acid stability in two in vitro models of oxidative stress." Polymers **6**(7): 1948-1957.
15. Tao, H. Q., K. Yang, Z. Ma, J. M. Wan, Y. J. Zhang, Z. H. Kang and Z. Liu (2012). "In vivo fluorescence imaging, biodistribution, and toxicology of photoluminescent carbon dots produced from carbon nanotubes and graphite." Small **8**(2): 281-290.
16. Wang, Y. F. and A. G. Hu (2014). "Carbon quantum dots: Synthesis, properties and applications." Journal of Materials Chemistry C **2**(34): 6921-6939.

17. Xu, M., G. He, Z. Li, F. He, F. Gao, Y. Su, L. Zhang, Z. Yang and Y. Zhang (2014). "A green heterogeneous synthesis of n-doped carbon dots and their photoluminescence applications in solid and aqueous states." Nanoscale **6**(17): 10307-10315.
18. Zhai, X. Y., P. Zhang, C. J. Liu, T. Bai, W. C. Li, L. M. Dai and W. G. Liu (2012). "Highly luminescent carbon nanodots by microwave-assisted pyrolysis." Chemical Communications **48**(64): 7955-7957.
19. Zhang, J. X., M. Zheng, F. L. Zhang, B. Xu, W. J. Tian and Z. G. Xie (2016). "Supramolecular hybrids of aiegen with carbon dots for noninvasive long-term bioimaging." Chemistry of Materials **28**(23): 8825-8833.
20. Zhang, Y., Y. J. Shen, X. Y. Teng, M. Q. Yan, H. Bi and P. C. Morais (2015). "Mitochondria-targeting nanoplatfom with fluorescent carbon dots for long time imaging and magnetic field-enhanced cellular uptake." ACS Applied Materials & Interfaces **7**(19): 10201-10212.
21. Zhu, H., X. L. Wang, Y. L. Li, Z. J. Wang, F. Yang and X. R. Yang (2009). "Microwave synthesis of fluorescent carbon nanoparticles with electrochemiluminescence properties." Chemical Communications(34): 5118-5120.

Chapter 6: Assessing the Nanoparticle Transport through the Biological Barriers in the Eye

The results of this chapter have been compiled partially in Karakoçak B. B., Santeford A., Lee T. J., Biswas P., Apte R. S., Ravi, N. (2018) Crossing the Blood-Retinal Barrier: A Quantitative Study on Targeted Delivery of Gold Nanoparticles. In preparation.

Also, the results of this chapter have been partially published in Karakocak, B. B.; Liang, J.; Kavadiya, S.; Berezin, M. Y.; Biswas, P.; Ravi, N. Optimizing the Synthesis of Red-Emissive Nitrogen-doped Carbon Dots for Use in Bioimaging. ACS Appl. Nano Mater. DOI: 10.1021/acsanm.8b00799. Copyright 2018 American Chemical Society

Abstract

Rapid progress in nanotechnology has led to its implementation for *in-vivo* diagnosis and therapy. As an example, recent studies have shown that gold nanoparticles (Au NPs) can be used as both delivery and imaging agents. Carbon dots (CDs) also hold promise as potential imaging agents because they have much higher quantum yields than Au NPs. When nanoparticles are administered *in-vivo*, the systemic circulation distributes them to all body organs and to the targeted tissue. Precise characterization of nanoparticles' distribution and accumulation in different body parts in preclinical models has been investigated; however, the eye remains an unexplored exception. For nanoparticles to be considered successful bioimaging and drug delivery agents in ophthalmology, an adequate dose must reach the target tissue. Coating nanoparticles with hyaluronic acid (HA), a biocompatible CD44 receptor-ligand increases the delivered dose in the eye. In this work, HA was conjugated to both 20 nm Au NPs and to 5 nm carbon dots to enhance their delivered dose. This study tested intravitreal and intravenous injections of both nascent and HA-coated Au NPs (HA-S-Au NPs) and quantified their distribution in the retina and cornea. Next, nitrogen doped CDs (nCDs) were tested as imaging agents in *ex vivo* eye globes and a *post-mortem* whole-body mouse model. The results showed that following intravenous injections, Au NPs and HA-coated Au NPs reached their maximum concentrations in the retina at 20 and 25 minutes, respectively. Twice as many HA-Au NPs reached the retina than nascent Au NPs. After 24 hours, 8.55% of the Au NPs were left in the retina, whereas 12.06% of the HA-Au NPs remained. Finally, the *ex-vivo* imaging of porcine ocular globes and *post-mortem* imaging of a whole mouse demonstrated the utility of nCDs.

6.1 Introduction

Gold nanoparticles (Au NPs) can deliver ocular drugs to specific target sites in the eye, where they can also be used as imaging agents due to their unique surface plasmon resonance (Boisselier and Astruc 2009, Jeong Hun et al. 2009, Yanai et al. 2012, Pan et al. 2013, Su et al. 2013, Zhou et al. 2013). Since Au NPs can be exploited as both imaging and drug delivery agents, they hold promise to revolutionize the detection and treatment of many eye diseases. With their capability to target a specific ocular region, Au NPs can more readily deliver the desired therapeutic dose (Bakri et al. 2008, Choonara et al. 2010, Christoforidis et al. 2012, Gabriele Sandrian et al. 2012, Gan et al. 2013, Ferenchak et al. 2014). Numerous recent studies have suggested that ocular medicine will benefit enormously from the use of nanoparticles, and gold nanoparticles are one of the most promising agents (Bakri et al. 2008, Hayashi et al. 2009, Jeong Hun et al. 2009, Jin Hyoung et al. 2011, Williams and Klebe 2012, Skala et al. 2013, Cho et al. 2015).

Carbon dots (CDs), which measure less than 5 nm in diameter, are also the subject of several recent studies in bioimaging (Liu et al. 2017, Lin et al. 2018, Liu et al. 2018). As of May 2018, well-known chemical suppliers can provide commercially available but expensive blue/green emissive CDs (Aldrich 2018). Despite their expense (\$3/mg), these CDs are particularly interesting for their wavelength-dependent excitation/emission behavior (Gan et al. 2016), long fluorescence lifetime (Dong et al. 2015), good photostability (Miao et al. 2017), and relatively high biocompatibility (Zhang et al. 2015) as discussed in previous chapters. With this unique combination of properties, CDs have demonstrated promise for bioimaging applications, where high quantum yield and red/near-infrared excitability are key properties. In this dissertation, we have optimized a facile method of synthesizing red-emissive CDs. We have demonstrated their usefulness both in their nascent form (Chapter 4)

and HA-conjugated form (Chapter 5) for *in-vitro* imaging. However, it is also vital to demonstrate their usefulness in animal models as a prerequisite to clinical trials.

Intravitreal injections are one of the most common methods to treat retinal diseases.

Additionally, intravenous injections would be advantageous in ophthalmology if the NPs were designed to cross the blood-retinal barrier (BRB). It is worth noting that the BRB and the blood-brain barrier (BBB) have similar natures due to the similarity of their structure (Runkle and Antonetti 2011). Both barriers consist of an inner and outer barrier, which makes diffusion highly selective, due to the presence of tight junctions between the cells (London et al. 2013). However, if nanoparticles can cross the BRB, there is a high possibility of delivering a drug or gene to the brain as well.

Intravenous injections are advantageous over intravitreal injections due to their reproducible results, ease of their application, and ready patient compliance (Bourges et al. 2003, Diebold and Calonge 2010, Cho et al. 2015). The entire administered dose reaches the systemic circulation immediately, and the delivered dose can be accurately calibrated against the response of the target organ.

There have been several attempts to coat NPs with different conjugates to increase their delivered dose to the target organ/tissue. Many coating conjugates, ranging from synthetic ligands to natural biomolecules, have been used to improve the stability of particles and the efficiency of their delivery to specific cells or tissues (Manson et al. 2011, Lowe et al. 2015, Yilmaz et al. 2016, Lin et al. 2017). As discussed in Chapter 3, we chose hyaluronic acid (HA) as a coating material because it can prevent adsorption of proteins on the surfaces of biomaterials (Hans and Lowman 2002) and has an antifouling effect that arises from its hydrophilic and polyanionic characteristics (Lee et al. 2008, Santhanam et al. 2015). HA also scavenges free radicals and chelates pro-oxidant metals (Glucksam-Galnoy et al. 2012). It

exhibits many desirable physiological properties: For example, it can be either anti-inflammatory or pro-inflammatory, depending on its molecular weight. On the other hand, as demonstrated in Chapter 3, HA coating can increase the intracellular concentration of NPs because specific cell membrane receptors, specific to HA, will recognize the HA coating and facilitate endocytosis.

The main reason why intravenous injections are not preferred over other administration techniques is that the therapeutic agent has to cross at least two barriers (the BRB and BBB), which are very selective and do not allow the passage of large molecules. Thus, an effective concentration in the target organs (specifically the eye and the brain) is achievable.

Intravenously injected nanoparticles must escape elimination through the reticuloendothelial system to maintain a prolonged effective concentration. In addition, for the delivery agent to reach the target tissues/cells in the brain and the retina, the agent should overcome both barriers. The BBB and inner BRB are composed of endothelial cells lining the brain and retinal vasculatures as illustrated in Figure 6.1 (Petros and DeSimone 2010, Jo et al. 2015). The inner BRB is a dynamic structure consisting of retinal endothelial cells, pericytes, and astrocytes, and the outer BRB consists of tight junctions between retinal pigment epithelium (RPE) cells (Kim et al. 2006, Runkle and Antonetti 2011). Similarly, the BBB consists of the same structures except for the presence of the basal lamina, which can be considered as an additional membrane inside the BBB. In addition to the fact that the BRB is critical in physiological and pathological processes in the retina, the structure of the BRB is the limiting factor in targeted drug and gene delivery applications when the target organ is the eye.

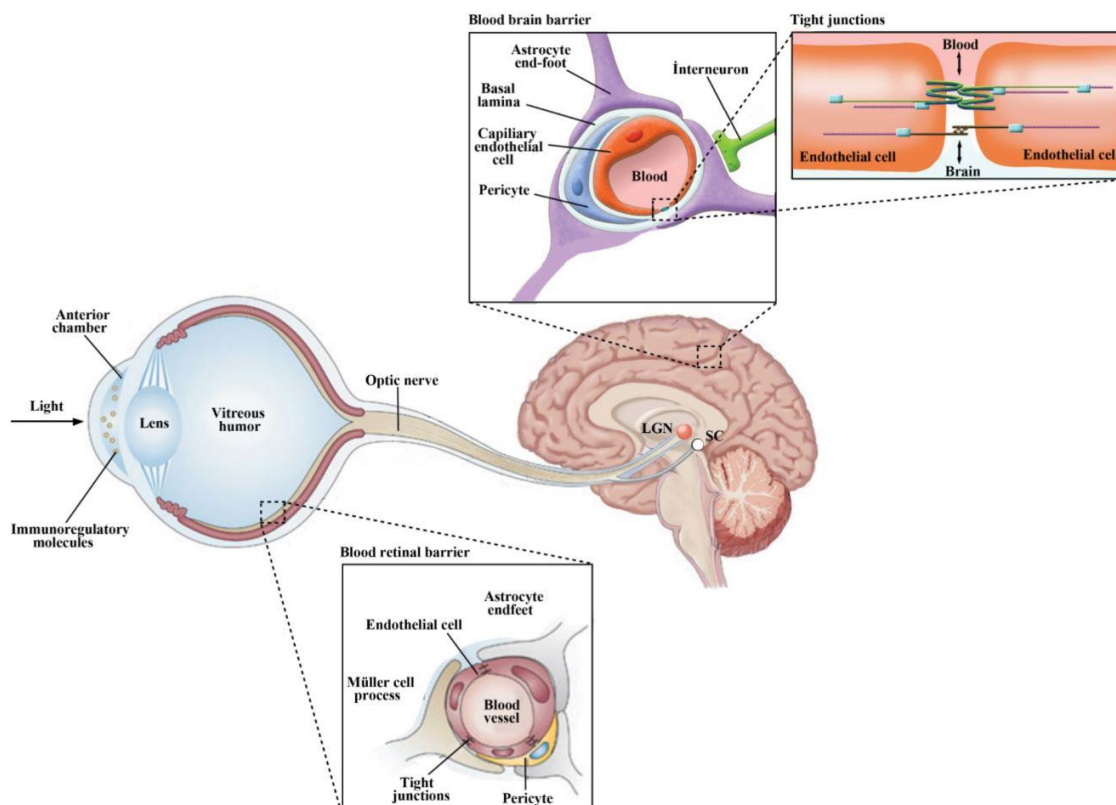


Figure 6.1 Structure of Blood Retina Barrier (BRB) and Blood Brain Barrier (BBB) (Adapted from (London et al. 2013)).

Nanoparticles administered into the body are eventually cleared by organs in the mononuclear phagocyte system which contains phagocytic cells in reticular connective tissue, such as the liver and spleen. Nanoparticles remain in these organs for a long time after being taken up by the macrophages, which increases the likelihood of unintended acute or chronic toxicity. However, very few studies (Jeong Hun et al. 2009, Hirn et al. 2011) showed accumulation of Au NPs in the eye, despite the bio-distribution of gold nanoparticles being well studied (Sonavane et al. 2008, Terentyuk et al. 2009, Johnston et al. 2010, Khlebtsov and Dykman 2011). Figure 6.2 illustrates the detailed structure of the blood-retinal barrier, with the absolute thicknesses of each section. The NP has to travel at least 11 μm to reach the rods and cones.

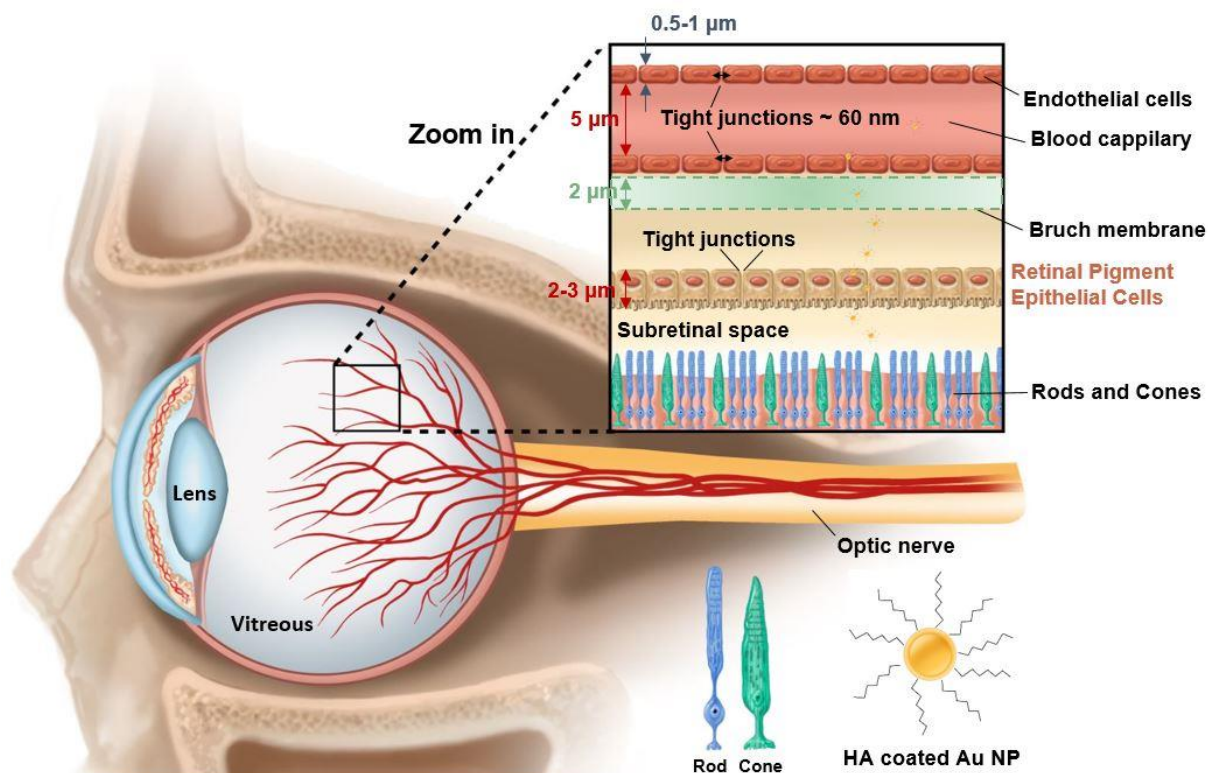


Figure 6.2 Detailed structure of the Blood Retina Barrier (BRB) and thicknesses of each section. The NP has to travel at least 11 μm while passing at least two layers of cells with tight junctions having an opening of 60 nm.

So far, one study has reported that Au NPs can cross the BRB, depending on their size (Jeong Hun et al. 2009). The authors reported that intravenously administered 20 nm spherical Au NPs with an exposure concentration of 1g/kg could pass through the blood-retina barrier and did not cause ocular toxicity. However, only TEM images of the retina were presented, and quantification was presented from only one representative TEM image. The fate, location, and concentration of the Au NPs which crossed the blood-retina barrier are unknown, and just one bioassay was performed (TUNEL), in which the apoptotic cell death count was found to be only eight cells, seven days following the intravenous injection.

It is clear that there is an urgent need for a comprehensive study reporting the quantification data on ocular locations of intravenously and intravitreally injected Au NPs. Further, for targeted drug and gene delivery applications, not only the fate of the NPs following

intravenous injection, but also the accumulated dose after a period of time (i.e., a minimum of 24 hours post-injection) must be reported before suggesting Au NPs as potentially safe agents.

In this Chapter, we aim to demonstrate that both nascent and HA-S-Au NPs cross the BRB while reporting the location and the accumulated amounts of Au NPs in different sections of the eye (cornea and retina).

The final part of this chapter describes a demonstration of the potential usefulness of red-emissive nCDs as bioimaging agents. The nCDs developed in Chapter 4 were injected intravitreally into *ex-vivo* porcine ocular globes and subcutaneously in euthanized mice, where they were readily detected.

6.2 Materials and Methods

6.2.1 Animals

The mouse eye has a long-established history in ophthalmology, specifically in retinal research, and is an appropriate model for our short-term study. We utilized C57BL/6 male mice from Jackson Laboratory (Bar Harbor, ME, USA) 6-8 weeks old, with a weight of 20-25 grams.

Care, use, and treatment of all animals in this study were in strict agreement with the Association for Research in Vision and Ophthalmology (ARVO) statement for the Use of Animals in Ophthalmic and Vision Research. An animal protocol (20170241) was established accordingly and approved by the Washington University in St. Louis Institutional Animal Care and Use Committee in November of 2017.

There were two main *in-vivo* studies. The first study demonstrated intravenous injections of both gold nanoparticles and carbon dots, and the second study consisted of intravitreal injections of the same nanoparticles.

6.2.2 Mimicking the blood-retinal barrier: Cell inserts

Prior to the intravenous injections, a preliminary study was conducted to test the ability of Au NPs to cross the tight junctions between the retinal pigment epithelial cells. Transwell® permeable supports with 6.5 mm inserts were used. There are two chambers (bottom and top) present in one Transwell®, and they are separated by a Coster 3450-polyester membrane, which has pore openings of 0.4µm in diameter. The retinal pigment epithelial cells (ARPE-19) are plated on these membranes at a concentration of 20,000 cells per transwell where the upper chamber volume is 200 µL, and the bottom chamber volume is 1000 µL.

In our previous cell attachment study (Chapter 4), the electrical impedance (ECIS) measurements showed that the time required for the ARPE-19 cells to reach over 90% confluency is approximately 24 hours. To reach a nice monolayer of cells ensuring the formation of tight junctions between them, the cells were grown inside the transwells for 72 hours, prior to the Au NP addition. We chose Au NPs with a diameter of 20 nm to observe NPs' ability to cross the tight junctions. After 72 hours, aliquots were collected from the bottom plate for inductively coupled plasma mass spectrometry (ICP-MS) analysis. The presence of Au NPs in the bottom chamber will serve as the evidence that the Au NPs are able to pass through the ARPE-19 cells' tight junctions. Cells attached to the transwell membrane will be fixed and examined with 3-D confocal microscopy to quantify the Au NP concentration within a cell.

6.2.3 Intravitreal and intravenous injections of Au NPs and CDs

The mice were anesthetized with Avertin (250 mg/kg), followed by intravenous and intravitreal injections of Au NPs or CDs. Au NPs with a diameter of approximately 20 nm were used either in end-thiolated hyaluronate coated (HS-HA) form or uncoated. The carbon dots (HA-conjugated and conjugated) were smaller than 5 nm. Information regarding

conjugation and a detailed physicochemical characterization was provided in Chapters 3 and 4 for Au NPs and CDs, respectively.

Intravitreal injections of Au NPs and CDs

C57BL/6 male mice were obtained from Jackson Laboratory (Bar Harbor, ME, USA). The eye was proposed using forceps, and an incision was made at the limbus by inserting and withdrawing a 30-gauge needle. A second 30-gauge hypodermic needle fitted on a Hamilton 700 series microsyringe (Hamilton, Reno, NV) was then inserted into the incision site to administer a 2 μ l intravitreal injection of Au NPs (0.05 mg/ml). The procedure was performed under a surgical microscope on both eyes of each animal. Phosphate-buffered saline (PBS) was used for sham injections.

Fresh porcine ocular globes were obtained from Trenton Processing Center, Trenton, IL. The excessive muscle and fat tissue around the eyes were excised, and the globes were placed in 1% antibiotic-antimycotic in 1x PBS. Intravitreal injections of nCDs were performed at a dose of 5 mg/ml with an injection volume of 50 μ L. The ocular globes (n=3) were imaged at the 6th and 30th minutes using the Multispectral FX Pro Imager (Bruker Biospin, Woodbridge, CT), $\lambda_{ex/em}$: 650/700 nm. The contrast based on the signal of nCDs was quantified and compared among ocular globes with and without the injection of nCDs with NIH ImageJ software (National Institutes of Health, Bethesda, MD).

Post-mortem imaging of nCDs

The nCDs were injected subcutaneously on the dorsal side of fresh mice cadaver (n = 3) for small-animal whole-body imaging. Deceased mice were shaved prior to nCD injection and imaging. Injections of nCDs in water (100 μ L solution per injection) were administered subcutaneously on left shoulder and right hip, at a dose of 33 μ g/g. Animals were imaged at 10 minutes post-injection using the Multispectral FX Pro Imager (Bruker Biospin,

Woodbridge, CT), λ ex/em: 550-600 nm/600-750 nm. The contrast based on the signal of nCDs was quantified and compared versus the negative control with NIH ImageJ software (National Institutes of Health, Bethesda, MD).

Intravenous injections of Au NPs to in-vivo mouse

Both nascent and HA-coated Au NPs at a concentration of 0.05 mg/ml were injected intravenously through the lateral saphenous vein of C57BL/6 mice. The injected nanoparticles were allowed to circulate for up to a maximum of 24 hours to ensure crossing the blood-retinal barrier. The mice were sacrificed at 5, 10, 15, 20, 25, 30, 60 minutes and finally at 24 hours post-injection. Next, eyes were harvested for *ex-vivo* imaging following cervical dislocation of the animal. The enucleated eyes were transferred into 4% paraformaldehyde (PFA) in 1x PBS as the cross-linking solution overnight. The eyes were then embedded in paraffin and sectioned at a thickness of 4 μ m.

Histology staining and imaging of eye tissue sections with coated and uncoated Au NPs

The 4 μ m tissue sections were stained with Mayer's hematoxylin and eosin Y (H&E; Richard-Allan Scientific, Kalamazoo, MI). Bright-field imaging was performed using a research light microscope (Olympus BX51, Lombard, IL) equipped with a color camera (D5-Fi1, Nikon) and a 10/0.30 Plan Fluor objective lens (Nikon).

Confocal microscopy imaging of eye tissue sections with coated and uncoated Au NPs

The 4 μ m tissue sections were incubated in ice-cold 1x PBS buffer containing 0.1% Triton (permeabilization agent) for 10 min at room temperature, then washed three times with ice-cold 1X PBS for 5 min each time. The tissue sections were then incubated with blocking buffer for 30 min before the addition of Alexa Fluor® 633 phalloidin (diluted 1:200 in blocking buffer) to stain the tight junction proteins, cadherin. The cells were subsequently washed three times with ice-cold 1X PBS for 3 min each time. To stain the nuclei,

SlowFade® Gold Antifade Mountant with DAPI (diluted 1:100 in 1X PBS) was used. The slides containing tissue sections were incubated overnight at 4 °C.

Electroretinogram analysis

ERG was performed as previously described (Ban et al. 2017) using the UTAS-E3000 Visual Electrodiagnostic System running EM for Windows (LKC Technologies, Gaithersburg, MD, USA). In brief, we extracted quantitative measurements from the ERG waveforms using an existing Microsoft Excel macro that defines the a-wave amplitude as the difference between the average pre-trial baseline and the trough of the average trace and defines the b-wave amplitude as the difference between the trough to the peak, without subtracting oscillatory potentials. Statistical analyses were performed using the paired t-test to analyze variance and pattern electroretinographic variables. A *P*-value of 0.05 was considered statistically significant. Results were expressed as mean (SD).

6.3 Results and Discussion

6.3.1 Demonstration of 20 nm Au NPs crossing the tight junctions of retinal pigment epithelial (RPE) *in-vitro*

We successfully demonstrated that 20 nm Au NPs were able to cross the tight junctions formed between the ARPE-19 cells. According to the results obtained (Figure 6.3), by the end of 24 hours, 70.3% of the Au NPs accumulated inside the cells. 7.2% of the Au NPs could cross the cell insert membrane and the tight junctions between the ARPE-19 cells. 22.4% of the NPs could not enter the cells and could not pass the membrane.

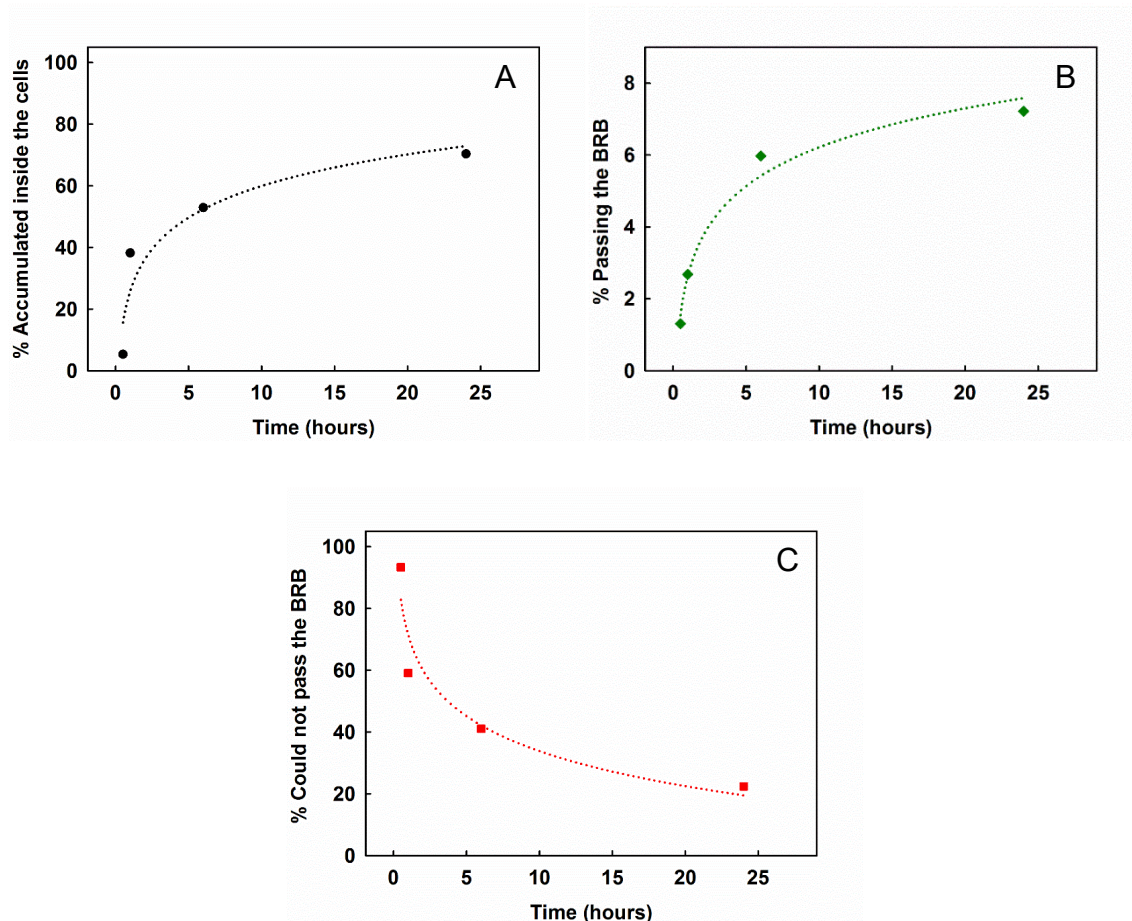


Figure 6.3 ICP-MS quantification results for the Au NPs that could cross both the tight junctions formed in between the RPE cells and the insert membrane. The amount that is detected in the bottom chamber of the inserts is denoted as % of NPs that can cross the BRB, as this in-vitro experimental design is a widely expected in-vitro model as proof of concept for the NPs crossing the BRB.

6.3.2 Distribution of intravitreally injected HA-coated and uncoated Au NPs in the cornea

Figure 6.4 displays optical images with H&E staining of a typical mouse eye section. All the sections of both the cornea and retina are labeled in Figures 6.4.A and 6.4.B, respectively.

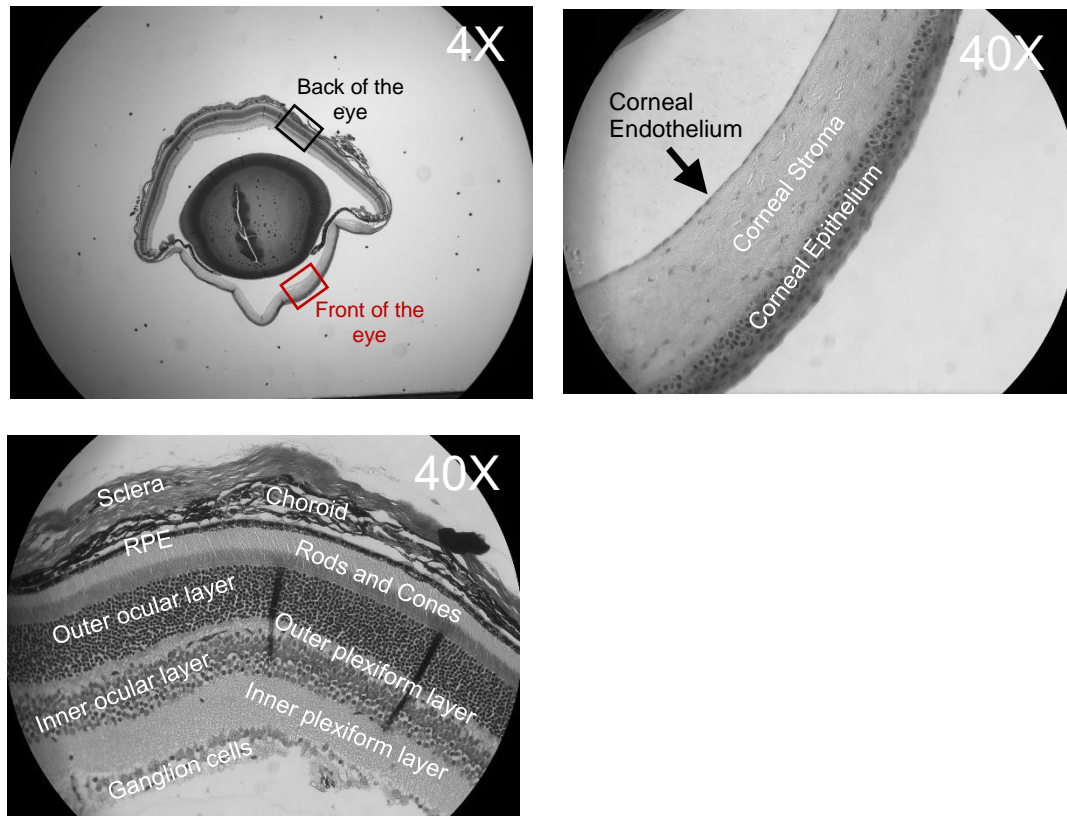


Figure 6.4 H&E stained optical microscopy images of the eye. (A) The whole cross-section. (B) 40X magnification of the front of the eye, where the cornea is present. (C) 40X magnification of the back of the eye, where the retina is located. The parts of the cornea and retina are labeled.

Figure 6.5 displays an optical image of a paraffined section of an eye after an intravitreal injection of 2 μ l Au NPs. As can be seen, there is retinal detachment, which can be due to the invasive nature of the intravitreal injection. The eye globe is small (3.4 ± 0.2 mm in equatorial diameter, and 22 ± 5 μ l in volume) (Wisard et al. 2010) and the injection needle was a relatively large microsyringe.

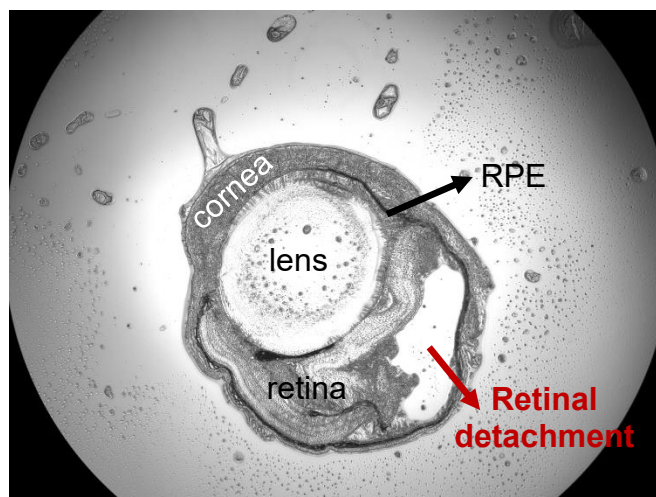


Figure 6.5 Optical microscopy images of a paraffined section of an 8-week old C57BL/6 mouse eye. The main eye sections – cornea, lens, retina, along with RPE cells are labeled. Following the intravitreal injection of Au NPs, the retina was detached.

Next, the distributions of uncoated Au NPs and HA-S-Au NPs in the eye are displayed (Figure 6.6). Confocal microscopy detected the Au NPs because they are inherently fluorescent, and they absorb light in 480-600 nm region (Boisselier and Astruc 2009, Zhou et al. 2013, Linlin et al. 2015), depending on their size.

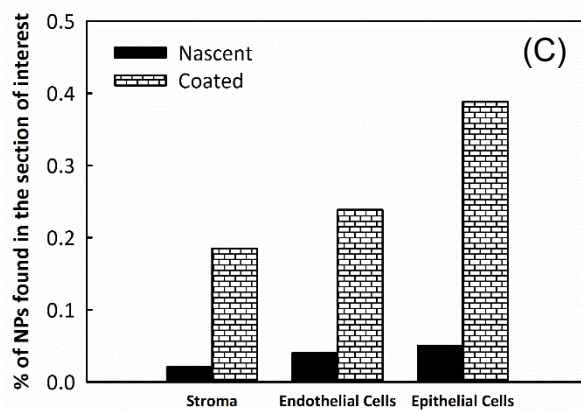
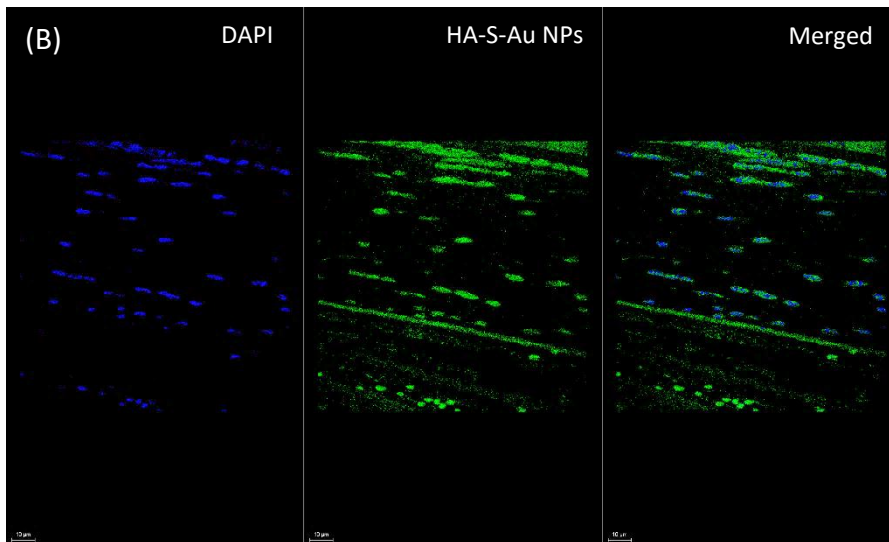
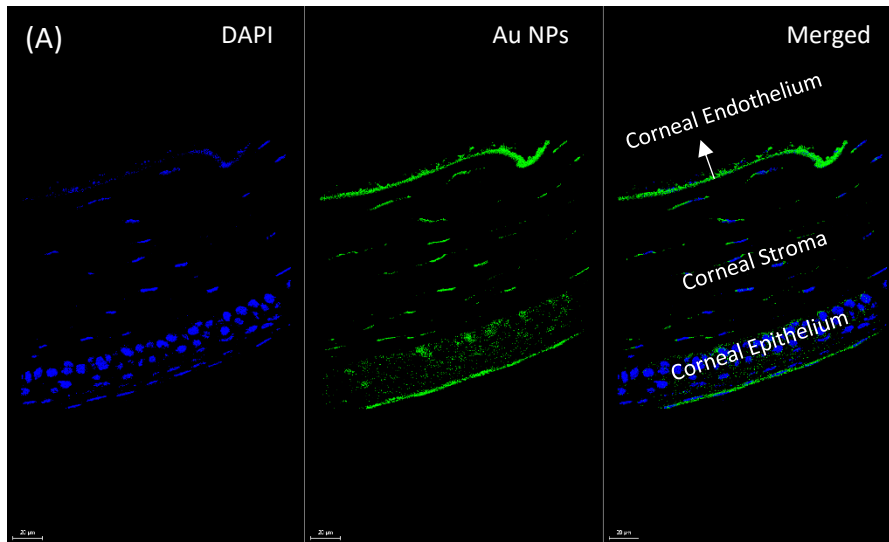


Figure 6.6 Confocal microscopy images of the cornea of an 8-week-old C57BL/6 mouse 24 hours post-injection of (A) nascent Au NPs, (B) HA-S-Au NPs. The nucleus is stained with DAPI and blue in color, and Au NPs are green. There are more HA-coated Au NPs detected in all sections of the cornea. (C) ImageJ analysis quantified the amounts of Au NPs in each section.

ImageJ analysis revealed that the HA coating consistently enabled significantly more Au NPs to enter the cornea (Figure 6.6C). In the stroma, approximately 850% more Au NPs were detected when they are coated with HA (0.019% vs. 0.18% of the NPs injected into the mouse eyes). Moreover, 360% more HA-coated Au NPs were detected in the corneal endothelium cells (0.039 vs. 0.18%), and finally, 700% (0.047 vs. 0.38%) more HA-Au NPs were detected in the corneal epithelial cells, where the maximum amount of NPs was detected. This consistent difference can be attributed to enhanced endocytosis of HA-coated Au NPs, because HA is recognized by the CD44 receptors expressed on the corneal epithelial cell membranes (Contreras-Ruiz et al. 2011, Karakocak et al. 2018). The distribution of Au NPs was not analyzed, because the retinal detachment would render results inaccurate.

6.3.3 Distribution of intravenously injected uncoated and HA-coated Au NPs in the eye

Several series of confocal images were taken for mouse tissue sections. As explained in the statistical analysis section, at least three replicas were used for each time point of sacrifice. There were eight time points (5, 10, 15, 20, 25, 30, and 60 minutes, and 24 hours), and both HA-coated and uncoated Au NPs were injected intravenously (30-50 μ l, depending on the weight of the mouse). Sham injections were done with 1X PBS.

Distribution analysis of Au NPs in the cornea

Figure 6.7 displays confocal images of Au NPs post injection for all the time points tested. The signal from the second channel, where only the Au NPs can be detected (488 nm excitation λ , 500-550 nm emission λ) was the highest at the 15th minute.

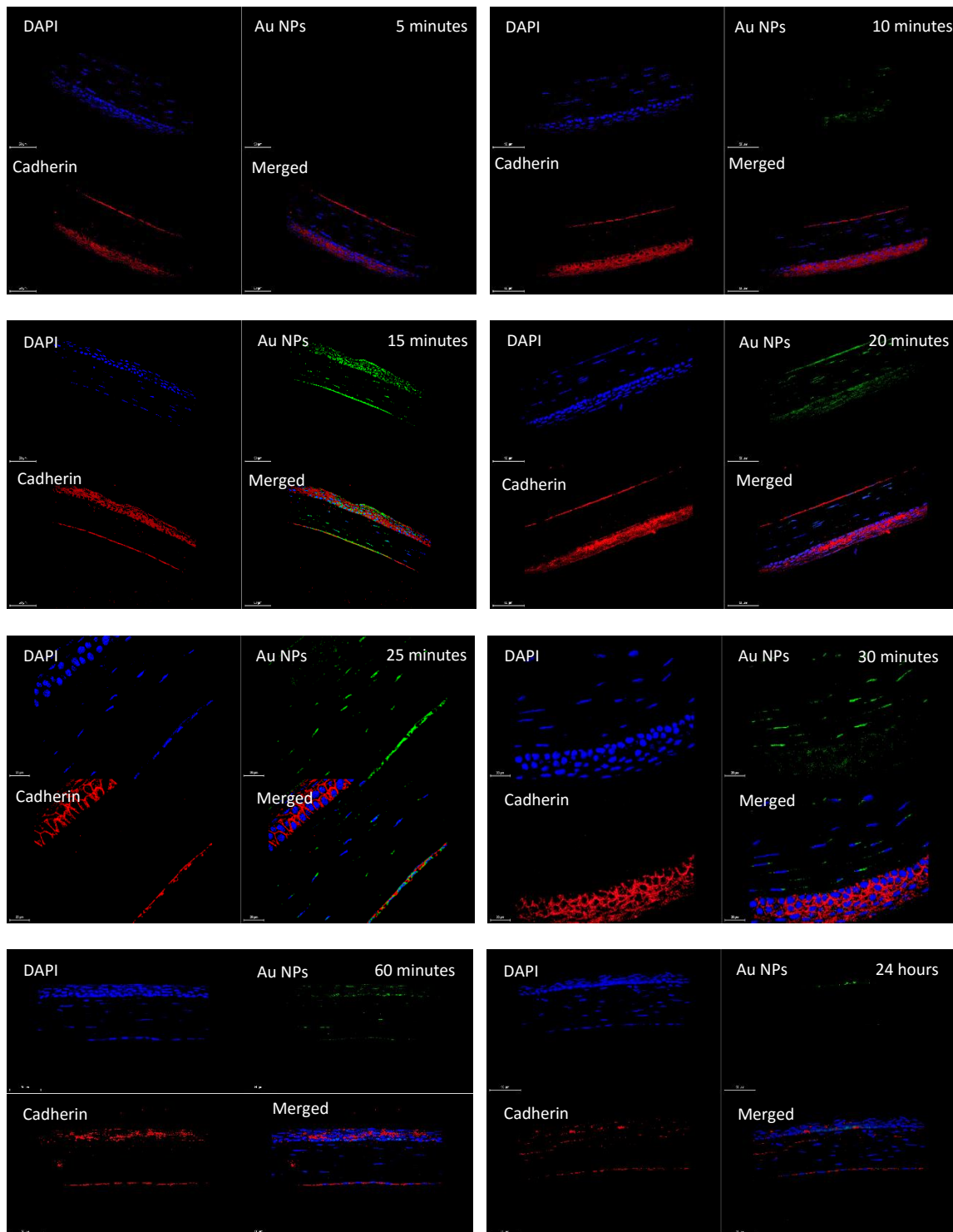


Figure 6.7 The red staining corresponds to cadherin, a tight junction protein; the nucleus is stained with DAPI and blue, and Au NPs are green. The fourth image in each time point is a merged version of the previous three images. The amount of Au NPs that reached the cornea peaked at 15 minutes post injection, as can be seen. Scale bars are 50 μm .

Next, the amount of Au NPs in each part of the cornea was quantified using ImageJ analysis, with the results shown in Figure 6.8. The NPs were most internalized by the endothelial cells, reaching a peak concentration at minute 15 post-injection. On the other hand, the least amount

of NPs was detected in the stroma, followed by the corneal epithelial cells. The corneal stroma, the nutrition source of the cornea, is composed of collagen fibril assemblies and maintains the corneal transparency where growth factors and cytokines are produced (Mohan et al. 2012, Williams and Klebe 2012, Zhang et al. 2017). The extracellular matrix is also mainly composed of collagen (Zhang et al. 2017). Unlike the corneal epithelium and corneal endothelium, the cell number concentration is relatively less in the stroma. Hence it can act as a void space where the transport of NPs is diffusion driven, is mainly by a concentration gradient. As a result, NPs may tend to move faster in the stroma than in the epithelium and endothelium. Thus, their residence time in the stroma will be much shorter than in the other parts of the cornea, which can explain the relatively less accumulation observed in the stroma.

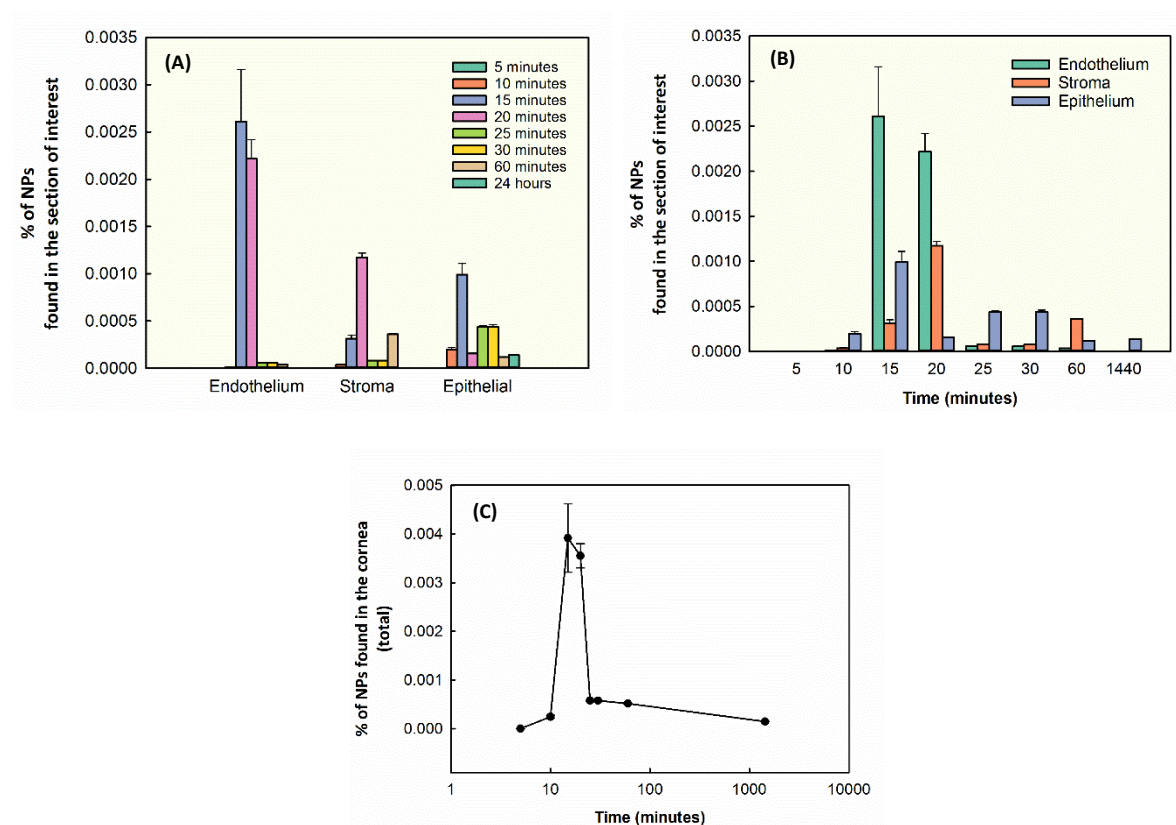
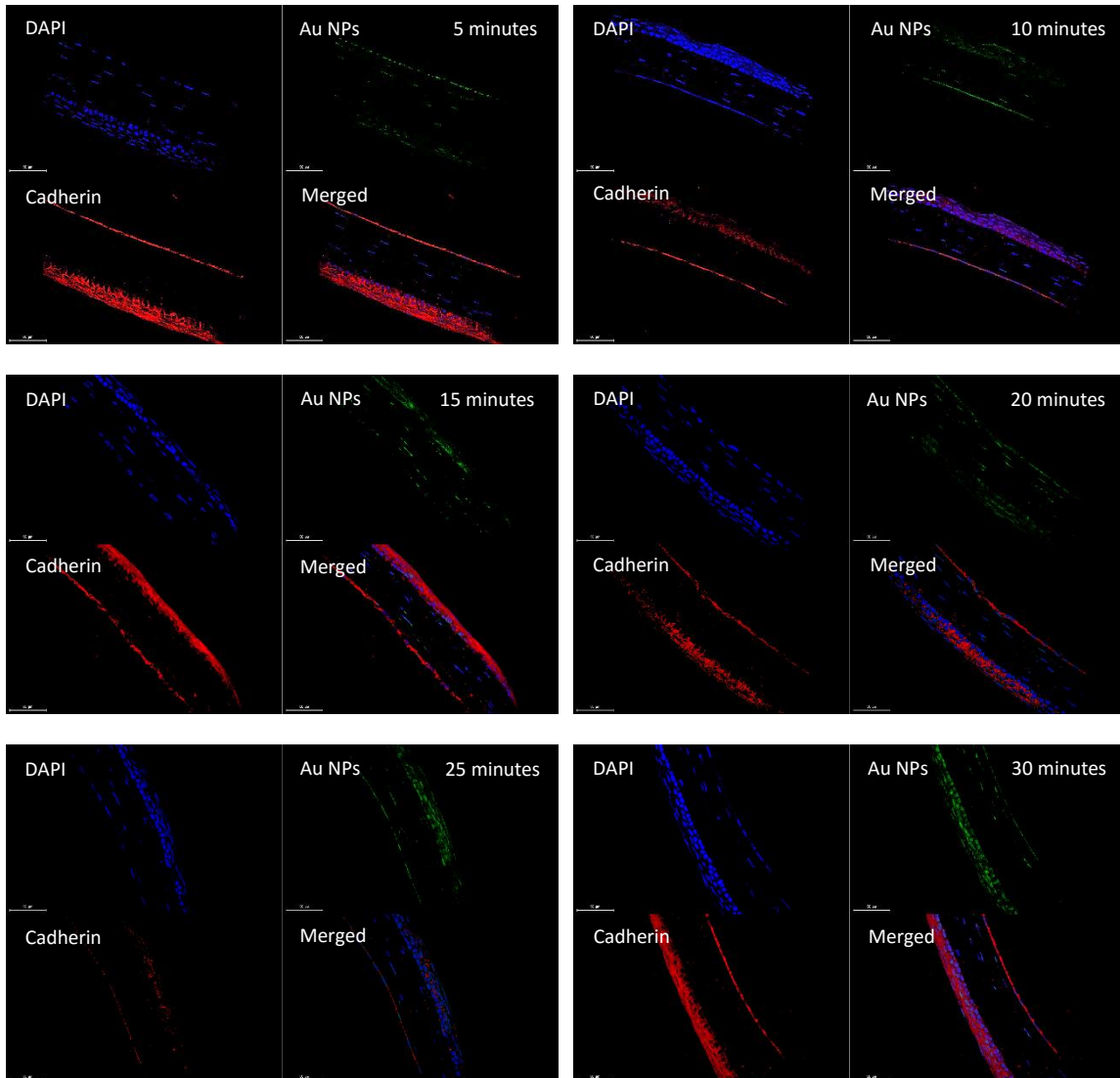


Figure 6.8 Au NP quantification results in the cornea. (A) The amount of Au NPs accumulated in each main section of the cornea: endothelium, stroma, and epithelium. (B) The results plotted as a function of time. (C) The cumulative amount of NPs found in the cornea as a function of time. It took more than 5 minutes, and less than 10 minutes for NPs to reach the cornea. The delivered amount of NPs reaching the cornea peaks at minute 15. After minute 25, the amount remaining in the cornea significantly decreases. By the end of 24 hours, only 3.74% of the peak Au NP concentration remains in the cornea.

Distribution analysis of HA-S-Au NPs in the cornea

Figure 6.9 displays confocal images of HA-S-Au NPs post injection for all the time points tested. At 60 minutes post-injection, the signal from the second channel, where only the Au NPs can be detected (excitation λ : 488 nm, emission λ : 500-550 nm) was the highest. This finding means that HA coating slows down the NP transport significantly.



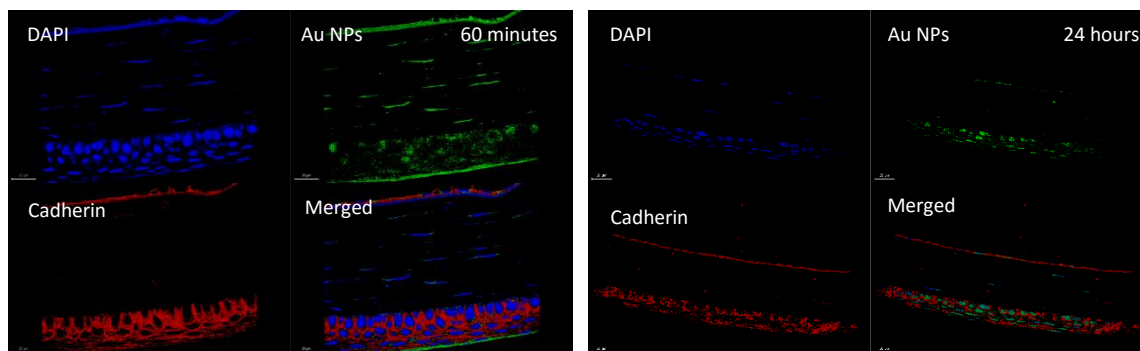


Figure 6.9 The red staining corresponds to cadherin, a tight junction protein, the nucleus is stained with DAPI and blue; and Au NPs are green. The fourth image in each time point is the merged version of all three previous images. The intensity of the signal coming from the second channel is proportional to the amount Au NPs present. The amount of Au NPs that reached the cornea peaked at 60 minutes post injection, as it can be clearly seen. Scale bars are 50 μm .

Next, the amount of HA-S-Au NPs in each part of the cornea was quantified using ImageJ analysis. Figures 6.10 summarizes the quantification analysis results. The HA-coated Au NPs were most internalized by the epithelial cells, unlike the nascent Au NPs, reaching a peak concentration at minute 60 post-injection. This behavior can be attributed to HA-CD44 receptor interactions on the corneal epithelial cell membrane. This result is in accordance with our findings in Chapter 3, where we showed that CD44 receptors significantly increased the intracellular concentration of HA-Au NPs for cells that express CD44 receptors on their cell membrane. As before, the least amount of NPs was detected in the stroma, which can again be explained by the rate of the diffusion concentration gradient driven transport of NPs. Overall, the total amount of HA-S-Au NPs was approximately 14% more than the total uncoated Au NPs reaching the cornea. By the end of 24 hours, 17.10% of the peak Au NPs concentration remained in the cornea. These results prove that HA facilitated Au NP transport and was able to carry the Au NPs through the tight junctions more efficiently.

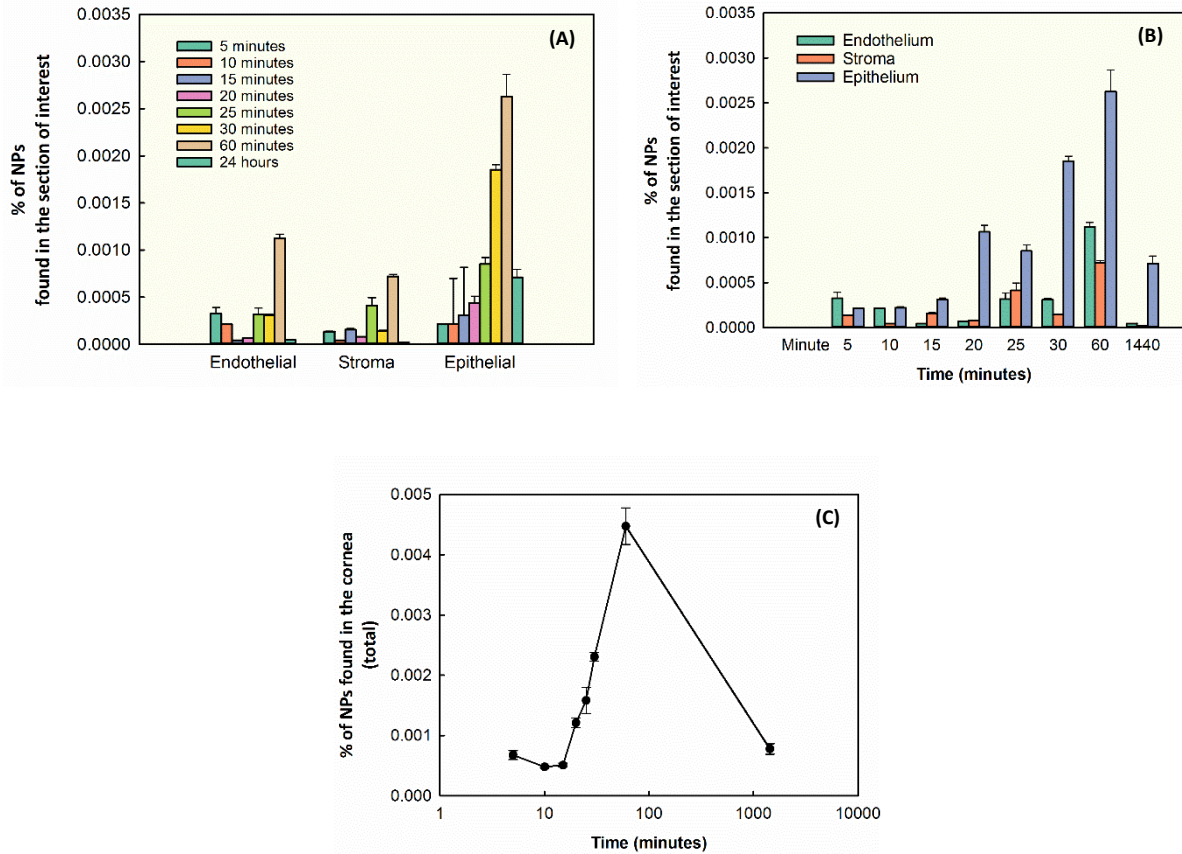


Figure 6.10 HA-S-Au NP quantification results in the cornea. (A) The amounts of Au NPs accumulated in each section of the cornea: endothelium, stroma, and epithelium. (B) The precise amounts in each section of the cornea are plotted as a function of time. (C) The cumulative amount of NPs found in the cornea as a function of time. It took the first NPs less than 5 minutes to reach the cornea. The amount of HA-S-Au NPs reaching the cornea peaks at minute 60. After minute 60, the amount left in the cornea significantly decreases. By the end of 24 hours, 17.10 % of the peak HA-S-Au NP concentration remains in the cornea.

Distribution analysis of Au NPs in the retina

Figure 6.11 displays confocal images of Au NPs post injection for all the time points tested. 25 minutes post injection, it was observed that the signal from the second channel, where only the Au NPs can be detected (488 nm excitation λ , 500-550 nm emission λ) was the highest, similar to the time point where the amount Au NPs accumulated in the cornea peaked.

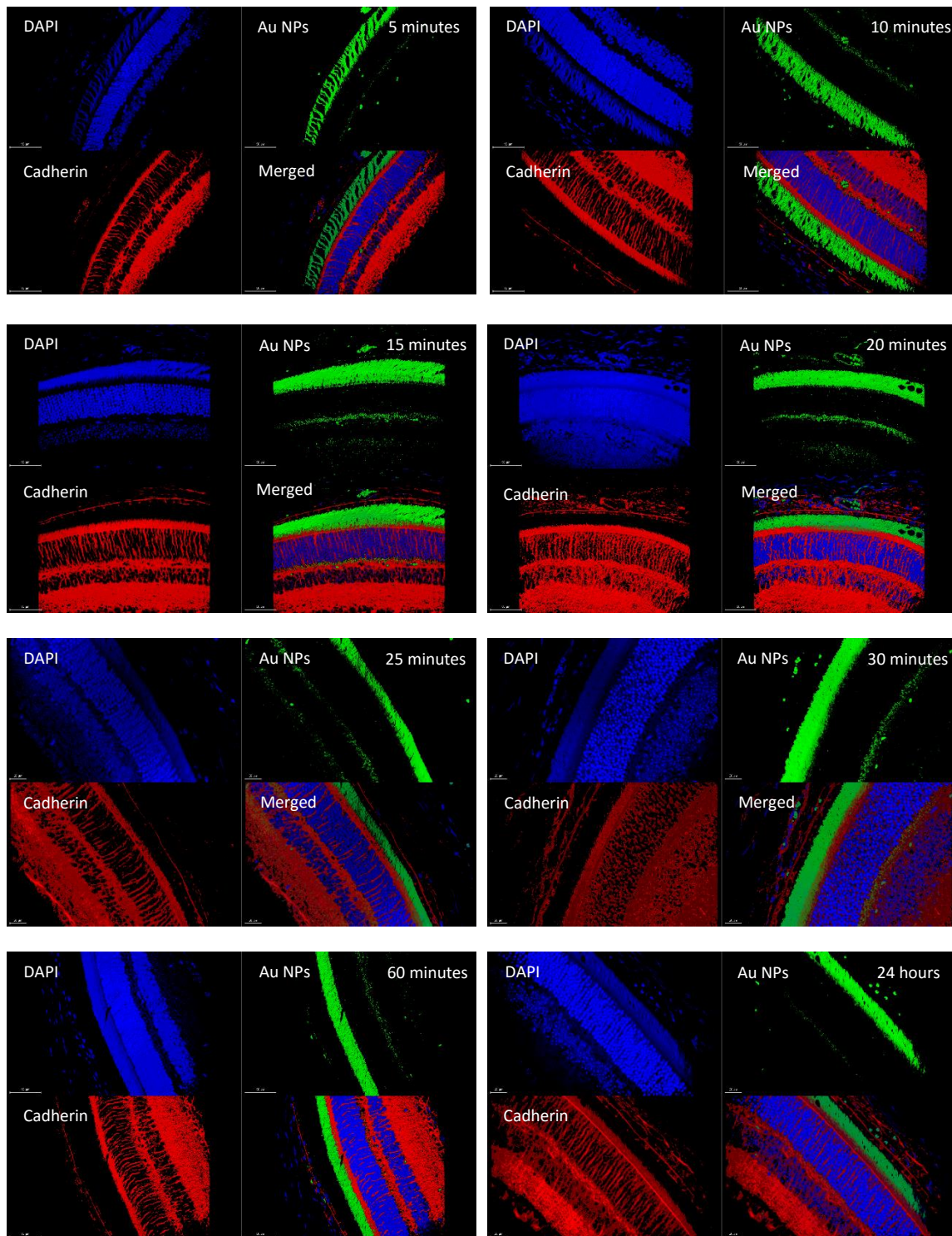


Figure. 6.11 The red staining corresponds to cadherin, a tight junction protein, the nucleus is stained with DAPI and blue; and Au NPs are green. The fourth image in each time point is the merged version of all three previous images. The intensity of the signal coming from the second channel is proportional to the amount of Au NPs present. The amount of Au NPs that reached the retina was peaked at 20 minutes post injection, as it can be clearly distinguished from the images. Scale bars are 50 μm .

Figures 6.12 summarizes the quantification analysis results of Au NPs accumulated in the retina. According to the results obtained, the NPs were internalized the most in the outer

retina where outer nuclear layer and outer plexiform layer are the regions of interest, reaching to a peak concentration at minute 20, post-injection. On the other hand, it was found that the least amount of NPs was detected in retinal epithelial cells, followed by inner retina where inner ocular layer, inner plexiform layer, and ganglion cells are present. This finding can be explained by the following behavior: As a result of the intravenous injections, the only way the NPs to enter the eye is via the blood flow and the first port of their entry is the choroid. As illustrated in Figure 6.2, the RPE is the second set of cells with tight junctions that NPs need to pass. As there is no flow present in the rest of the eye apart from the choroid, the NP transport is diffusion driven, where the concentration gradient is the main driving force. Therefore, the amount of NPs is expected to be less in RPE as they are prone to diffuse through the deep layers of the retina where the concentration is less.

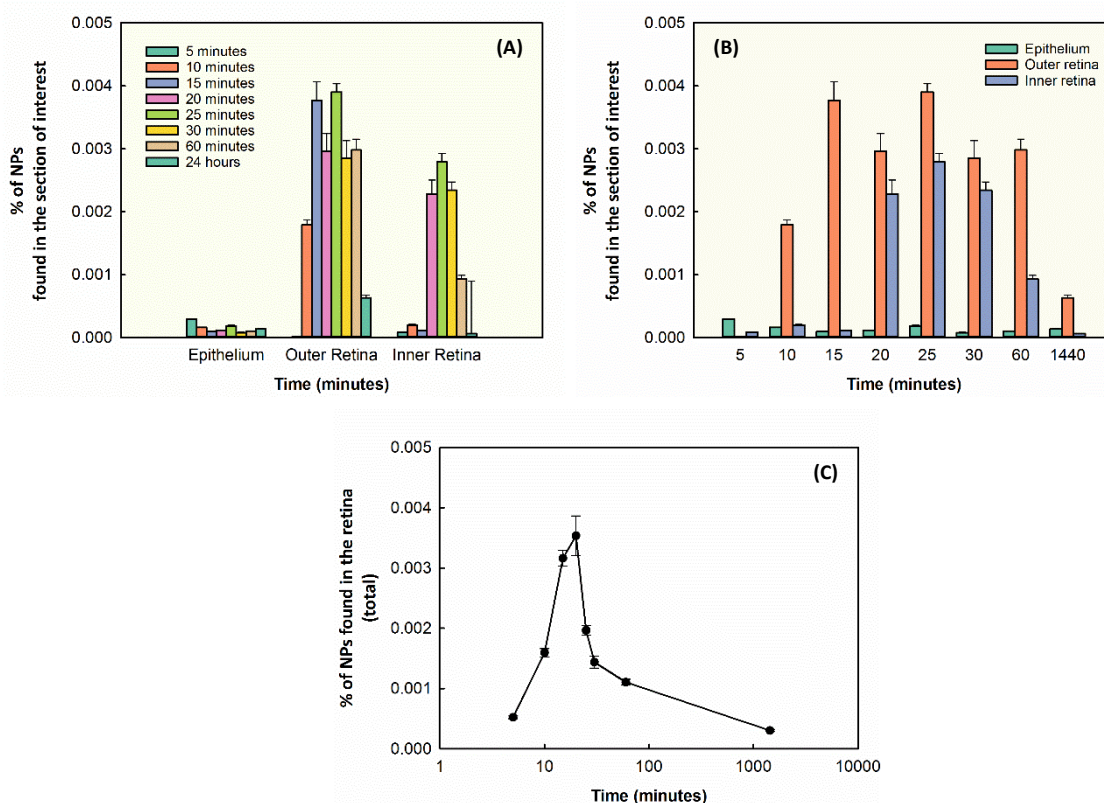
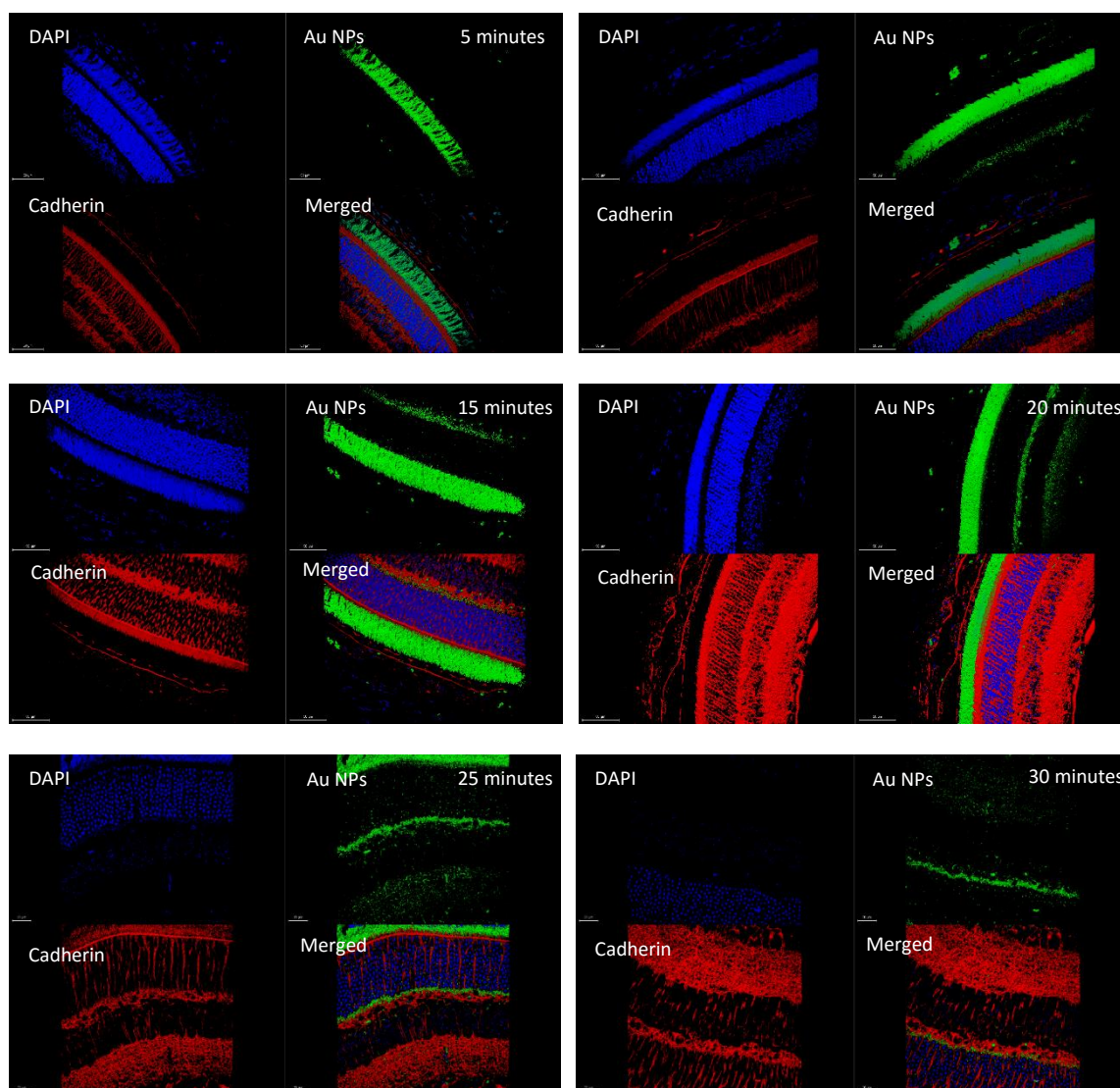


Figure 6.12 Au NP quantification results in the retina. (A) The amount of Au NPs accumulated in each main section of the retina: retinal epithelium, the outer retina, and the inner retina. The outer retina consists of the outer plexiform layer and outer nuclear layer, whereas the inner retina is composed of the inner plexiform layer, inner nuclear layer and the extension of the ganglion cells. (B) The results are plotted as a function of time for each central section of the retina. (C) The cumulative amount of NPs found in the retina as a function of time.

The amount of Au NPs reaching the cornea peaks at minute 20. After the end of one hour, the amount remaining in the retina significantly decreases. By the end of 24 hours, 8.55% of the peak Au NP concentration remains in the retina.

Distribution analysis of HA-S-Au NPs in the retina

Figure 6.13 displays the confocal images of HA-S-Au NPs in the retina post injection for all the time points tested. 25 minutes post injection, it was observed that the signal from the second channel, where only the Au NPs can be detected (excitation λ : 488 nm, emission λ : 500-550 nm) was the highest. Unlike the results for the cornea, the HA coating did not slow down the NP transport significantly (only by 5 minutes retardation for the NPs to reach their peak concentration).



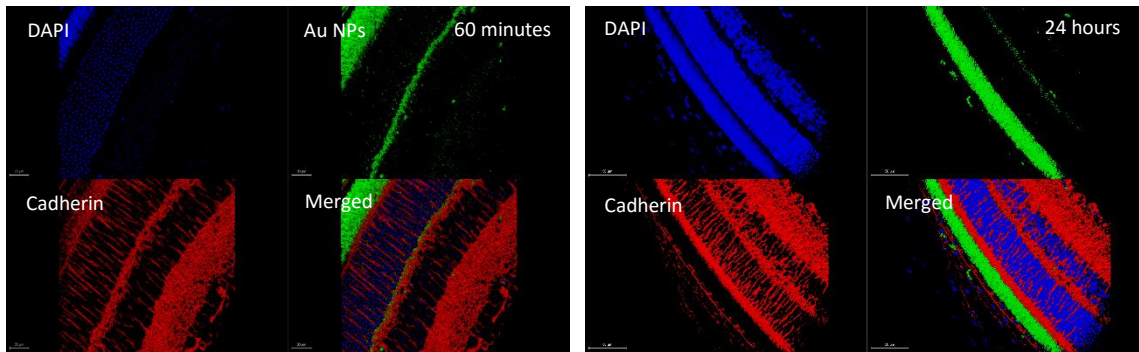


Figure 6.13 The red staining corresponds to cadherin, a tight junction protein, the nucleus is stained with DAPI and blue; and Au NPs are green. The fourth image in each time point is the merged version of all three previous images. The intensity of the signal coming from the second channel is proportional to the NPs present. The amount of HA-S-Au NPs that reached the retina was peaked at 25 minutes post injection, as it can be clearly distinguished from the images. Scale bars are 50 μm .

Figures 6.14 summarizes the quantification analysis results of HA-S-Au NPs accumulated in the retina. According to the results obtained, similar to the results of uncoated Au NPs, the NPs were most internalized in the outer retina where outer nuclear layer and outer plexiform layer are the regions of interest, reaching to a peak concentration at minute 25 post-injection. On the other hand, it was found that the least amount of NPs was detected in retinal epithelial cells, followed by inner retina where inner ocular layer, inner plexiform layer, and ganglion cells are present. Overall, the amount of HA-S-Au NPs that reached the retina was approximately twice as more than the uncoated Au NPs that reached the retina. This means that the HA coating can significantly enhance the amount of payload that can be delivered to the retina. The HA coating not only improved the delivery of Au NPs but also increased the amount that remained after a day by approximately 5% (8.55% vs. 12.06%).

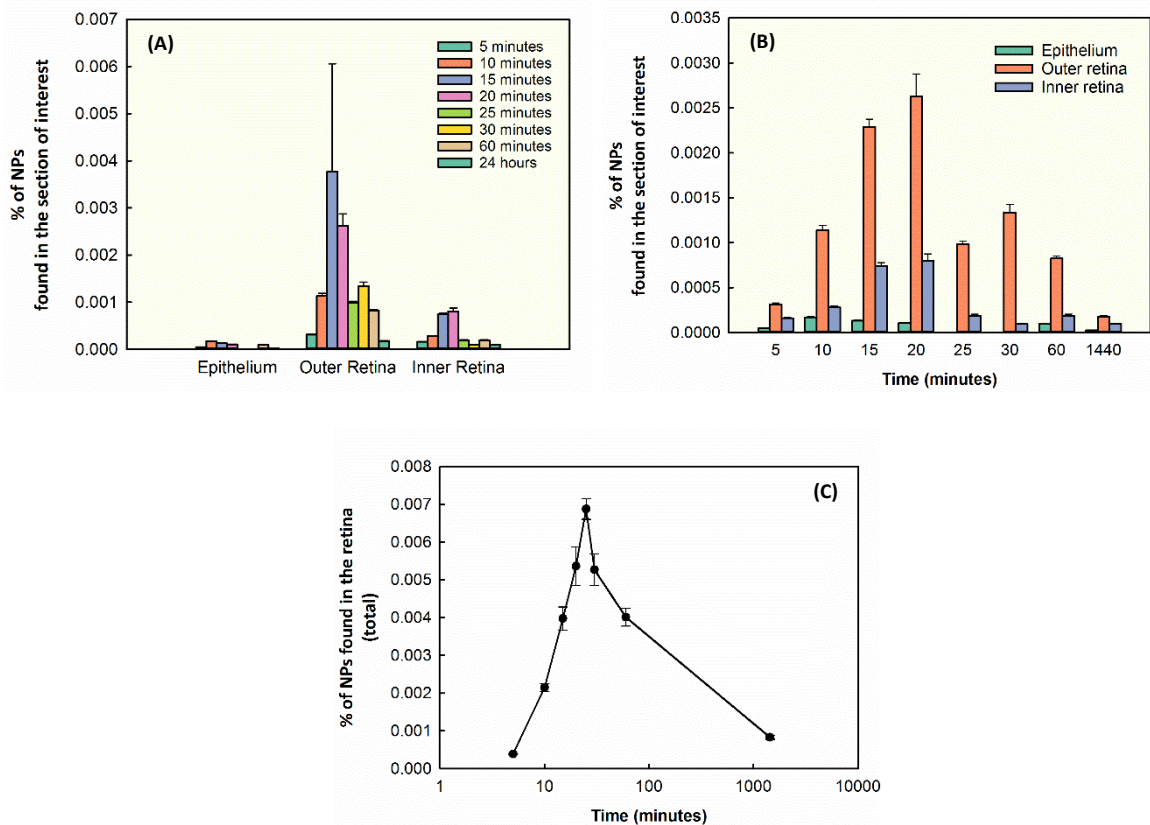


Figure 6.14 HA-S-Au NP quantification results in the retina. (A) The amount of HA-S-Au NPs accumulated in each main section of the retina: retinal epithelium, the outer retina, and the inner retina. The outer retina consists of the outer plexiform layer and outer nuclear layer, whereas the inner retina is composed of the inner plexiform layer, inner nuclear layer and the extension of the ganglion cells. (B) The results are plotted as a function of time for each main section of the retina. (C) The cumulative amount of NPs found in the retina as a function of time. The amount reaches the retina peaks at minute 25. After 24 minutes, the amount remains in the retina significantly decreases. By the end of 24 hours, 12.06% of the peak Au NP concentration remains in the retina.

Imaging of nitrogen-doped CDs in ex-vivo porcine ocular globes

Clinically, the particles need to diffuse through the layers of the eye to reach the desired part within for specific ocular treatments and bioimaging (Kompella et al. 2013). On the other hand, systemic administration of nanoparticles as drug nanovesicles and bioimaging agents are also of interest due to enhanced tumor uptake (Huang and Hainfeld 2013, Wang et al. 2013). For bioimaging applications, imaging agents, which optically active in the deep-red and NIR region are desirable due to their lower energy and reduced scattering interactions as compared to the short-wavelength light.

Post intravitreal injection images of 50 μ l of nCDs with the highest amine/acid ratio showed that the nCDs were excitable at a corresponding longer wavelength, for example, 650 nm with an emission at 700 nm (Figure 6.15).

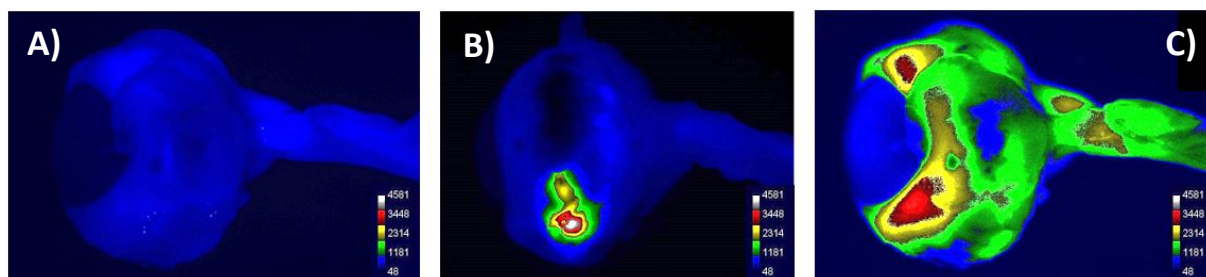


Figure 6.15. Ex-vivo ocular globe images obtained with a small animal imager (excitation λ_{ex} = 650 nm, λ_{em} = 700 nm). Porcine ocular globes with nCDs injections. (A) No injection of CDs, control. (B) Post-injection at 6 minutes. (C) Post-injection at 30 minutes.

Contrast based on the intensity density calculations conducted with ImageJ software showed that the normalized signal per region of interest (ROI) area was 1.63, 38.21, and 49.39 for Figs. 6.15A, 6.15B, and 6.15C, respectively. Also, it was observed that the nCDs diffused through the vitreous to cornea within half an hour (Fig. 6.15) suggesting that nCDs are suitable, low-toxicity (*vide supra*) candidates for ocular bioimaging applications.

6.3.4 Post-mortem imaging of CDs

The nCDs were injected subcutaneously into fresh mice cadaver ($n = 3$) for small-animal whole-body imaging. Deceased mice were shaved prior to nCD injection and imaging. Injections of nCDs in water (100 μ L solution per injection) were administered subcutaneously on left shoulder and right hip, at a dose of 33 μ g/g. Animals were imaged at 10 minutes post-injection using the Multispectral FX Pro Imager (Bruker Biospin, Woodbridge, CT), $\lambda_{ex/em}$: 550-600 nm/600-750 nm. The contrast based on the signal of nCDs was quantified and compared versus the negative control with NIH ImageJ software (National Institutes of Health, Bethesda, MD).

For *post-mortem* imaging analysis of the nitrogen-doped CDs (nCDs) developed in Chapter 4, a local administration route (subcutaneous injection) was adopted, which is expected to avoid nCDs entering the bloodstream. The nCDs with the highest amine/acid ratio (2.0) were injected subcutaneously (100 μ L per injection) into *post-mortem* mice at two different locations. We observed that a fluorescence area was formed around both injection sites (Figure 6.16).

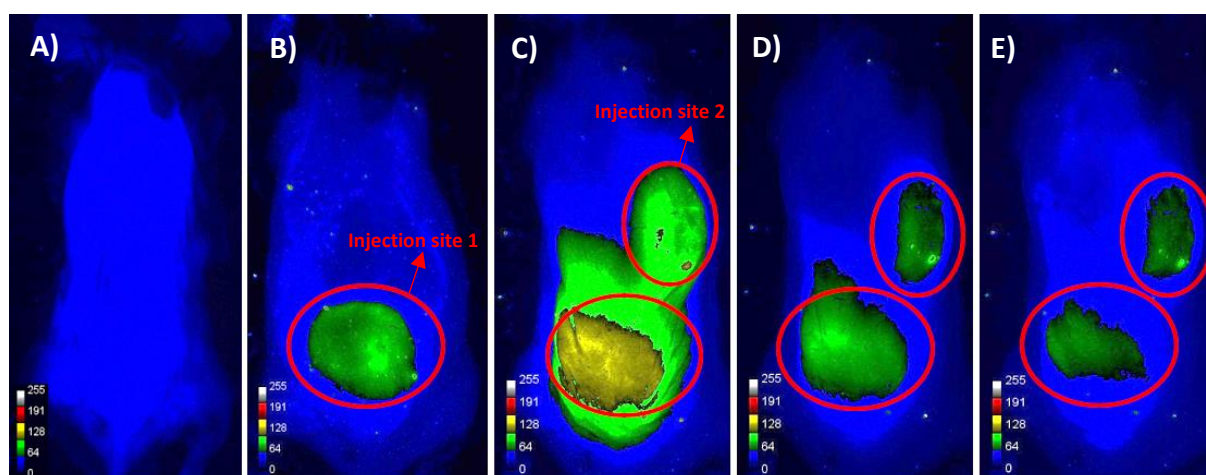


Figure 6.16. Post-mortem images of mice with nCDs obtained with the small animal imager, Bruker spectral FX. (A) No injection of CDs, control. $\lambda_{ex} = 550$ nm, $\lambda_{em} = 600$ nm. With nCD injections (B) After first injection, $\lambda_{ex} = 550$ nm, $\lambda_{em} = 600$ nm. (C) After second injection, $\lambda_{ex} = 550$ nm, $\lambda_{em} = 600$ nm. (D) $\lambda_{ex} = 550$ nm, $\lambda_{em} = 700$ nm. (E) $\lambda_{ex} = 600$ nm, $\lambda_{em} = 750$ nm.

The images generated sufficient contrast to be quantified with ImageJ software based on intensity density calculations normalized with respect to the ROI (9.29, 35.00, 54.89, 33.33, and 31.02, for Figs. 6.16A, B, C, D, and E, respectively) at 550 and 600 nm excitation wavelengths. The images prove that the nCDs could be used for whole animal imaging applications.

6.3.5 Electroretinogram analysis of intravenously injected uncoated and HA-coated Au NPs in the eye

In-vivo studies are necessary to assess the ocular toxicity of nanoparticles since the response of the target cell/organ may be influenced by interactions between different types of cells; additionally, defense mechanisms might be different at the organ level. Electroretinogram

(ERG) analysis is a well-established technique that can record the electrical activity of the retina triggered by light and therefore is a suitable method for assessing the toxicity of the NPs. The ERG signal is generated mainly by voltage changes caused by radial currents (along the axis of photoreceptors and bipolar cells) flowing in the resistive extracellular space of the retina (Jaakko and Plonsey 1995).

The first ERG signal was recorded in 1865 by Holmgren from the surface of a fish eye (Armington 1974). Einthoven and Jolly (Einthoven and Jolly 1908) divided the ERG response to the onset of light into three different waves, called a- (Penn and Hagins 1969), b- (Stockton and Slaughter 1989), and c- (Steinber.Rh et al. 1970) waves, that are now known to reflect mainly the activity of photoreceptors, bipolar cells, and pigment epithelium cells, respectively. The applied amplitude depends on the stimulating and physiological conditions, but ranges are in several hundred of a microvolt.

We carried out ERG analysis for 8-weeks old mice both at Day 1 and Day 7 post injection of Au and HA-S-Au NPs (Figure 6.17). The results showed no significant difference between the signals among the control, nascent, and HA-S-Au NPs. This means neither Au NPs nor HA-S-Au NPs caused toxicity at the injection doses tested.

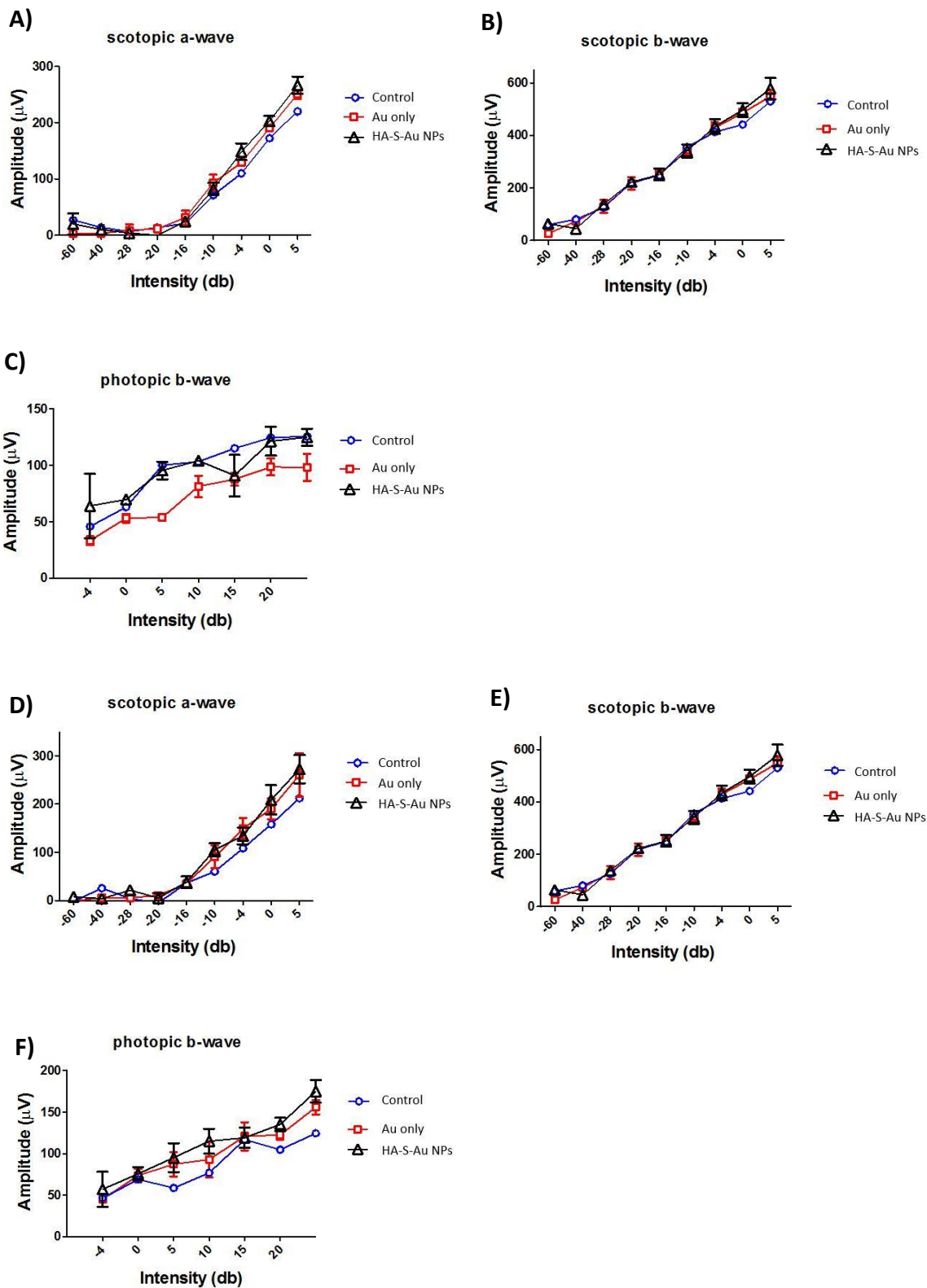


Figure 6.17. ERG analysis of nascent and HA-S-Au NPs: 1-day post-injection (A) scotopic a-wave (B) scotopic b-wave (C) photopic b-wave and 1-week post-injection (D) scotopic a-wave (E) scotopic b-wave (F) photopic b-wave. The results showed no significant difference among all the measurements obtained.

6.3.6 Histology staining and imaging of eye tissue sections with uncoated Au NPs and HA-S-Au NPs

For concision, the results of this section are provided in Appendix V.

6.4 Conclusions

Intravitreal injections of Au NPs caused retinal detachment, and therefore, were not investigated further. The amount reaching the cornea was quantified for both coated and uncoated Au NPs. HA coating enabled significantly more Au NPs to enter and remain in the cornea. In the stroma, approximately 850% more Au NPs were detected when they are coated with HA (0.019% vs. 0.18% of the NPs injected to the mice). Similarly, approximately 360% more HA-coated Au NPs were detected in corneal endothelium cells (0.039 vs. 0.18%), and finally, 700% (0.047 vs. 0.38%) more HA-Au NPs were detected in the corneal epithelial cells.

As a result of intravenous injections, 20 nm Au NPs not only reached the eye and crossed the blood-retinal barrier, but also were able to reach all the way to the cornea. By conjugating Au NPs with HS-HA, we were able to increase the delivered dose to the cornea and retina by approximately 14% and almost 100%, respectively. The amounts of uncoated and coated Au NPs that reached the retina peaked at 20 and 25 minutes, respectively. The amounts of uncoated and coated Au NPs remaining in the retina at the end of 24 hours were 8.55% and 12.06%, respectively.

Without and with HS-HA coating, the Au NP amounts reaching the cornea peaked at 15 minutes and 60 minutes, respectively. For delivery to the cornea, the HA coating significantly retarded the time for the NPs to reach their maximum concentration; however, this effect was not apparent for the delivery of NPs to the retina. By the end of 24 hours, the amounts of nascent and HS-S-Au NPs remaining in the cornea were 3.74% and 17.10%, respectively.

Following intravenous injections, both the ERG analysis and histology analysis showed no apparent toxicity induced by either Au NPs or HA-S-Au NPs at this injection dose (0.05 mg/ml).

Ex vivo porcine eye images showed that intravitreally injected nCDs could effectively diffuse through the vitreous to the cornea, and *post-mortem* whole-body mouse images also demonstrated that the nCDs provide suitably strong signals for bioimaging applications.

6.5 References

1. Aldrich, S. (2018). "Commercially available graphene quantum dots." Retrieved 2018, from <https://www.sigmaaldrich.com/>.
2. Armington, C. L. (1974). The electroretinogram by John C. Armington, Elsevier Science & Technology Books.
3. Bakri, S. J., J. S. Pulido, P. Mukherjee, R. J. Marler and D. Mukhopadhyay (2008). "Absence of histologic retinal toxicity of intravitreal nanogold in a rabbit model." Retina **28**(1): 147-149.
4. Ban, N., Y. Ozawa, H. Osada, J. B. Lin, E. Toda, M. Watanabe, K. Yuki, S. Kubota, R. S. Apte and K. Tsubota (2017). "Neuroprotective role of retinal sirt3 against acute photo-stress." Aging and Mechanisms of Disease **3**(1): 19.
5. Boisselier, E. and D. Astruc (2009). "Gold nanoparticles in nanomedicine: Preparations, imaging, diagnostics, therapies and toxicity." Chemical Society Reviews **38**(6): 1759-1782.
6. Bourges, J. L., S. E. Gautier, F. Delie, R. A. Bejjani, J. C. Jeanny, R. Gurny, D. BenEzra and F. F. Behar-Cohen (2003). "Ocular drug delivery targeting the retina and retinal pigment epithelium using polylactide nanoparticles." Investigative Ophthalmology & Visual Science **44**(8): 3562-3569.
7. Cho, W. K., S. Kang, H. Choi and C. R. Rho (2015). "Topically administered gold nanoparticles inhibit experimental corneal neovascularization in mice." Cornea **34**(4): 456-459.
8. Choonara, Y. E., V. Pillay, M. P. Danckwerts, T. R. Carmichael and L. C. du Toit (2010). "A review of implantable intravitreal drug delivery technologies for the treatment of posterior segment eye diseases." Journal of Pharmaceutical Sciences **99**(5): 2219-2239.
9. Christofridis, J. B., S. Chang, A. Jiang, J. Wang and C. M. Cebulla (2012). "Intravitreal devices for the treatment of vitreous inflammation." Mediators of Inflammation **2012**: 126463-126471.
10. Contreras-Ruiz, L., M. de la Fuente, J. E. Parraga, A. Lopez-Garcia, I. Fernandez, B. Seijo, A. Sanchez, M. Calonge and Y. Diebold (2011). "Intracellular trafficking of hyaluronic acid-chitosan oligomer-based nanoparticles in cultured human ocular surface cells." Molecular Vision **17**(34-35): 279-290.
11. Diebold, Y. and M. Calonge (2010). "Applications of nanoparticles in ophthalmology." Progress in Retinal and Eye Research **29**(6): 596-609.
12. Dong, X. W., L. M. Wei, Y. J. Su, Z. L. Li, H. J. Geng, C. Yang and Y. F. Zhang (2015). "Efficient long lifetime room temperature phosphorescence of carbon dots in a potash alum matrix." Journal of Materials Chemistry C **3**(12): 2798-2801.
13. Einthoven, W. and W. A. Jolly (1908). "The form and magnitude of the electrical response of the eye to stimulation by light at various intensities." Quarterly Journal of Experimental Physiology **1**: 373-416.
14. Ferenchak, K., R. Duval, J. A. Cohen and M. W. MacCumber (2014). "Intravitreal bevacizumab for postoperative recurrent vitreous hemorrhage after vitrectomy for proliferative diabetic retinopathy." Retina **34**(6): 1177-1181.
15. Gabriele Sandrian, M., G. Wollstein, J. S. Schuman, R. A. Bilonick, Y. Ling, H. Ishikawa, L. Kagemann and K. C. McKenna (2012). "Inflammatory response to intravitreal injection of gold nanorods." British Journal of Ophthalmology **96**(12): 1522-1529.
16. Gan, L., J. Wang, Y. Zhao, D. Chen, C. Zhu, J. Liu and Y. Gan (2013). "Hyaluronan-modified core-shell liponanoparticles targeting cd44-positive retinal pigment epithelium cells via intravitreal injection." Biomaterials **34**(24): 5978-5987.

17. Gan, Z. X., H. Xu and Y. L. Hao (2016). "Mechanism for excitation-dependent photoluminescence from graphene quantum dots and other graphene oxide derivatives: Consensus, debates and challenges." Nanoscale **8**(15): 7794-7807.
18. Glucksam-Galnoy, Y., T. Zor and R. Margalit (2012). "Hyaluronan-modified and regular multilamellar liposomes provide sub-cellular targeting to macrophages, without eliciting a pro-inflammatory response." Journal of Controlled Release **160**(2): 388-393.
19. Hans, M. L. and A. M. Lowman (2002). "Biodegradable nanoparticles for drug delivery and targeting." Current Opinion in Solid State & Materials Science **6**(4): 319-327.
20. Hayashi, A., A. Naseri, M. E. Pennesi and E. de Juan, Jr. (2009). "Subretinal delivery of immunoglobulin g with gold nanoparticles in the rabbit eye." Japon Journal of Ophthalmology **53**(3): 249-256.
21. Hirn, S., M. Semmler-Behnke, C. Schleh, A. Wenk, J. Lipka, M. Schaffler, S. Takenaka, W. Moller, G. Schmid, U. Simon and W. G. Kreyling (2011). "Particle size-dependent and surface charge-dependent biodistribution of gold nanoparticles after intravenous administration." European Journal of Pharmaceutics and Biopharmaceutics **77**(3): 407-416.
22. Huang, H. S. and J. F. Hainfeld (2013). "Intravenous magnetic nanoparticle cancer hyperthermia." International Journal of Nanomedicine **8**: 2521.
23. Jaakko, M. and R. Plonsey (1995). "Bioelectromagnetism - principles and applications of bioelectric and biomagnetic fields." Oxford University Press pp: 583-584.
24. Jeong Hun, K., K. Jin Hyoung, K. Kyu-Won, K. Myung Hun and Y. Young Suk (2009). "Intravenously administered gold nanoparticles pass through the blood-retinal barrier depending on the particle size, and induce no retinal toxicity." Nanotechnology **20**(50): 505101 -505101.
25. Jin Hyoung, K., K. Myung Hun, J. Dong Hyun, Y. Young Suk, L. Tae Geol and K. Jeong Hun (2011). "The inhibition of retinal neovascularization by gold nanoparticles via suppression of vegfr-2 activation." Biomaterials **32**(7): 1865-1871.
26. Jo, D. H., J. H. Kim and T. G. Lee (2015). "Size, surface charge, and shape determine therapeutic effects of nanoparticles on brain and retinal diseases." Nanomedicine-Nanotechnology Biology and Medicine **11**(7): 1603-1611.
27. Johnston, H. J., G. Hutchison, F. M. Christensen, S. Peters, S. Hankin and V. Stone (2010). "A review of the in vivo and in vitro toxicity of silver and gold particulates: Particle attributes and biological mechanisms responsible for the observed toxicity." Critical Reviews in Toxicology **40**(4): 328-346.
28. Karakocak, B. B., J. Liang, P. Biswas and N. Ravi (2018). "Hyaluronate coating enhances the delivery and biocompatibility of gold nanoparticles." Carbohydrate Polymers **186**: 243-251.
29. Khlebtsov, N. and L. Dykman (2011). "Biodistribution and toxicity of engineered gold nanoparticles: A review of in vitro and in vivo studies." Chemical Society Reviews **40**(3): 1647-1671.
30. Kim, J. H., J. A. Park, S. W. Lee, W. J. Kim, Y. S. Yu and K. W. Kim (2006). "Blood-neural barrier: Intercellular communication at glio-vascular interface." Journal of Biochemistry and Molecular Biology **39**(4): 339-345.
31. Kompella, U., A. Amrite, R. Ravi and S. Durazo (2013). "Nanomedicines for back of the eye drug delivery, gene delivery, and imaging." Progress in Retinal and Eye Research **36**: 172-198.
32. Lee, H., K. Lee, I. K. Kim and T. G. Park (2008). "Synthesis, characterization, and in vivo diagnostic applications of hyaluronic acid immobilized gold nanoprobe." Biomaterials **29**(35): 4709-4718.

33. Lin, L.-Y., S. Kavadiya, B. B. Karakocak, Y. Nie, R. Raliya, S. T. Wang, M. Y. Berezin and P. Biswas (2018). "ZnO 1- x/carbon dots composite hollow spheres: Facile aerosol synthesis and superior co 2 photoreduction under uv, visible and near-infrared irradiation." Applied Catalysis B: Environmental.
34. Lin, W. J., W.-C. Lee and M.-J. Shieh (2017). "Hyaluronic acid conjugated micelles possessing cd44 targeting potential for gene delivery." Carbohydrate Polymers **155**: 101-108.
35. Linlin, Z., K. Tae-Hyun, K. Hae-Won, A. Jin-Chul and K. So Yeon (2015). "Surface-enhanced raman scattering (sers)-active gold nanochains for multiplex detection and photodynamic therapy of cancer." Acta Biomaterialia **20**: 155-164.
36. Liu, H., Y. Zhang, J. H. Liu, P. Hou, J. Zhou and C. Z. Huang (2017). "Preparation of nitrogen-doped carbon dots with high quantum yield from bombyx mori silk for fe(iii) ions detection." RSC Advances **7**(80): 50584-50590.
37. Liu, J. J., D. W. Li, K. Zhang, M. X. Yang, H. C. Sun and B. Yang (2018). "One-step hydrothermal synthesis of nitrogen-doped conjugated carbonized polymer dots with 31% efficient red emission for in vivo imaging." Small **14**(15): 10.
38. London, A., I. Benhar and M. Schwartz (2013). "The retina as a window to the brain-from eye research to cns disorders." Nature Reviews Neurology **9**(1): 44-53.
39. Lowe, S., N. M. O'Brien-Simpson and L. A. Connal (2015). "Antibiofouling polymer interfaces: Poly(ethylene glycol) and other promising candidates." Polymer Chemistry **6**(2): 198-212.
40. Manson, J., D. Kumar, B. J. Meenan and D. Dixon (2011). "Polyethylene glycol functionalized gold nanoparticles: The influence of capping density on stability in various media." Gold Bulletin **44**(2): 99-105.
41. Miao, R., S. F. Zhang, J. F. Liu and Y. Fang (2017). "Zinc-reduced cqds with highly improved stability, enhanced fluorescence, and refined solid-state applications." Chemistry of Materials **29**(14): 5957-5964.
42. Mohan, R. R., J. C. K. Tovey, A. Sharma and A. Tandon (2012). "Gene therapy in the cornea: 2005-present." Progress in Retinal and Eye Research **31**(1): 43-64.
43. Pan, Y., H. Ding, L. Qin, X. Zhao, J. Cai and B. Du (2013). "Gold nanoparticles induce nanostructural reorganization of vegfr2 to repress angiogenesis." Journal of Biomedical Nanotechnology **9**(10): 1746-1756.
44. Penn, R. D. and W. A. Hagins (1969). "Signal transmission along retinal rods and origin of electroretinographic a-wave." Nature **223**(5202): 201-&.
45. Petros, R. A. and J. M. DeSimone (2010). "Strategies in the design of nanoparticles for therapeutic applications." Nature Reviews Drug Discovery **9**(8): 615-627.
46. Runkle, E. A. and D. A. Antonetti (2011). "The blood-retinal barrier: Structure and functional significance." Methods in Molecular Biology **686**: 133-148.
47. Santhanam, S., J. Liang, R. Baid and N. Ravi (2015). "Investigating thiol-modification on hyaluronan via carbodiimide chemistry using response surface methodology." Journal of Biomedical Materials Research Part A **103**(7): 2300-2308.
48. Skala, M. C., M. J. Crow, A. Wax and J. A. Izatt (2013). "Three-dimensional molecular imaging with photothermal optical coherence tomography." Methods in Molecular Biology **1026**: 85-92.
49. Sonavane, G., K. Tomoda and K. Makino (2008). "Biodistribution of colloidal gold nanoparticles after intravenous administration: Effect of particle size." Colloids and Surfaces B: Biointerfaces **66**(2): 274-280.
50. Steinber.Rh, R. Schmidt and K. T. Brown (1970). "Intracellular responses to light from cat pigment epithelium - origin of electroretinogram c-wave." Nature **227**(5259): 728-730.

51. Stockton, R. A. and M. M. Slaughter (1989). "B-wave of the electroretinogram - a reflection of on bipolar cell-activity." Journal of General Physiology **93**(1): 101-122.
52. Su, S., X. Zuo, D. Pan, H. Pei, L. Wang, C. Fan and W. Huang (2013). "Design and applications of gold nanoparticle conjugates by exploiting biomolecule-gold nanoparticle interactions." Nanoscale **5**(7): 2589-2599.
53. Terentyuk, G. S., G. N. Maslyakova, L. V. Suleymanova, B. N. Khlebtsov, B. Y. Kogan, G. G. Akchurin, A. V. Shantrocha, I. L. Maksimova, N. G. Khlebtsov and V. V. Tuchin (2009). "Circulation and distribution of gold nanoparticles and induced alterations of tissue morphology at intravenous particle delivery." Journal of Biophotonics **2**(5): 292-302.
54. Wang, J., G. Zhang, Q. Li, H. Jiang, C. Liu, C. Amatore and X. Wang (2013). "In vivo self-bio-imaging of tumors through in situ biosynthesized fluorescent gold nanoclusters." Scientific Reports **3**: 1157.
55. Williams, K. A. and S. Klebe (2012). "Gene therapy for corneal dystrophies and disease, where are we?" Current Opinion in Ophthalmology **23**(4): 276-279.
56. Wisard, J., M. A. Chrenek, C. Wright, N. Dalal, M. T. Pardue, J. H. Boatright and J. M. Nickerson (2010). "Non-contact measurement of linear external dimensions of the mouse eye." Journal of Neuroscience Methods **187**(2): 156-166.
57. Yanai, A., U. O. Hafeli, A. L. Metcalfe, P. Soema, L. Addo, C. Y. Gregory-Evans, K. Po, X. Shan, O. L. Moritz and K. Gregory-Evans (2012). "Focused magnetic stem cell targeting to the retina using superparamagnetic iron oxide nanoparticles." Cell Transplant **21**(6): 1137-1148.
58. Yilmaz, G., B. Demir, S. Timur and C. R. Becer (2016). "Poly(methacrylic acid)-coated gold nanoparticles: Functional platforms for theranostic applications." Biomacromolecules **17**(9): 2901-2911.
59. Zhang, L., M. C. Anderson and C.-Y. Liu (2017). "The role of corneal stroma: A potential nutritional source for the cornea." Journal of Nature and Science **3**(8): 1-5.
60. Zhang, Y., Y. J. Shen, X. Y. Teng, M. Q. Yan, H. Bi and P. C. Morais (2015). "Mitochondria-targeting nanoplatfrom with fluorescent carbon dots for long time imaging and magnetic field-enhanced cellular uptake." ACS Applied Materials & Interfaces **7**(19): 10201-10212.
61. Zhou, C., S. Yang, J. Liu, M. Yu and J. Zheng (2013). "Luminescent gold nanoparticles: A new class of nanoprobes for biomedical imaging." Experimental Biology and Medicine **238**(11): 1199-1209.

Chapter 7: Conclusions and Suggestions for Future Work

The results of this chapter have been partially compiled in Karakoçak, B. B., Biswas, P., and Ravi N. (2018). Applications of Gold Nanoparticles in Ophthalmology. Prog. Retin. Eye Res. In preparation.

7.1 Conclusions

This section summarizes the major findings of this dissertation.

7.1.1 Assessing the biocompatibility of Au NPs with retinal cells and providing a solution for their toxicity (Chapters 2 and 3)

While Au NPs are widely explored in various biomedical fields, including ophthalmology, their toxicity to ocular cells has not been investigated. The first part of this dissertation (Chapter 2) assessed the *in-vitro* toxicity of different sizes and shapes of Au NPs with a retinal pigment epithelial cell line. The results showed that the toxicity is dependent on both the size and shape of the nanoparticles. Au nanocubes were not detected in the cells, so their toxicity, if any, could not be assessed. Au nanorods and nanospheres did enter the cells, although nanospheres larger than 50 nm could not enter. The critical observation, however, is that for particles small enough to enter, when the concentration is expressed as a function of surface area per unit volume, size has no effect on consequent toxicity. For similar surface area concentrations, spherical Au NPs in the range of 5-30 nm had almost the same biocompatibility. The observed toxicity was a result of surface interactions inside the cell, which are directly correlated to the surface area concentration of the NPs.

The toxicity of Au NPs arises from ROS activity, which was shown to be correlated to the total available surface area (Pan et al. 2007, Jiang et al. 2008). Hyaluronic acid (HA), as discussed in Chapter 3, is a free radical quencher that is natural and consequently biocompatible (Balogh et al. 2003). We sought a way to mitigate the toxicity of Au NPs by coating them with end-thiolated hyaluronate (HS-HA). The homogenous coating was facilitated by the thiol group's affinity to the Au surface. We successfully coated different sizes of Au NPs (5, 10, 20, 50, and 100 nm) with HS-HA and both verified and quantified the coating amount with thermal gravimetric and total organic carbon analysis. As expected, the HS-HA coating significantly enhanced the biocompatibility of Au NPs; unexpectedly, the

coating also considerably improved the internalization of larger Au NPs (50 and 100 nm), which in their nascent form could not enter the cell. HA acted as a Trojan horse to carry in larger Au NPs without triggering apoptosis and generating ROS. The outcomes of this study could be valuable in treating inflamed, proliferating, or cancer cells that express CD44 receptors.

7.1.2 Creating biocompatible red-emissive carbon dots for use in ophthalmology (Chapters 4 and 5)

For the first time, we developed and optimized a facile and economical synthesis of deep red to near-infrared (600-700 nm) emissive nitrogen-doped CDs (nCDs) that uses simple dialysis to isolate the product (Chapter 4). A central-composite design response surface methodology (CCD-RSM) design was utilized (Stat-Ease, Design-Expert[®] software, version 9.0) to optimize the effect of three factors in the synthesis of nCDs – the molar ratio of amine to acid, the duration of pyrolysis (microwave exposure time), and the concentration of the reactants. The characterization results respectively showed that as the amine to acid ratio increased, both the MW and size of the nCDs increased. Based on high-resolution XPS analysis, the formation of C–N bonds and the presence of pyrrolic N content appear to be keys to creating red-emissive nCDs. Both of these critical parameters reached a maximum at an amine/acid ratio of 2.0. We hypothesize that, based on the structure of citric acid, one of the most probable products (or moieties) contributing to deep-red-emissivity of nCDs could be *N,N'*-substituted-pyrrolo[2,3-*b*]pyrrole. The quantum yield of the nCDs was found to be 15% in DI water. Next, a detailed cytotoxicity analysis found that up to 0.6 mg/ml exposure concentration, the nCDs induced no apparent toxicity. However, there is still motivation for enhancing their biocompatibility because repetitive injections may be required for high-resolution imaging.

Using the HA conjugation technique for enhancing the biocompatibility and intracellular concentration of Au NPs, we conjugated CDs with HA by a carbodiimide coupling of the amines on CDs and the carboxylic acids on HAs (Chapter 5). Confocal imaging analysis revealed that the nCDs and their conjugates fluoresced at different wavelengths, depending upon the excitation wavelength without a loss in the emitted signal. Three different cell lines were exposed to nCDs and HA-nCDs. Confocal microscopy images showed enhanced internalization of HA-nCDs, which was facilitated by CD44 receptors. Although the intracellular concentration was increased, a biocompatibility assessment revealed that ROS production was reduced by a factor of two, while apoptosis initiation was decreased by more than an order of magnitude. HA is known to be a natural antioxidant. When carbon dots induce ROS generation, the HA acts as a ROS scavenger and reduces the intracellular ROS concentration, thus reducing the incidence of apoptosis. These observations suggest the use of HA as a conjugate carrier for CDs into CD44 rich cells.

The formation of C–N bonds and presence of pyrrolic nitrogen on the surface of the nCDs are critical parameters in creating red-emissive carbon dots. In the complementary work, we found that HA conjugation not only enhances the payload delivered to the cells but also significantly decreases the signs of toxicity. This work also yielded a recipe for creating biocompatible red-emissive CDs, ruling out the effects of pyrolysis time and citric acid concentration and emphasizing the amount of nitrogen.

7.1.3 Demonstration of the usefulness of gold nanoparticles and carbon dots *in-vivo* (Chapter 6)

Upon completing the *in-vitro* toxicity assessment of both nanomaterial products, we conducted *in-vivo* studies (Chapter 6). *In-vivo* studies are necessary to assess the ocular toxicity of nanoparticles, since the response of the target cell/organ may be influenced by

interactions between different types of cells; additionally, defense mechanisms might be different at the organ level.

Prior to any *in-vivo* tests, a preliminary *in-vitro* study tested the ability of Au NPs to cross the tight junctions between retinal pigment epithelial cells. Transwell® permeable supports were used to simulate the blood-retinal barrier (BRB). The results showed that 20 nm Au nanospheres successfully crossed the permeable supports covered with confluent retinal pigment epithelial cells. Based on this finding, we used 20 nm Au nanospheres in the following experiments and coated them with HS-HA. We used intravitreal and intravenous injections to deliver Au NPs in a C57BL/6 mouse model.

Following the intravitreal injections, histology and confocal imaging analysis revealed retinal detachment. Therefore, we quantified the amount of Au NPs with and without the HA coating only in the cornea. The HA coating revealed a almost one-fold increase in the amount of Au NPs detected in all three layers of the cornea: the corneal endothelium, stroma, and epithelium. For both nascent and coated Au NPs, no sign of toxicity was observed in the entire cornea. Next, we injected both nascent and coated Au NPs intravenously through the lateral saphenous vein of C57BL/6 mice. Using confocal imaging, we quantified the amount of Au NPs as a function of time in all layers of the retina and cornea. The Au NPs reached the eye in less than 5 minutes and achieved a maximum concentration within approximately 20 minutes in the retina. On the other hand, the amount of HA-S-Au NPs in the retina peaked at 25th minute. Due to the enhanced permeabilization and retention (EPR) effect of NPs, 8.55 and 12.06% of the uncoated and HA-coated Au NPs that reached the retina remained after 24 hours. The thicknesses of the inner and outer retina were measured and compared among the control animals. Although the thicknesses of the inner and outer retina were highly variable from animal to animal, there were no signs of toxicity for both uncoated and coated Au NPs.

For nitrogen-doped carbon dots (nCDs), we used the best performing nCDs with the highest amine to acid ratio, 2.0. The nitrogen-coated carbon dots, whose sizes are typically below 5 nm, were injected into porcine eye globes and post-mortem C57BL/6 mice. *Ex-vivo* porcine eye images showed that 50 μ L of intravitreally injected nCDs could efficiently diffuse through the vitreous to the cornea. *Post-mortem* whole-body mouse images also demonstrated that 100 μ L of nCDs which were injected subcutaneously on the dorsal side of the mice, was sufficient to generate a strong signal upon excitation by Bruker spectral FX small animal imager built-in laser at a wavelength of 600 nm. This result proved that the nCDs created in this study are suitable for bioimaging applications.

7.2 Suggestions for Future Work

7.2.1 Selecting a disease model to demonstrate the usefulness of the Au NPs as targeted drug delivery agents

Angiogenesis, the growth of new capillaries from blood vessels, and vascular maintenance are essential for proper organ development and functioning, particularly in the metabolically demanding eye, a part of the CNS. The mouse retina is a direct extension of the brain and serves as a useful model system for studying angiogenesis in the CNS because the mouse retina vascularizes after birth within a couple months.

Neovascularization, the natural formation of new blood vessels in response to pathological stimuli, is a typical characteristic of vision-threatening retinal diseases. Examples include proliferative diabetic retinopathy (PDR) and neovascular AMD, which are the leading causes of blindness in the Western world (Farjo and Ma 2010, Honda et al. 2013, Kompella et al. 2013). Other examples include retinopathy of prematurity (ROP), retinal vein obstruction (RVO), pathogenic myopia, uveitis, and neovascular glaucoma (Williams and Klebe 2012, Monika et al. 2013). In these diseases, intraretinal or choroidal neovascularization is initiated by ischemia, a potent trigger for the local production of angiogenic factors, which induce the

growth of new capillaries from an existing vessel (Folkman and Shing 1992, Carmeliet 2003, Usui et al. 2015). As stated in this dissertation, Au NPs are inherently anti-angiogenic, which makes them potential treatment agents for angiogenesis-related ocular diseases, even without carrying an additional drug. On the other hand, it has been shown that Au NPs can also be used to image blood vessels with optical tomography (OCT), because certain shapes, such as Au nanorods, depending on their aspect ratio, can be excited in the near-infrared region (Lapierre-Landry et al. 2017). Hence, it would be valuable to study how inherently anti-angiogenic Au NPs could effectively eliminate new blood vessel formation. Specifically, Au nanorods with high aspect ratios, along with Au nanospheres, could be used to image the angiogenic progress in real-time, if they can be excited in the near-infrared region. A fundamental study of the inhibition mechanism, using at least two sizes and shapes of Au nanoparticles, could be conducted in a similar manner to that described in Chapter 6, such a fundamental study would be a prerequisite to a clinical trial.

7.2.2 Controlled dose-dependent *in-vivo* studies

In our *in vivo* work, we found that the dose delivered to the retina via intravenous injections was less than 5%, and thus a design to increase the delivered dose is needed. In chapter 5, the transport through the retinal layers was studied; however, only one injected dose was tested. A dose-dependent study would help to identify the critical dose for different disease models without causing toxicity. The levels of administered and delivered doses during the experiments in Chapter 5 suggest that the administered dose can be increased further, because both coated and uncoated Au NPs did not induce toxicity at 0.05 mg/ml. Furthermore, it was observed that the NPs peak in the retina at the 20th minute and then gradually decrease. By the end of 24 hours, the amount remained was still low (8.55% of the peak concentration in the retina), therefore a controlled release methodology could also be proposed to prevent

repetitive invasive injections. For example, engineered nanoparticles could be designed to maximize the delivered dose in the eye.

7.2.3 Long-term toxicity analysis of engineered gold nanoparticles as a prerequisite to clinical trials

The safety profile of Au NPs remains largely undefined. Gold, a chemically inert material, is generally considered biocompatible at low doses and has been used in some routine clinical practices, such as in treating rheumatoid arthritis, for many years (Ellman et al. 1940). Also, there is an ongoing clinical trial on using PEG-coated silica-gold nanoshells for near-infrared facilitated thermal ablation (Anselmo and Mitragotri 2016). Several studies have reported no significant short-term toxicity of Au NPs (1 day to 3 months) (Connor et al. 2005, Chen et al. 2013, Axiak-Bechtel et al. 2014, You et al. 2014). On the other hand, other studies have reported that at the cellular level, Au NPs induce toxicity by causing actin stress (Pernodet et al. 2006) and initiating apoptosis (Cho et al. 2009). At the organ level, Au NPs were shown to cause inflammation in the liver (Sadauskas et al. 2009). To better understand the combined cellular responses to NP exposure, systematic long-term *in-vivo* studies are required. *In-vitro* studies and short-term *in-vivo* studies are necessary to provide data for a proof of concept. Subsequently, in order to take it to the next level, clinical trials, long-term *in-vivo* tests are mandatory.

Based on their anatomical and physiological similarities with humans, domestic pigs (*Sus scrofa*) and various minipig breeds are considered important animal species in translational research (Gutierrez et al. 2015). For example, the Göttingen minipig (Bode et al. 2010), the most widely used experimental minipig breed, shares physiological similarities with humans, in particular with regards to the cardiovascular, urinary, integumentary, and digestive systems, as well as the size of the eye (3/4 scale compared to human eye) (Vezina 2018).

These features, along with the lower mature body weight of minipigs and their earlier sexual

maturity compared to other nonrodent species, have led to the increasing use of minipigs as species in preclinical safety testing. Across various marketed drug products, safety studies with minipigs have shown good accordance between the effects seen in this non-clinical model and clinical outcomes in patients (Ganderup 2012). Future work could focus on developing systematic long-term (6 months and beyond) *in-vivo* studies using Göttingen minipigs to ensure the safe use of Au NPs.

7.2.4 Synthesis of red-emissive carbon dots with ultrahigh quantum yield

Quantum yield, the ratio of the photons absorbed to photons emitted, is an essential parameter in determining the usefulness of a fluorescent material. As discussed earlier, fluorescent carbon dots with high quantum yields have emerged as a new class of phosphors for various applications. Specifically, for bioimaging applications, synthesis of red-emissive, thermally and photocatalytically stable, biocompatible carbon dots with high quantum yield is highly desired. Although blue and green emissive CDs with high QYs have been obtained (Bourlinos et al. 2008, Zhu et al. 2009, Wang et al. 2010, Bourlinos et al. 2012, Sun et al. 2012, Zhu et al. 2013, Hola et al. 2014, Sun et al. 2014, Xu et al. 2014, Yang et al. 2015), the synthesis of red emissive CDs with high QYs still stands as a significant challenge. The larger size of the sp^2 π -conjugation domains makes them more susceptible to defect formation and more vulnerable to environmental perturbation. According to the literature (Sun et al. 2012, Sun et al. 2016, Wang et al. 2017) and our own study, the intense absorption band of the red-CDs could be tentatively ascribed to the $n \rightarrow \pi^*$ transition of π systems containing C–N/C=N or C–O structures. However, the obtained quantum yields are relatively lower than the theoretical maximum, so a more in-depth study is still required to clarify this issue and increase the quantum yield further. Parameters that may contribute to the quantum yield have not been thoroughly evaluated, specially for creating red fluorescence emission. Additionally, concerns have been raised regarding the validity of the quantum yield measurements for red

fluorescence, especially in such a minuscule size range (3-5 nm), where the dots photoresponse may be very unstable.

Reduction with NaBH_4 has been introduced as one strategy to increase the QY of CDs (Zheng et al. 2011, Zhang et al. 2015). Reducing the carbon dots led to a decrease in the number of carbonyl groups but increased hydroxyl related defects, and hydroxy carbon has been shown to increase the quantum yield of CDs in other studies (Liu et al. 2017, Liu et al. 2018). Zn conjugation can also potentially increase the fluorescence intensity of carbon dots, but the excitation wavelength is shifted towards the blue region (Miao et al. 2017). Taken together, a method to promote hydroxy carbon and, as we identified in this thesis, to increase the pyrrolic nitrogen amount on the surface of the CDs could create highly efficient red-emissive carbon dots.

Future work could focus on the design and evaluation of methods for creating red-emissive carbon dots with high quantum yield. Zn involvement, the use of different nitrogen sources to promote C–N bonding and hydroxy carbon formation on the surface of CDs, and the use of reducing methods could all be further investigated. Some preliminary work on evaluating quantum yield measurements of red emissive carbon dots is discussed in Appendix V.

7.3. References

1. Anselmo, A. C. and S. Mitragotri (2016). "Nanoparticles in the clinic." Bioengineering & Translational Medicine **1**(1): 10-29.
2. Axiak-Bechtel, A. M., A. Upendran, J. C. Lattimer, J. Kelsey, C. S. Cutler, K. A. Selting, J. N. Bryan, C. J. Henry, E. Boote, D. J. Tate, M. E. Bryan, K. V. Katti and R. Kannan (2014). "Gum arabic-coated radioactive gold nanoparticles cause no short-term local or systemic toxicity in the clinically relevant canine model of prostate cancer." International Journal of Nanomedicine **9**: 5001-5011.
3. Balogh, G. T., J. Illes, Z. Szekely, E. Forrai and A. Gere (2003). "Effect of different metal ions on the oxidative damage and antioxidant capacity of hyaluronic acid." Archives of Biochemistry and Biophysics **410**(1): 76-82.
4. Bode, G., P. Clausing, F. Gervais, J. Loegsted, J. Luft, V. Nogues and J. Sims (2010). "The utility of the minipig as an animal model in regulatory toxicology." Journal of Pharmacological and Toxicological Methods **62**(3): 196-220.
5. Bourlinos, A. B., A. Stassinopoulos, D. Anglos, R. Zboril, V. Georgakilas and E. P. Giannelis (2008). "Photoluminescent carbogenic dots." Chemistry of Materials **20**(14): 4539-4541.
6. Bourlinos, A. B., R. Zboril, J. Petr, A. Bakandritsos, M. Krysmann and E. P. Giannelis (2012). "Luminescent surface quaternized carbon dots." Chemistry of Materials **24**(1): 6-8.
7. Carmeliet, P. (2003). "Angiogenesis in health and disease." Nature Medicine **9**(6): 653-660.
8. Chen, H., A. Dorrigan, S. Saad, D. J. Hare, M. B. Cortie and S. M. Valenzuela (2013). "In vivo study of spherical gold nanoparticles: Inflammatory effects and distribution in mice." PLoS ONE **8**(2): e58208.
9. Cho, Y., S. Challa, D. Moquin, R. Genga, T. D. Ray, M. Guildford and F. K.-M. Chan (2009). "Phosphorylation-driven assembly of the rip1-rip3 complex regulates programmed necrosis and virus-induced inflammation." Cell **137**(6): 1112-1123.
10. Connor, E. E., J. Mwamuka, A. Gole, C. J. Murphy and M. D. Wyatt (2005). "Gold nanoparticles are taken up by human cells but do not cause acute cytotoxicity." Small **1**(3): 325-327.
11. Ellman, P., J. S. Lawrence and G. P. Thorold (1940). "Gold therapy in rheumatoid arthritis." British Medical Journal **2**(4157): 314.
12. Farjo, K. M. and J.-X. Ma (2010). "The potential of nanomedicine therapies to treat neovascular disease in the retina." Journal of Angiogenesis Research **2**: 21.
13. Folkman, J. and Y. Shing (1992). "Angiogenesis." Journal of Biological Chemistry **267**(16): 10931-10934.
14. Ganderup, N. C. (2012). "Adverse responses to drugs in man: Critical comparison of reported toxicological findings in minipigs and humans." The Minipig in Biomedical Research: 573-594.
15. Gutierrez, K., N. Dicks, W. G. Glanzner, L. B. Agellon and V. Bordignon (2015). "Efficacy of the porcine species in biomedical research." Frontiers in Genetics **6**: 293: 1-9.
16. Hola, K., Y. Zhang, Y. Wang, E. P. Giannelis, R. Zboril and A. L. Rogach (2014). "Carbon dots-emerging light emitters for bioimaging, cancer therapy and optoelectronics." Nano Today **9**(5): 590-603.
17. Honda, M., T. Asai, N. Oku, Y. Araki, M. Tanaka and N. Ebihara (2013). "Liposomes and nanotechnology in drug development: Focus on ocular targets." International Journal of Nanomedicine **8**: 495-504.

18. Jiang, J., G. Oberdorster, A. Elder, R. Gelein, P. Mercer and P. Biswas (2008). "Does nanoparticle activity depend upon size and crystal phase?" Nanotoxicology **2**(1): 33-42.
19. Kompella, U., A. Amrite, R. Ravi and S. Durazo (2013). "Nanomedicines for back of the eye drug delivery, gene delivery, and imaging." Progress in Retinal and Eye Research **36**: 172-198.
20. Lapiere-Landry, M., A. Y. Gordon, J. S. Penn and M. C. Skala (2017). "In vivo photothermal optical coherence tomography of endogenous and exogenous contrast agents in the eye." Scientific Reports **7**: 9.
21. Liu, H., Y. Zhang, J. H. Liu, P. Hou, J. Zhou and C. Z. Huang (2017). "Preparation of nitrogen-doped carbon dots with high quantum yield from bombyx mori silk for fe(iii) ions detection." Rsc Advances **7**(80): 50584-50590.
22. Liu, J. J., D. W. Li, K. Zhang, M. X. Yang, H. C. Sun and B. Yang (2018). "One-step hydrothermal synthesis of nitrogen-doped conjugated carbonized polymer dots with 31% efficient red emission for in vivo imaging." Small **14**(15): 10.
23. Miao, R., S. F. Zhang, J. F. Liu and Y. Fang (2017). "Zinc-reduced cqds with highly improved stability, enhanced fluorescence, and refined solid-state applications." Chemistry of Materials **29**(14): 5957-5964.
24. Monika, M., K.-K. Katarzyna and K. Leszek (2013). "Present-day conservative treatment retinopathy of prematurity." Klinika Oczna **115**(1): 65-68.
25. Pan, Y., S. Neuss, A. Leifert, M. Fischler, F. Wen, U. Simon, G. Schmid, W. Brandau and W. Jahnen-Dechent (2007). "Size-dependent cytotoxicity of gold nanoparticles." Small **3**(11): 1941-1949.
26. Pernodet, N., X. Fang, Y. Sun, A. Bakhtina, A. Ramakrishnan, J. Sokolov, A. Ulman and M. Rafailovich (2006). "Adverse effects of citrate/gold nanoparticles on human dermal fibroblasts." Small **2**(6): 766-773.
27. Sadauskas, E., G. Danscher, M. Stoltenberg, U. Vogel, A. Larsen and H. Wallin (2009). "Protracted elimination of gold nanoparticles from mouse liver." Nanomedicine: Nanotechnology, Biology and Medicine **5**(2): 162-169.
28. Sun, L., L. Wang, C. G. Tian, T. X. Tan, Y. Xie, K. Y. Shi, M. T. Li and H. G. Fu (2012). "Nitrogen-doped graphene with high nitrogen level via a one-step hydrothermal reaction of graphene oxide with urea for superior capacitive energy storage." RSC Advances **2**(10): 4498-4506.
29. Sun, M. Y., S. N. Qu, Z. D. Hao, W. Y. Ji, P. T. Jing, H. Zhang, L. G. Zhang, J. L. Zhao and D. Z. Shen (2014). "Towards efficient solid-state photoluminescence based on carbon-nanodots and starch composites." Nanoscale **6**(21): 13076-13081.
30. Sun, S., L. Zhang, K. Jiang, A. Wu and H. Lin (2016). "Toward high-efficient red emissive carbon dots: Facile preparation, unique properties, and applications as multifunctional theranostic agents." Chemistry of Materials **28**(23): 8659-8668.
31. Usui, Y., P. D. Westenskow, S. Murinello, M. I. Dorrell, L. Scheppeke, F. Bucher, S. Sakimoto, L. P. Paris, E. Aguilar and M. Friedlander (2015). Angiogenesis and eye disease. Annual Review of Vision Science **1**: 155-184.
32. Vezina, M. (2018). "Intravitreal and subretinal administration in minipigs."33.
Wang, F., S. P. Pang, L. Wang, Q. Li, M. Kreiter and C. Y. Liu (2010). "One-step synthesis of highly luminescent carbon dots in noncoordinating solvents." Chemistry of Materials **22**(16): 4528-4530.
34. Wang, Z. F., F. L. Yuan, X. H. Li, Y. C. Li, H. Z. Zhong, L. Z. Fan and S. H. Yang (2017). "53% efficient red emissive carbon quantum dots for high color rendering and stable warm white-light-emitting diodes." Advanced Materials **29**(37): 7.
35. Williams, K. A. and S. Klebe (2012). "Gene therapy for corneal dystrophies and disease, where are we?" Current Opinion in Ophthalmology **23**(4): 276-279.

36. Xu, M., G. He, Z. Li, F. He, F. Gao, Y. Su, L. Zhang, Z. Yang and Y. Zhang (2014). "A green heterogeneous synthesis of n-doped carbon dots and their photoluminescence applications in solid and aqueous states." Nanoscale **6**(17): 10307-10315.
37. Yang, Y. M., W. Q. Kong, H. Li, J. Liu, M. M. Yang, H. Huang, Y. Liu, Z. Y. Wang, Z. Q. Wang, T. K. Sham, J. Zhong, C. Wang, Z. Liu, S. T. Lee and Z. H. Kang (2015). "Fluorescent n-doped carbon dots as in vitro and in vivo nanothermometer." ACS Applied Materials & Interfaces **7**(49): 27324-27330.
38. You, J., J. Zhou, M. Zhou, Y. Liu, J. D. Robertson, D. Liang, C. Van Pelt and C. Li (2014). "Pharmacokinetics, clearance, and biosafety of polyethylene glycol-coated hollow gold nanospheres." Particle and Fibre Toxicology **11**(1): 26.
39. Zhang, W. K., Y. Q. Liu, X. R. Meng, T. Ding, Y. Q. Xu, H. Xu, Y. R. Ren, B. Y. Liu, J. J. Huang, J. H. Yang and X. M. Fang (2015). "Graphenol defects induced blue emission enhancement in chemically reduced graphene quantum dots." Physical Chemistry Chemical Physics **17**(34): 22361-22366.
40. Zheng, H. Z., Q. L. Wang, Y. J. Long, H. J. Zhang, X. X. Huang and R. Zhu (2011). "Enhancing the luminescence of carbon dots with a reduction pathway." Chemical Communications **47**(38): 10650-10652.
41. Zhu, H., X. L. Wang, Y. L. Li, Z. J. Wang, F. Yang and X. R. Yang (2009). "Microwave synthesis of fluorescent carbon nanoparticles with electrochemiluminescence properties." Chemical Communications (34): 5118-5120.
42. Zhu, S., Q. Meng, L. Wang, J. Zhang, Y. Song, H. Jin, K. Zhang, H. Sun, H. Wang and B. Yang (2013). "Highly photoluminescent carbon dots for multicolor patterning, sensors, and bioimaging." Angewandte Chemie-International Edition **52**(14): 3953-3957.

Appendix I. Supporting Materials for **Chapter 2**

Table of Contents

(A) Materials and Methods

(B) Results

(C) Discussion

(A) Materials and Methods

Table S1. Summary of experiments performed

Section	Description	Details of the measurement performed	Instruments/methodology used	Objective
1	Synthesis of NPs	Au NPs	Seed-mediated approach	Comparative toxicity study of different shape and size of the Au NP
2	Characterization of Au NPs and exposure to ARPE-19 cell line	Morphological study and Optical absorption of Au NPs	TEM and UV-Vis	Confirmation of the shape and physical dimension of NPs by TEM and supporting information on morphology using UV-Vis measurements was collected
		Hydrodynamic diameter measurements	DLS	Confirmation of the size of NPs in DI water and DMEM and 31.6 μ M HCl.
		Surface chemistry, zeta potential measurements	DLS	Determination of the ionic strength effects on dispersion characteristics
		Plating the cells and NP exposure study	Determination of the concentration in the media using ICP-MS	Determination of the exposure concentration of the NPs for ARPE 19
Microbial growth on basal nutrient medium	Test the sterile (free from microbial contamination) nature of the synthesized NPs			
3	Toxicity assessment of the ARPE-19 cell line	MTT assay	Colorimetric cell viability measurement	Studying the viability of the cells after different NP exposure concentrations
				Studying the role of size of the Au nanoparticles
				Detecting the effect of shape of the Au nanoparticles
		Confirmation of the presence of NPs inside ARPE-19 cells		
ECIS measurements	Cell attachment measurement	Monitoring the cell attachment behavior as the cells are exposed to Au NPs		
4	Investigation for the internalization of NPs	Confocal Microscopy	Confocal Microscopy, nanoplasmonic imaging	To confirm the internalization of the Au NPs

1. Synthesis of Au Nanoparticles

Gold (Au) nanoparticles were synthesized using seed-mediated approach. Details of the synthesis method for each nanoparticle are given below.

Au nanospheres were synthesized in two steps by seed-mediated approach (Wu et al. 2010) using cetyl trimethyl ammonium chloride (CTAC) as a surfactant. In the first step, seed solution was prepared by vigorous mixing (500 rpm for 1h at 30°C) of 10 mL of HAuCl₄ (2.5×10^{-4} M) aqueous CTAC (0.1 M) solution with 0.45 mL of ice cold NaBH₄ (0.02 M). The seed solution was aged for 60 minutes (at 30°C) to decompose the excess of NaBH₄. In the second step, the growth solution was prepared by adding 514 μL of HAuCl₄ (4.86 mM), 10 μL of NaBr (0.01 M) and 90 μL of ascorbic acid (0.04M) to 5 mL of aqueous CTAC (0.1 M) solution. To this colorless solution, 25 μL of seed solution was added under vigorous agitation and left undisturbed overnight at room temperature. The size of the sphere was controlled by varying the molar ratio of ascorbic acid to seed solution.

Gold nanocubes were synthesized in three steps. In the first step, the seed solution was prepared similarly to the gold nanospheres. Two growth solutions were prepared by adding of 5 ml of aqueous CTAC (0.1 M), 514 μL of HAuCl₄ (4.86 mM), 10 μL of NaBr (0.01 M), 4625 μL of ultrapure water and 90 μL of ascorbic acid (0.04M). The total solution volume of each growth solution was 10 mL. The 25 μL of prepared seed solution was added to the first growth solution with immediate vortex for a few seconds from this 25 μL of solution was added to the second growth solution and kept overnight at room temperature without disturbing.

Gold nanorods were synthesized using a seed-mediated approach (Jana et al. 2001) in which seed solution was prepared by adding 0.6 mL of an ice-cold solution of 10 mM sodium borohydride

into 10 mL of magnetically stirred 0.1M CTAB and 2.5×10^{-4} M HAuCl₄ aqueous solution at room temperature. The color of the seed solution changed from yellow to brown as an indicator of Au nanoparticle formation. Simultaneously, growth solution was prepared by mixing 10 mL of 0.1M CTAB, 0.8 mL of 10 mM AgNO₃, 5 mL of 10 mM HAuCl₄, and 0.11 mL of 0.1M ascorbic acid in the same order. The solution was homogenized by gentle stirring. To the resulting colorless solution 0.024 mL of freshly prepared seed solution was added, and the mixture was set aside in dark for 14 h at room temperature.

2. Characterization of nanoparticles and exposure to ARPE-19 cell line

2.1. Morphological study by transmission electron microscopy (TEM) and UV-Vis analysis

TEM micrographs were obtained using an FEI Spirit TEM (Hillsboro, OR, USA) operated at 120 kV. A 400-mesh Formvar[®] carbon-coated copper grid was glow-discharged in a vacuum evaporator (Denton, Moorestown, NJ, USA) for 30 seconds to make the grid hydrophilic and, thus, attractive to particles. The sample was prepared by placing 2 μ L of sonicated colloidal NP solution onto the grid and wicking off the excess sample with filter paper after 30 seconds. To further confirm the size, UV-Vis measurements were performed. Cary 50 Bio UV-Vis spectrophotometer (Varian, Palo Alto, CA) was used for recording of absorption spectra of NPs.

2.2. Hydrodynamic diameter, agglomeration, and sedimentation profile

Malvern Zetasizer Nano ZS (Malvern Instruments, Westborough MA, and USA) equipped with a backscattering detector (173°) was used for hydrodynamic size measurements of the synthesized nanoparticles. Samples were dispersed in water, followed by sonication for 15 minutes to homogeneously disperse them in the solution; they were then filtered through a pre-rinsed 0.2

μm filter followed by equilibration (typically 5 minutes) at 25 °C. A minimum of three measurements per sample was taken. The NP sedimentation rate was visually quantified up to 72 hours in both dispersant solvents, i.e., water and cell culture media.

2.3. Surface chemistry: zeta potential measurements

A Malvern Zetasizer Nano ZS was used to measure the zeta potential at 25 °C for all samples. Samples were loaded into a pre-rinsed folded capillary cell for the zeta potential measurements. An applied voltage of 100 V was used for the NP colloids, and a minimum of three measurements was performed per sample. The surface zeta potential of NPs dispersed in deionized (DI) water as well as in the cell culture medium, i.e., Dulbecco's modified Eagle's medium (DMEM), and in 8.3mM Hydrochloric acid solution was measured. Zeta potential of the cell culture media (C-DMEM/F12) was measured as -8.09 mV. Thus, it was confirmed that changing the solvent (from DI water to C-DMEM/F12) plays a critical role in zeta potential of the NPs.

2.4. Validation of NP concentration

Quantitative determination of Au (Gold) concentrations in stock solutions were performed by an inductively coupled plasma-mass spectrophotometer, also referred to as an ICP-MS (Elan DRC II, PerkinElmer, Norwalk, CT). Synthesized NPs were dispersed in water as a stock solution for the preparation of ICP-MS analysis. Then, 100 μL of stock solution was digested in triplicates using an equal volume of aquaregia (3 mL of HCl: 1 mL of HNO_3). Aqueous dilutions of the stock suspension were subjected to analysis using direct nebulization into the ICP-MS and were quantified against external calibration curves.

3. Toxicity assessment of the ARPE-19 cell line

3.1. Establishment of ARPE-19 cell line

ARPE-19 cells were maintained at 37 °C in a humidified atmosphere of 5% CO₂. Cells were grown in 75 mm flasks and maintained with DMEM, composed of a nutrient mixture F12 (1:1) supplemented with 10% FBS, 2 mL⁻¹ glutamine, 100 U mL⁻¹ penicillin, and 100 U mL⁻¹ streptomycins. Cell media were changed every 3 days. Cultures were passaged by dissociation in 0.25% (w/v) trypsin-EDTA in Hanks' balanced salt solution (HBSS). Cells were seeded in 100 mm x 20 mm plates. All the cells in the same passages were grown to 70–90% confluence before seeding on a 96-well plate for assay.

3.2. Cell attachment study: ECIS measurements

In this technique, cells were plated in wells containing gold electrodes connected to an ECIS system. As the cell morphology and attachment to the electrodes present in the bottom of the well changed, the resistance across the electrodes also changed. The change in resistance at different frequencies from 400 to 64,000 Hz can be measured over time. At high frequencies, current couples through the insulating cell membrane with minimal current passing through the solution channel under and between adjacent cells. The impedance (capacitive reactance) of the membrane is relatively small and, hence, can be used to monitor the establishment of a confluent cell layer. On the other hand, at low frequencies, current predominantly flows through the solution channel under and between adjacent cells, and the membrane impedance is high. As a result, low-frequency impedance can be used to monitor the solution paths around the cells and, hence, the layer's cell to cell barrier functions (Arndt et al. 2004). The addition of Au NPs further complicates the impedance of the system. However, at a frequency of 4000 Hz, the contribution of resistance from cells was dominant over the contribution of resistance from Au

NPs with media (Kandasamy et al. 2010). Hence, a frequency of 4000 Hz was chosen to monitor cell growth and biocompatibility. The time required for retinal cells (both primary RPE and ARPE-19 cells) was determined via impedance measurements. As can be seen in Figure S1., by the end of the first day, the ARPE-19 cells did reach confluency; however, pRPE cells required more time to become confluent.

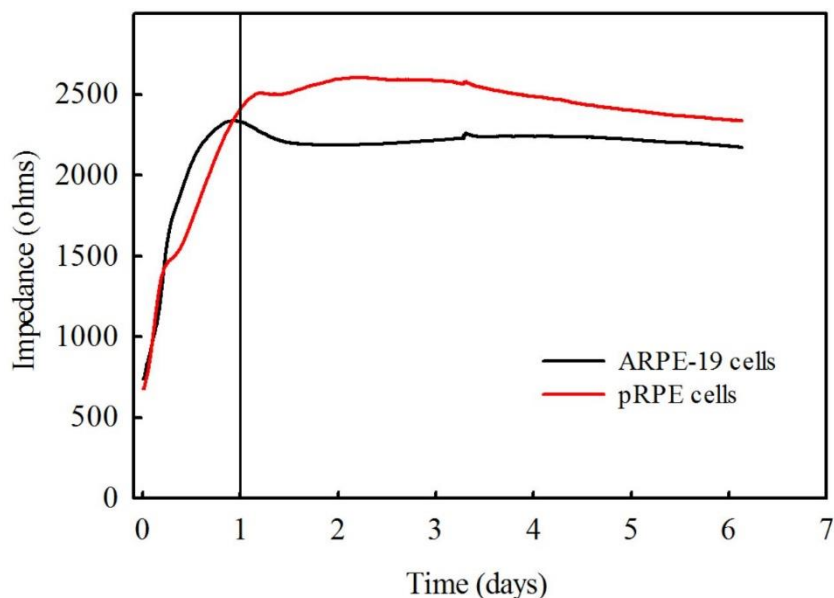


Figure S1. ARPE-19 and primary retinal (pRPE) cells attachment behavior for more than six weeks were monitored real time via ECIS measurements. By the end of the 24th hour, the ARPE-19 cells reached confluency; however pRPE required more than 26 hours to transition from logarithmic growth phase to stationary phase (become confluent).

4. Investigation for the internalization of NPs

4.1. Nucleus staining and sample preparation for confocal imaging

ARPE-19 cells were fixed by immersion in a 4% paraformaldehyde (PFA), as the cross-linking solution, for 10 minutes at room temperature. The cells were then washed three times by immersion in ice-cold 1X PBS (phosphate buffer saline) for five minutes each time. The fixed

cells were incubated in ice-cold 1X PBS buffer containing 0.1% Triton (permeabilization agent) for 10 minutes at room temperature. After that, the cells were washed three times again with ice-cold 1x PBS for five minutes each. The cell slides were then incubated with blocking buffer for 30 minutes before addition of slow fade. The cells were subsequently washed three times with ice-cold 1X PBS for five minutes each. For the staining of the nucleus, SlowFade® Gold Antifade Mountant with DAPI (diluted 1:100 in 1X PBS) was used, and the cells were incubated with the above cell slides overnight at 4 °C. Then the cells were again washed three times with ice-cold 1X PBS for five minutes each. Finally, the cell slides were transferred to a confocal microscope for optical analyzes. The used laser wavelengths were 488 and 533 nm for DAPI (nucleus staining) and for Au NP detection respectively.

(B) Results

1. UV-Vis characterization of synthesized ENP

Nanoparticles were also characterized by UV-Vis absorption spectroscopy. The distinct band maxima for Au spheres (5, 10, 20, and 30 nm) were measured at 510-540 nm. For Au cube (50 nm) and Au spheres (50 and 100 nm), peaks were detected at 556, 536, and 573 nm, respectively. Au nanorods showed two absorption peaks at 517 and 761 nm due to their morphological aspect ratio.

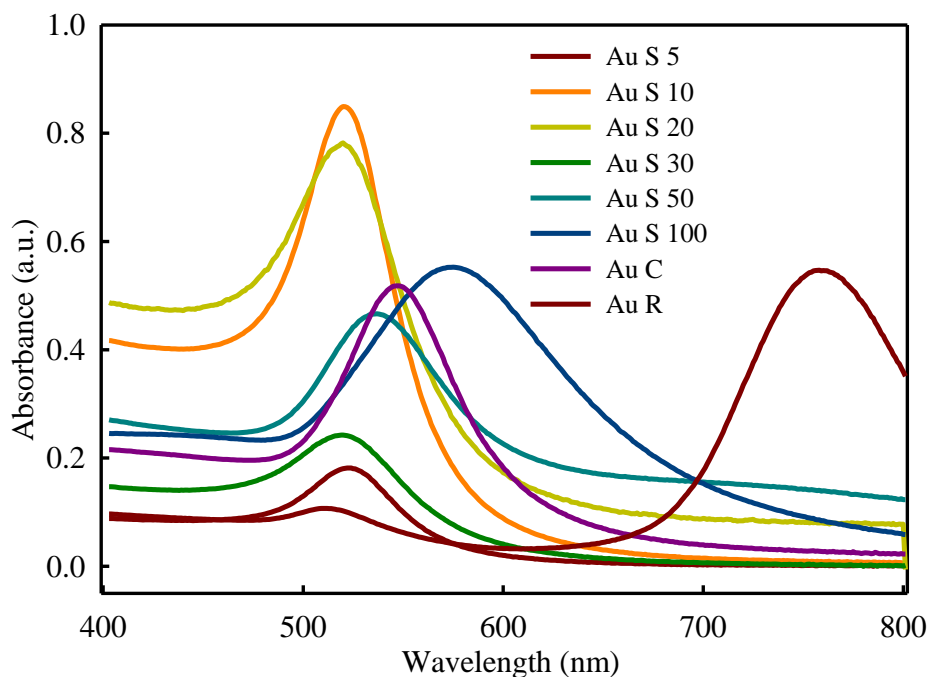


Figure S2. UV-Vis absorption spectra of synthesized Au NPs

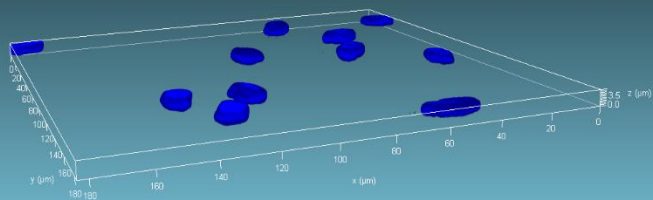
Table S2. Influence of exposure media on physicochemical properties of NPs

NP type	pH		Zeta Potential (mV)		Hydrodynamic Diameter (nm)		Sedimentation % (after 72 hours)*	
	DI water	DMEM	DI water	DMEM	DI water	DMEM	DI Water	DMEM
Au S 5	3.2	7.5	37.5 (± 0.38)	0.12 (± 0.46)	4.83 (± 1.52) [#]	8.27 (± 2.66)	NO	NO*
Au S 10	3.3	7.6	33.5 (± 0.14)	0.18 (± 0.28)	8.89 (± 2.80)	17.81 (± 5.77)	NO	NO*
Au S 20	3.2	7.8	24.8 (± 0.08)	1.72 (± 0.52)	14.57 (± 4.54)	29.11 (± 9.16)	NO	NO
Au S30	3.2	7.6	21.4 (± 0.50)	1.58 (± 0.46)	29.39 (± 7.55)	42.62 (± 13.34)	NO	NO
Au S 50	3.4	7.6	42.1(± 1.72)	-11.9 (± 1.27)	45.57 (± 14.27)	66.83 (± 22.37)	NO	<33
Au S 100	3.3	7.8	28.1(± 1.60)	-12 (± 0.58)	98.25 (± 31.38)	120.15 (± 39.85)	NO	<33
Au cube	7.6	7.7	40.6 (± 0.72)	-6.33 (± 0.16)	50.25 (± 16.74)	60.12 (± 21.26)	~33	~33
Au rods	3.8	7.7	36.9 (± 0.21)	-7.40 (± 0.09)	120.25 (± 44.99)	130.45 (± 51.85)	~33	~33
DMEM	7.7	7.7	-8.09 (± 0.06)	-8.09 (± 0.06)	NM	NM	NO	NO

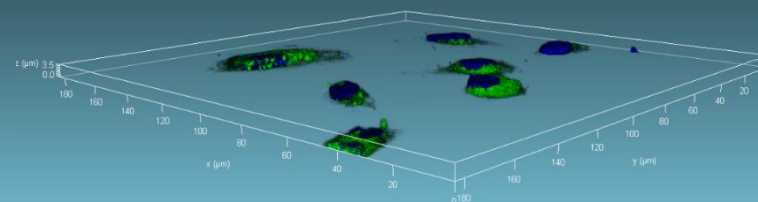
[#] Standard deviation

*values presented in %, based on visual appearance; NO: Not observed; NM: Not measured

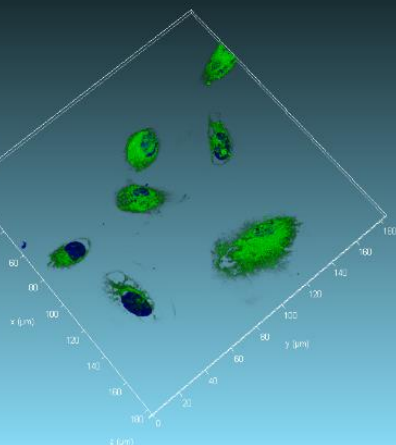
(a)



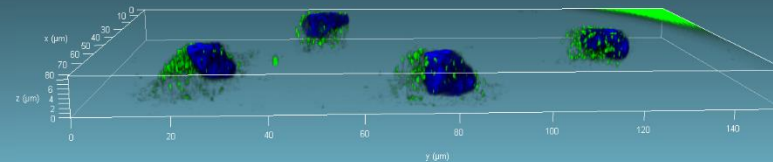
(b)

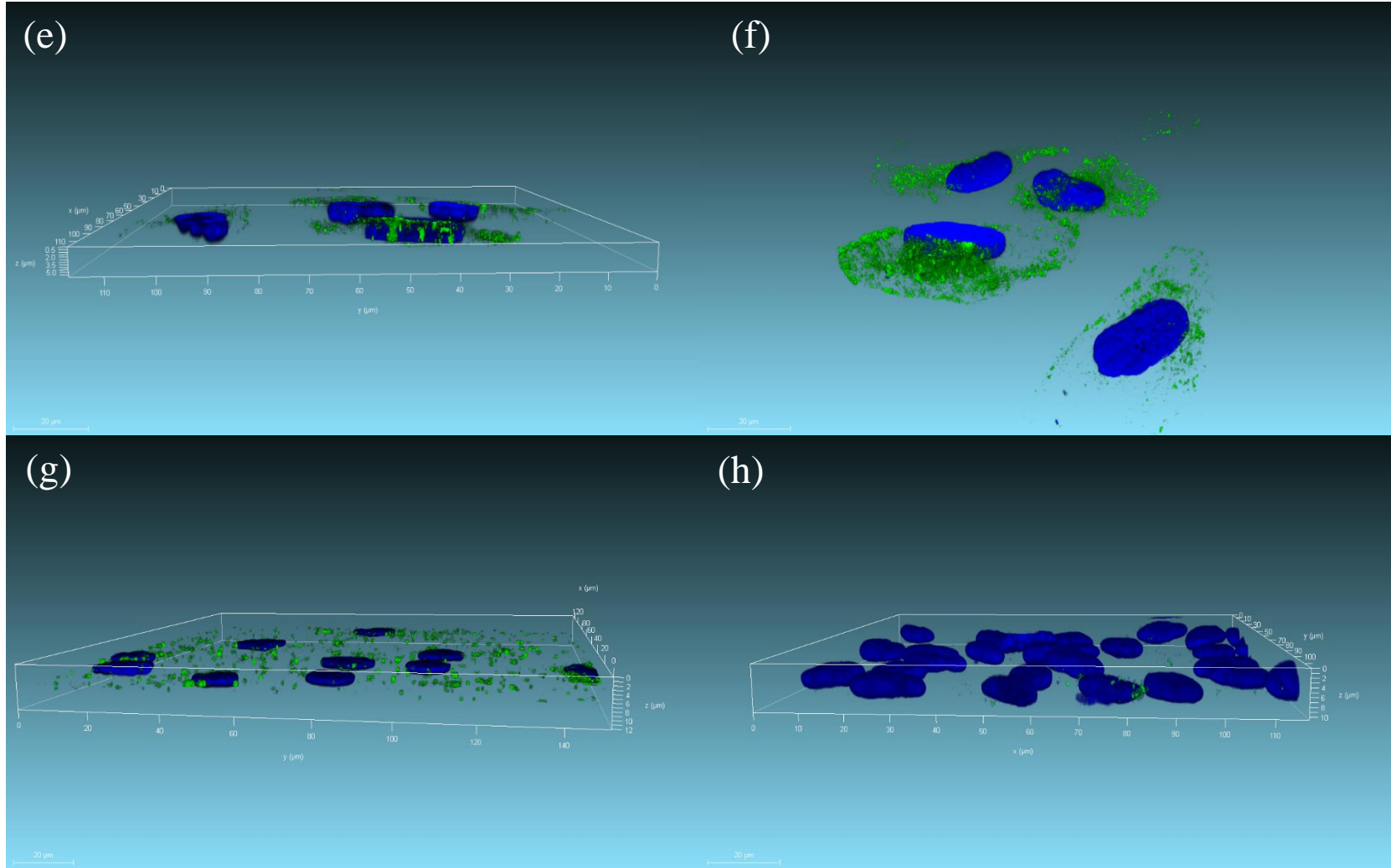


(c)



(d)





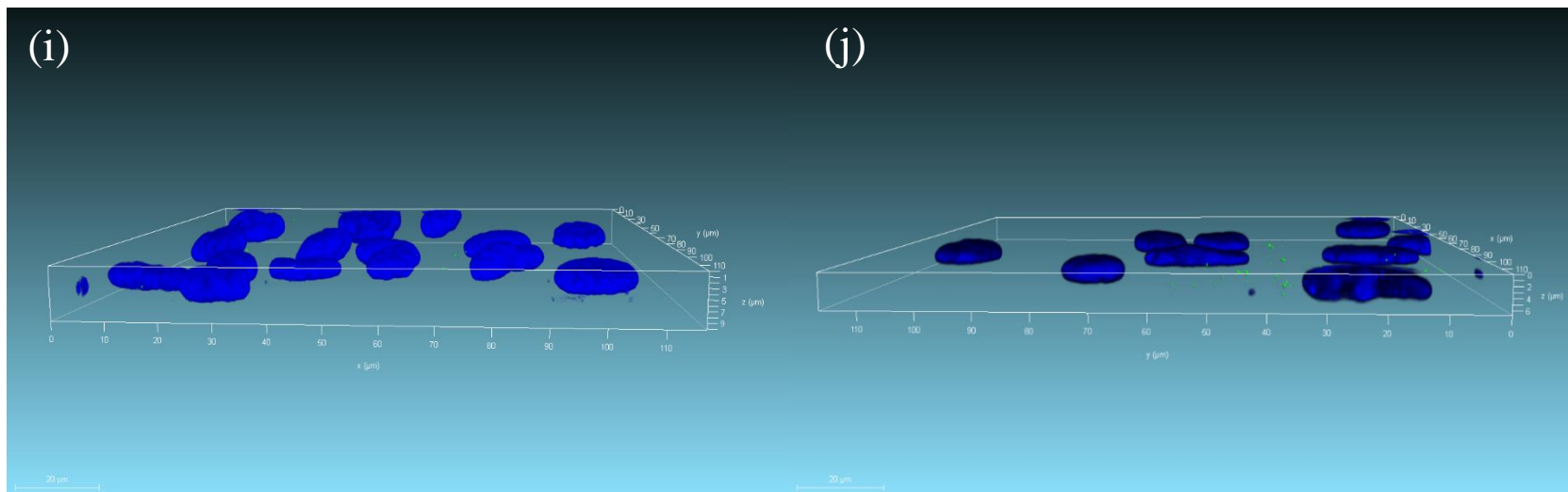


Figure S3. 3D Confocal microscopic images of nanoparticles inside cells after 72 h of exposure. All figures are from the same stack of cells, in which nuclei are present. Included are (a) cells without nanoparticle exposure, (b) ARPE-19 cells exposed to 5-nm Au spheres (LD_{50} : 0.030 mg/ml) with green dots representing Au NPs inside cells in the vicinity of the nucleus and voids (exact areas are shown with white arrows) representing loss of cytoplasm on the observed layer. (c) Void like structures can be seen at ARPE-19 cells exposed to 5-nm Au spheres (LD_{50} : 0.030 mg/ml) (d) ARPE-19 cells exposed to 10-nm Au spheres (LD_{50} : 0.057 mg/ml, with particles inside cells and nuclei. (e) ARPE-19 cells exposed to 20 nm Au spheres at a critical concentration of LD_{50} : 0.113 mg/ml; the presence of particles inside cells and nuclei is confirmed. (f) ARPE-19 cells exposed to 0.129 mg/ml of 30-nm Au spheres. (g) LD_{50} :0.050 mg/ml of 10×90 nm Au nanorods inside cells and nuclei. (h) 0.129 mg/ml of 50- nm Au spheres. (i) 0.129 mg/ml of 100-nm Au spheres. Internalization of 50- and 100-nm Au spheres may be hindered by their large size. The available surface area, the key metric for biocompatibility, is much less for 50- and 100-nm Au spheres compared than for ARPE-19 cells exposed to smaller Au nanospheres. (j) 0.129 mg/ml of Au nanocubes.

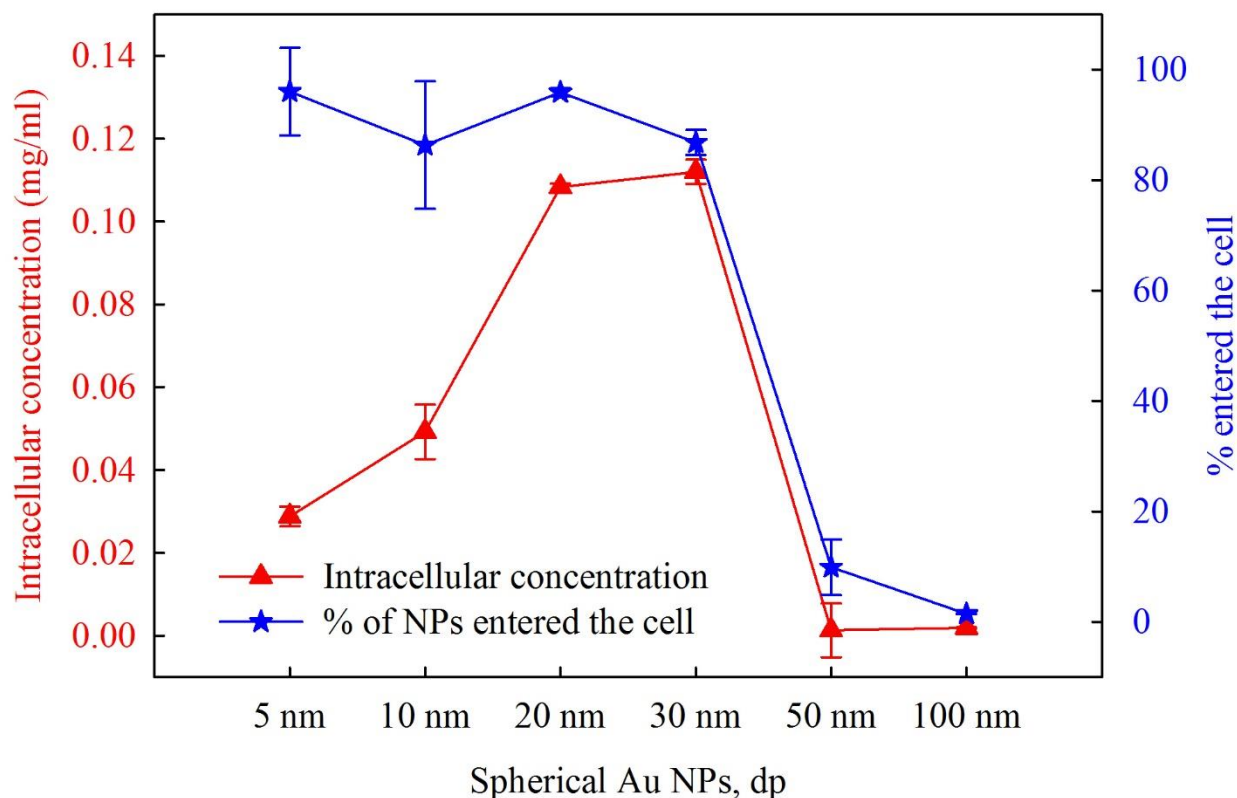


Figure S4. Inductively coupled plasma mass spectrometer (ICP-MS) measurement results for the aliquots collected after the washing procedure prior to Confocal microscopy imaging.

REFERENCES

1. H. L. Wu, C. H. Kuo and M. H. Huang, *Langmuir*, 2010, **26**, 12307-12313.
2. N. R. Jana, L. Gearheart and C. J. Murphy, *Advanced Materials*, 2001, **13**, 1389-1393.
3. S. Arndt, J. Seebach, K. Psathaki, H. J. Galla and J. Wegener, *Biosensors & Bioelectronics*, 2004, **19**, 583-594.
4. K. Kandasamy, C. S. Choi and S. Kim, *Nanotechnology*, 2010, **21**, 10.

Appendix II. Supporting Materials for
Chapter 3

¹H NMR, FTIR, and GPC analysis of end-thiol modified HA (HS-HA). The HS-HA was characterized using ¹H NMR spectroscopy. ¹H NMR spectrum was obtained on a Varian Unity Inova 500 (Palo Alto, CA). HS-HA samples were dissolved in D₂O (8 mg/mL) with NaOD (20 μmol). Each sample was scanned for 128 times at 25 °C. The infrared spectra of HS-HA was obtained using a fourier transform spectroscopy (Spectrum GX, PerkinElmer, USA). The infrared spectra of the samples were measured over a wavelength range of 4000 - 500 cm⁻¹. Transmission spectra was taken in the spectral range by the accumulation of at least 64 scans with a resolution of 4 cm⁻¹. The GPC system used a VE 1122 pump with a VE 7510 degasser (Viscotek/Malvern, Houston, TX) equipped with a TDA302 triple detector system that measured the refractive index (RI), multi-angle laser light scattering, and viscosity. The column used was a G5000PWXL (Tosoh Biosep, Montgomeryville, PA). Viscotek Omniseq software was used to calculate the RI area, weight-averaged molecular weight, intrinsic viscosity, and hydrodynamic radius. Samples (100 μL) were injected at a concentration of 2 mg/mL. The column buffer (pH 7.6) contained 20 mM of sodium phosphate and 100 mM of NaCl. The flow rate was 0.8 mL/min. Measurements were conducted at 37 °C.

Particle size measurements. The morphologies and the size of the synthesized uncoated Au NPs were examined by high-resolution transmission electron microscopy (HR-TEM, Tecnai TM Spirit, FEI Co.), operated at 200 kV accelerating voltage. A 400 mesh TEM grid (CF400-Cu-UL, Electron Microscopy Sciences, PA) was used. A Malvern Zetasizer Nano ZS (Malvern Instruments, Westborough MA) equipped with a backscattering detector (173°) was used for hydrodynamic size measurements of synthesized nanoparticles. Samples were dispersed in water, then sonicated for 15 min to homogeneously disperse them in the solution, after which they were filtered through a prerinsed 0.22 μm sterile filter, then equilibrated (typically for 5 min) at 25 °C. At least three measurements per sample were taken. The

hydrodynamic diameter and zeta potential of NPs in solution before and after their exposure to cell culture medium was measured in batch mode using DLS.

Ellman's reaction. The amount of thiol content of end-thiolated hyaluronate (HS-HA) was also determined spectrophotometrically, using an Ellman's reagent as described by Ellman (Ellman 1959). Briefly, 10 mg of lyophilized sample was diluted with 2 mL of N₂-bubbled water. To 100 mL of this sample, 500 mL of 0.1 M phosphate buffer (pH 8), 400 mL of water, and 50 mL of Ellman's reagent were added. Samples were incubated for 15 min at room temperature in dark and their absorbance measured at $\lambda = 412$ nm in a Varian Cary 5000 spectrophotometer. Thiol content was calculated as per the equation:

$$\text{SH (moles) / HA (g)} = (\text{Ab}/13,600) \times (\text{V}_{\text{total}} / \text{V}_{\text{sample}}) \times (1/\text{HA}_{\text{conc}}) \quad (1)$$

where Ab is the absorbance and V_{total} is the total volume, whereas V_{sample} is the sample volume and 13,600 is the extinction coefficient. The concentration of the HA (HA conc) is in mg/mL.

Total organic carbon (TOC) measurements. We used a Shimadzu TOC-VWP to determine the carbon content of HS-HA-Au NPs in the solid phase. Lyophilized samples were weighed before pretreatment with acid to remove and measure all inorganic carbon. During the TOC analysis, the sample underwent combustion heating to 680 °C. During decomposition, the CO₂ generation was recorded. The inorganic carbon (IC) was measured by acid digestion of the sample, followed by nitrogen sparging (CO₂ isolation). Subtracting the inorganic carbon from the total carbon yield the total organic carbon, corresponding to the HA content of the sample.

Thermal gravimetric analysis (TGA). A TA Q5000 thermal gravimetric analyzer was used. Any change in sample mass, a function of increasing temperature and time, was measured. HA is known to decompose at 220-280 °C (Jiang et al. 2015, Ahire et al. 2016). On the other hand, Au NPs under 150 nm in diameter possess lower melting temperature (above 426-976

°C) compared to bulk gold (1027 °C) (Buffat and Borel 1976). Taking bound water content into account from the TGA curves, the explicit Au content was determined by calculating the difference between the total mass of the sample and the HA content.

***In-vitro* cytotoxicity measurements on ARPE-19 MTT, ApoTox-Glo™, and ROS-Glo™ H₂O₂ assays.** For all three assays, the cells were distributed in a flat-bottom 96-well plate with a 150 µL volume (1.5×10^6 cells per 20 ml). After plating, cells were incubated for 48 h (37 °C, 5% CO₂), then exposed to different concentrations of NPs. Physically characterized particles were dispersed in DMEM to be used for cell exposure. For each size of Au NPs, concentrations of the exposed solutions were 0.01, 0.05, 0.1, and 0.5 mg/ml. The upper limit of exposure concentration was determined by the toxic potential of the NPs as reported in the literature (Karakocak et al. 2016). NP exposure was maintained for 24 h before assay measurements. In all biological and imaging tests, the cells without NP exposure served as a negative control

For the MTT assay, following the exposure of NPs, 100 µL of MTT (1 mg/l in growth media) were added to each well, and the plate was incubated for an additional 5 h at 37 °C in 5% CO₂. The resulting blue component, produced by the reduction of tetrazolium salt of MTT by mitochondrial dehydrogenase enzyme, was dissolved in 100 µL dimethyl sulfoxide (DMSO). The optical density of the colored product was read photometrically using a spectrophotometer at 540 nm with a microplate reader (Molecular Devices Spectra Max 190). The absorbance of untreated cells was used as a negative control. The percentage viability of the cells was calculated from the ratio of the mean optical density of the sample to the optical density of the negative control.

For all three assays, the cells were distributed in a flat-bottom 96-well plate with a 150 µL volume (1.5×10^6 cells per 20 ml). After plating, cells were incubated for 48 h (37 °C, 5% CO₂), then exposed to different concentrations of NPs. Physically characterized particles

were dispersed in DMEM to be used for cell exposure. For each size of Au NPs, concentrations of the exposed solutions were 0.01, 0.05, 0.1, and 0.5 mg/ml. The upper limit of exposure concentration was determined by the toxic potential of the NPs as reported in the literature.^{44, 45} NP exposure was maintained for 24 h before assay measurements.

For the MTT assay, following the exposure of NPs, 100 μ L of MTT (1 mg/l in growth media) were added to each well, and the plate was incubated for an additional 5 h at 37 °C in 5% CO₂. The resulting blue component, produced by the reduction of tetrazolium salt of MTT by mitochondrial dehydrogenase enzyme, was dissolved in 100 μ L dimethyl sulfoxide (DMSO). The optical density of the colored product was read photometrically using a spectrophotometer at 540 nm with a microplate reader (Molecular Devices Spectra Max 190). The absorbance of untreated cells was used as a negative control. The percentage viability of the cells was calculated from the ratio of the mean optical density of the sample to the optical density of the negative control.

The cells were cultured and treated with NPs in 96-well, clear-bottomed white plates for the apoptosis and ROS detection experiments. Caspase 3/7 activity, the key indicator for apoptosis, was evaluated using the ApoTox-Glo™ Triplex assay according to the manufacturer's protocol. The light output, measured with a luminometer, correlates with Caspase-3/7 activation, and luminescence was measured using a microplate reader (Molecular Devices Spectra Max 190).

ROS generation was evaluated with the ROS-Glo™ H₂O₂ assay according to the manufacturer's protocol. The light signal produced by recombinant Luciferase is proportional to the level of H₂O₂ in the cells. The luminescence was measured using a microplate reader (Molecular Devices Spectra Max 190).

Confocal Microscopy. ARPE-19, NIH 3T3, and CHO cells were seeded in CELLview™ plates at 5×10^4 cells/well for 24 h. After 24 h of NP exposure, the cells were fixed and washed with PBS three times before imaging. All cells were fixed by immersion in 4% paraformaldehyde (PFA) as the cross-linking solution for 10 min at room temperature. The cells were then washed three times with ice-cold 1x PBS for 3 min each time. The fixed cells were incubated in ice-cold 1x PBS buffer containing 0.1% Triton (permeabilization agent) for 10 min at room temperature, then washed three times with ice-cold 1x PBS for 5 min each time. The CELLview™ plates were then incubated with blocking buffer for 30 min before the addition of Alexa Fluor® 633 phalloidin (diluted 1:200 in blocking buffer). The cells were subsequently washed three times with ice-cold 1x PBS for 3 min each time. To stain the nuclei, SlowFade® Gold Antifade Mountant with DAPI (diluted 1:100 in 1x PBS) was used. The cells were incubated overnight at 4 °C.

During confocal microscopy analysis, the laser wavelengths were 405, 525, and 633 nm for DAPI (nucleus staining), for Au NP detection, and for actin visualization, respectively. Several different images (based on the thickness of the cell, the number of images with the same Z-stack thickness vary) were taken through different optical sections by collecting Z-stacks with a thickness of 35 nm. A negative control sample (untreated cells) was prepared with cells in the absence of nanoparticles.

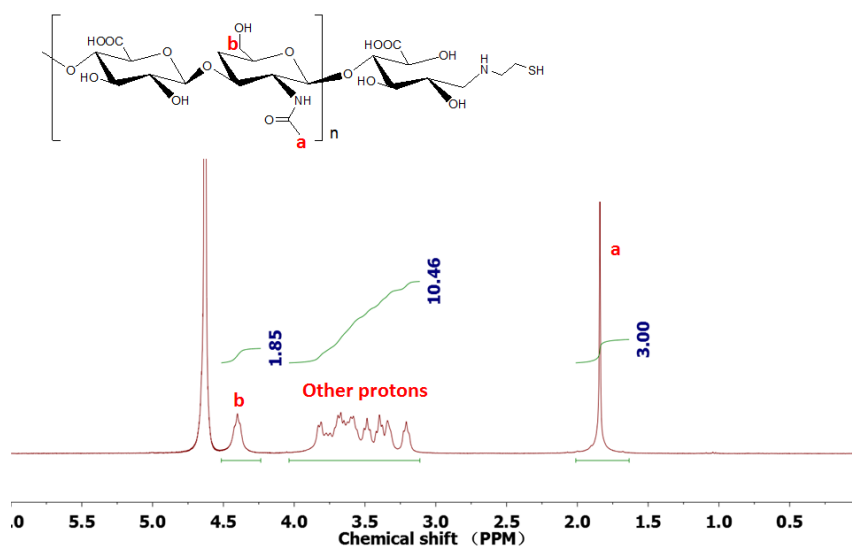


Fig. S1. NMR spectrum of end-thiolated hyaluronate. Typical hyaluronate peaks are presented in the spectrum. Extremely low level of the chain-end thiols caused its signals to be buried among other peaks or noise.

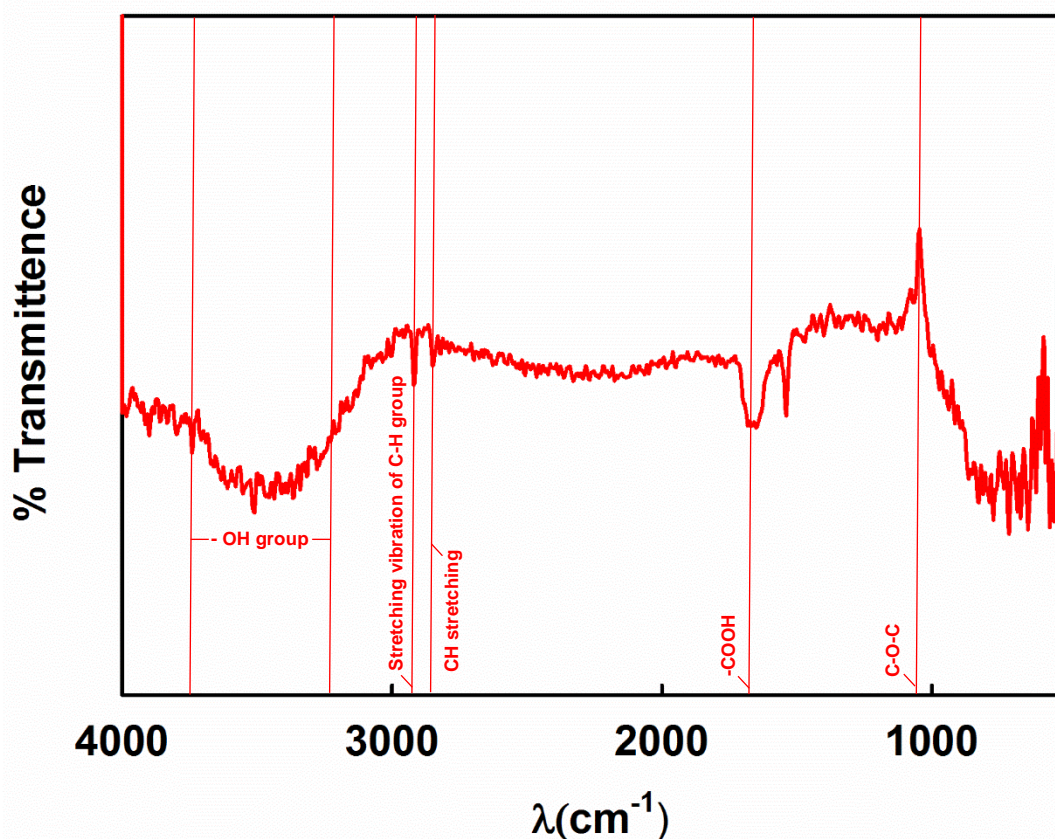


Fig. S2. FTIR transmittance spectrum of end-thiolated hyaluronate. For hyaluronic acid, -OH group is found at 3200-3700 cm^{-1} . Stretching vibration of C-H and CH stretching can be seen at 2915 cm^{-1} and 2845 cm^{-1} , respectively. Carboxylic groups and C-O-C bonds can be detected at 1660 cm^{-1} and 1045 cm^{-1} , respectively. Typical the -SH signal (2560 cm^{-1}) is

buried in the noise due to the low amount of SH in the HA sample as quantified with Ellman's assay ($[-SH]/[HA \text{ repeating units}] = 0.025$).

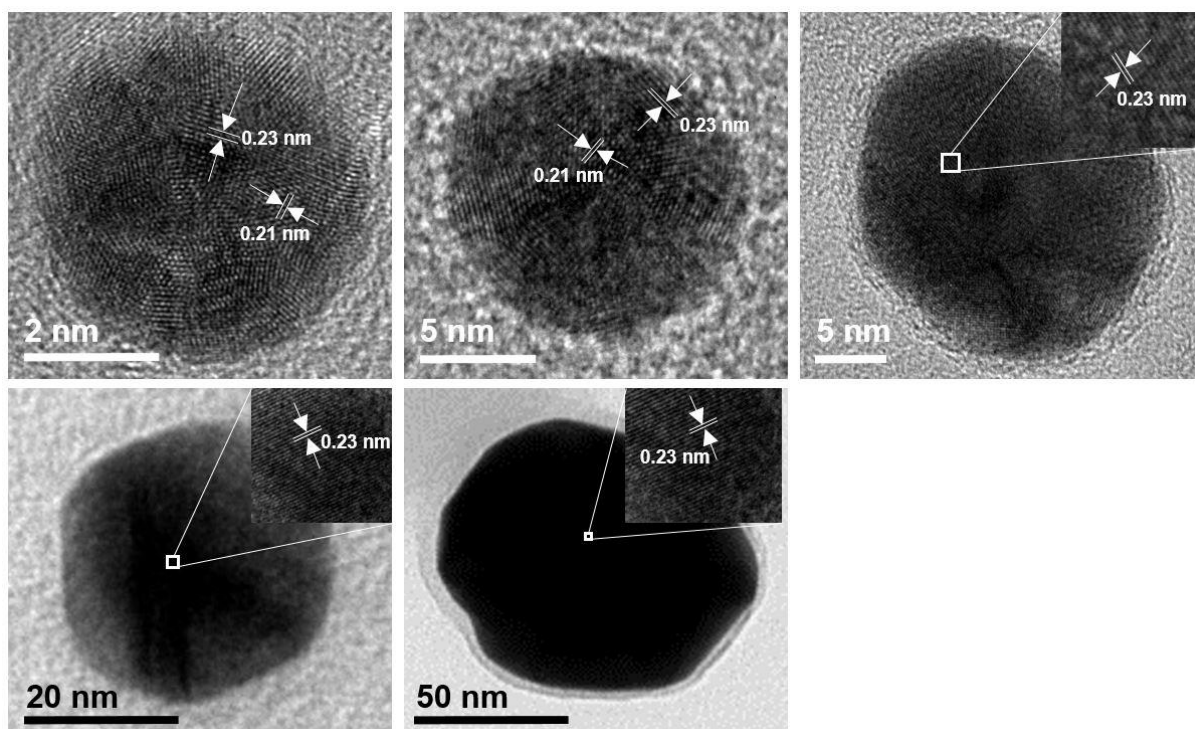


Fig. S3. HR-TEM images of different sizes of uncoated gold nanoparticles. Facets are detected with the thicknesses of 0.21 nm and 0.23 nm.

Table S1. The amount of HA molecules per unit Au surface area was calculated based on TGA and TOC analysis, respectively.

TGA									
Au dp (nm)	Amount of HA (g)	Amount of Au (g)	Total mass of the sample (g)	Mass of one Au NP (g)	# of Au NPs in the sample	Mass of one HA molecule (mg), MW: 19.69 kDa	# of HA molecules in the sample	Total surface area of Au NPs in the sample	# of HA molecules per unit surface area (nm ²)
5	2.15E-02	6.32E-02	8.47E-02	1.08919E-18	5.80E+16	3.26E-20	6.59E+17	4.13E+18	0.16
10	7.27E-03	6.29E-02	7.02E-02	6.85845E-18	9.17E+15	3.26E-20	2.23E+17	2.22E+18	0.10
20	3.17E-03	1.10E-01	1.13E-01	9.21237E-17	1.20E+15	3.26E-20	9.74E+16	1.64E+18	0.06
50	1.71E-03	2.57E-01	2.58E-01	1.49173E-15	1.72E+14	3.26E-20	5.25E+16	1.51E+18	0.03
100	2.30E-04	7.80E-02	7.82E-02	1.34871E-14	5.78E+12	3.26E-20	7.06E+15	2.20E+17	0.03

TOC									
Au dp (nm)	Amount of HA (g)	Amount of Au (g)	Total mass of the sample (g)	Mass of one Au NP (g)	# of Au NPs in the sample	Mass of one HA molecule (mg), MW: 19.69 kDa	# of HA molecules in the sample	Total surface area of Au NPs in the sample	# of HA molecules per unit surface area (nm ²)
5	1.82E-02	4.880E-02	6.700E-02	1.08919E-18	4.48E+16	3.26E-20	5.58E+17	3.19E+18	0.18
10	8.95E-03	8.605E-02	9.500E-02	6.85845E-18	1.25E+16	3.26E-20	2.75E+17	3.04E+18	0.09
20	2.05E-03	7.695E-02	7.900E-02	9.21237E-17	8.35E+14	3.26E-20	6.29E+16	1.15E+18	0.05
50	5.02E-04	7.850E-02	7.900E-02	1.49173E-15	5.26E+13	3.26E-20	1.54E+16	4.62E+17	0.03
100	1.72E-04	6.283E-02	6.300E-02	1.34871E-14	4.66E+12	3.26E-20	5.28E+15	1.77E+17	0.03

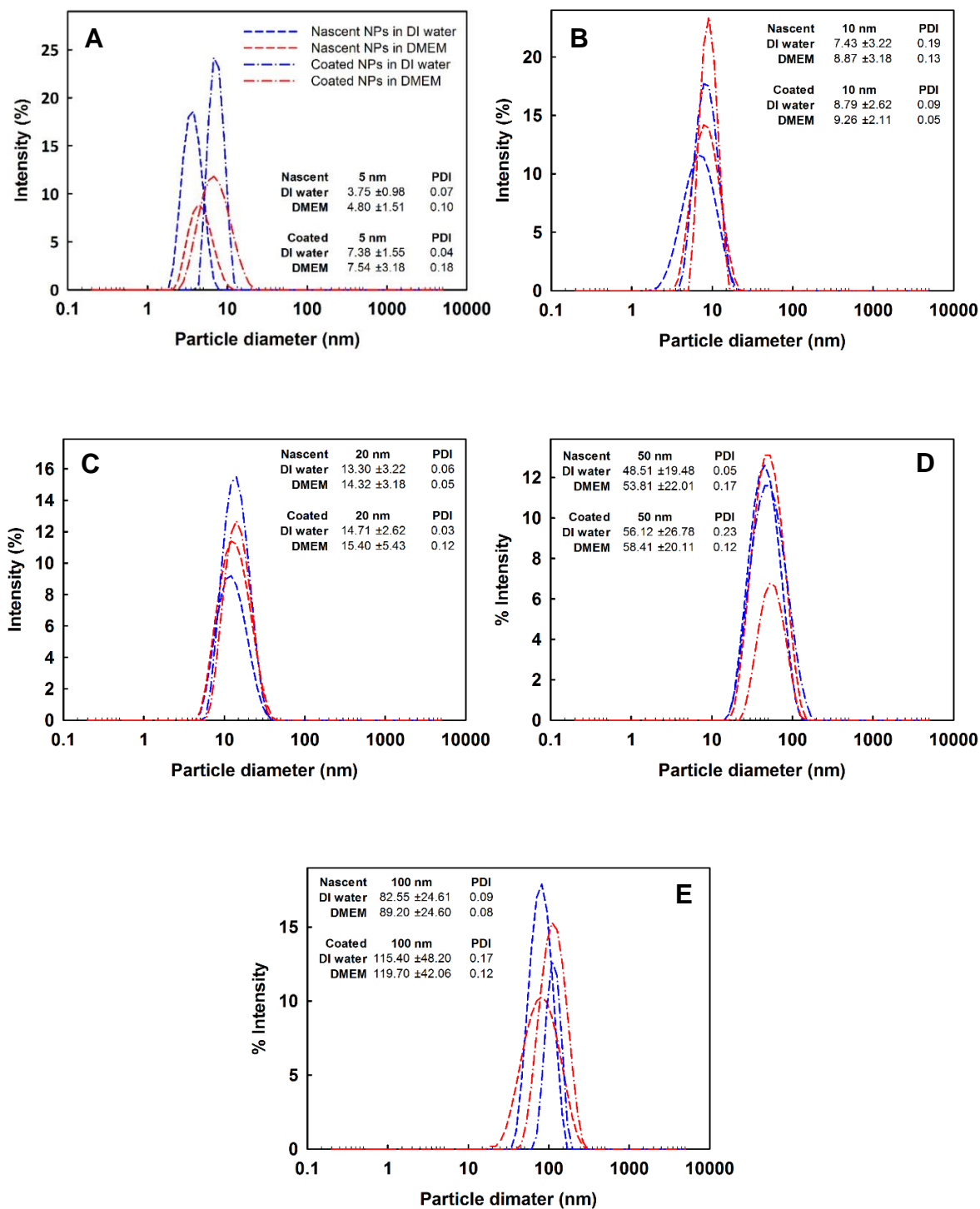


Fig. S4. Particle size distributions for nascent and coated Au NPs obtained with DLS measurements. (A) 5nm, (B) 10 nm, (C) 20 nm, (D) 50 nm, (E) 100 nm.

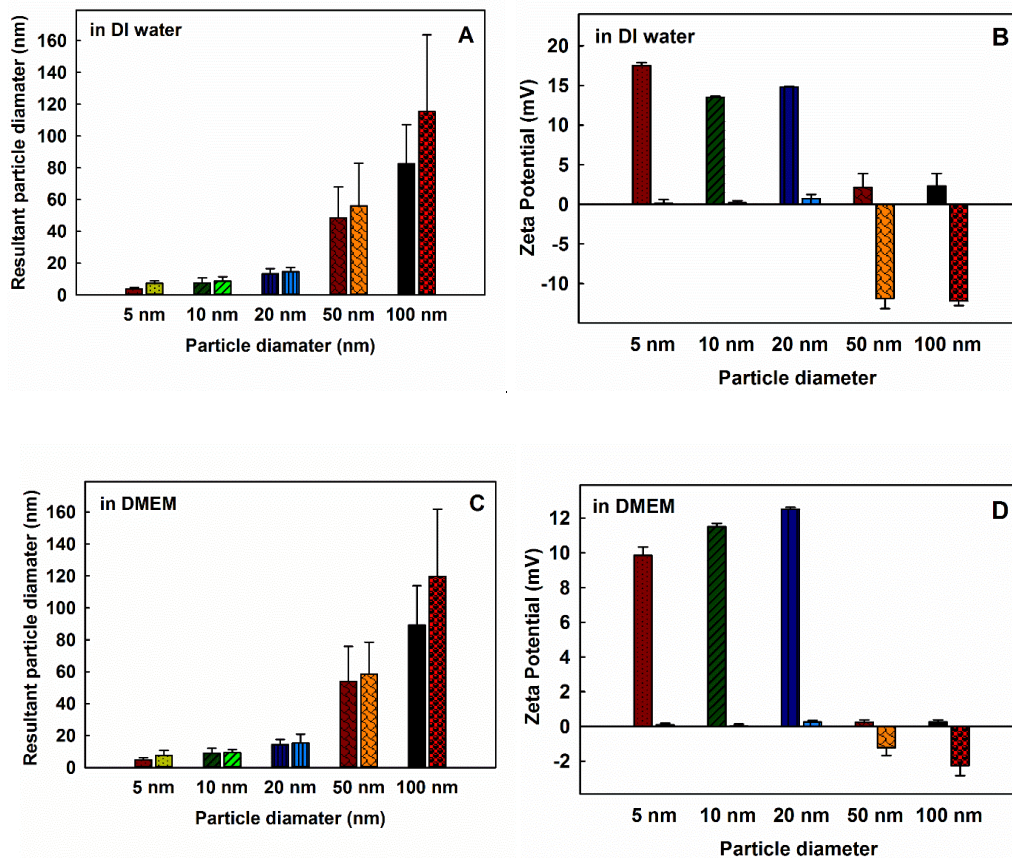
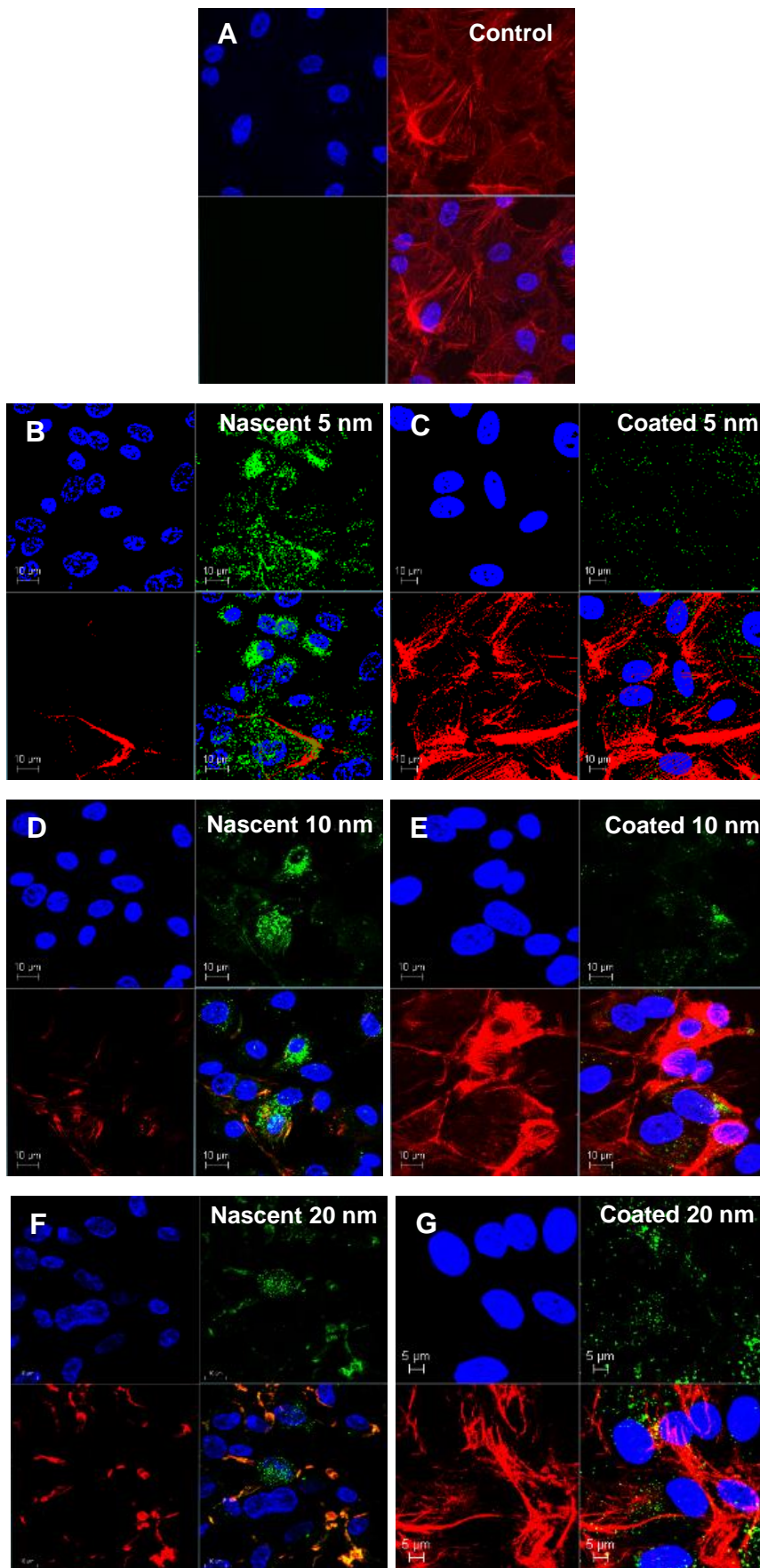


Fig. S5. Physical characterization of nascent and coated Au NPs by DLS measurements in DI water (A) particle size (B) zeta potential measurement results. The same particles exposed to DMEM (C) particle size (D) zeta potential measurement results. When the HA-HA-Au NPs are exposed to DMEM, the increase in particle size is much less compared to the nascent Au NPs, due to HS-HA coating, which prevents protein adsorption on the NP surface.

Nascent 5 nm,
 Coated 5 nm,
 Nascent 10 nm,
 Coated 10 nm,
 Nascent 20 nm,
 Coated 20 nm,
 Nascent 50 nm,
 Coated 50 nm,
 Nascent 100 nm,
 Coated 100 nm.



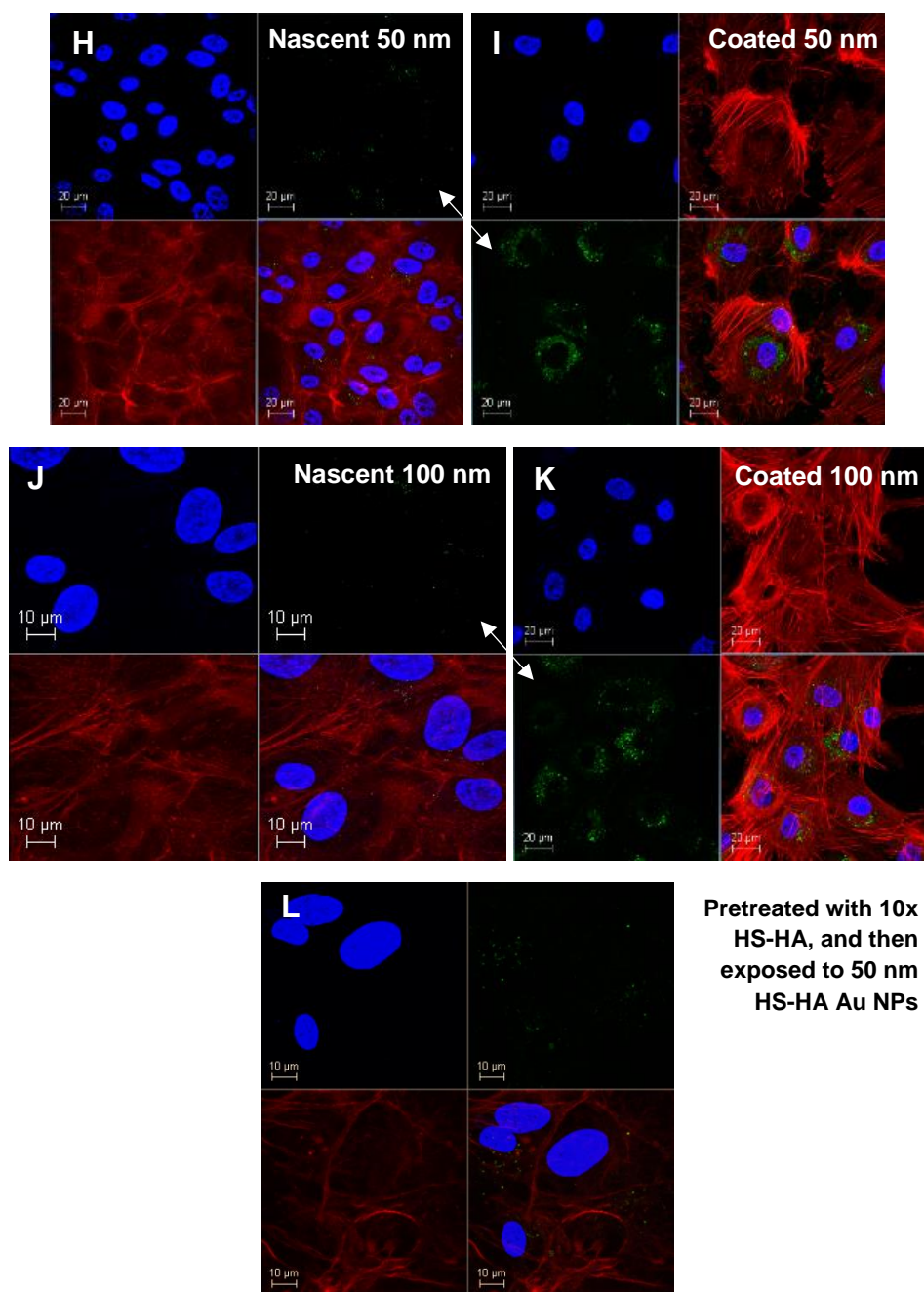
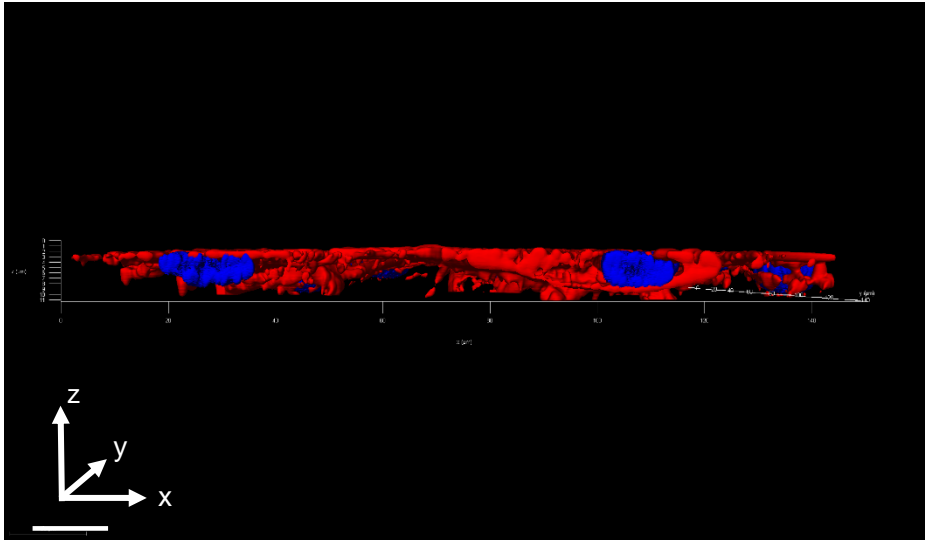
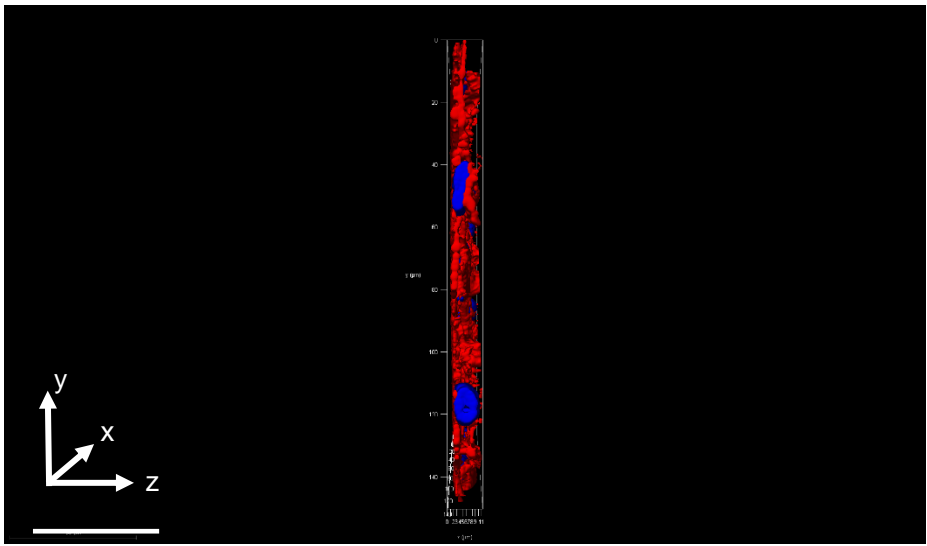
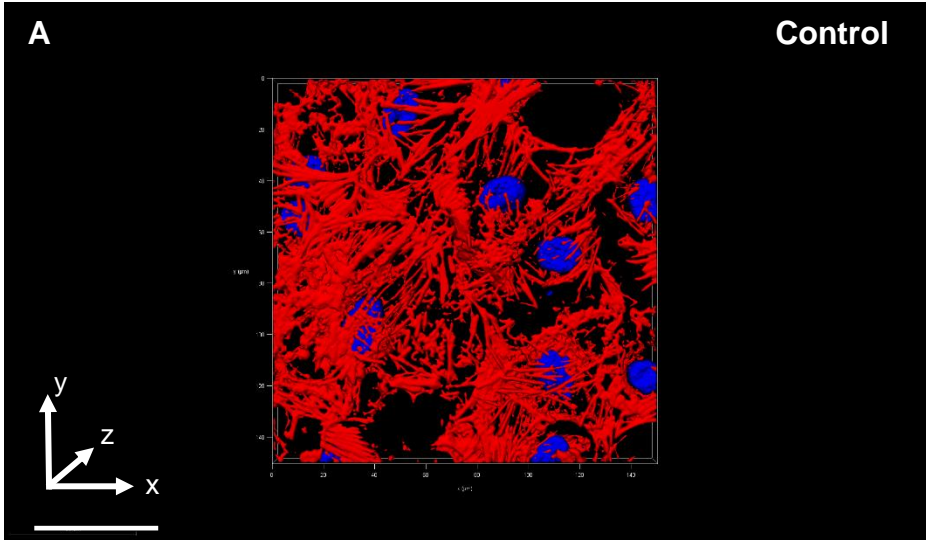


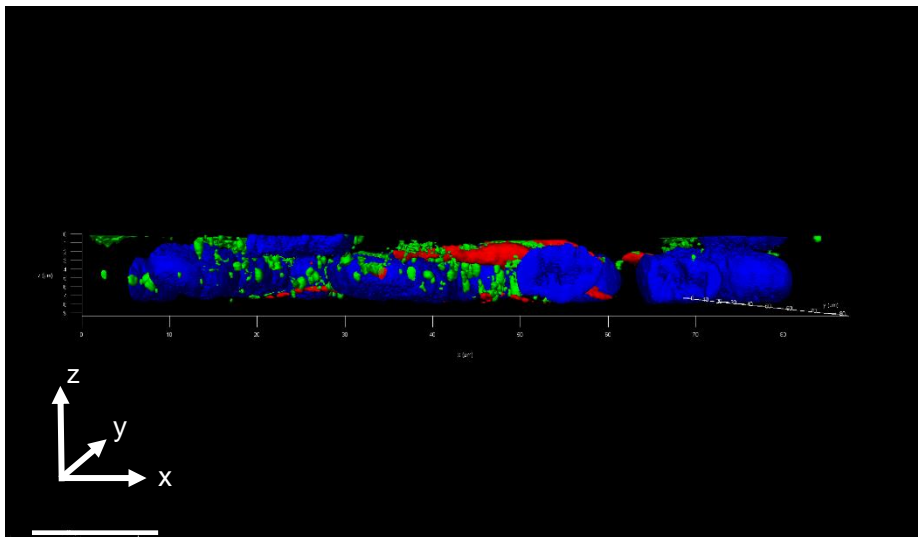
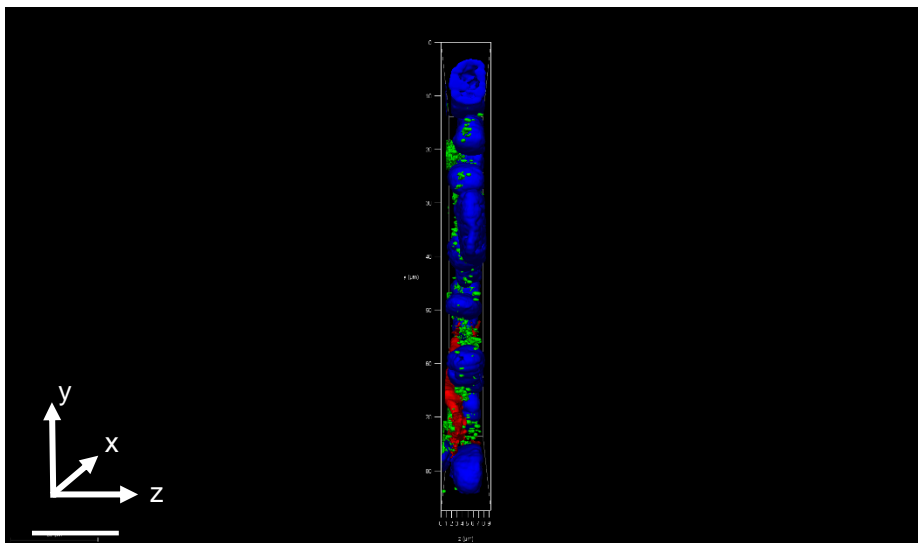
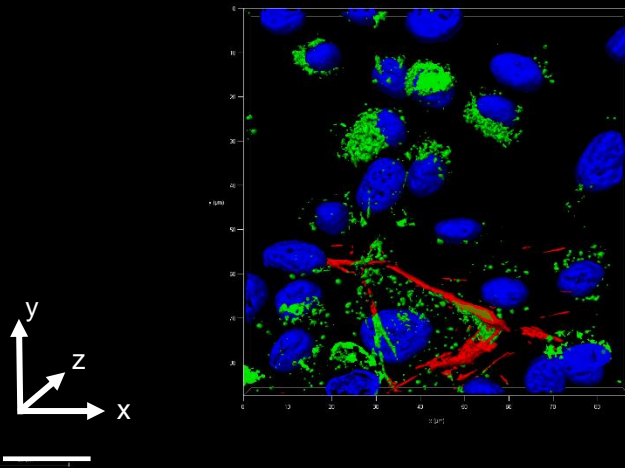
Fig. S6. The red staining corresponds to actin, the nucleus is blue, and Au NPs are green. 2D confocal images for uncoated and HS-HA-coated Au NPs. (A) ARPE-19 cells without Au NP addition, the control. The cells were exposed to (B) 5-nm nascent Au NPs, (C) HA-coated Au NPs, (D) 10-nm nascent Au NPs, (E) HA-coated Au NPs, (F) 20-nm nascent Au NPs, and (G) HA-coated Au NPs. The last six images indicate that the coating slightly affects the internalized number of Au NPs. (H) 50-nm nascent Au NPs, (I) HA coated Au NPs, (J) 100-nm nascent Au NPs, and (K) HA coated Au NPs. All the exposure experiments were conducted at the lethal dose (LD_{50}) of the nanoparticle of interest. The difference in the

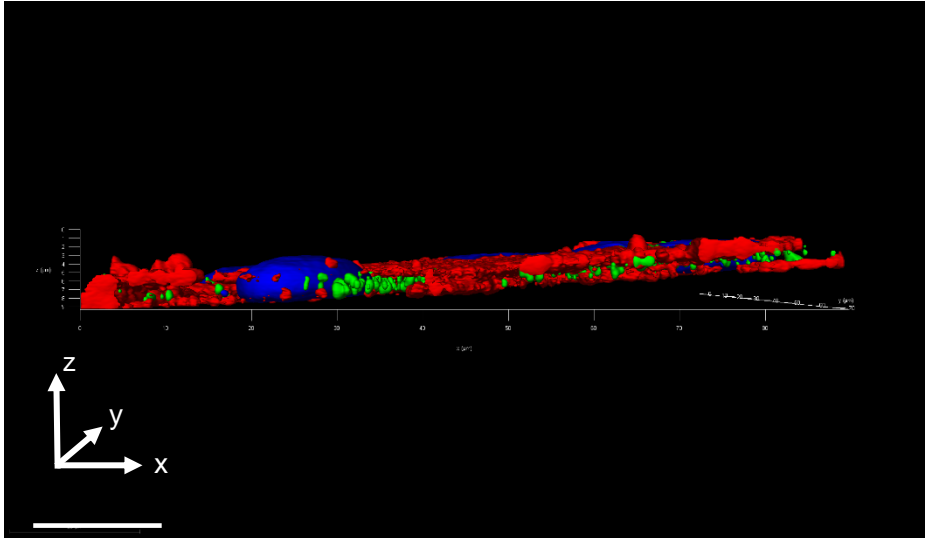
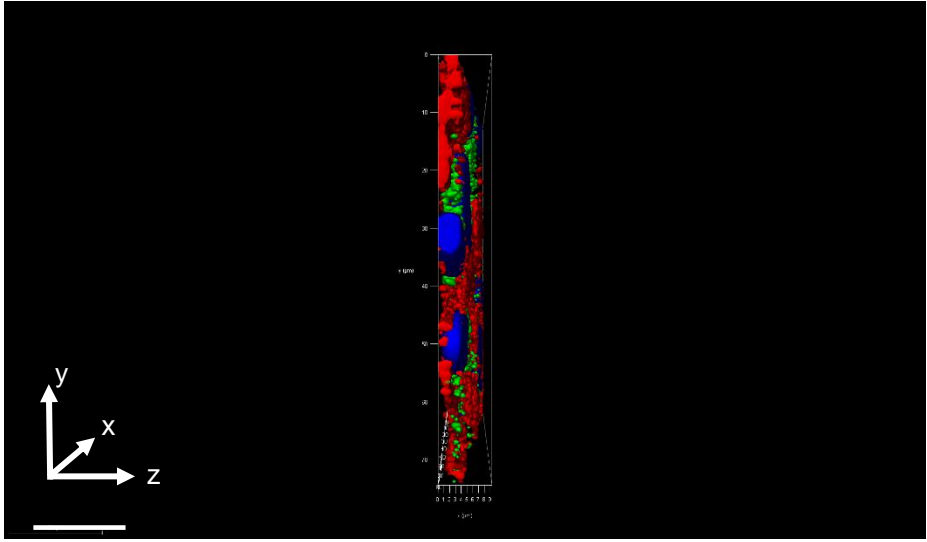
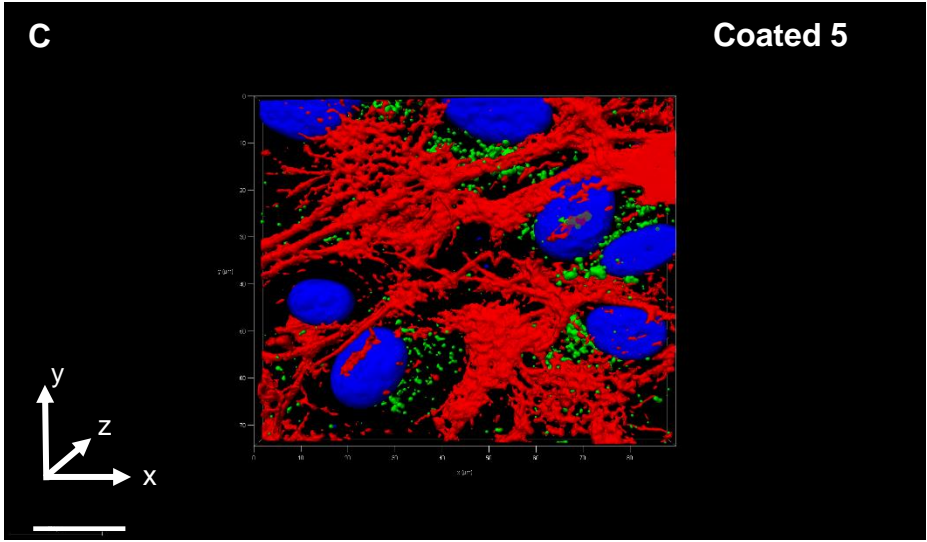
number of internalized NPs (indicated with arrows) increased significantly with the presence of HA coating for the larger particles. Also, when the cells are exposed to coated NPs, the actin density is not hindered, unlike the cells which are exposed to nascent NPs. (L) ARPE-19 cells were treated with 10x HS-HA prior to the addition of 0.5 mg/ml HS-HA coated 50-nm Au NPs. The internalization of HS-HA-Au NPs was significantly more than for the cells which were not pretreated with HA. This finding confirms the role of CD44 receptors on receptor-mediated endocytosis of HA-Au NPs in retinal cells.

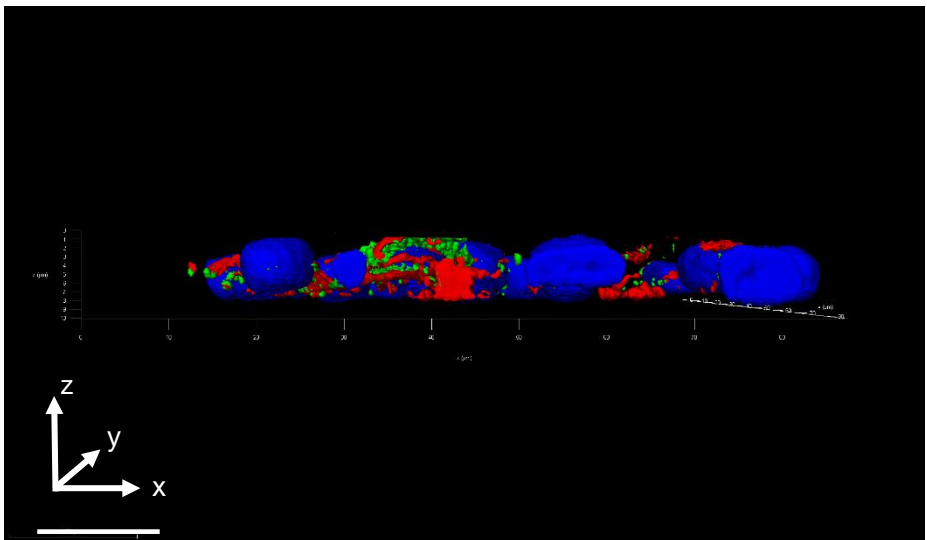
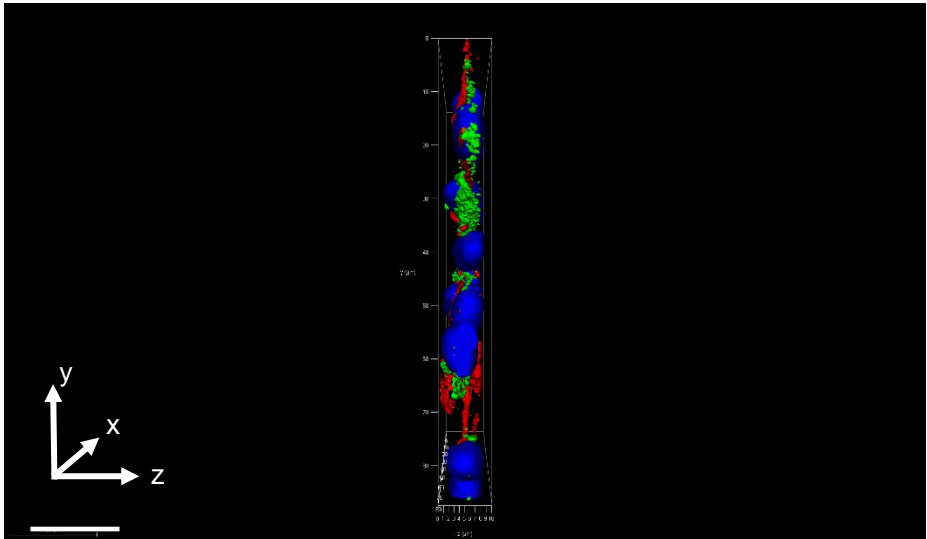
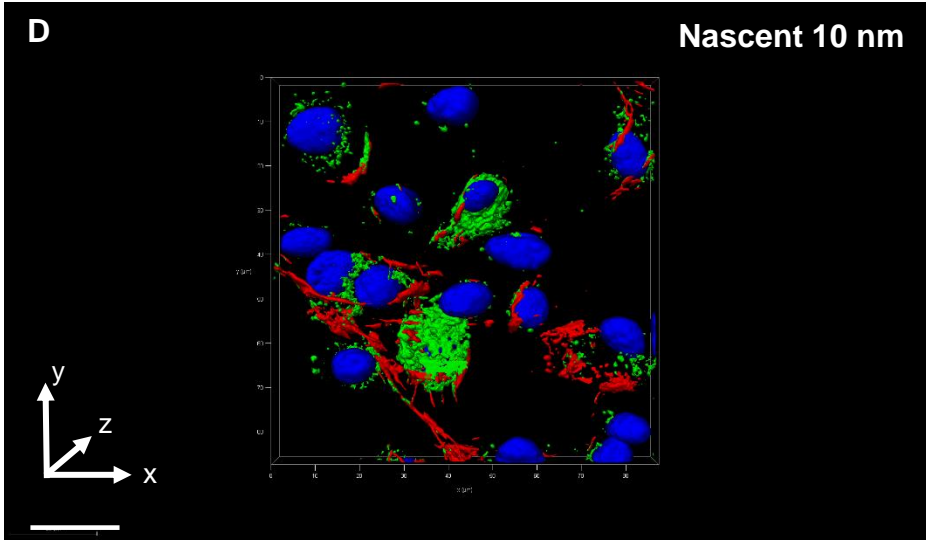


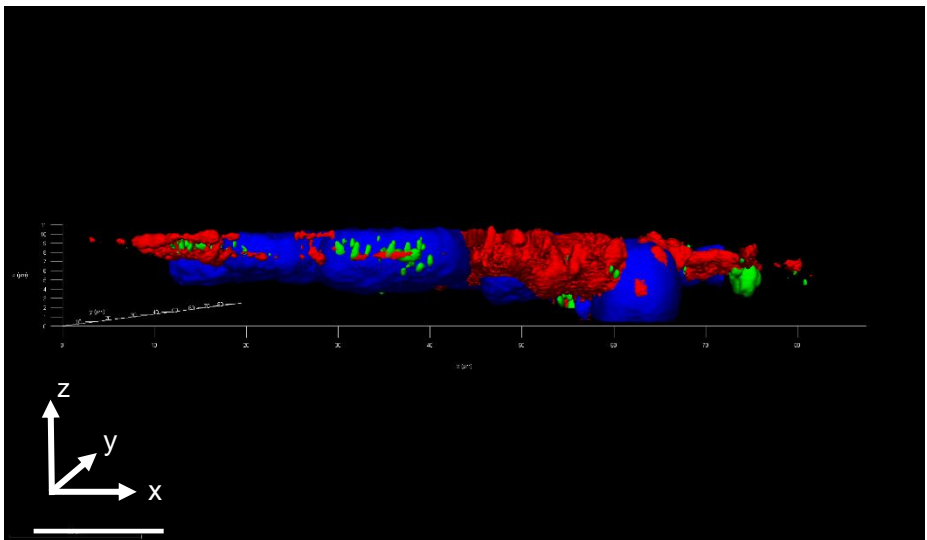
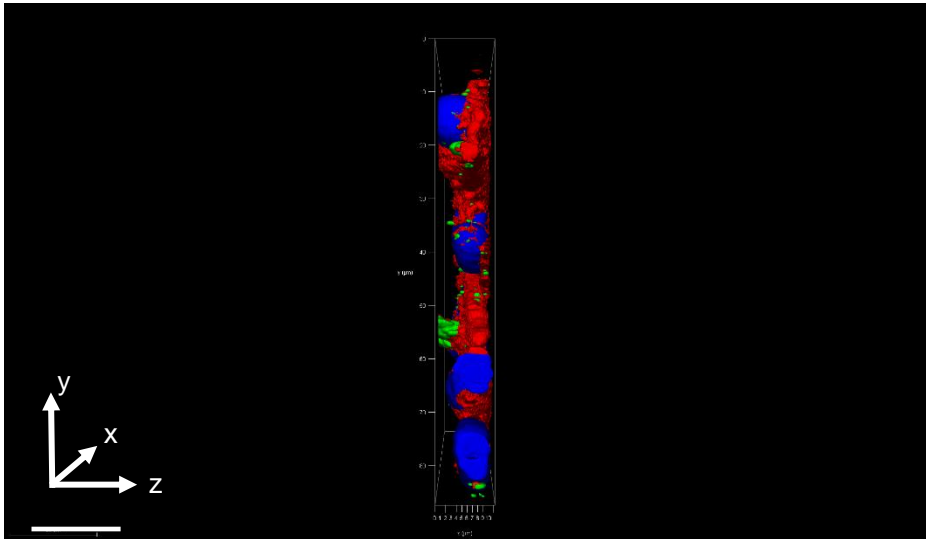
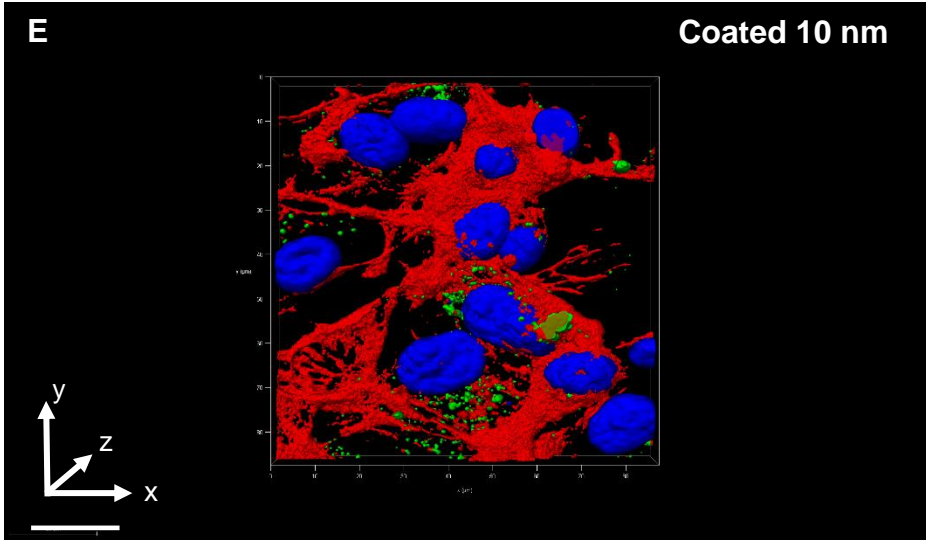
B

Nascent 5 nm



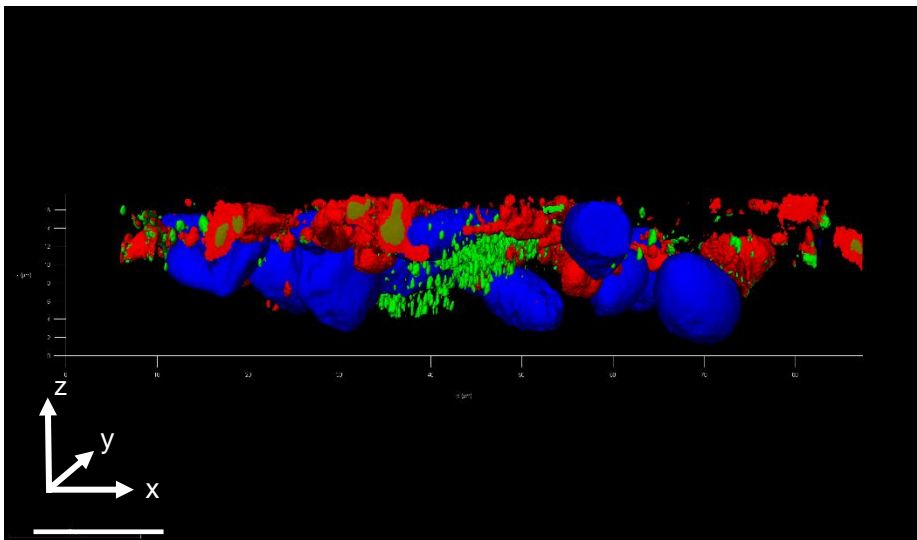
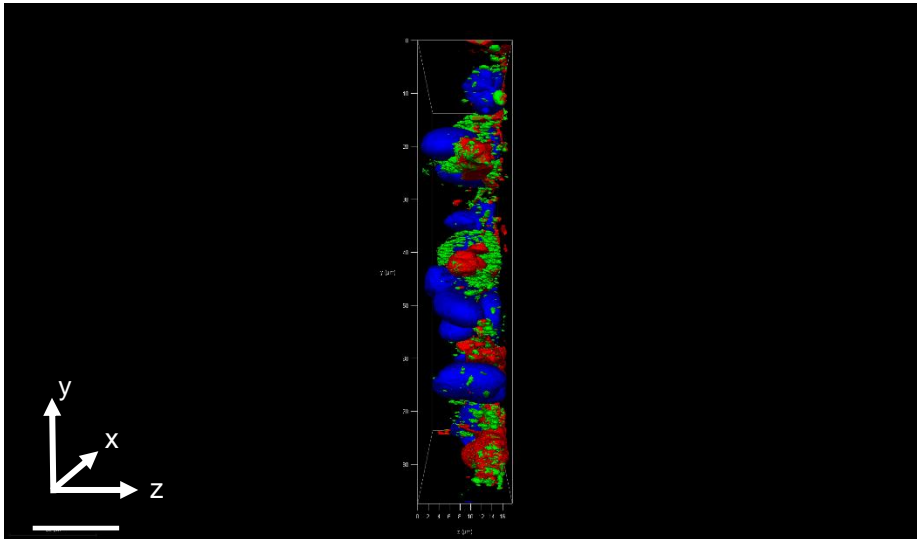
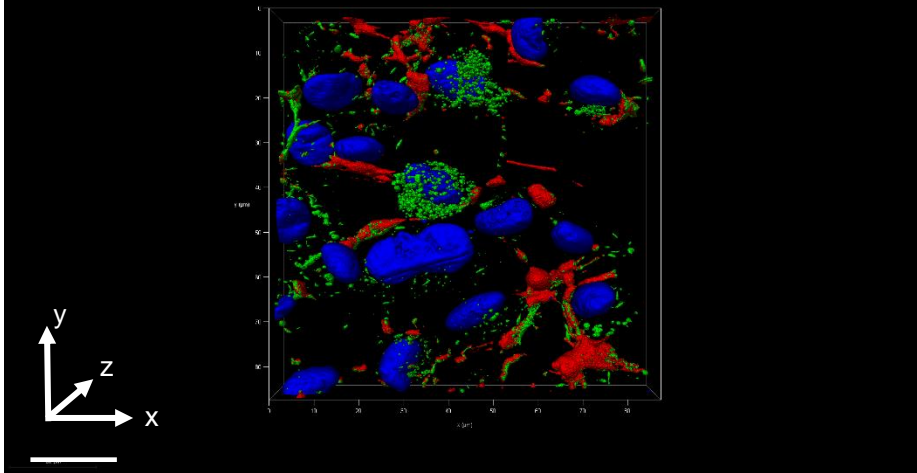


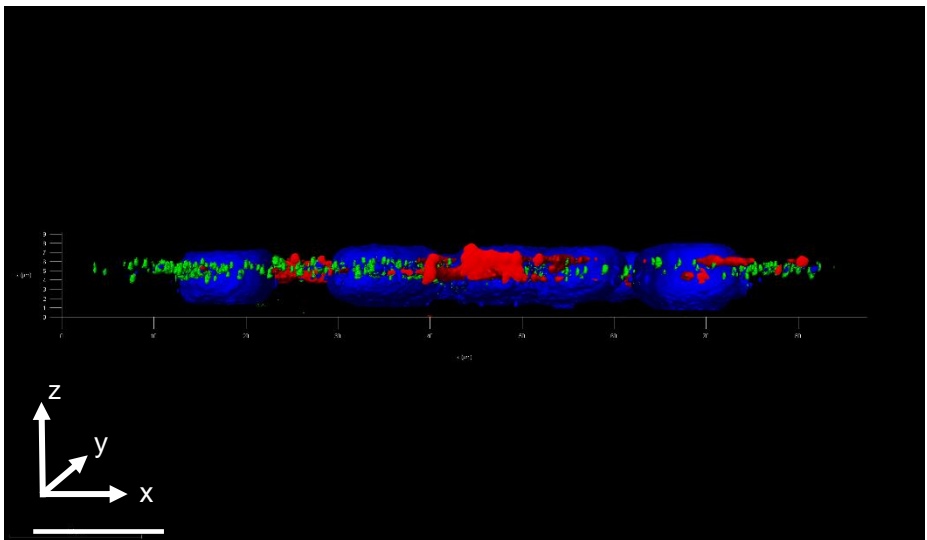
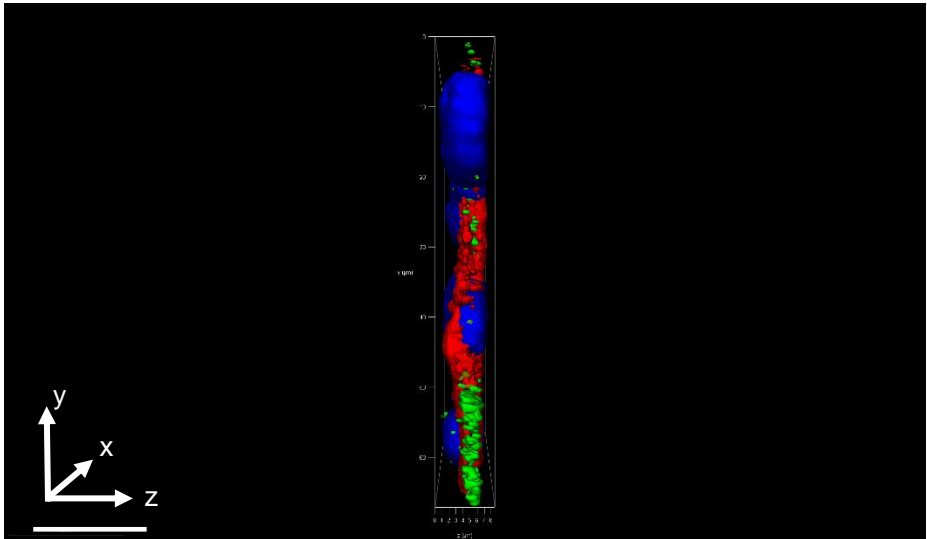
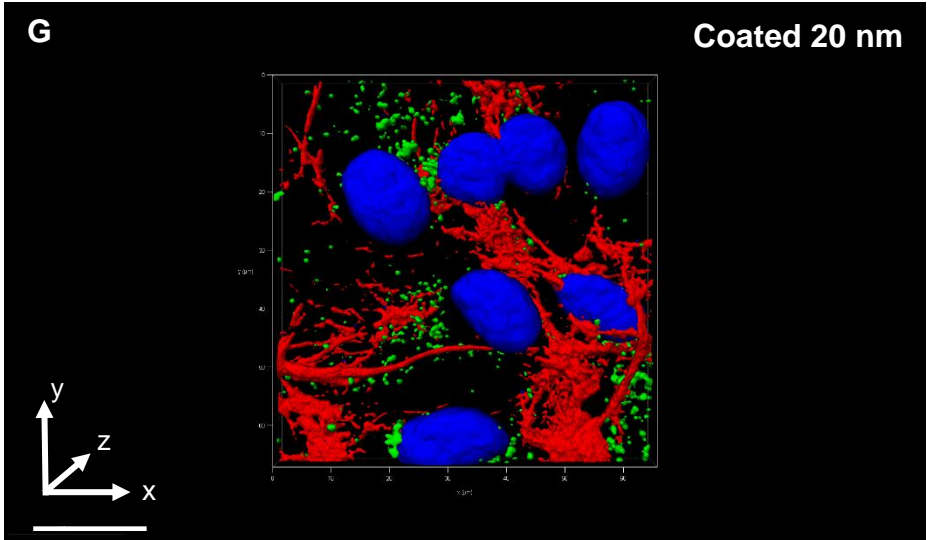




F

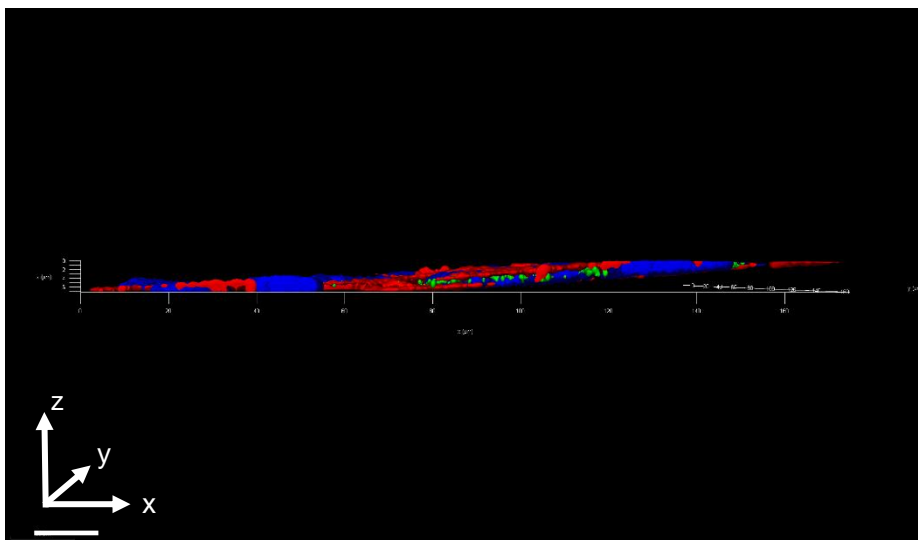
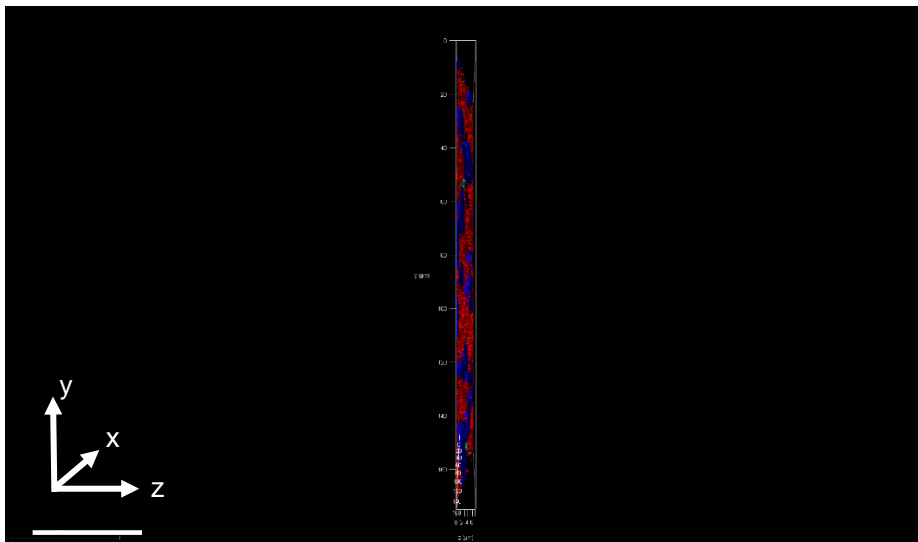
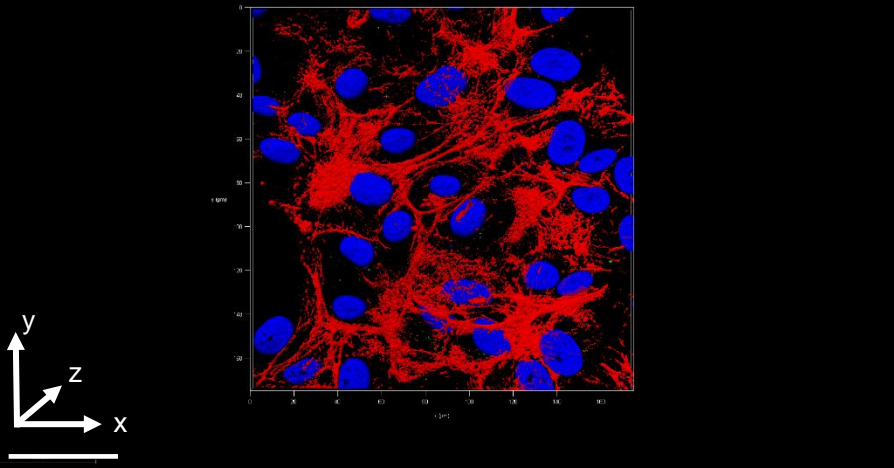
Nascent 20 nm

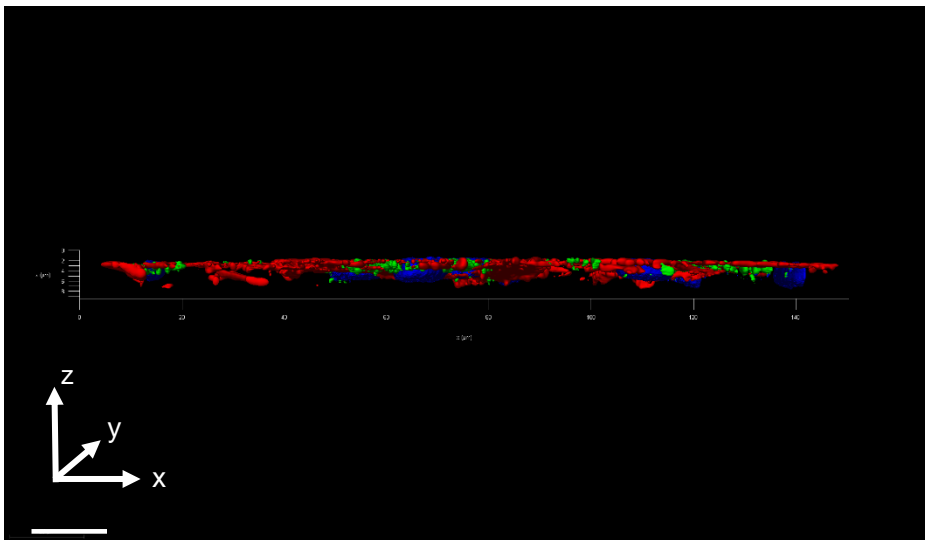
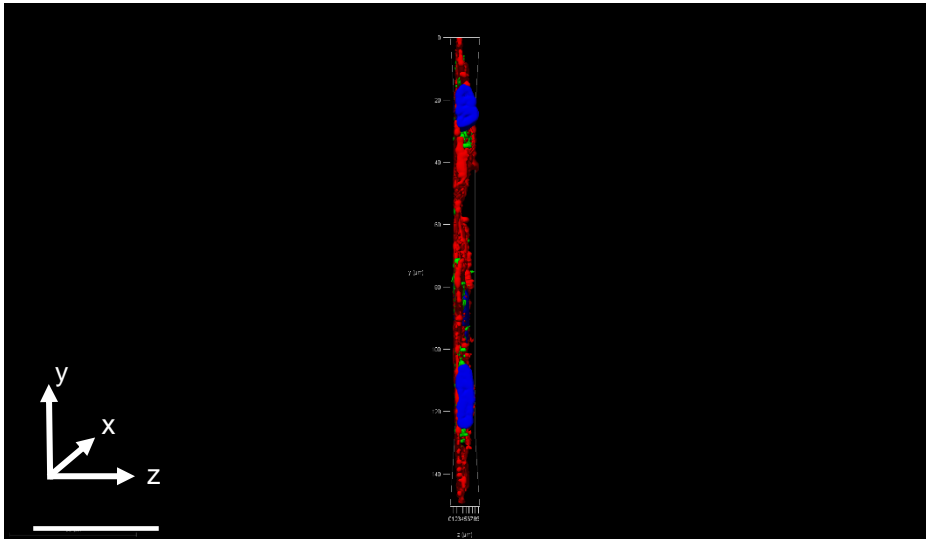
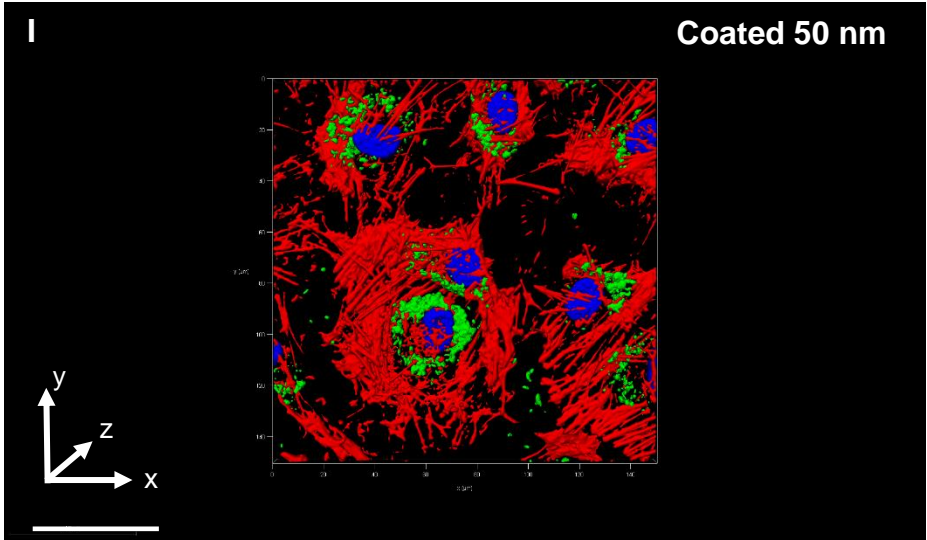




H

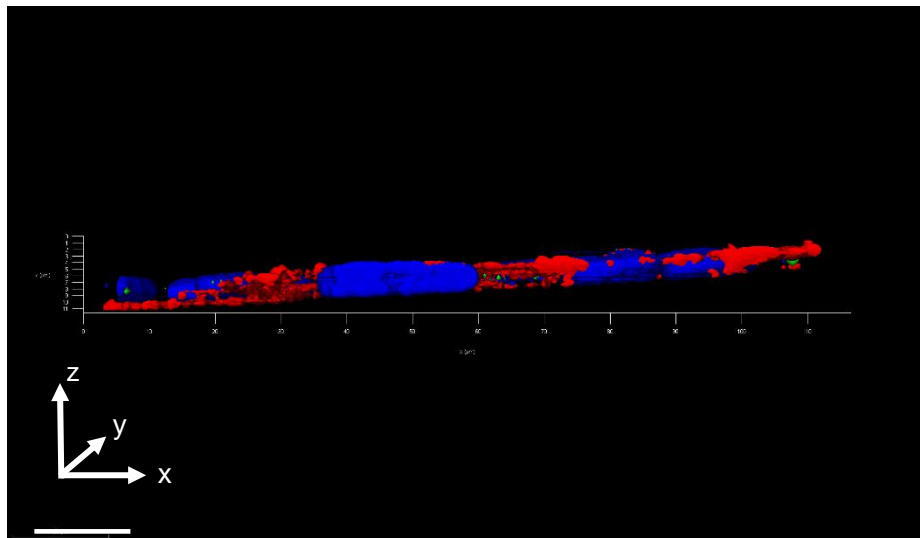
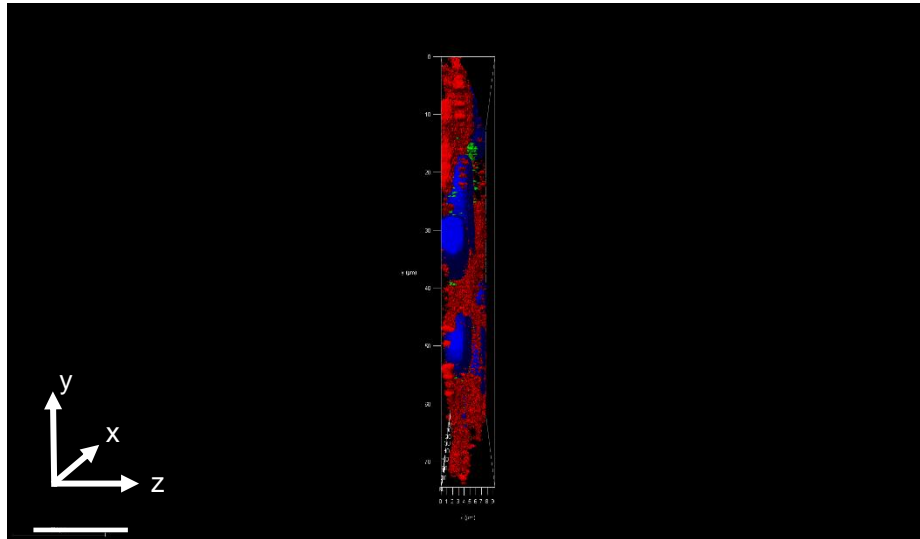
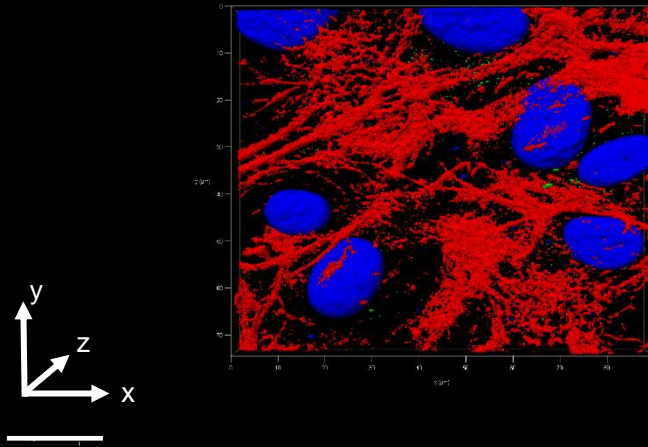
Nascent 50 nm

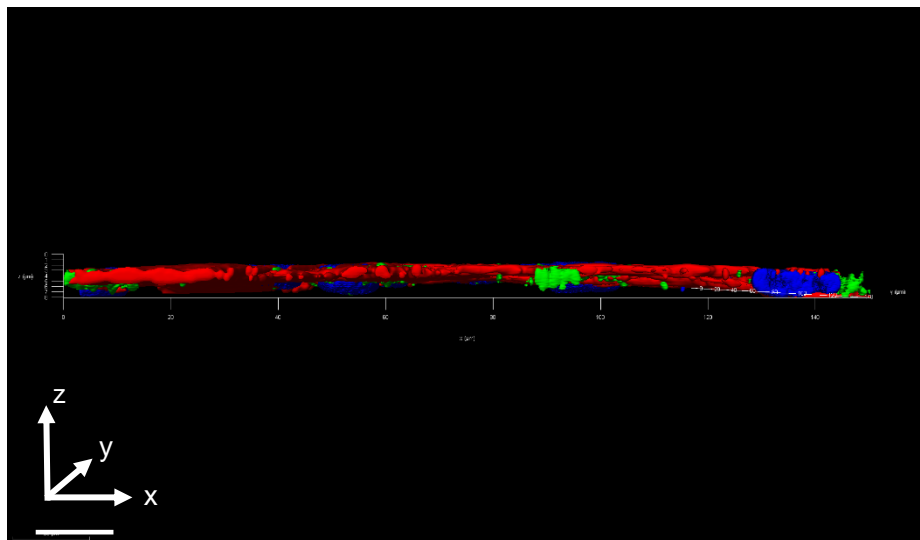
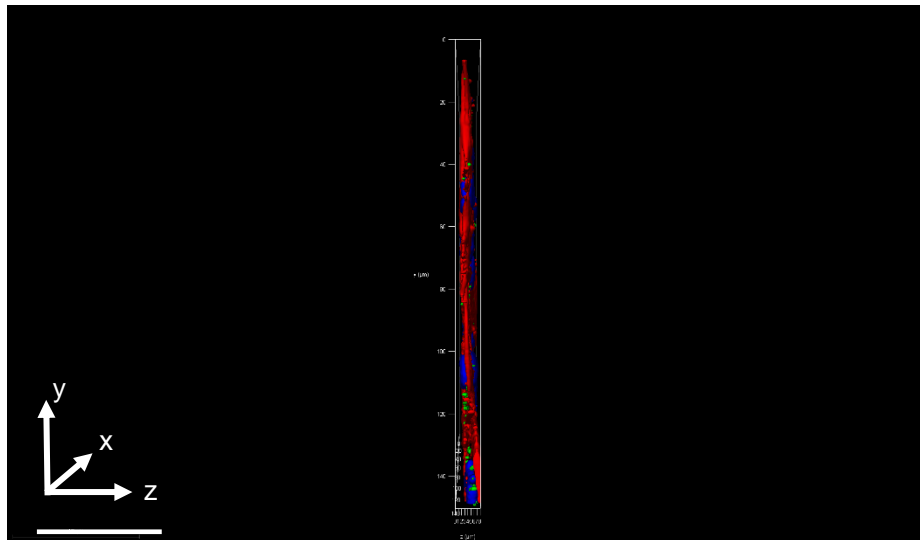
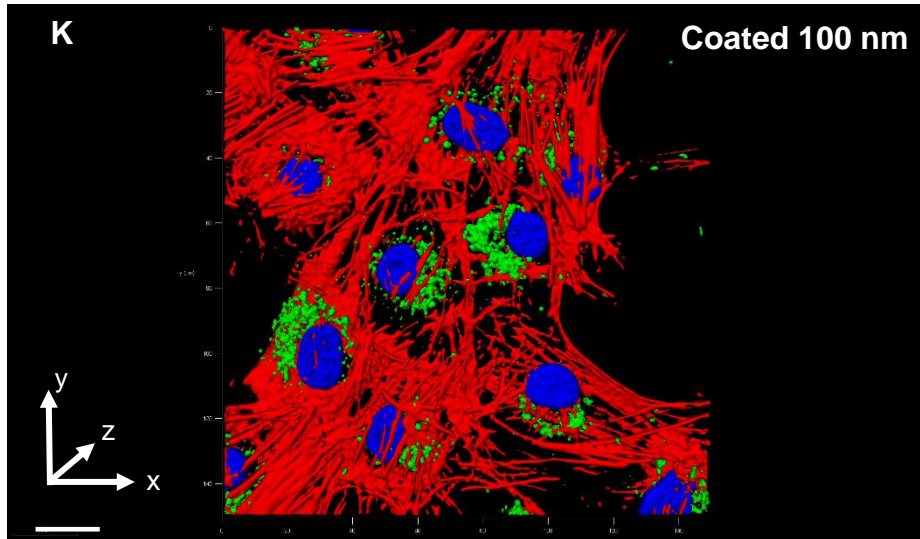




J

Nascent 100 nm





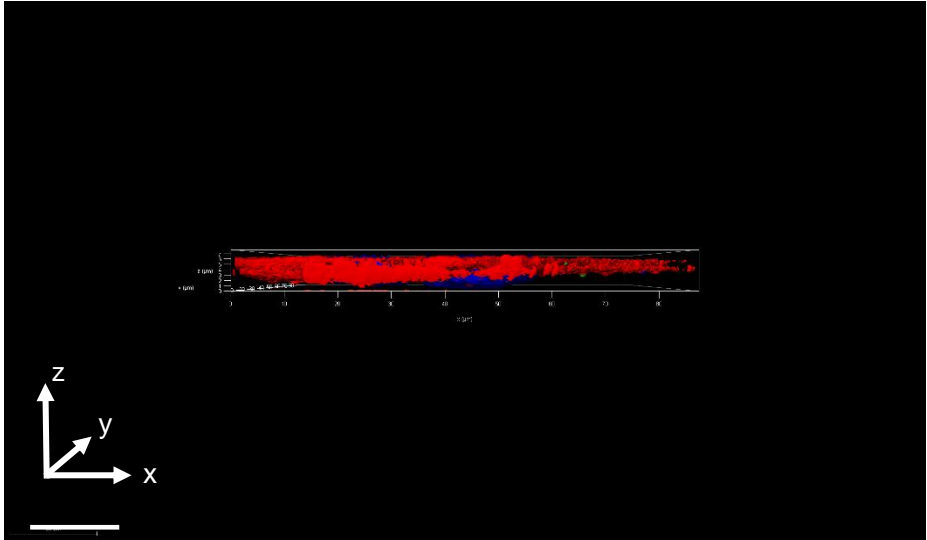
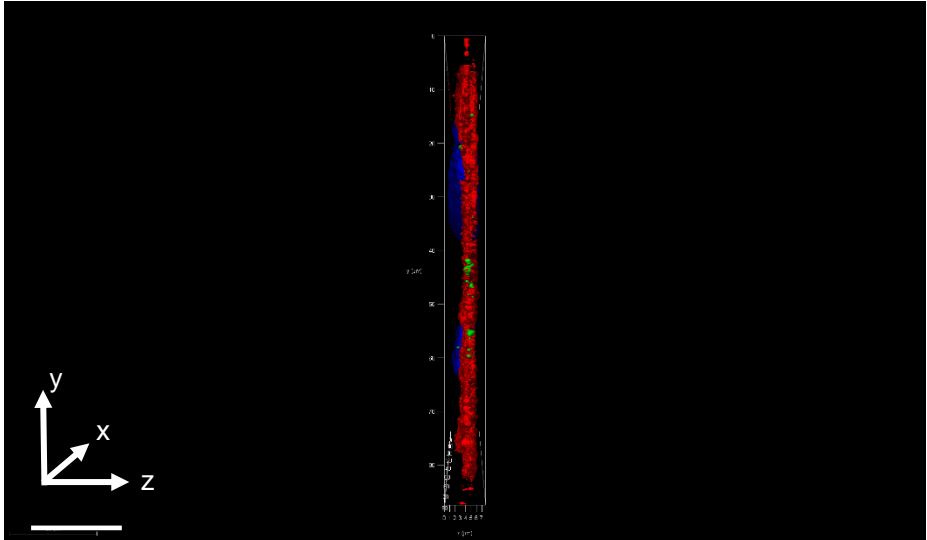
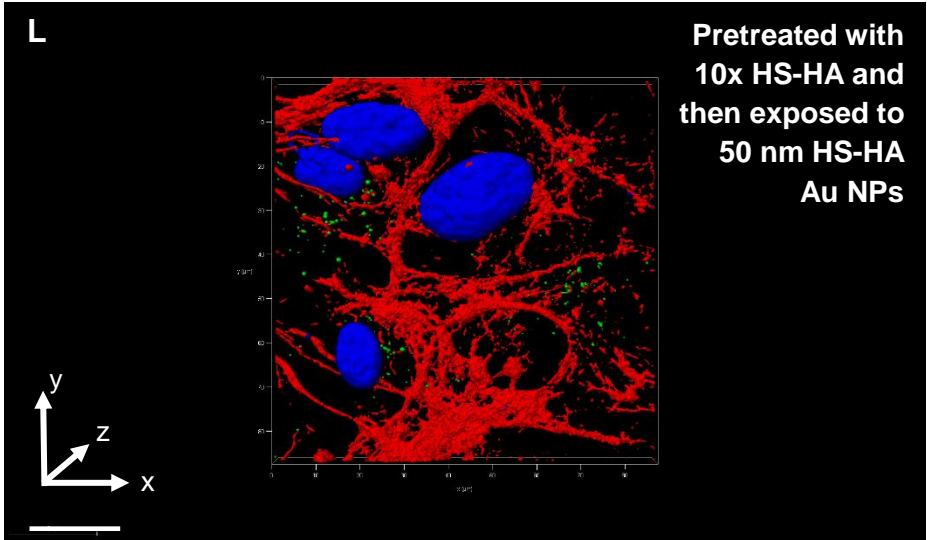
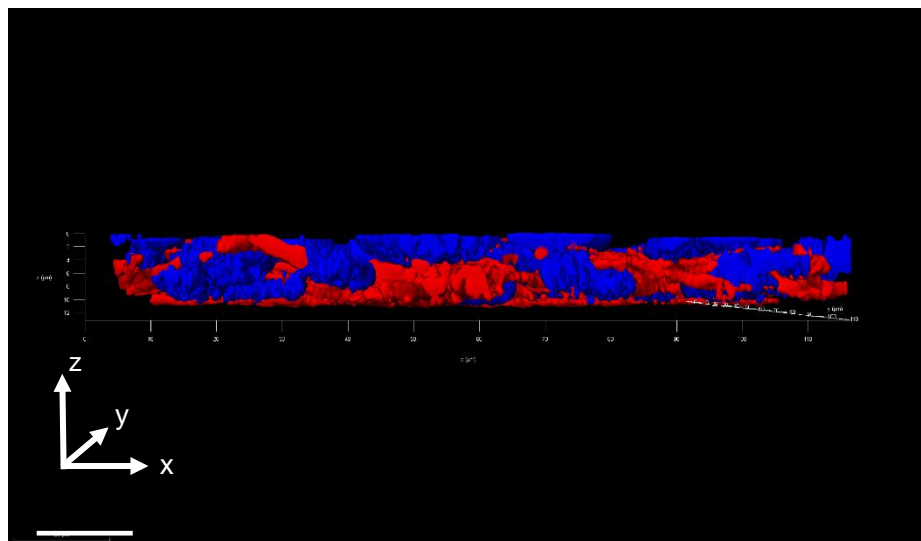
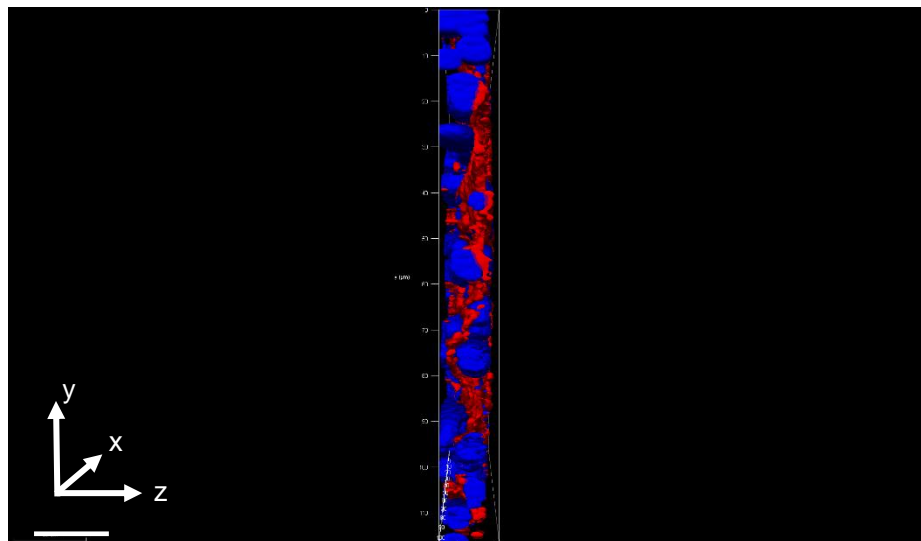
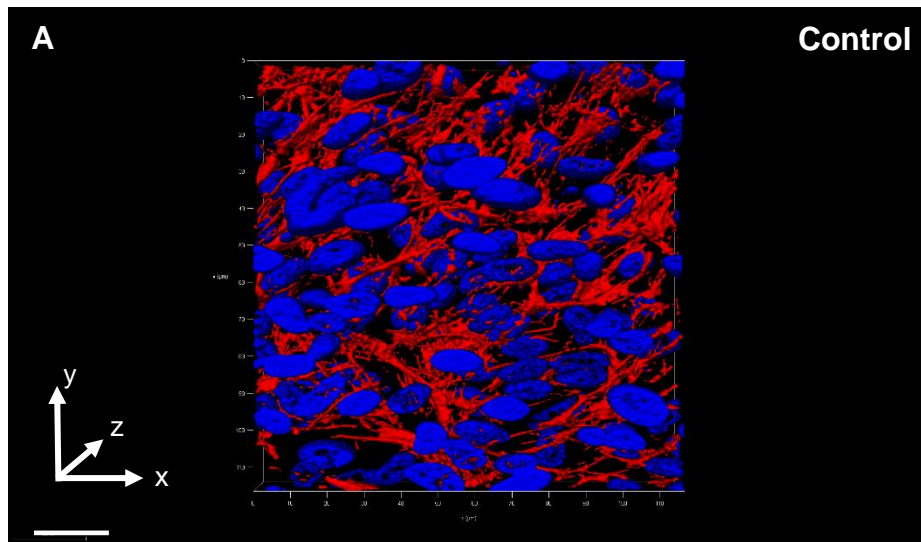
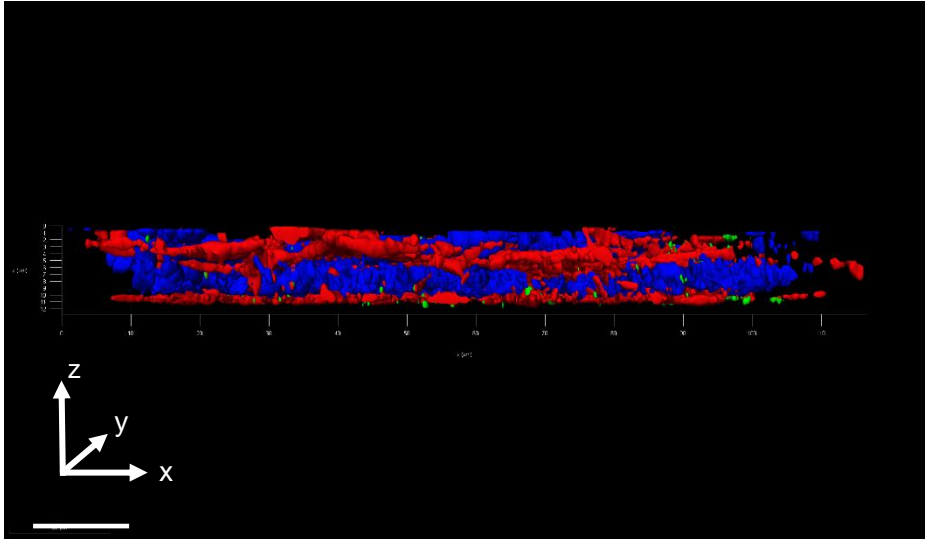
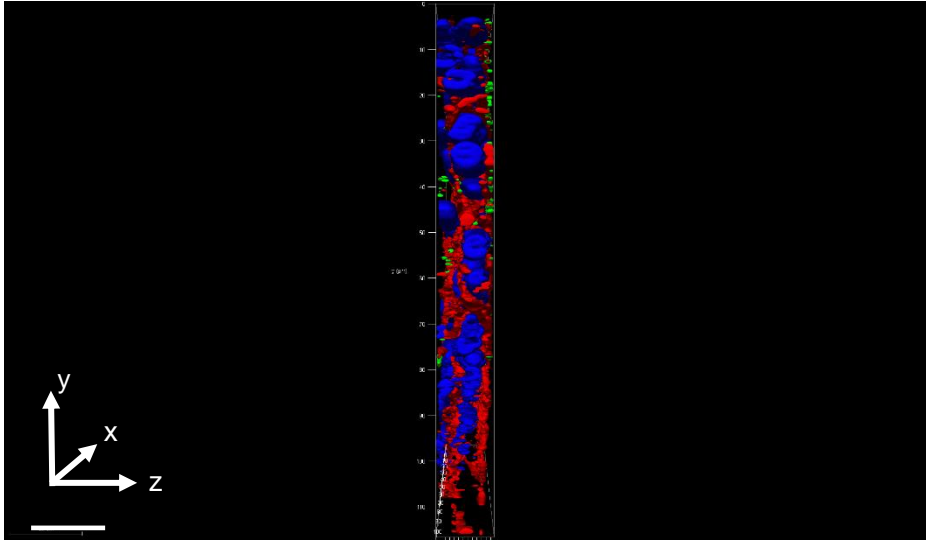
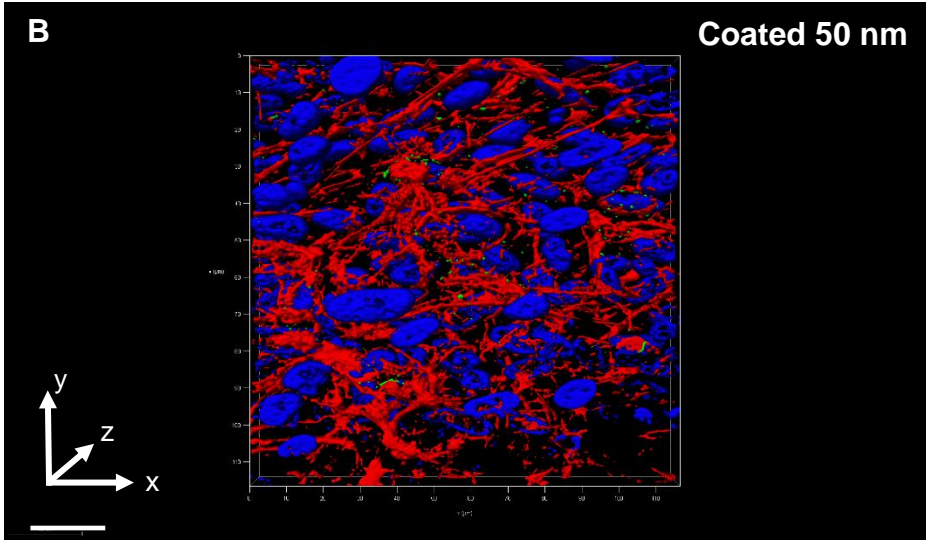


Fig. S7. The red staining corresponds to actin, the nucleus is blue, and Au NPs are green. (A) ARPE-19 cells without Au NP addition, the control. The ARPE-19 cells were exposed to (B) 5-nm nascent Au NPs, (C) 5-nm HS-HA Au NPs, (D) 10-nm nascent Au NPs, (E) 10-nm HS-HA Au NPs, (F) 20-nm nascent Au NPs, (G) 20-nm HS-HA Au NPs, (H) Cells exposed to 50-nm nascent Au NPs, (I) ARPE-19 cells with HS-HA Au NPs, where the size increased to 95.07 ± 25.98 , as shown by DLS results, (J) Cells exposed to 100-nm nascent Au NPs, (K) ARPE-19 cells with HS-HA-coated Au NPs, where the size increased to 127.5 ± 42.21 , as shown by DLS. Although the nascent and relatively smaller nanoparticles did not enter the cells, when coated with SH-HA, the NPs presence in the cells was drastically increased. Also, when the cells are exposed to coated NPs, the actin density is not hindered, unlike the cells which are exposed to nascent NPs. (L) ARPE-19 cells treated with 10x SH-HA prior to the addition of 0.5 mg/ml HS-HA Au NPs. The internalization of HA-Au NPs was significantly less than for cells which were not pretreated with HA. This finding confirms the role of CD44 receptors on receptor-mediated endocytosis of HS-HA Au NPs. Scale bars are 20 μ m.





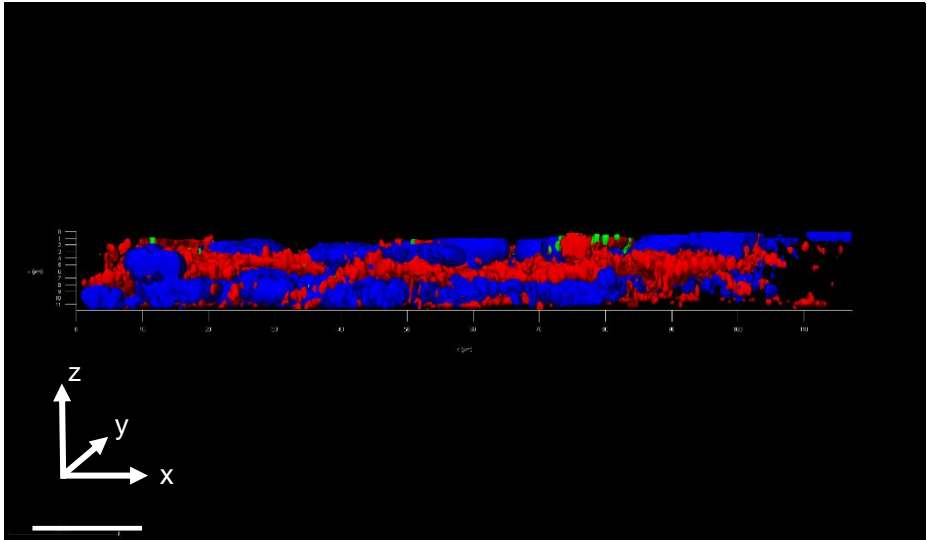
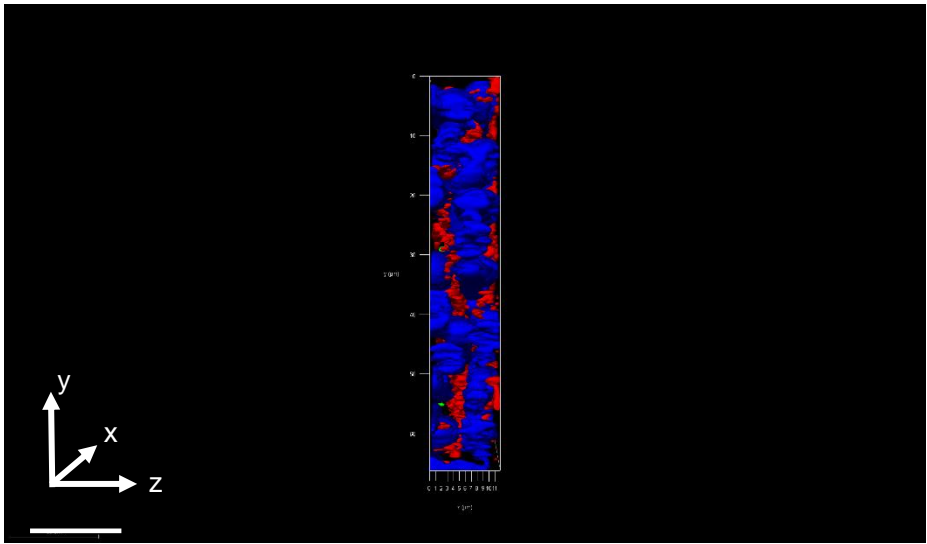
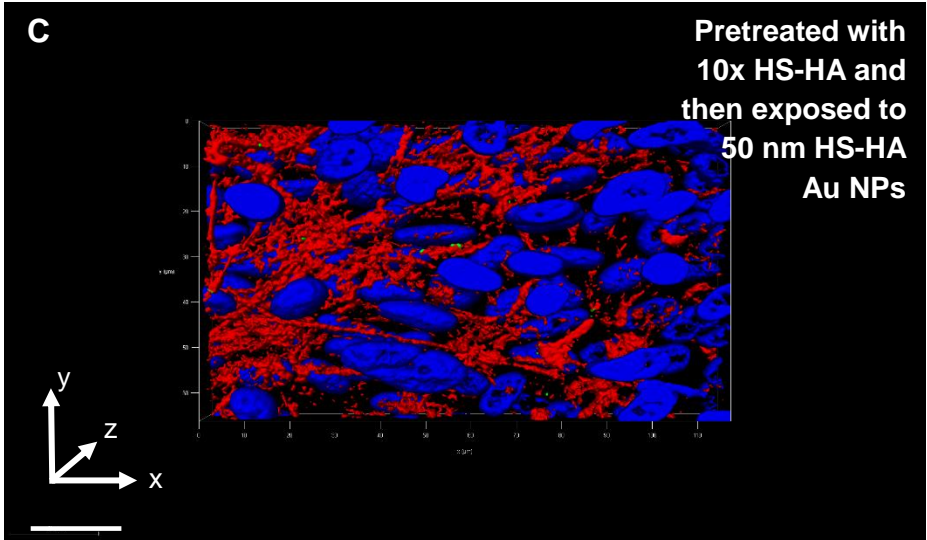
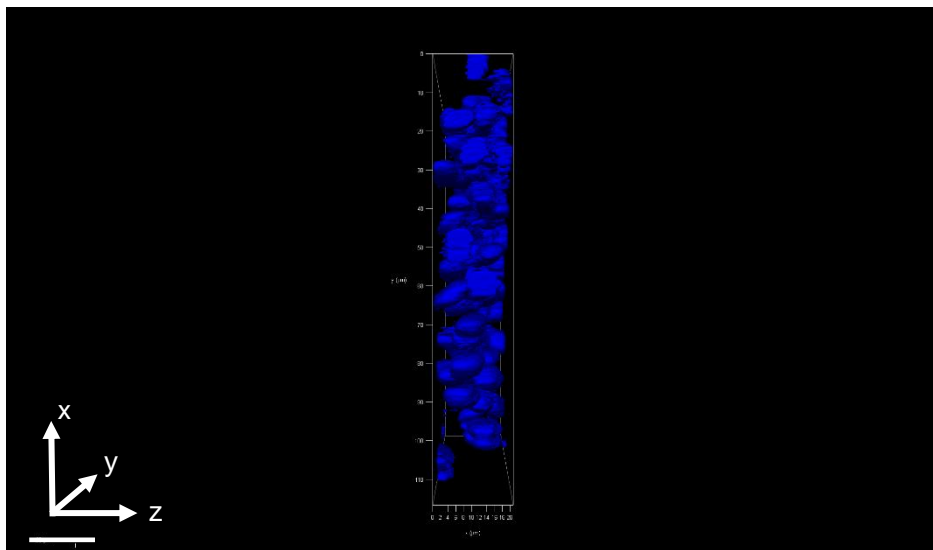
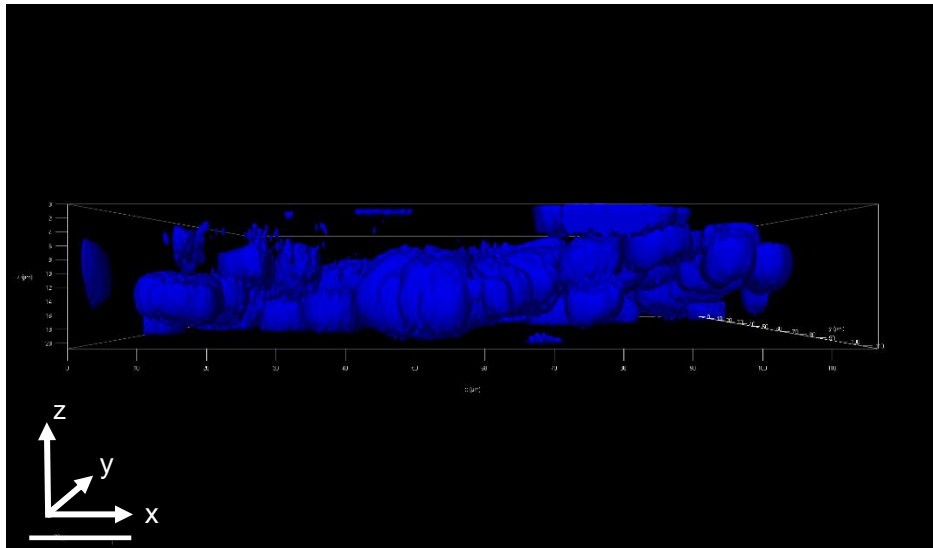
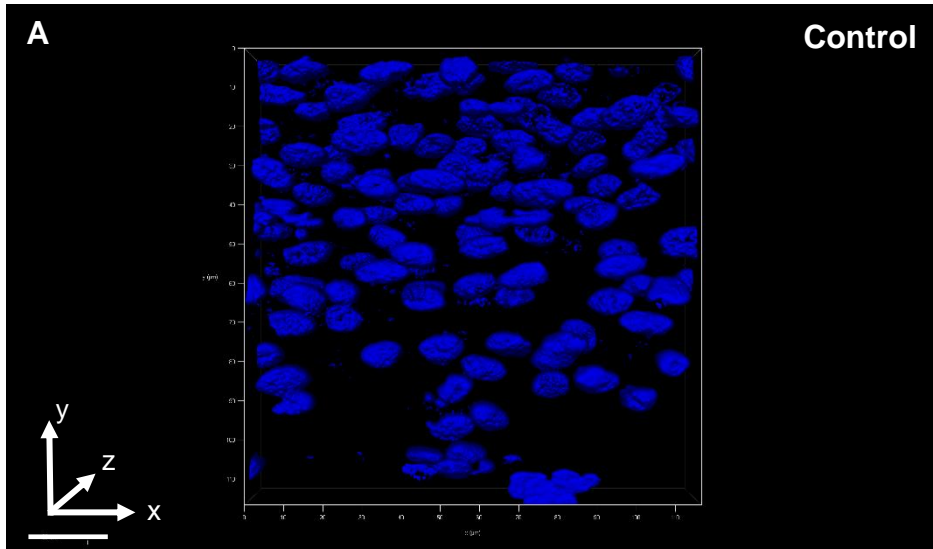
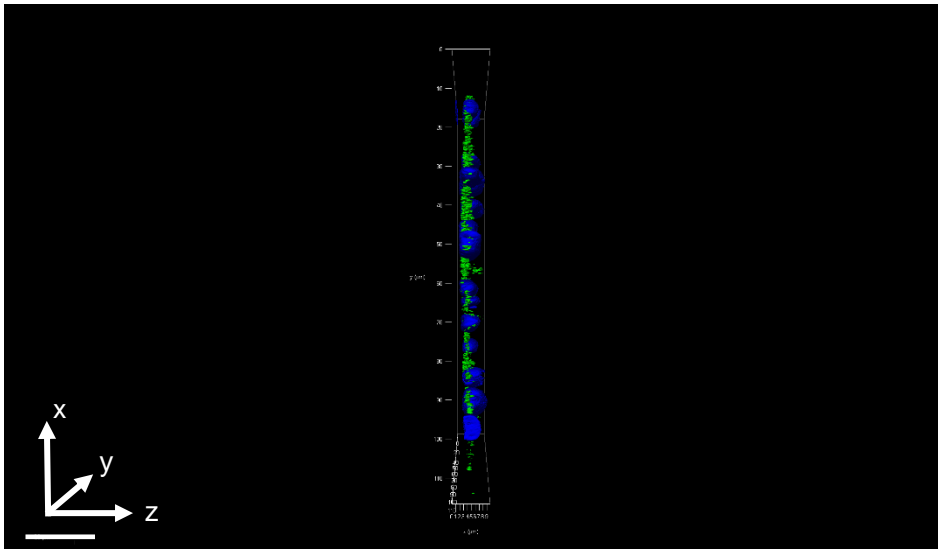
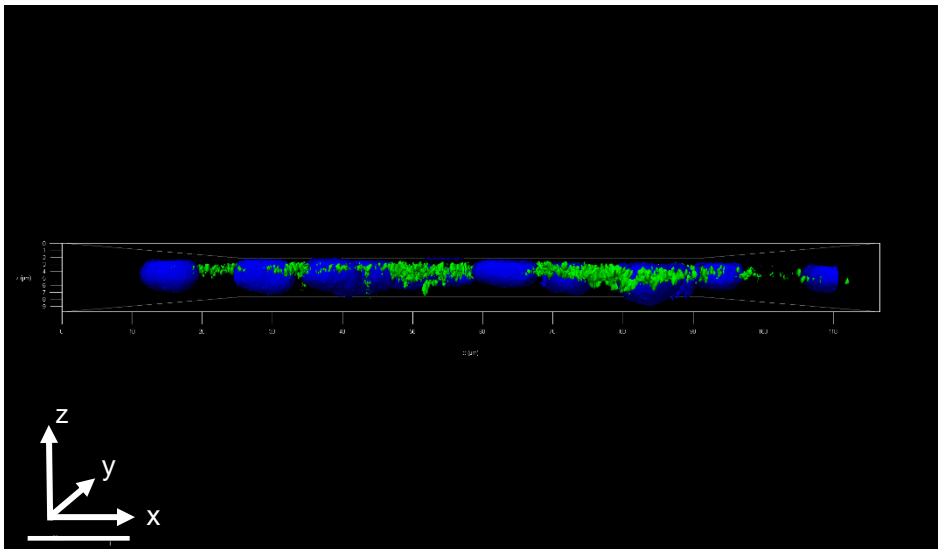
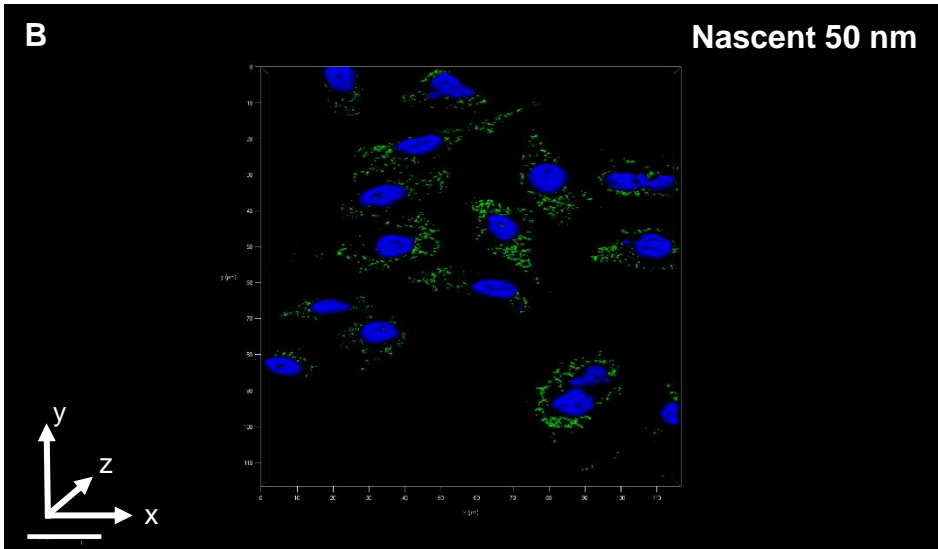
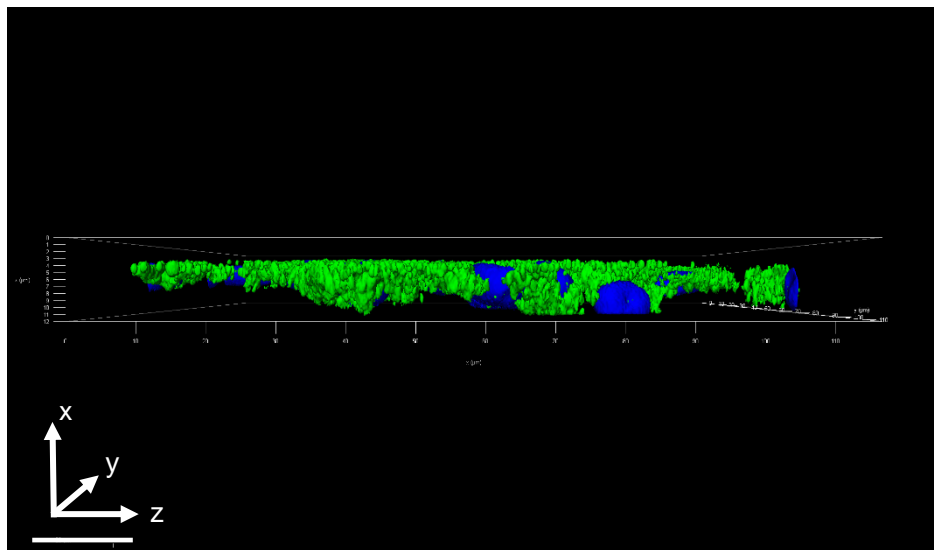
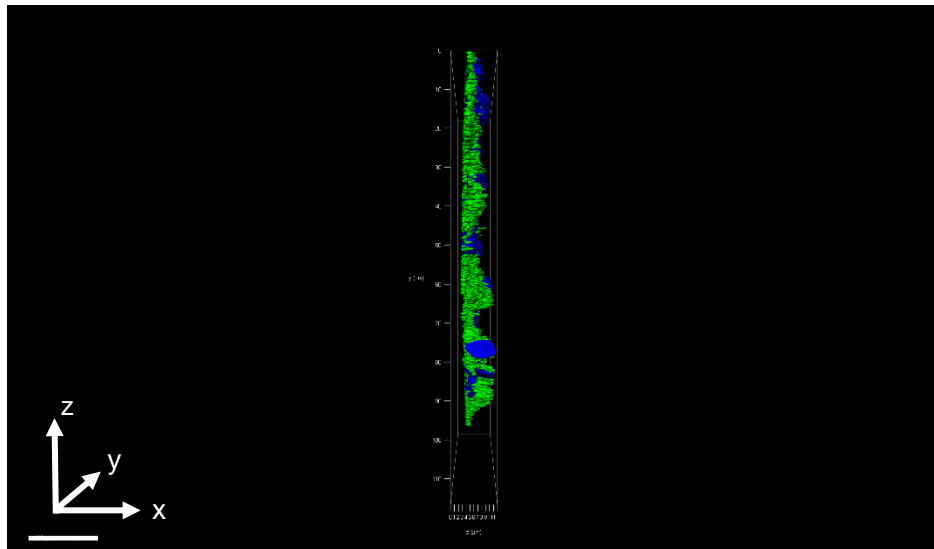
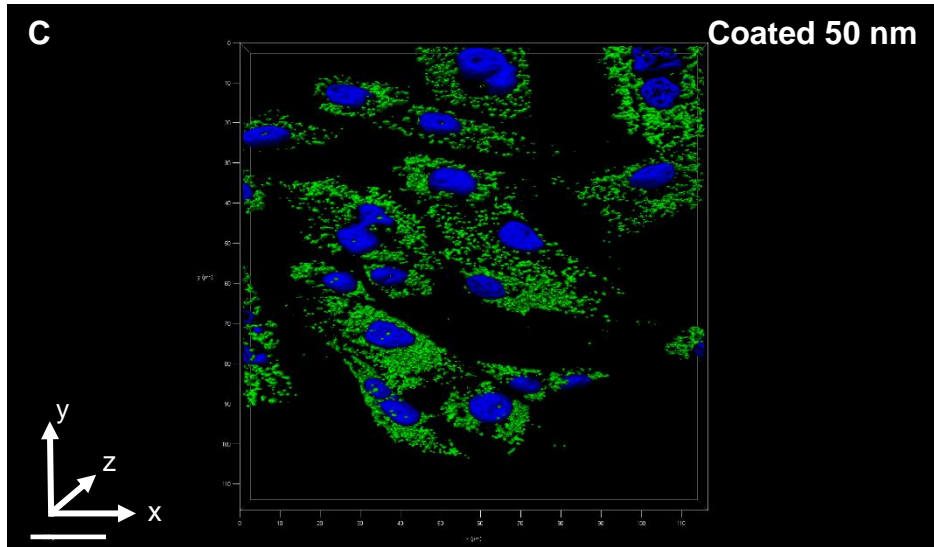


Fig. S8. The red staining corresponds to actin, the nucleus is blue, and Au NPs are green. (A) 3T3 cells without Au NP addition, the control, (B) 3T3 cells exposed to HA-Au NPs (dp=50 nm), (C) 3T3 cells treated with 10x end-thiolated HA prior to the exposure to 0.5 mg/ml HA coated 50-nm Au NPs. The internalization of 50-nm Au NPs was not affected by the presence of HA coating because 3T3 cells are known to have a fewer number of CD44 receptors which is the analog for the CD44 receptor. Scale bars are 20 μ m.







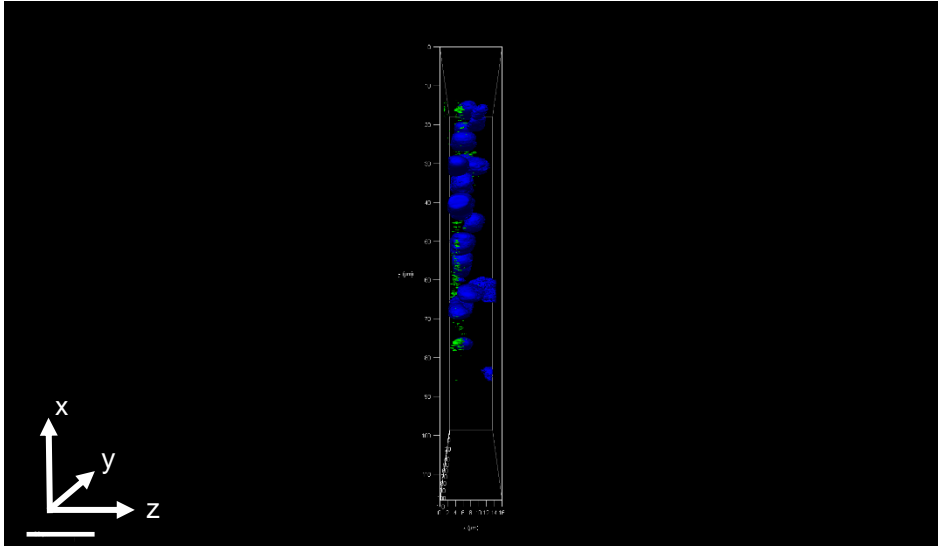
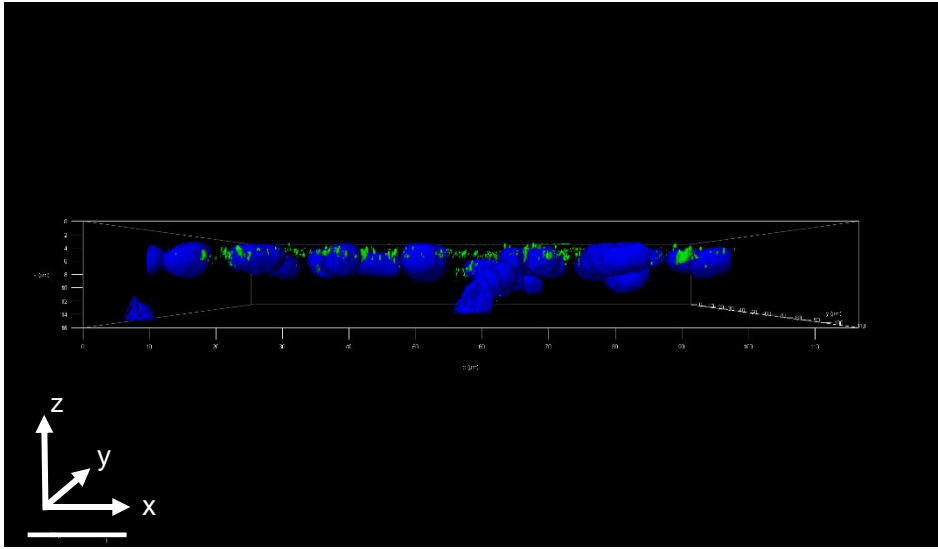
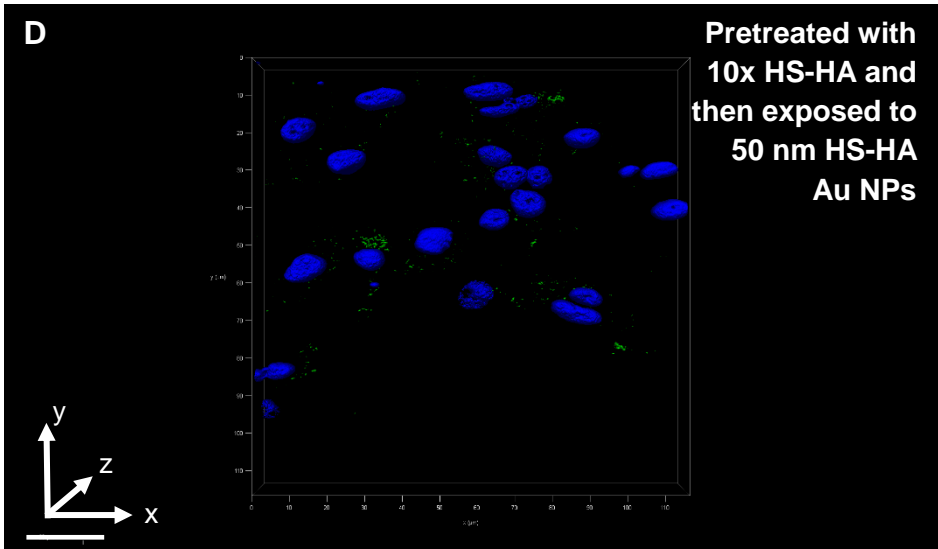


Fig. S9. The CHO cells were not stained for actin. The nucleus is blue and Au NPs are green. CHO cells (A) without Au NP addition, the control. (B) cells exposed to nascent Au NPs (dp=50 nm). (C) cells exposed to 50- nm HS-HA-Au NPs. (D) cells treated with 10x end-thiolated HA prior to exposure to 50- nm HS-HA coated Au NPs. The internalization of 50- nm Au NPs was affected drastically by the presence of HA coating because CHO cells are known have CD44 receptors, and since they are cancer cells, the number of receptors expressed is higher than normal cells. Scale bars are 20 μ m.

REFERENCES

1. G. L. Ellman, *Archives of Biochemistry and Biophysics*, 1959, **82**, 70-77.
2. B.-P. Jiang, L. Zhang, Y. Zhu, X.-C. Shen, S.-C. Ji, X.-Y. Tan, L. Cheng and H. Liang, *Journal of Materials Chemistry B*, 2015, **3**, 3767-3776.
3. J. J. Ahire, D. Robertson, D. P. Neveling, A. J. van Reenen and L. M. T. Dicks, *Rsc Advances*, 2016, **6**, 34791-34796.
4. P. Buffat and J. P. Borel, *Physical Review A*, 1976, **13**, 2287-2298.
5. B. B. Karakocak, R. Raliya, J. T. Davis, S. Chavalmane, W.-N. Wang, N. Ravi and P. Biswas, *Toxicology In Vitro*, 2016, **37**, 61-69.

Appendix III. Supporting Materials for
Chapter 4

Table S1. Experimental conditions (factors) of each nCDs synthesis using CCD-RSM design

Runs	CA wt%	NH₂/COOH	Reaction Time (s)
1	10.0	0.75	88
2	11.2	0.48	80
3	10.0	0.75	100
4	10.0	0.75	88
5	8.8	1.02	95
6	12.0	0.75	88
7	8.8	0.48	80
8	10.0	0.75	75
9	10.0	0.75	88
10	11.2	1.02	95
11	10.0	0.75	88
12	8.0	0.75	88
13	8.8	0.48	95
14	8.8	1.02	80
15	10.0	0.75	88
16	10.0	1.20	88
17	10.0	0.30	88
18	10.0	0.75	88
19	11.2	0.48	95
20	11.2	1.02	80

Table S2. The effect of molar ratio of reactants to *pyrrolic* N content and MW of nCDs.

Molar ratio of EA/CA	XPS results (intensity, au) Pyrrole content	Maldi-TOFF results m/z
0.5	413.0	799.6
1.0	778.0	1215.0
2.0	1663.0	1512.0

Table S3. Quantum yield measurements of nCDs.

NH ₂ /COOH	Quantum Yield, Φ (%)
0.25	7.0
0.50	15.0
1.00	10.7
1.50	13.9
2.00	10.3

1.1. Statistical Analysis.

For PL results at the short wavelength, the analysis of variance suggested that the quadratic regression model was most appropriate among all polynomial regression models. First, the sequential model sum of squares indicated that the quadratic regression was the highest order, with the sequentially added terms being significant, and the model was not aliased (F -value = 14.06 and P -value = 0.001, when comparing the quadratic regression to the 2FI regression). Second, the lack of fit F -value = 0.62, and the P -value = 0.67, which jointly imply that the quadratic model fits well, while lower order models all indicated a significant lack of fit. Thus, quadratic regression was used in this analysis, as below:

$$PL (Ex 350 \text{ nm}, Em 460 \text{ nm}) = -2.21 \times 10^6 + 4.38 \times 10^5 \times (amine/acid) + 4.89 \times 10^4 \times Time - 815 \times (amine/acid) \times Time - 2.27 \times 10^5 \times (amine/acid)^2 - 277 \times Time^2 \quad (\text{Eq. S1})$$

This quadratic model is graphically represented in Fig. 1 by a three-dimensional response surface. The model is statistically significant, with a model F -value = 13.23 and P -value = 0.0001. The coefficient of determination $R^2 = 0.84$, and the adjusted $R^2 = 0.77$, indicating a good fit; further, the predicted $R^2 = 0.63$ is in reasonable agreement with the adjusted R^2 , suggesting the quadratic regression model also has high predictive ability for new observations.

The normal probability plot in Fig. 1A shows points close to the diagonal, which means a normal pattern was observed for the regression residuals. The residual plot shows no outlier or special pattern for the data. Thus, there were no problems detected from the model diagnostics.

As predicted by the model, CDs with the highest intensity of PL at $\lambda_{ex}/\lambda_{em} = 350 \text{ nm}/460 \text{ nm}$ were produced with an amine/acid ratio of 0.75 and a reaction time 88.0 seconds.

The sequential model sum of squares indicates that the linear regression is the suggested highest order, with the sequentially added terms being significant, and again the model is not aliased (F -value = 63.07 and P -value < 0.0001 when comparing the linear regression to the mean regression). Second, the lack of fit F -value = 1.42 and the P -value = 0.37, which jointly imply no significant lack of fit relative to the pure error. Thus, the linear regression was used in this analysis. The linear equation is listed below:

$$PL (Ex 540 \text{ nm}, Em 600 \text{ nm}) = -822 + 1.48 \times 10^3 \times (amine/acid) + 9.42 \times Time - 12.3 \times (amine/acid) \times Time \quad (\text{Eq. S2})$$

This linear model is graphically presented in Fig. 1B by a three-dimensional response surface. The model is statistically significant, and again the model F -value = 93.45 and P -value < 0.0001. The coefficient of determination $R^2 = 0.95$, and the adjusted $R^2 = 0.94$, indicating a good fit; the predicted $R^2 = 0.91$ is in reasonable agreement with the adjusted R^2 , suggesting the linear model also has high predictive ability for new observations. The normal probability plot in Fig. 1B shows points close to the diagonal, which means a normal pattern was observed for the regression residuals. The residual plot shows no outlier or special pattern for the data. Thus, there were no problems detected from the model diagnostics.

***In vitro* Cytotoxicity Measurements on Retinal Pigment Epithelial (ARPE-19), Lens Epithelial, and Chinese Hamster Ovary (CHO) cells with MTT, ApoTox-Glo™, and ROS-Glo™ H₂O₂ assays.**

For all three assays, the cells were distributed in a flat-bottom 96-well plate with a 150 μ L volume (1.5×10^6 cells per 20 ml). After plating, cells were incubated for 48 h (37 °C, 5% CO₂), then exposed to different concentrations of nCDs. nCDs exposure was maintained for 24 h before assay measurements. In all biological and imaging tests, the cells without NP exposure served as a negative control

For the MTT assay, following the exposure of nCDs, 100 μ L of MTT (1 mg/l in growth media) were added to each well, and the plate was incubated for an additional 5 h at 37 °C in 5% CO₂. The resulting blue component, produced by the reduction of tetrazolium salt of MTT by mitochondrial dehydrogenase enzyme, was dissolved in 100 μ L dimethyl sulfoxide (DMSO). The optical density of the colored product was read photometrically using a spectrophotometer at 540 nm with a microplate reader (Molecular Devices Spectra Max 190). The absorbance of untreated cells was used as a negative control. The percentage viability of

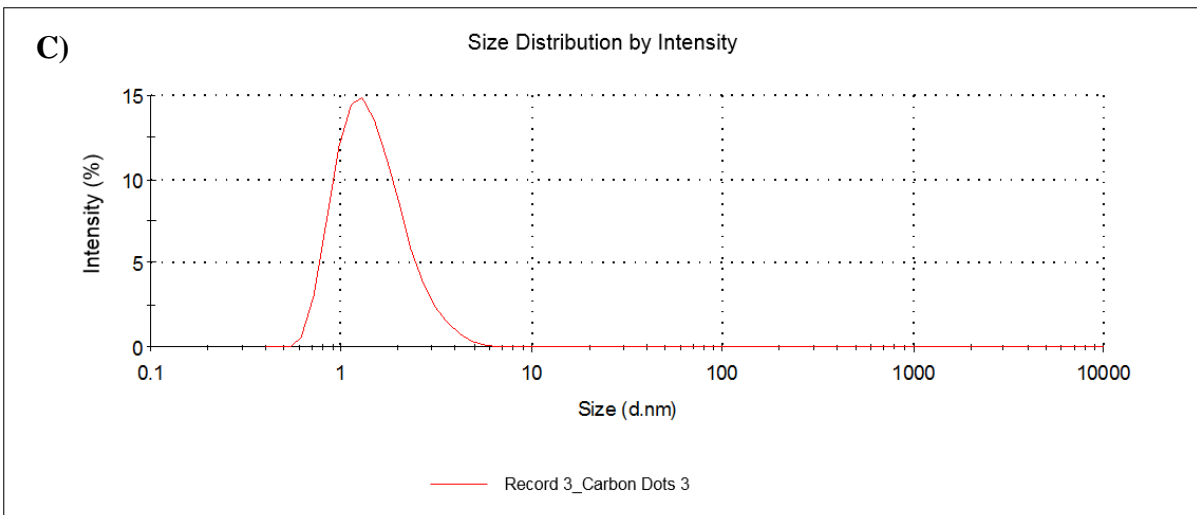
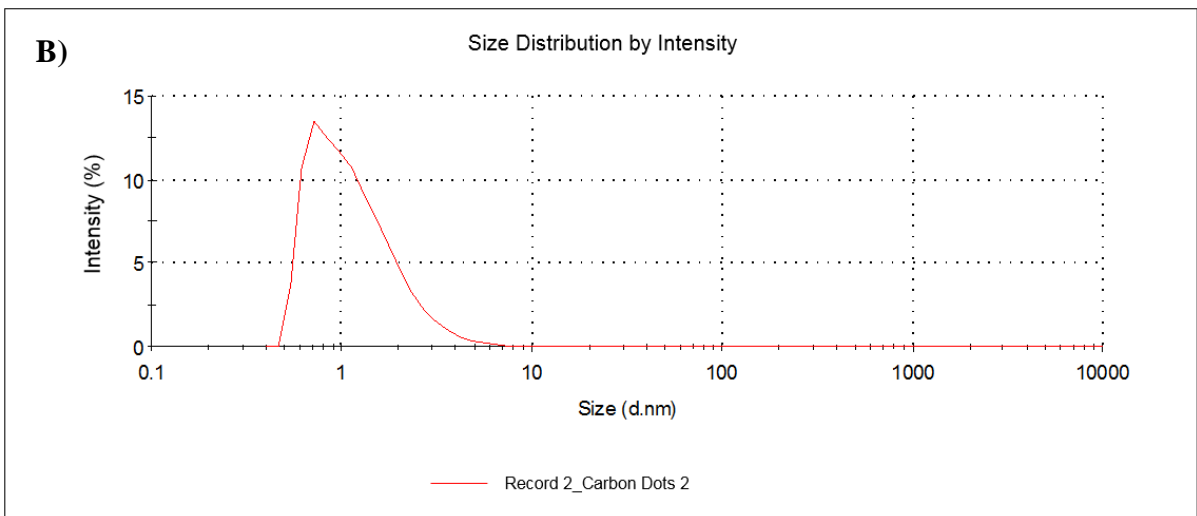
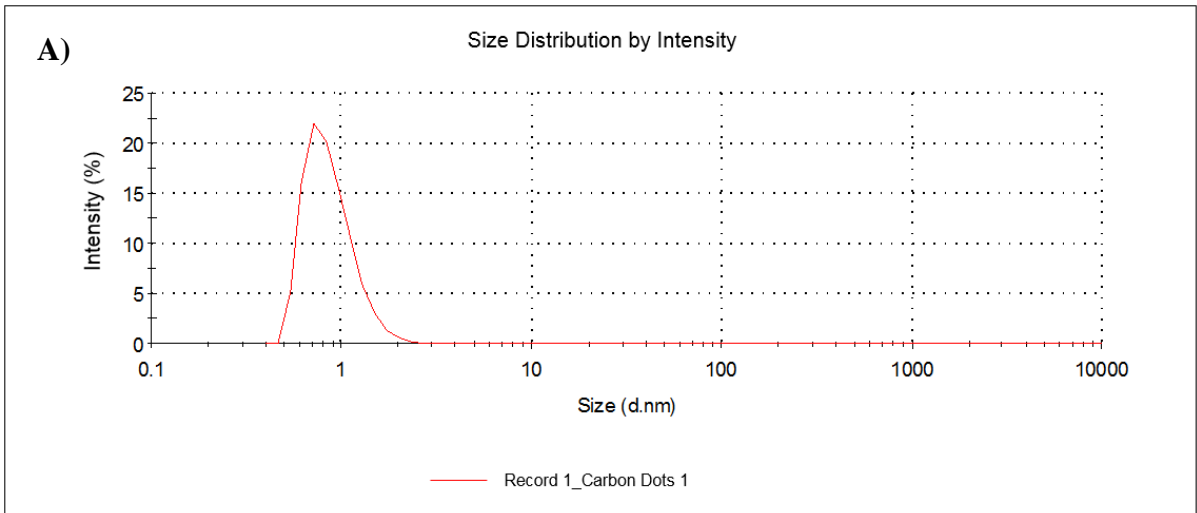
the cells was calculated from the ratio of the mean optical density of the sample to the optical density of the negative control.

The cells were cultured and treated with nCDs in 96-well, clear-bottomed white plates for the apoptosis and ROS detection experiments. Caspase 3/7 activity, the key indicator for apoptosis, was evaluated using the ApoTox-Glo™ Triplex assay according to the manufacturer's protocol. The light output, measured with a luminometer, correlates with Caspase-3/7 activation, and luminescence was measured using a microplate reader (Molecular Devices Spectra Max 190).

ROS generation was evaluated with the ROS-Glo™ H₂O₂ assay according to the manufacturer's protocol. The light signal (luminescence) produced by recombinant Luciferase is proportional to the level of H₂O₂ in the cells. The luminescence was measured using a microplate reader (Molecular Devices Spectra Max 190).

1.3. *In vitro* imaging of nCDs

All cells were fixed by immersion in 4% paraformaldehyde (PFA) as the cross-linking solution for 10 min at room temperature. The cells were washed three times with ice-cold 1x PBS, for 3 min each time. The fixed cells were incubated in ice-cold 1x PBS buffer containing 0.1% Triton (permeabilization agent) for 10 min at room temperature, then washed three times with ice-cold 1x PBS, for 5 min each time. The CELLview™ plates were then incubated with blocking buffer for 30 min at room temperature. The cells were subsequently washed three times with ice-cold 1x PBS for 3 min each time. To stain the nuclei, SlowFade® Gold Antifade Mountant with DAPI (diluted 1:100 in 1x PBS) was used. The cells were then kept at 4 °C overnight. The cells were again washed three times with ice-cold 1x PBS for 5 min each time before being transferred to the confocal microscope for visual analyses.



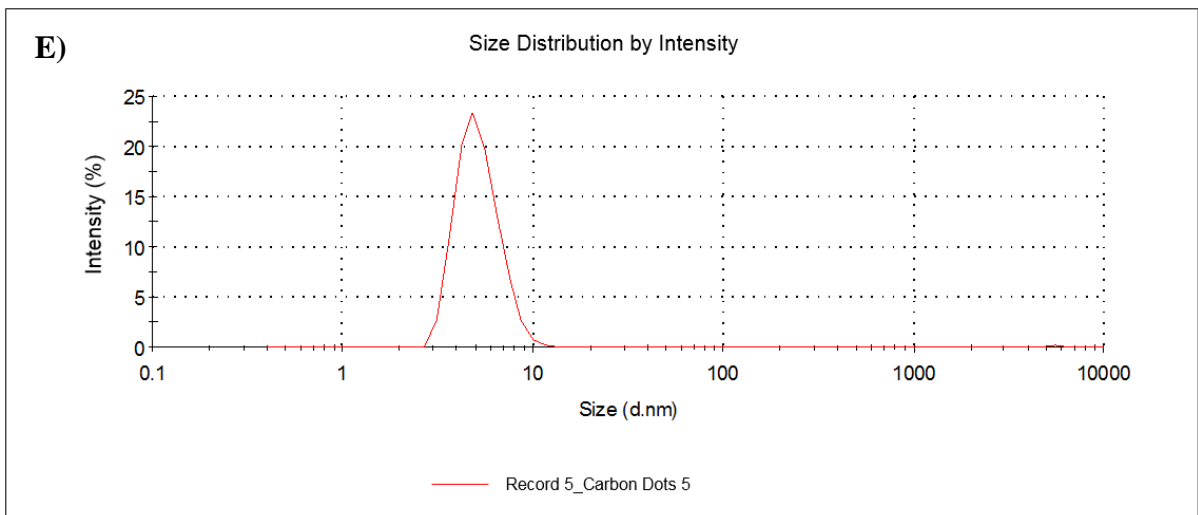
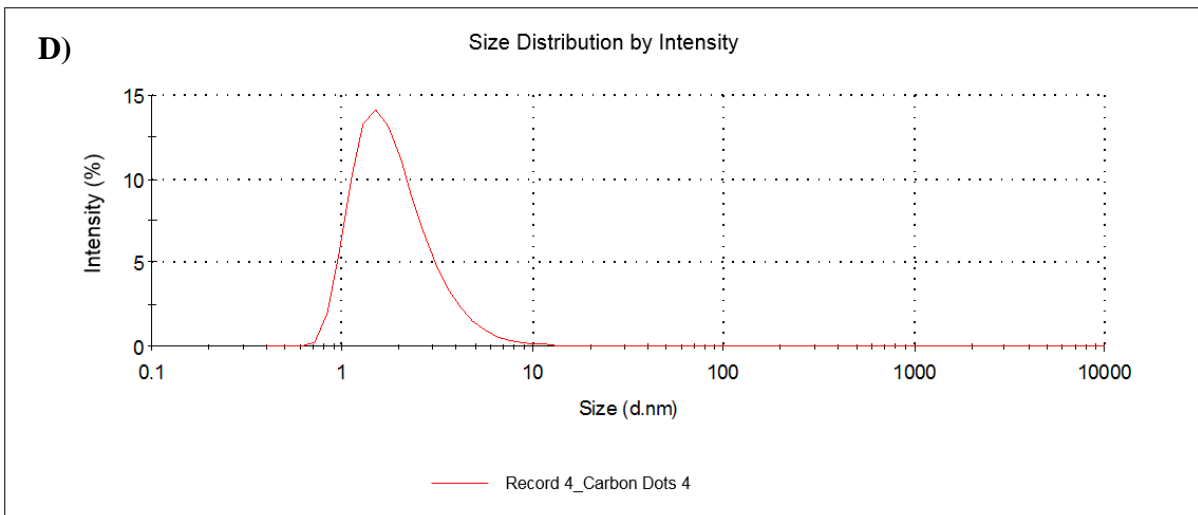
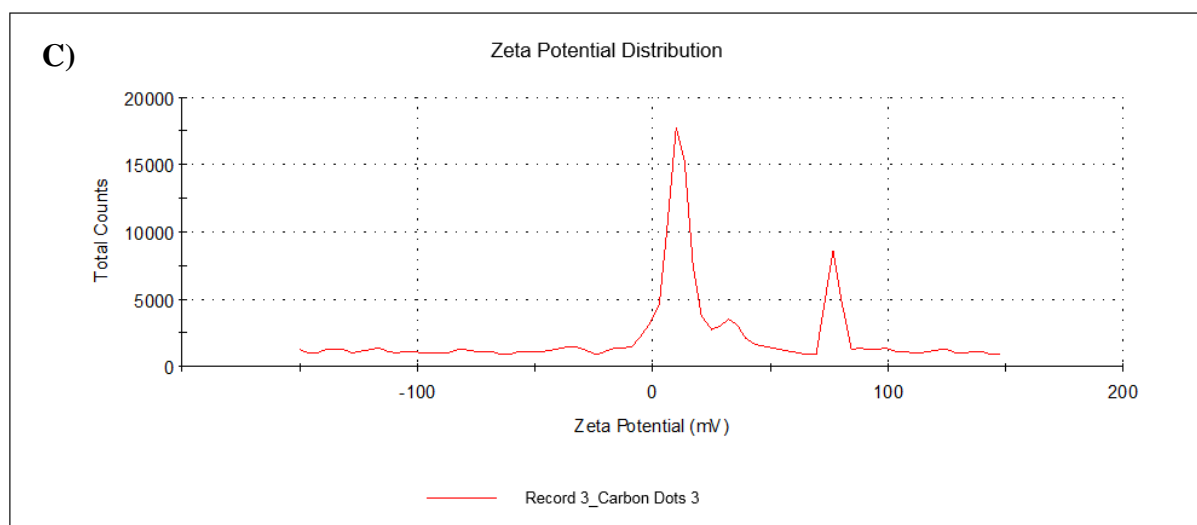
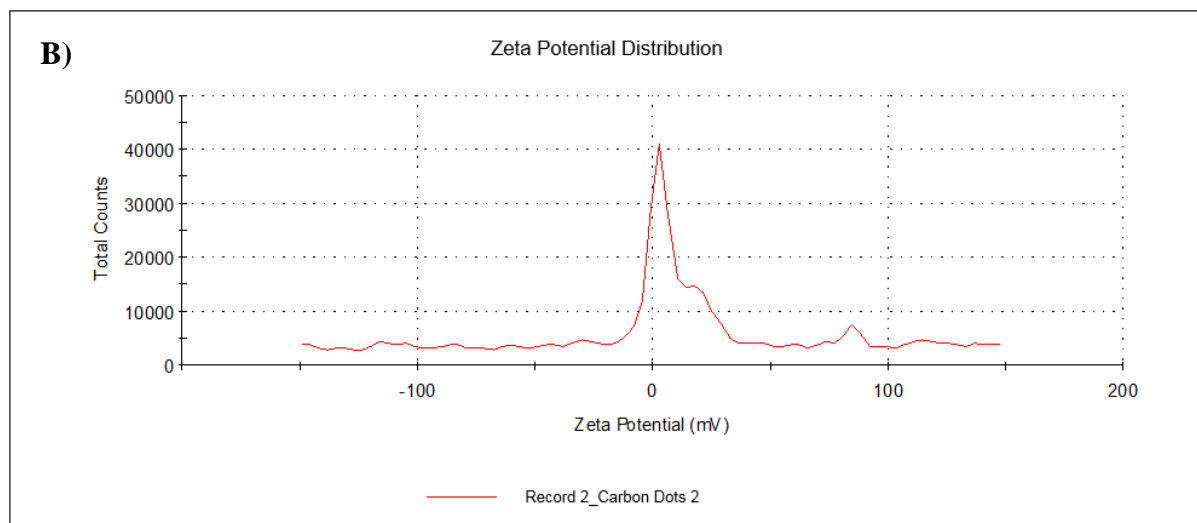
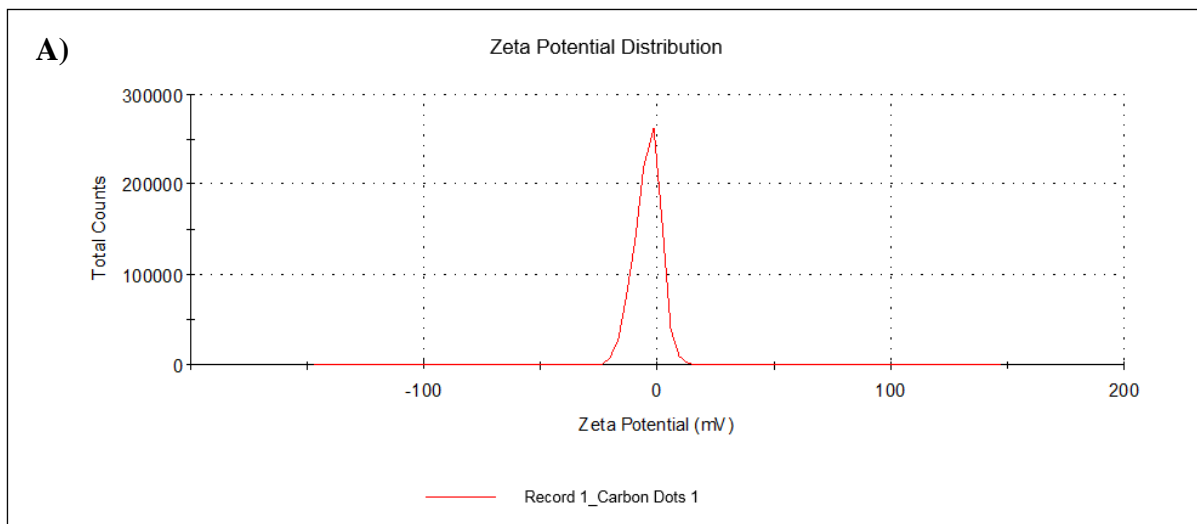


Figure S1. Hydrodynamic size measurement raw results of nCDs with amine/acid ratio of (A) 0.25, (B) 0.50, (C) 1.00, (D) 1.50, (E) 2.00.



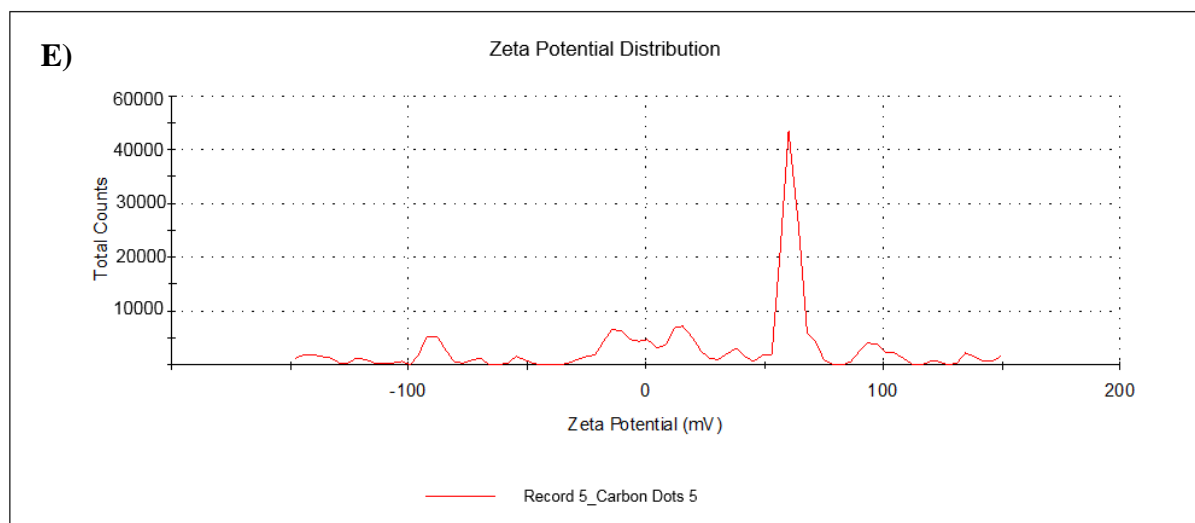
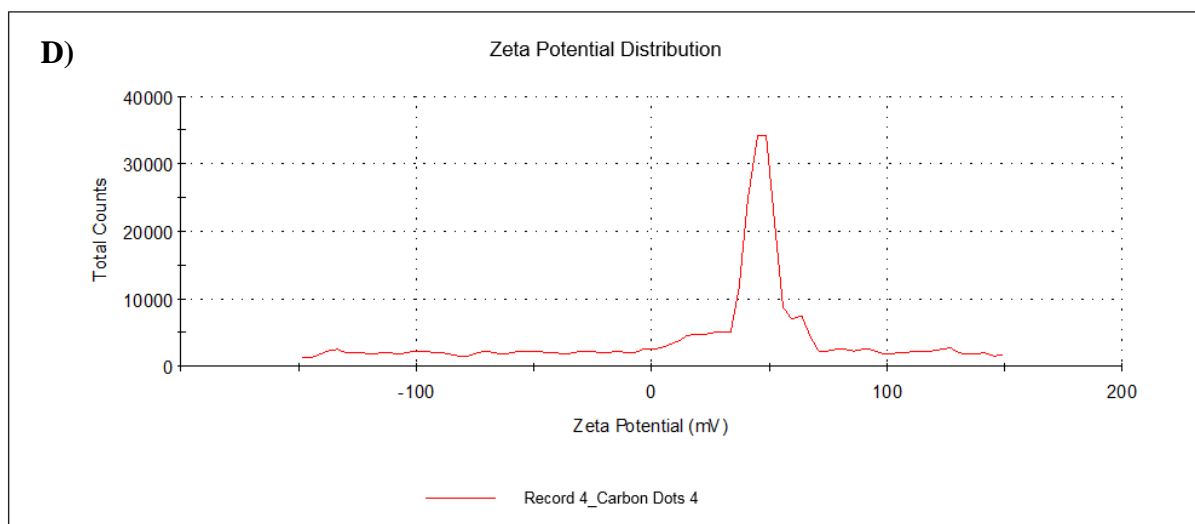


Figure S2. Zeta potential measurement raw results of nCDs with amine/acid ratio of (A) 0.25, (B) 0.50, (C) 1.00, (D) 1.50, (E) 2.00.

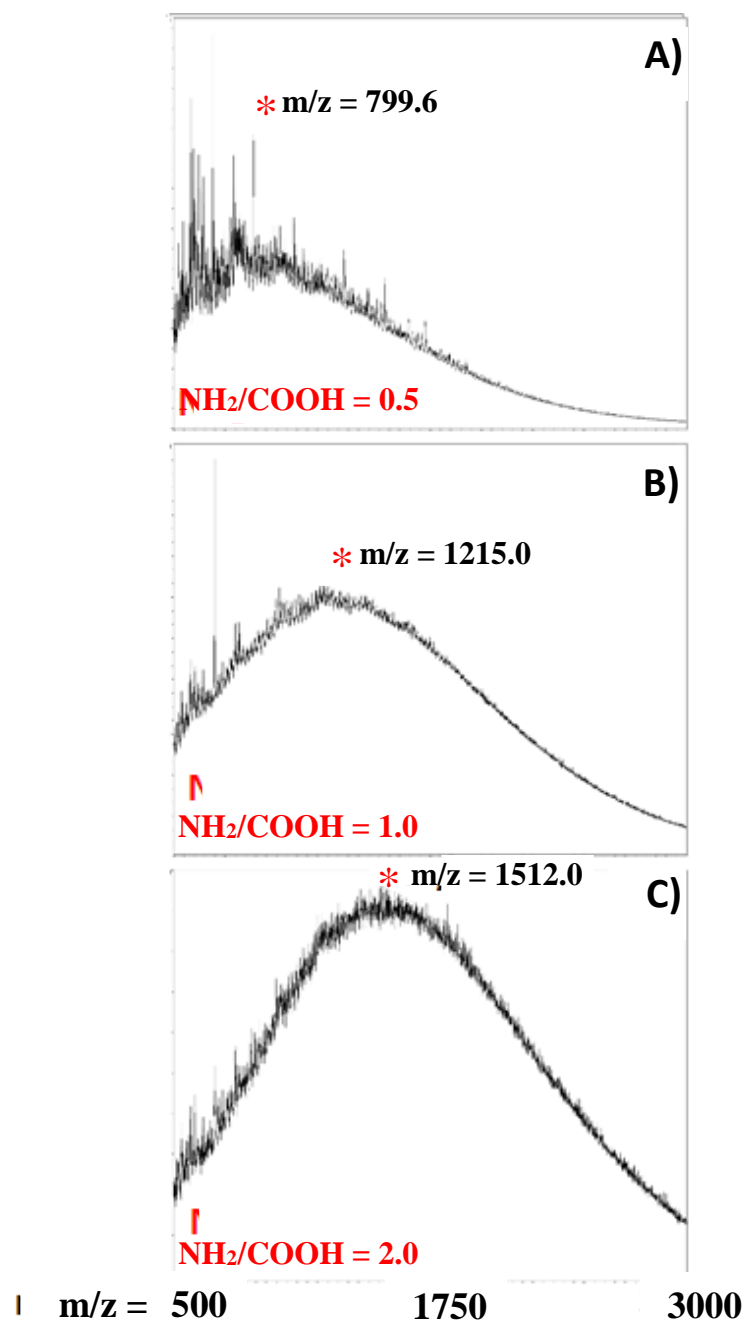


Figure S3. MALDI-TOF mass spectra of CDs with NH₂/COOH ratios of (A) 0.5, (B) 1.0, and (C) 2.0.

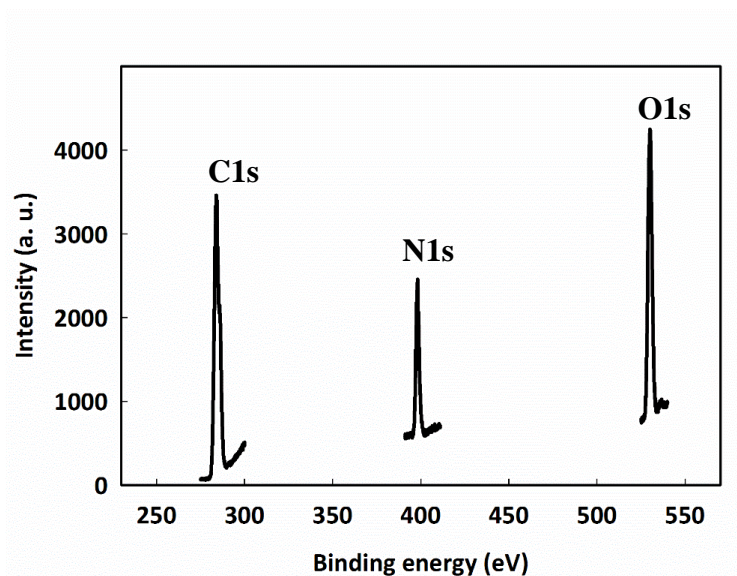


Figure S4. Broad spectrum XPS analysis results of nCDs

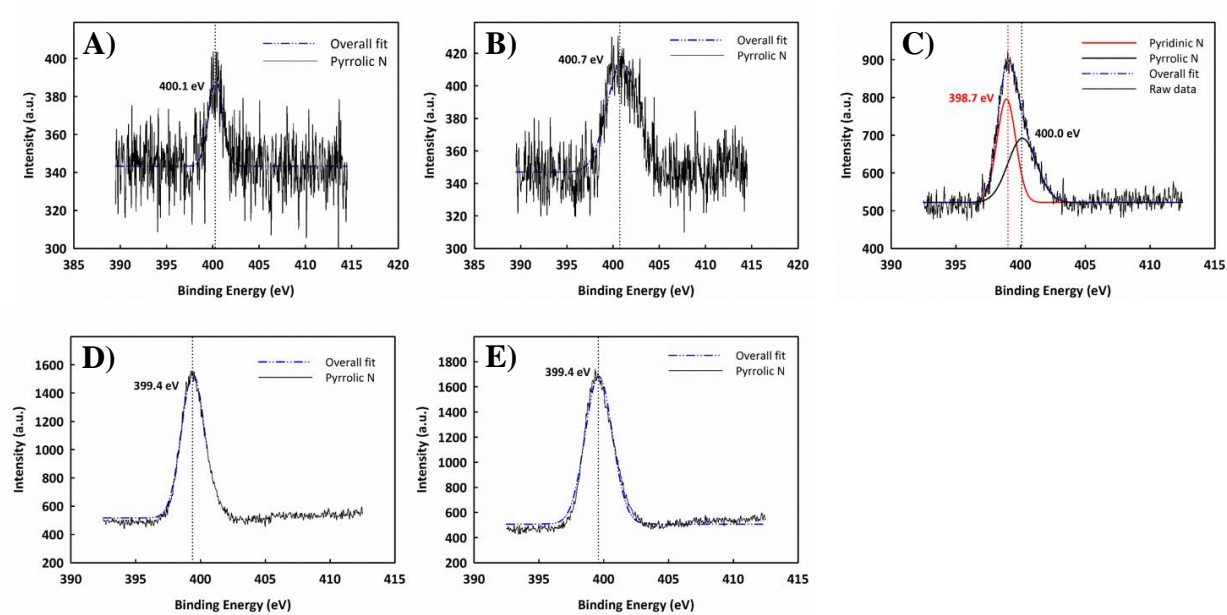


Figure S5. High resolution N1s XPS analysis results of nCDs with amine/acid ratio of (A) 0.25, (B) 0.50, (C) 1.00, (D) 1.50, (E) 2.00.

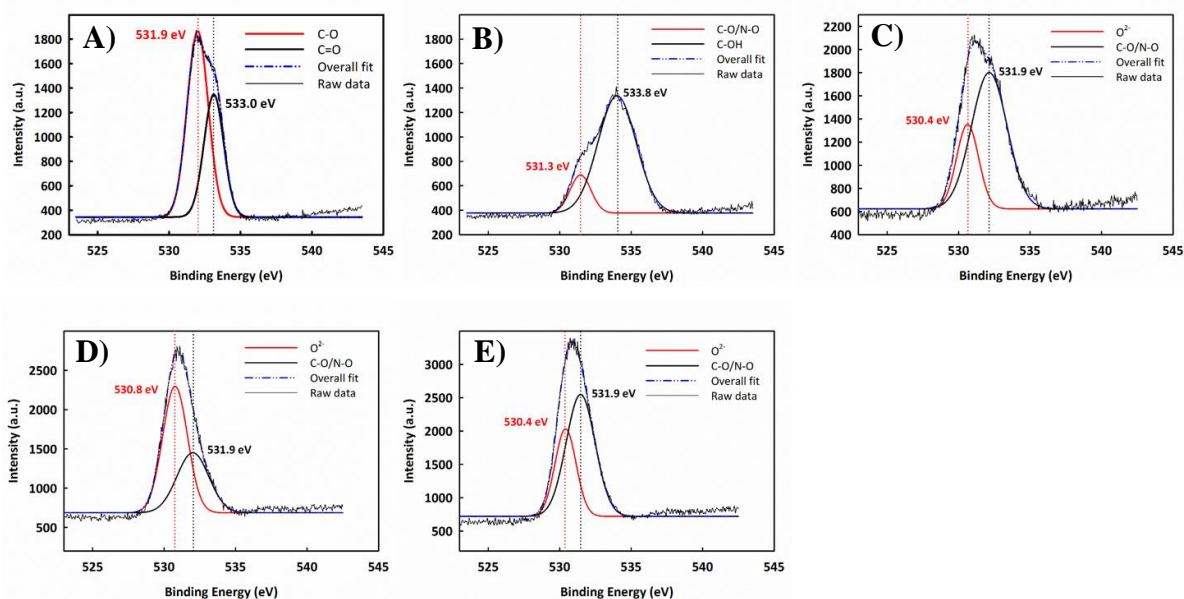


Figure S6. High resolution O1s XPS analysis results of nCDs with amine/acid ratio of (A) 0.25, (B) 0.50, (C) 1.00, (D) 1.50, (E) 2.00.

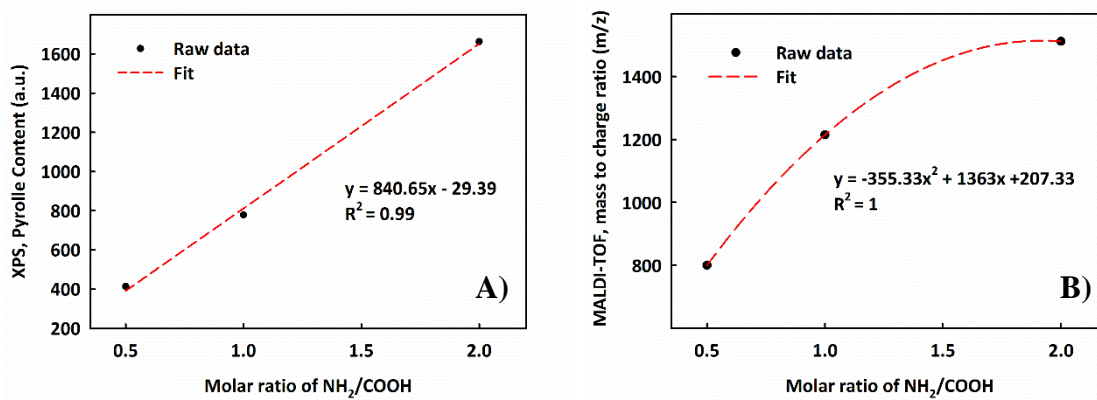


Figure S7. Correlation of the molar ratio of reactants to (A) pyrrole content and (B) MW of nCDs.

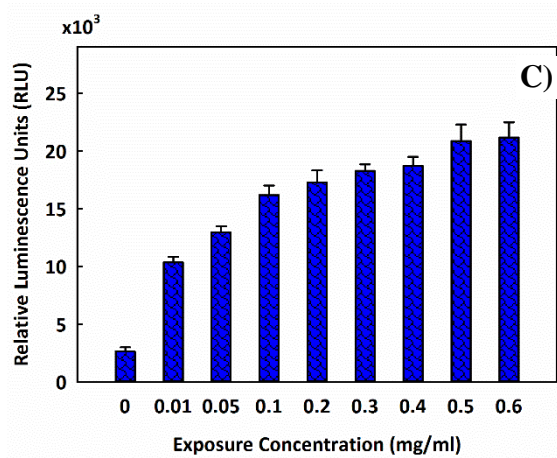
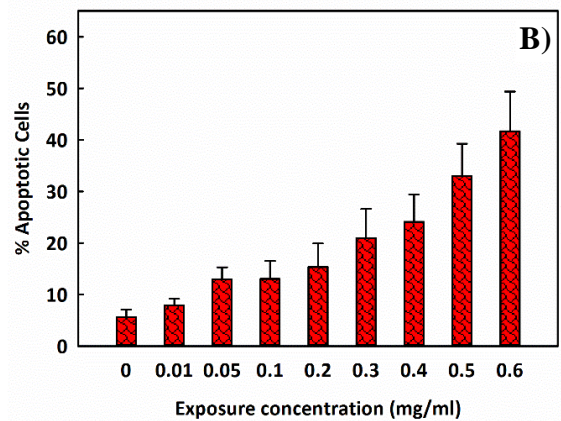
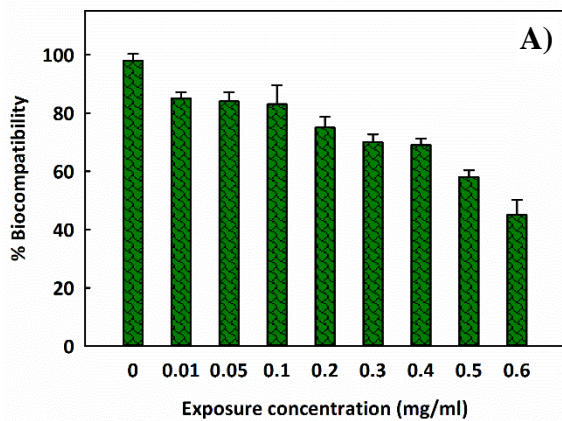


Figure S8. Biocompatibility results of retinal pigment epithelial (ARPE-19) (a) cell viabilities ((b) apoptotic cell percentage (c) ROS generation after incubation with nCDs for 24 h at concentrations up to 0.6 mg/mL. Data are expressed as mean \pm SD from three independent experiments ($*P < 0.05$).

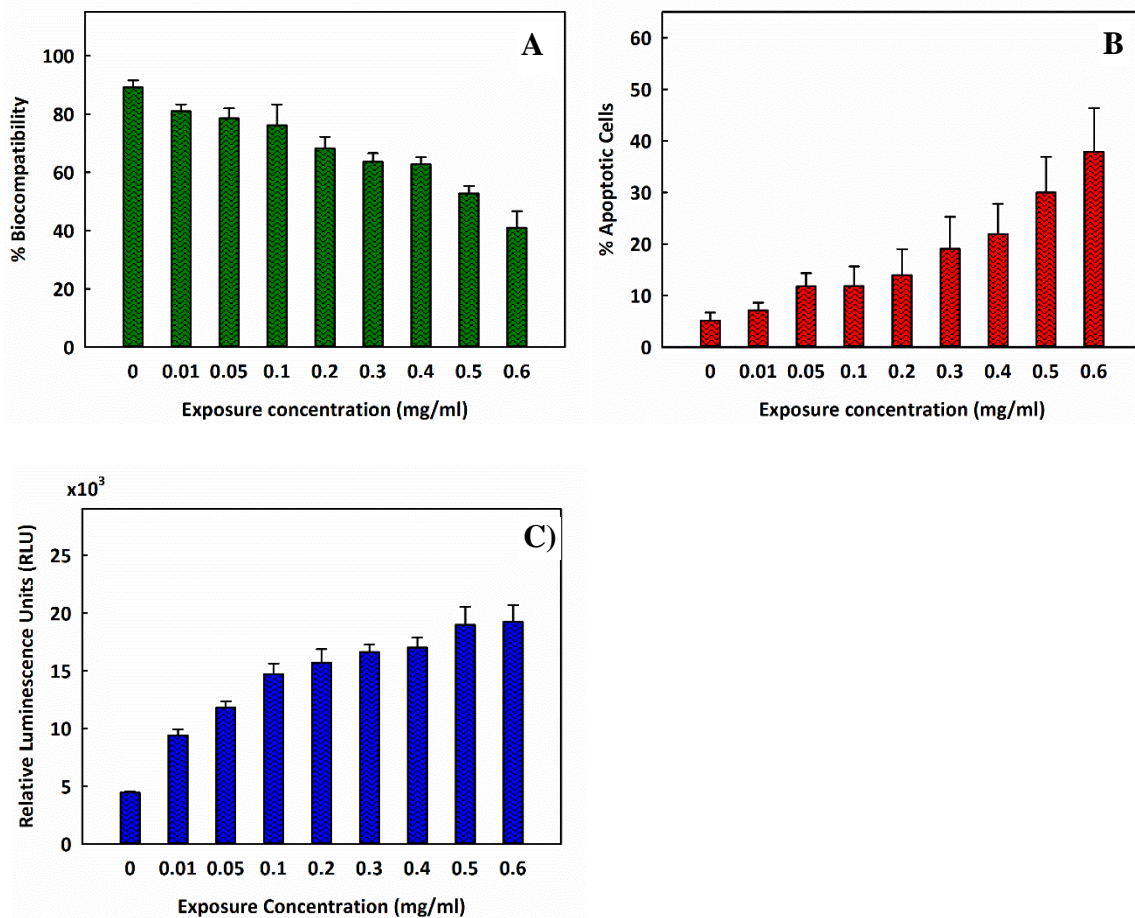


Figure S9. Biocompatibility results of lens epithelial (a) cell viabilities (b) apoptotic cell percentage (c) ROS generation after incubation with nCDs for 24 h at concentrations up to 0.6 mg/mL. Data are expressed as mean \pm SD from three independent experiments ($*P < 0.05$).

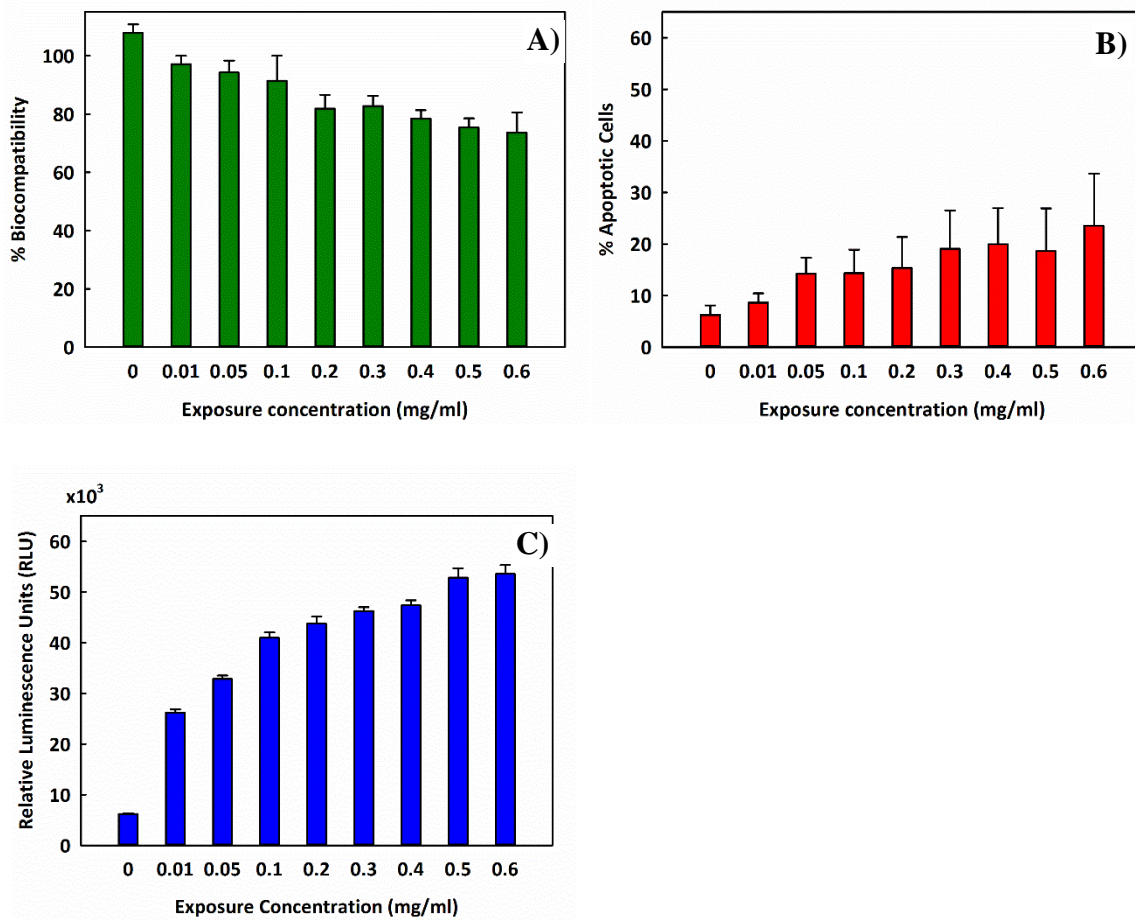


Figure S10. Biocompatibility results of CHO (a) cell viabilities (b) apoptotic cell percentage (c) ROS generation after incubation with nCDs for 24 h at concentrations up to 0.6 mg/mL. Data are expressed as mean \pm SD from three independent experiments ($*P < 0.05$)

Appendix IV.

Post Intravenous Injection Histology Analysis for Uncoated and Coated Au NPs

Post Intravenous Injection Histology Analysis for Uncoated and Coated Au NPs







Figure 1. Histology analysis after intravenously administered Au NPs. (A) 5 minutes (B) 10 minutes (C) 15 minutes (D) 20 minutes (E) 25 minutes post injection.



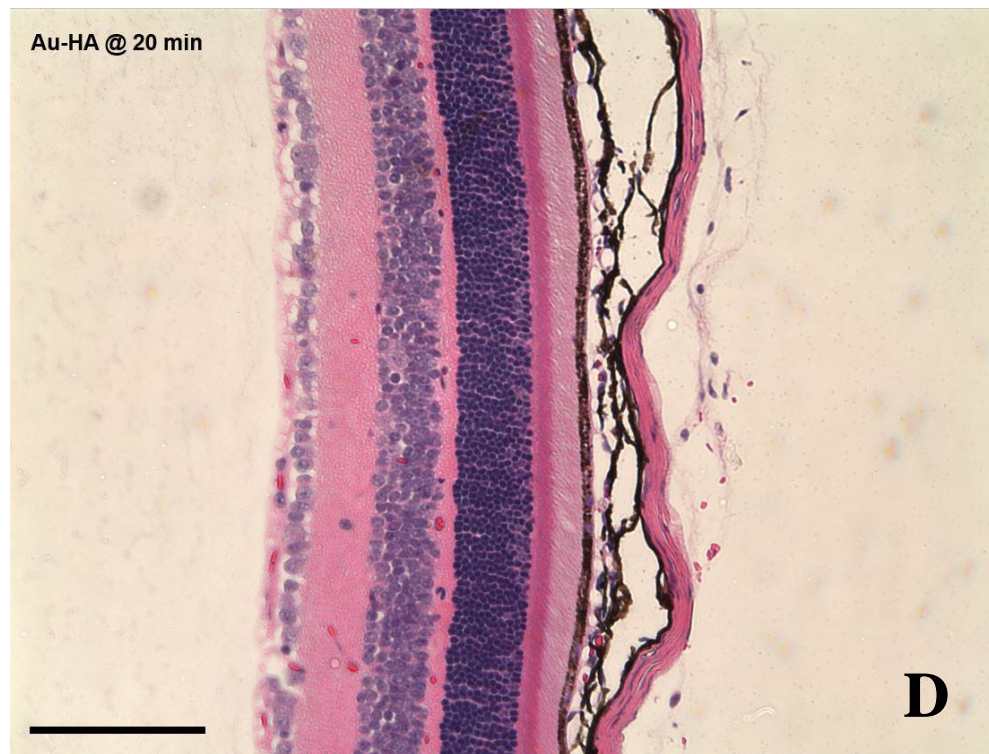
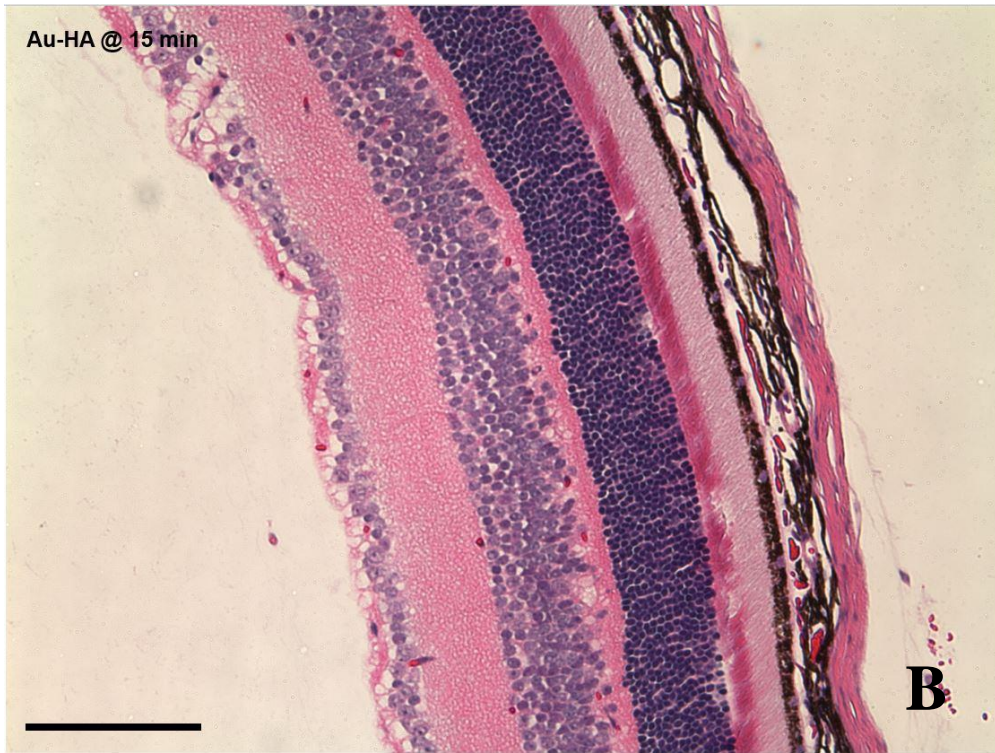




Figure 2. Histology analysis after intravenously administered HA-S-Au NPs. (A) 5 minutes (B) 10 minutes (C) 15 minutes (D) 20 minutes (E) 25 minutes post injection. All the sections of both cornea and retina are intact.

Appendix V.

A Highly Sensitive Non-enzymatic Glucose Sensor based on Cu/Cu₂O/CuO Ternary Composite Hollow Spheres Prepared in a Furnace Aerosol Reactor

The results of this appendix have been reprinted with permission from Lin L. Y,
Karakoçak B. B*, Kavadiya S., Biswas P. A Highly Sensitive Non-enzymatic Glucose
Sensor Based on Cu/Cu₂O/CuO Ternary Composite Hollow Spheres Prepared in a Furnace
Aerosol Reactor. 2018. Sens. Actuators B. Chem. 259: 745-752. Copyright 2018 Elsevier*

Abstract

A novel ternary composite, Cu/Cu₂O/CuO hollow spheres (HSs), synthesized using an aerosol furnace reactor (FuAR) was investigated for the first time as a non-enzymatic electrochemical biosensor for glucose detection. The composite HSs were synthesized by aerosolizing a mixture of copper nitrate, citric acid, and ammonia through a FuAR. Interestingly, the addition of ammonia played a crucial role in the *in-situ* formation of hollow Cu/Cu₂O/CuO ternary composites. The HSs modified electrode was employed for non-enzymatic glucose detection where it exhibited a detection limit of 0.39 μM and an outstanding sensitivity of 8726 $\mu\text{A cm}^{-2} \text{mM}^{-1}$ which is superior to existing Cu/Cu₂O HSs and CuO HSs modified electrodes. The high sensitivity was attributed to the synergy arising from the ternary composition's interfacing with multiple Cu redox couples. The Cu/Cu₂O/CuO HSs modified electrode also showed excellent selectivity in detecting glucose in the presence of interfering species, including chloride salts of Na⁺, K⁺, Ca²⁺, and anions of ascorbic acid (AA), dopamine (DA), and uric acid (UA). This simple and scalable FuAR technique will attract interest and enable in designing other high-performance metal/metal oxide composites for commercial glucose sensing applications.

1. Introduction

In the last few decades, the development of highly sensitive and selective glucose sensors with wide detection ranges has received considerable attention in clinical diagnosis and the food industry [1]. Currently, glucose oxidase (GOD)-based glucose biosensors comprise more than 85% of the sensor market, owing to their simplicity, high sensitivity, good selectivity, and reliability [2]. Nevertheless, the enzymes involved are quite sensitive to temperature, pH, and humidity, which significantly impede further development of enzyme-based biosensors. Given the inherent drawbacks of enzymes, non-enzymatic glucose sensors based on the electrocatalytic oxidation of glucose by a variety of electrocatalysts have been attracting much interest as promising alternatives.

Nanostructured metal/metal oxides are good candidates for electrocatalysts because of their low cost, high stability, and excellent redox behaviors across various potential ranges under a wide variety of reaction conditions [3]. Among the electrocatalysts for glucose sensors, copper oxides (Cu_2O and CuO) are of particular interest for their high activity in electro-oxidation of glucose, and low overpotential for electron-transfer reactions [4,5]. Various Cu-based metal oxides have been demonstrated as non-enzymatic glucose sensors and showed varying sensitivity, selectivity, and stability during electro-oxidation of glucose [4,6–8]. It has been demonstrated that the morphological characteristics of metal oxides affect the electrochemical sensitivity of glucose biosensors [9,10]. In particular, hollow structures can be an effective morphological alternative to designing high-performance electrode materials. Their unique properties – a high exposed surface area, hollow interior, thin walls, and excellent permeability could enable electrodes to be exposed to a larger electrode-glucose contact area and reduce the electron diffusion path, resulting in improved electrochemical activity [4,11].

The redox activation of the electrode materials in electrocatalytic processes is another major factor contributing to the sensitivity of electrochemical glucose detections. A composite material with multiple redox couples promotes redox reactions and enhances electrocatalytic activity [12,13]. For example, compared with pure CuO, a CuO/Cu₂O composite showed superior electrocatalytic activity in glucose oxidation [14]. This superiority is primarily attributed to the presence of a mixed-valence Cu²⁺/Cu⁺ system that promotes redox reactions between electrode materials and glucose, thus improves the performance of CuO/Cu₂O. Also, the incorporation of metallic Cu into the Cu-oxide (e.g., Cu₂O) has also been reported to be beneficial for enhancing electro-conductivity and electrocatalytic activity toward glucose oxidation [15,16]. More recent studies emphasized the synergistic effect of multiple oxidation species in improving the glucose detection performance [17–20]. Therefore, designing a Cu-based composite material consisting of mixed valences of Cu, Cu₂O [Cu⁺], and CuO [Cu²⁺] may be a good strategy to improve the sensitivity of the electrochemical glucose sensor further.

In this work, a single-step synthesis of Cu/Cu₂O/CuO composite hollow spheres (HSs) as non-enzymatic glucose sensors using an aerosol furnace reactor (FuAR) is presented for the first time. A triple oxidation state system of the Cu/Cu₂O/CuO composite HSs was synthesized to promote redox reactions and improve electrochemical sensitivity. To the best of our knowledge, this is the first study demonstrating the use of Cu/Cu₂O/CuO composite HSs as a non-enzymatic glucose sensor. The formation mechanism of the Cu/Cu₂O/CuO HSs was investigated in detail, and electrochemical studies to demonstrate the selectivity and sensitivity to glucose were established. This sensitivity was compared to those of Cu/Cu₂O HSs and CuO HSs prepared using the same FuAR method, and the reasons for the differences are elucidated.

2. Experimental

2.1. Reagents and Materials

All materials were of analytical grade and used as received without further purification. Copper nitrate hemipentahydrate, citric acid, ammonia (NH₃), glucose, ascorbic acid (AA), uric acid (UA), dopamine (DA), sodium hydroxide (NaOH), potassium chloride (KCl), sodium chloride (NaCl), calcium chloride (CaCl₂), fetal calf serum (FCS) were obtained from Sigma-Aldrich (St. Louis, MO). LIQUION™ Nafion™ containing solution was purchased from Ion Power Nafion™ Store (Newcastle, DE). Alumina micropolish powder (0.05 μm) was obtained from Buehler (Lake Bluff, IL).

2.2. Preparation of Cu/Cu₂O/CuO HSs

The Cu/Cu₂O/CuO composite HSs were synthesized in a lab-built furnace aerosol reactor, depicted in **Fig. S1**. To prepare the precursor solution, 1.86 g of copper nitrate hemipentahydrate (8 mmol) and 0.845 g of citric acid (4.4 mmol) were dissolved in 40 ml of DI water, followed by the addition of 1.9 ml of ammonia solution (28-30 wt. %) under constant stirring. The precursor mixture was then nebulized into aerosol droplets by using a collision nebulizer (BGI Incorporated) and delivered by a nitrogen flow (14 psi) through a 1 mm ID quartz tube 25 mm long surrounded by a furnace thermostatically controlled at 850 °C. The particle residence time inside the furnace aerosol reactor was calculated to be 1.2 seconds. The products were collected downstream of the reactor on a membrane filter, washed thoroughly with DI water, and finally dried in an oven at 110 °C for 6 hours.

2.3. *Material characterization*

The morphologies of the synthesized hollow spheres were examined by field emission scanning electron microscopy (FE-SEM, Nova NanoSEM 230, FEI Co.), and transmission electron microscopy (TEM, Tecnai TM Spirit, FEI Co.). The crystal phase of the material was determined by X-ray diffraction (XRD, D8 Advance, Bruker, USA) with Cu K α radiation ($\lambda = 1.548 \text{ \AA}$). The chemical composition of the material was determined with X-ray photoelectron spectroscopy (XPS) analysis, performed on a PHI 5000 VersaProbe II equipped with monochromatic Al K α (1486.6 eV) X-ray source. The XPS peak fitting was done in OriginLab, OriginPro (Northampton, MA) software using Lorentz distribution. The surface area and pore size distribution were analyzed using the nitrogen physisorption method (Autosorb-1, Quantachrome Instruments, Boynton Beach, FL). In total, 79 adsorption and desorption points were analyzed using the nitrogen physisorption method. The surface area was calculated using the Brunauer–Emmett–Teller (BET) method, and the pore size distribution was obtained from the desorption isotherm, which is more appropriate than the adsorption isotherm for evaluating the pore size distribution of an adsorbent. For the same volume of gas, the desorption isotherm exhibits a lower relative pressure, resulting in a lower free energy state, i.e., one closer to true thermodynamic stability.

2.4. *Electrode fabrication and electrochemical measurement*

An enzyme-free amperometric electrochemical sensor was prepared with a modified glassy carbon electrode (GCE, 3 mm diameter) at room temperature. Before modification, the bare GCE was polished to a mirror-like surface with 0.05 μm alumina slurry and then washed ultrasonically in deionized water for at least two minutes. Electrochemical measurements were performed with a lab-built three-electrode cell setup. For the working electrode, 10 mg of the material powder was dispersed in 5 ml of deionized water, followed by the addition of 1 ml of Nafion solution (0.05 wt. %). After approximately 30 min of

ultrasonication, 20 μl of the suspension, which contained 33 μg of the powdered material, was dropped onto the pretreated GCE and dried at 60 $^{\circ}\text{C}$ for 20 min. A Pt wire was used as the counter electrode and Ag/AgCl as the reference electrode. Cyclic voltammetry (CV) measurements and chronoamperometry (CA) were performed using a CHI 760E electrochemical workstation. For glucose detection experiments, the workstation was operated at +0.55 V with continuous stirring to ensure efficient convective mass transport. In the experiment, 200 μl of glucose was added incrementally to 2 ml of 0.1 M NaOH aqueous solution. Then, interfering anion and cation experiments were conducted. Finally, the short-term (1000 s) and long-term (21 days) stability of the electrode was tested. All the measurements were carried out at room temperature in a normal atmosphere.

Electrochemical impedance spectroscopy (EIS) was performed using the same three-electrode system in 100 mM KCl electrolyte solution containing equimolar (0.01 M/0.01 M) $[\text{Fe}(\text{CN})_6]^{4-/3-}$ at a bias potential of 0.55 V by applying an AC voltage with 5 mV amplitude in a frequency range from 0.1 Hz to 1 MHz.

3. Results and Discussion

3.1. Synthesis and characterization of Cu/Cu₂O/CuO HSs

The formation of Cu/Cu₂O/CuO HSs is illustrated in **Fig. 1**. The formation of mixed-phased copper oxide HSs is based on an *in-situ* gas release mechanism in a single aerosol droplet, where citric acid acts as a blowing agent. Further information regarding the formation mechanism can be found in the Supporting Information (**SI-2**). The phase composition of the aerosol-made materials was investigated by XRD, with the results displayed in **Fig. 2a**. When using nitrogen as a carrier gas in the FuAR process, the powder prepared from the precursor solution containing copper nitrate–citric acid is identified as Cu/Cu₂O [13]. The addition of ammonia in the precursor solution (copper nitrate–citric acid–ammonia) results in the formation of Cu/Cu₂O/CuO hybrids [21]. The peaks are

identified with standard pdf card for Cu (pdf # 01-071-4611), Cu₂O (pdf # 04-016-6875) and CuO (pdf # 04-007-0518). It can be seen that the intensities of the Cu₂O crystalline phases decrease with corresponding increases in the intensities of the CuO peaks, implying a growing amount of CuO at the expense of Cu₂O. On the other hand, the pure CuO phase is clearly identified in the CuO HSs sample obtained in airflow during the FuAR process. The phase composition of Cu/Cu₂O/CuO is determined by XPS analysis. High-resolution XPS was performed to identify Cu peaks. The binding energy for Cu and Cu⁺¹ peaks are very close and therefore difficult to distinguish. There are satellite peaks corresponding to electronic shake-up that are present for CuO. The ratio of Cu(II)/(Cu(0)+Cu(I)) present in the composite HSs is calculated to be 2.47 based on the ratio of their XPS peak areas.

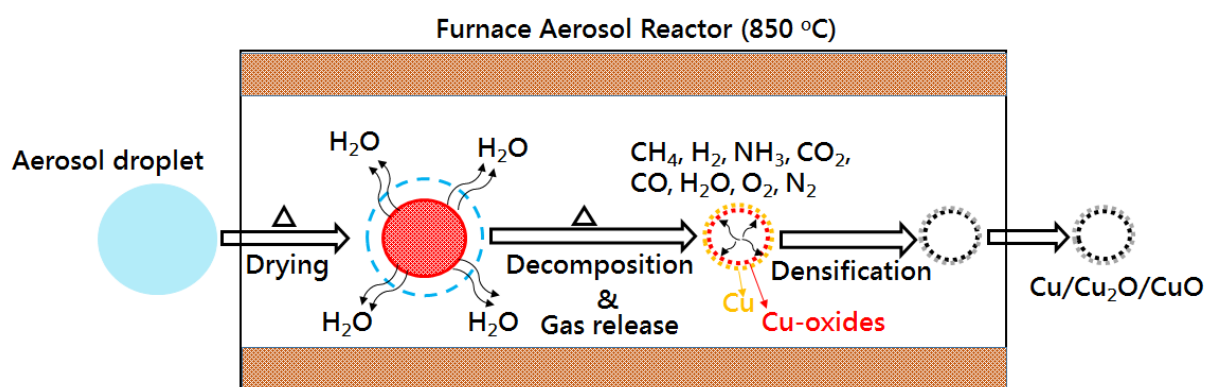


Fig. 1. The formation mechanism of Cu/Cu₂O/CuO HSs. The aerosol droplet consisting copper nitrate, and citric acid in ammonia enters the reactor. The increase in temperature inside the reactor leads to evaporation of water and decomposition of the precursors. The final product is the copper oxide particles in powdered form, which are collected on a membrane filter.

The morphology of the synthesized Cu/Cu₂O/CuO was investigated by SEM and TEM.

Most of the Cu/Cu₂O/CuO particles are spherical with diameters ranging from 0.05 to 3 μm. Also, hollow as well as fractured particles are observed (**Fig. 2b**). The hollow structure of the Cu/Cu₂O/CuO spheres was further verified by the bright contour at the center of the

sphere in the TEM image (**Fig. 2c**), and the shell thickness is estimated to be ~30 nm (**Fig. 2d**). Similar hollow morphologies are also found in both Cu/Cu₂O HSs and CuO HSs samples (**Fig. S4**). The Brunauer–Emmett–Teller specific surface area (S_{BET}) and pore volume (V_{p}) of Cu/Cu₂O/CuO HSs measured using the nitrogen physisorption method were determined to be 11.3 m²/g and 0.12 cm³/g, respectively. In comparison, the S_{BET} and V_{p} values of Cu/Cu₂O and CuO HSs were 13.2 and 0.10 cm³/g, and 5.3 m²/g and 0.078 cm³/g, respectively.

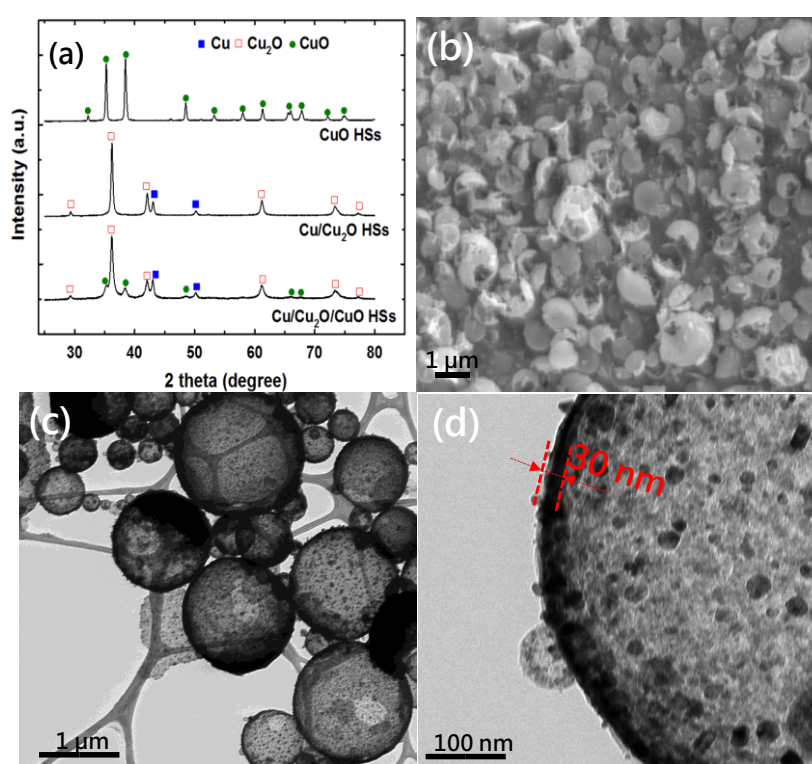


Fig. 2. (a) Powder XRD patterns of CuO, Cu/Cu₂O, and Cu/Cu₂O/CuO HSs samples, (b) SEM (scale bar 1 μm), and (c) TEM image (1 μm) of Cu/Cu₂O/CuO HSs, (d) high-resolution TEM image (100 nm) of Cu/Cu₂O/CuO HSs showing the wall thickness of approximately 30 nm.

3.2. Electrochemical performance analysis

All three aerosol-made HSs composites – Cu/Cu₂O/CuO, Cu/Cu₂O, and CuO – were applied as a non-enzymatic glucose sensor by depositing an aqueous solution containing powdered composite and Nafion on a glassy carbon electrode (GCE) surface. Cyclic

voltammetry measurements were performed to investigate the modified electrode's electrocatalytic activity toward glucose oxidation. As shown in **Fig. 3a**, in the presence of 10 μM glucose, the oxidation of glucose started at an onset potential of 0.40 V for both the Cu/Cu₂O-GCE and the CuO-GCE. In comparison, an increasing current signal was observed for the Cu/Cu₂O/CuO-GCE starting at a lower positive onset potential of 0.30 V. The current signal was 5.9 and 3.9 times higher than for the Cu/Cu₂O-GCE and CuO-GCE, respectively. Most notably, the combination of Cu, Cu₂O, and CuO in a composite significantly enhanced the electrochemical performance of the electrode, which may result from the synergistic effect of improved electron transfer between the ternary compositions. To prove this, we performed electrical impedance spectroscopy (EIS) measurement on these electrodes (**Fig. 3b**). After modification of the GCE electrode with the composites, the semicircle diameter, which represents the resistance to electron transfer of the modified layer increases, indicating the attachment of material on the conductive GCE electrode surface. It is observed that the order of electron transfer resistance is Cu/Cu₂O/CuO < CuO < Cu/Cu₂O, with Cu/Cu₂O having a very high resistance. EIS results show that the electron transfer ability of the ternary composite (Cu/Cu₂O/CuO) is very rapid.

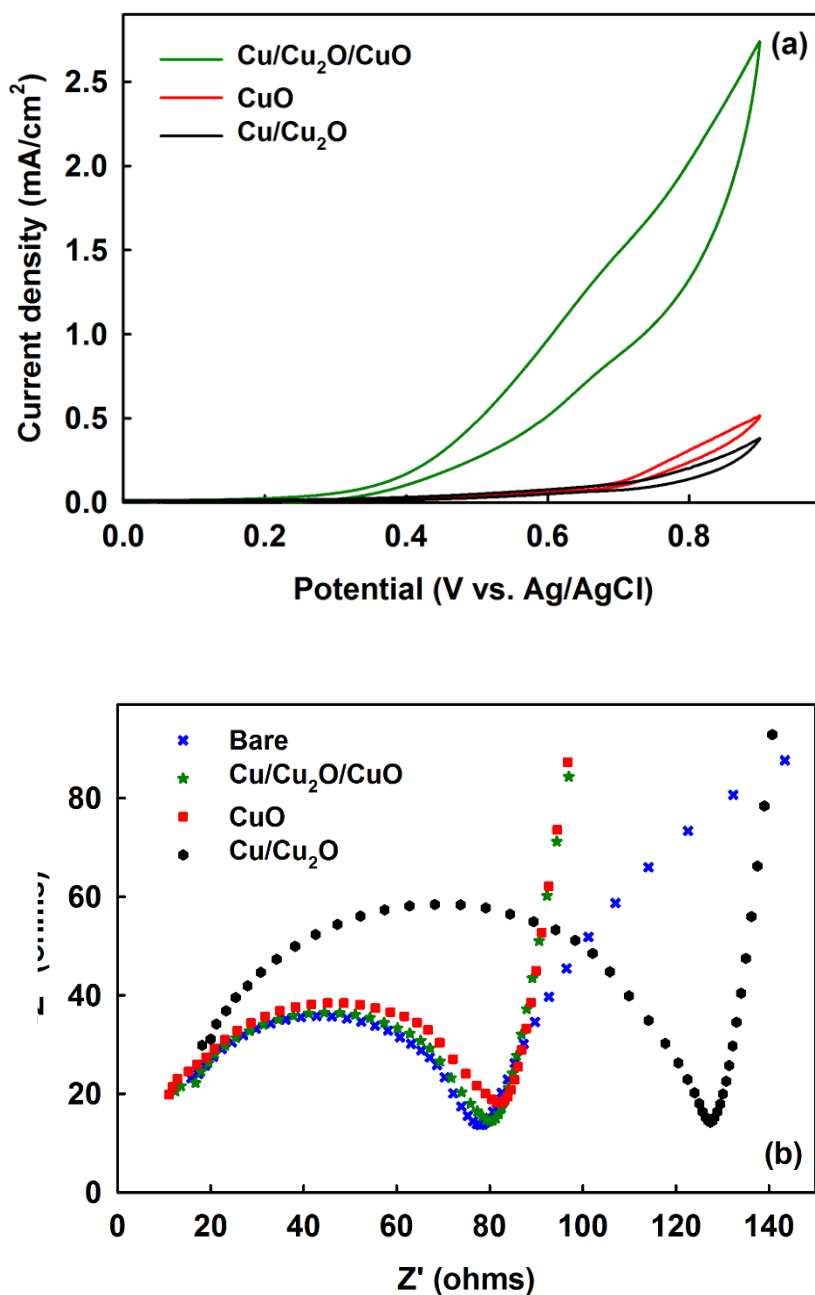
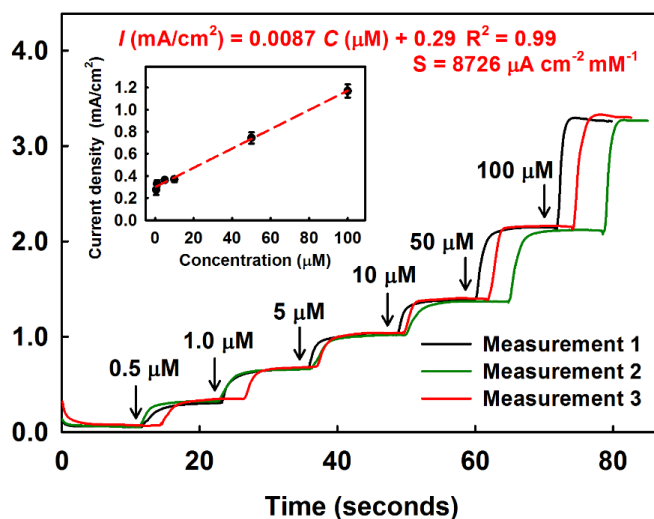
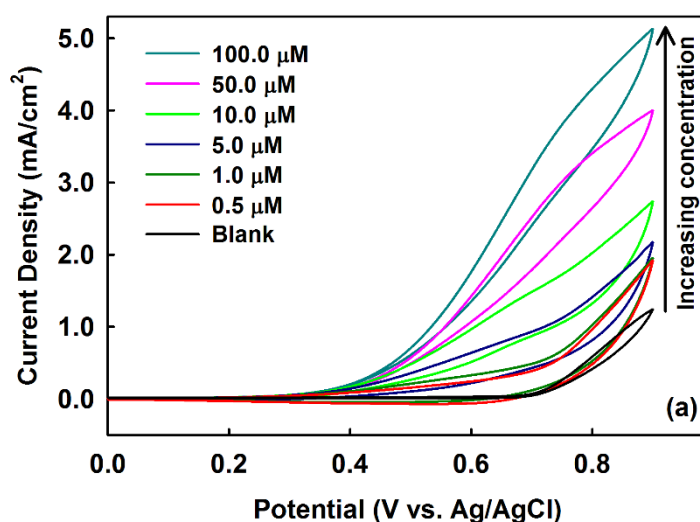


Fig. 3. (a) Cyclic Voltammetry (CV) curves at 50 mV/s of Cu/Cu₂O/CuO, CuO, and Cu/Cu₂O-modified GCEs in 0.1 M NaOH with a glucose concentration of 10 μ M. (b) Electrical impedance spectroscopy (EIS) data recorded on bare GCE, Cu/Cu₂O/CuO, CuO, and Cu/Cu₂O-modified GCEs. EIS parameters: frequency range of 0.1–10⁶ Hz, and 5 mV amplitude of sine voltage signal.

Fig. 4a displays the CV curves of the Cu/Cu₂O/CuO-GCE in a 0.1 M NaOH solution in the presence of various concentrations of glucose at 50 mV/s. The electrode's response was very weak in the absence of glucose (black curve), but the electro-oxidation current increases steadily with an increase of glucose concentration up to 100 μM. Furthermore, CVs of the Cu/Cu₂O/CuO-GCE were recorded in 100 μM glucose solution at different scan rates (5 mV/s to 200 mV/s) (**Fig. S5**). It was found that anodic peak current increases with the increasing scan rate potential. The inset shows anodic peak current is linearly correlated to the square root of the scan rate, implying that the electrode surface oxidation reaction is not electrocatalyst kinetics limited, but instead, a typical diffusion-controlled process.



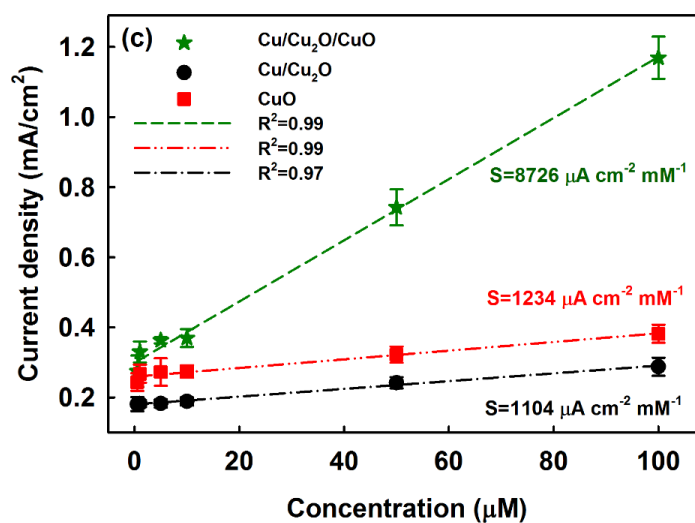


Fig. 4. (a) CV curves at 50 mV/s of Cu/Cu₂O/CuO modified GCE in 0.1 M NaOH with glucose concentrations from 0 to 100 µM. (b) Amperometric response at 0.55 V of the Cu/Cu₂O/CuO modified GCE to successive ~10 s additions of glucose to 0.1 M NaOH. The inset is the corresponding calibration curve. (c) Calibration plot derived from the amperometric responses at 0.55 V versus an Ag/AgCl reference electrode for all three composites: Cu/Cu₂O/CuO, Cu/Cu₂O, and CuO. Cu/Cu₂O/CuO-modified GCE showed outstanding sensitivity.

For a healthy individual, the body's homeostatic mechanism restores the blood glucose level at 4.4-6.6 mM; whereas diabetic blood sugar can increase up to 15.0 mM [22,23]. In light of this information, the amperometric response of the Cu/Cu₂O/CuO-GCE to 0.5 µM – 30 mM glucose was tested. The amperometric responses of the modified electrode to 0 µM – 100 µM glucose addition is presented in Fig. 4b and responses to higher concentrations of glucose additions (1 mM – 30 mM) are plotted in Fig. S6. The responses of three independent experiments were used to calculate the standard error. The results indicated a sensitive amperometric response for the entire glucose concentration range tested. The insets in Fig. 4b and Fig. S6 show the calibration curve of the modified electrode based on the amperometric results. The clear stepwise linear increments over the entire concentration

range indicate that the Cu/Cu₂O/CuO-GCE can monitor glucose sensitively. The fitting equation was $I \text{ (mA/cm}^2\text{)} = 0.0087 C \text{ (}\mu\text{M)} + 0.29$, with a correlation coefficient of 0.99 for the concentration up to 100 μM (**Fig. 4b**). The detection limit was found to be 0.39 μM , as calculated by $3\sigma/S$, where σ and S respectively denote the standard deviation of the background current ($1.1 \times 10^{-3} \text{ mA/cm}^2$) and the slope of the calibration curve (8.7×10^{-3}).

Based on the amperometric results, the current density calibration curve results for the modified GCE with all three composites – Cu/Cu₂O/CuO, Cu/Cu₂O, and CuO – in 0.1 M NaOH with a glucose concentration of 1-100 μM at a scan rate of 50 mV/s was created (**Fig. 4c**). For comparison, **Table 1** lists the analytical performances of other existing Cu-based composite modified GCE sensors along with our findings. The sensitivity of the CuO-modified GCE was found to be $1234 \mu\text{A mM}^{-1} \text{ cm}^{-2}$, similar to the values reported previously on the CuO-modified electrodes [11,24]. Furthermore, similar to the results reported for the Cu/Cu₂O modified GCE [12], the sensitivity of the Cu/Cu₂O modified GCE was determined to be $1104 \mu\text{A mM}^{-1} \text{ cm}^{-2}$. Although compared with previously reported values, our results showed a slight enhancement in the sensitivity of GCEs modified with either Cu/Cu₂O or CuO, we wanted to take the modification composition recipe one step further, and created the Cu/Cu₂O/CuO composite. An outstanding sensitivity of $8726 \mu\text{A mM}^{-1} \text{ cm}^{-2}$ was achieved by the Cu/Cu₂O/CuO-GCE, which is 7-fold higher than those of the Cu/Cu₂O and CuO modified GCEs (**Fig. 4c**).

The glucose sensing performance in this study and that of other non-enzymatic sensors available in the literature are summarized in **Table 1**. Clearly, the Cu/Cu₂O/CuO modified GCE developed in this study had the highest sensitivity among all non-enzymatic glucose sensors under comparable conditions, except for Ag-carboxylate functionalized SiO₂. The sensitivity of Ag-carboxylate functionalized SiO₂ (potential, 0.62 V; electrolyte, 0.1 M NaOH; sensitivity, $9091 \mu\text{A mM}^{-1} \text{ cm}^{-2}$) is slightly higher than that of the Cu/Cu₂O/CuO

ternary composite HSs (potential, 0.55 V; electrolyte, 0.1 M NaOH; sensitivity, 8726 $\mu\text{A mM}^{-1} \text{cm}^{-2}$). Nevertheless, the need for an expensive noble metal precursor as well as the multi-step synthesis procedures (thermal treatment, refluxing, filtration, and washing) and long reaction time (100 h) of Ag-carboxylate functionalized SiO_2 might limit its potential use for practical applications. As a result, our sensor is successful in detecting the glucose concentration for the entire range tested (0.5 μM to 30 mM) with a detection limit of 0.39 μM .

Table 1. Analytical performance comparison of non-enzymatic electrochemical sensors for glucose detection.

Electrodes	Applied potential (V)	Electrolyte	Sensitivity ($\mu\text{A mM}^{-1} \text{cm}^{-2}$)	Linear range	Detection limit	Reference
Cu/Cu ₂ O/CuO HSs/GCE	0.55	NaOH	8726	0.5 μM - 30 mM	0.39 μM	Current work
Cu/Cu ₂ O nanohybrids	0.55	CuSO ₄ +Lactic Acid+NaOH/KOH	1434	Up to 40 mM	1.6 μM	[18]
Cu/Cu _x O	0.5	NaOH	1620	0 - 6 mM	49 μM	[12]
Hollow Cu ₂ O nanospheres	0.6	NaOH	2038	1.25 - 37.5 μM	0.41 μM	[4]
Cu ₂ O nanourchin	0.5	KOH	2682	0.1 - 3 mM	1.52 μM	[32]
Cu ₂ O/Cu	0.5	NaOH	6681	1 μM - 1.8 mM	0.67 μM	[33]
Anneal shrunked Cu ₂ O dendrites	0.45	NaOH	5040	0.001 - 1.4 mM	0.13 μM	[8]
Cu/CuO	0.6	NaOH	1887	2 μM -3.56 mM	0.05 μM	[34]
CuO nanowires/carbon cloths	0.55	NaOH	2973	Up to 1.12 mM	1 μM	[35]
CuO nanospheres/carbon	0.55	NaOH	4902	Up to 1 mM	1 μM	[35]
Sandwich structured CuO	0.6	NaOH	5343	Up to 3.2 mM	~1 μM	[36]
Ag-carboxylate functionalized SiO ₂	0.62	NaOH	9091	0.004 - 5.5 mM	0.33 μM	[37]
Nano Ni/Ti electrode	0.5	NaOH	7320	0.05 - 0.6 mM	1.2 μM	[38]
Cu-Ag/nanofiber	0.55	NaOH	7746	0.005 - 3.5 mM	0.08 μM	[28]
Cu-Cu ₂ O/TiO ₂	0.65	NaOH	4895	0.1 - 2.5 mM	8.6 μM	[17]
3D graphene-Co ₃ O ₄	0.58	NaOH	3390	Up to 0.08 mM	< 0.025 μM	[39]
Pd-CuO/reduced graphene oxide/screen printed electrode	0.6	NaOH	3355	0.006 - 22 mM	0.03 μM	[40]

Currently, the mechanism for glucose electrooxidation on the Cu-based electrodes in an alkaline medium is not entirely clear; nevertheless, it is believed that a Cu^{3+} species, rather than Cu^+ or Cu^{2+} , serve as the electron-transfer mediator [25]. Also, it was demonstrated that the electro-oxidation of glucose in an alkaline medium requires the presence of oxide, hydroxide, and/or oxyhydroxide groups [26]. That is, the electro-oxidation of glucose on the Cu or Cu composite occurs through reaction with CuOOH to form $\text{Cu}(\text{OH})_2$. Based on this assumption, a possible mechanism for glucose detection on the Cu/ Cu_2O / CuO modified GCE is proposed in **Fig. 5**. During electrochemical measurements, $\text{Cu}(0)$, $\text{Cu}(\text{I})$ and $\text{Cu}(\text{II})$ would be oxidized to $\text{Cu}(\text{III})$, which could catalyze glucose oxidation to generate gluconolactone.

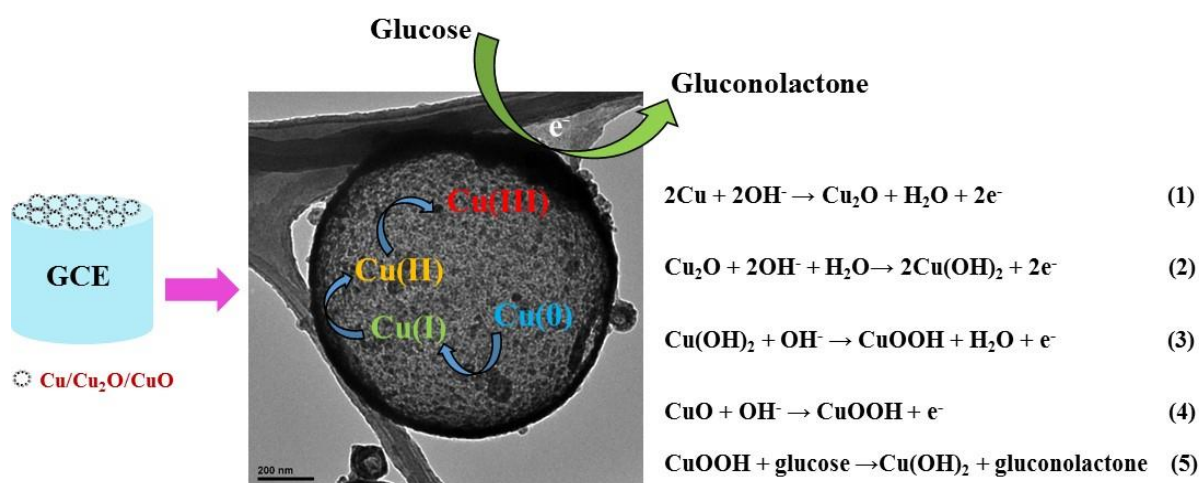


Fig. 5. The schematic representation of the mechanism of glucose sensing with Cu/ Cu_2O / CuO composite HSs.

Recent studies showed that improved electrocatalytic activity could be achieved by the synergistic effect of binary composition interfaces, in which the electrons are rapidly transferred between the redox couples [27,28]. Hassan and Hamis [29] found that the electrocatalytic activity toward glucose oxidation of a Cu electrode can be significantly enhanced by the co-deposition of CuO . The same study also mentioned that CuO facilitates

the transformation of the $\text{Cu}^{3+}/\text{Cu}^{2+}$ redox couple. In the case of the Cu/Cu₂O/CuO-modified GCE, CuO may facilitate the conversion of $\text{Cu}^{3+}/\text{Cu}^{2+}$ redox pairs, so, rapid electron transfer occurs between the Cu, Cu₂O, and CuO species. The highest electron transfer ability of the Cu/Cu₂O/CuO composite was also verified by the EIS results (**Fig. 3b**). Moreover, the high surface area of the Cu/Cu₂O/CuO (Section 3.1) could also play another crucial role in its superior electrocatalytic activity. It is widely accepted that highly efficient electrocatalysis often results from a large active surface area [13–15]. Hence, even though the electron transfer resistance of Cu/Cu₂O/CuO and CuO are similar, the high surface area and large pore volume of the Cu/Cu₂O/CuO provide more active sites and facilitates the glucose oxidation process. The surface area of Cu/Cu₂O is the highest, which might allow the glucose molecules access to the active sites more easily. However, Cu/Cu₂O's highest electron transfer resistance resulted in poor electrocatalytic performance. Overall, to achieve a remarkable sensing performance, the material should have not only low electron transfer resistance but also a high surface area, as achieved in the case of Cu/Cu₂O/CuO.

3.3. *Interference and Stability Studies*

To evaluate the selectivity of the Cu/Cu₂O/CuO-modified GCE sensor, we examined the effects of possibly interfering ions such as anions of chloride, uric acid (UA), ascorbic acid (AA), and dopamine (DA) which typically coexist with glucose in human blood. To test the Cl⁻ ion interference, chloride was added in the form of NaCl, KCl, and CaCl₂. According to blood test reference charts [22], for a healthy individual, the relative ratios of glucose to Na⁺, K⁺, Ca²⁺ are 1:26, 1:1, 1:2. The ratios of AA, DA, and UA to glucose are 1:69, 1:13, 1:423, respectively [22]. As a result, for the interference study, the ratio of glucose to possibly interfering Cl salts was conservatively selected to be 1:30, higher than the highest healthy ratio; whereas the proportion of potentially interfering anions to glucose was

chosen to be 1:10, lower than the lowest healthy ratio. According to the amperometry results (**Fig. 6**), current signals from interfering ions is insignificant, and a clear response from glucose is obtained in the presence of these ions. The observations confirm that the Cu/Cu₂O/CuO modified GCE demonstrates excellent detection specificity for glucose in the presence of selected anions, which may hinder glucose selectivity. The high selectivity of the sensor towards glucose may be attributed to the negative sulfonate groups present on the Nafion that hinder the attachment of the interfering anions on the electrode surface and secure the surface for glucose attachment [16,30].

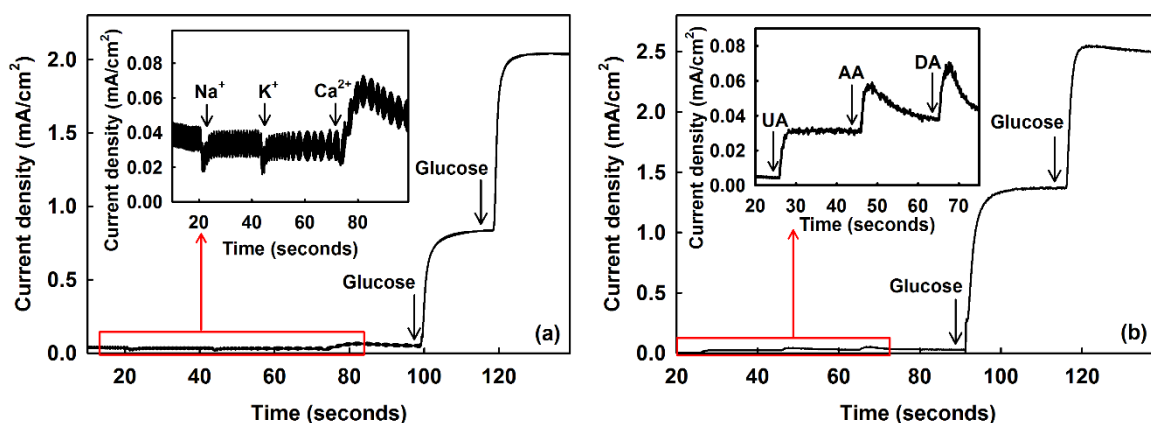


Fig. 6. Amperometric response of the Cu/Cu₂O/CuO-modified GCE to the successive additions of 50 and 100 μM of glucose in the presence of (a) 3 mM Na⁺, K⁺, and Ca²⁺, respectively. (b) 10 μM of UA, AA, and DA, respectively.

The stability of the hollow Cu/Cu₂O/CuO-GCE was investigated by measuring its amperometric response to 50 μM glucose for an extended period, for this case, 21 days. The electrode was exposed to air, and the amperometric response was measured at Day 1, Day 7, Day 14 and Day 21 (**Fig. S7** and **Table S1**). The efficiency dropped by $\sim 24\%$ by the 14th day and then remained stable until the end of the 21st day. Ultimately, the Cu/Cu₂O/CuO-GCE preserved a high sensitivity of $6545 \mu\text{A mM}^{-1} \text{cm}^{-2}$ until the end of the 21st day.

Cu/Cu₂O/CuO was further characterized following the glucose sensing test by both TEM

and XRD analyses. As shown in **Fig. S8(a)**, the hollow spherical structure was still well retained over the used Cu/Cu₂O/CuO sample. However, the used Cu/Cu₂O/CuO sample shows a different phase composition compared to the fresh Cu/Cu₂O/CuO (**Fig. S8(b)**). The intensity of the Cu₂O phases decreases to a certain extent with corresponding increase in the intensity of the CuO peaks, implying a growing amount of CuO at the expense of Cu₂O. As explained earlier, the sensing performance also diminishes with time and number of measurements. A simultaneous decrease in the sensing performance and change in the material composition indicate that the electrocatalytic performance of the Cu/Cu₂O/CuO is affected by the ratio of each component. Accordingly, it is expected that engineering the phase composition of the Cu/Cu₂O/CuO composite could further enhance its electrocatalytic performance and stability. Based on the formation mechanism of these HSs described in the Supporting Information, we have also briefly discussed the synthesis parameters that can be used to control the composition, but the synthesis of material (Cu/Cu₂O/CuO) with exact controlled composition is out of the scope of this paper.

Next, we studied the short-term stability of the Cu/Cu₂O/CuO-modified GCE. As shown in **Fig. S9**, there is nearly no loss in the current signal over a period of 17 minutes for 100 μM glucose on 0.1 M NaOH at 0.55 V, showing the excellent stability of the electrode.

Moreover, the inset displays that it takes approximately 3 seconds to achieve a steady-state current, indicating the relatively rapid response of our sensor to glucose. Furthermore, to verify its workability with blood, we have tested our sensor's response to glucose in fetal calf serum (FCS), which is the blood fraction remaining after the natural coagulation of blood, followed by centrifugation to remove the remaining red blood cells. The serum perfectly mimics real blood due to its composition [29]. **Fig. S10** displays the results of the response to 5 mM glucose addition. The current response at 0.55 V from the proposed glucose sensor is in good agreement with the value obtained at pH 7, which indicates a

potential application in practice. Finally, we compared the sensing responses of electrode materials, specifically Cu/Cu₂O/CuO, synthesized in two different batches and the performance of modified GCEs were compared (**Fig. S11**). Both amperometric responses and CV analysis showed consistent sensing performance for detection of glucose.

4. Conclusions

Cu/Cu₂O/CuO ternary composite HSs were successfully synthesized by a facile FuAR method and were used as a non-enzymatic sensor for electrochemical detection of glucose. The performance of a Cu/Cu₂O/CuO-modified glassy carbon electrode (GCE) for the detection of glucose over a concentration range of 0.5 μ M - 30 mM was established. The results showed that the modified electrode had an outstanding sensitivity of 8726 μ A cm⁻² mM⁻¹, with a low detection limit of 0.39 μ M. The Cu/Cu₂O/CuO hollow spheres (HSs) modified GCE exhibited not only remarkable selectivity but also showed strong short-term stability and a fast and excellent selective response for glucose detection. We hypothesize that the outstanding sensing performance of the Cu/Cu₂O/CuO HSs modified electrodes originate from minimum resistance in the electron conduction between the electrode materials and availability of high surface area.

Acknowledgments

Support from the McDonnell Academy Global Energy and Environmental Partnership (MAGEEP) is gratefully acknowledged. Partial support from the Center for Multiple Myeloma Nanotherapy at Washington University in St. Louis through NNCI grant number U54CA199092 is gratefully acknowledged. The authors acknowledge Yao Nie for her help in XRD and SEM analysis.

References

- [1] W. Hu, D.-W. Sun, H. Pu, T. Pan, Recent Developments in Methods and Techniques for Rapid Monitoring of Sugar Metabolism in Fruits, *Compr. Rev. Food Sci. Food Saf.* 15 (2016) 1067–1079.
- [2] X. Niu, X. Li, J. Pan, Y. He, F. Qiu, Y. Yan, Recent advances in non-enzymatic electrochemical glucose sensors based on non-precious transition metal materials: opportunities and challenges, *RSC Adv.* 6 (2016) 84893–84905.
- [3] H. Zhu, L. Li, W. Zhou, Z. Shao, X. Chen, Advances in non-enzymatic glucose sensors based on metal oxides, *J. Mater. Chem. B.* 4 (2016) 7333–7349.
- [4] H. Cao, A. Yang, H. Li, L. Wang, S. Li, J. Kong, X. Bao, R. Yang, A non-enzymatic glucose sensing based on hollow cuprous oxide nanospheres in a Nafion matrix, *Sens. Actuators B Chem.* 214 (2015) 169–173.
- [5] K. Li, G. Fan, L. Yang, F. Li, Novel ultrasensitive non-enzymatic glucose sensors based on controlled flower-like CuO hierarchical films, *Sens. Actuators B Chem.* 199 (2014) 175–182.
- [6] M. Liu, R. Liu, W. Chen, Graphene wrapped Cu₂O nanocubes: Non-enzymatic electrochemical sensors for the detection of glucose and hydrogen peroxide with enhanced stability, *Biosens. Bioelectron.* 45 (2013) 206–212.
- [7] Y. Li, Y. Zhong, Y. Zhang, W. Weng, S. Li, Carbon quantum dots/octahedral Cu₂O nanocomposites for non-enzymatic glucose and hydrogen peroxide amperometric sensor, *Sens. Actuators B Chem.* 206 (2015) 735–743.
- [8] X. Niu, J. Pan, F. Qiu, X. Li, Y. Yan, L. Shi, H. Zhao, M. Lan, Anneal-shrunked Cu₂O dendrites grown on porous Cu foam as a robust interface for high-performance nonenzymatic glucose sensing, *Talanta.* 161 (2016) 615–622.
- [9] L. Tang, J. Lv, C. Kong, Z. Yang, J. Li, Facet-dependent nonenzymatic glucose sensing properties of Cu₂O cubes and octahedra, *New J. Chem.* 40 (2016) 6573–6576.
- [10] X. Zhang, G. Wang, X. Liu, J. Wu, M. Li, J. Gu, H. Liu, B. Fang, Different CuO nanostructures: Synthesis, characterization, and applications for glucose sensors, *J. Phys. Chem. C.* 112 (2008) 16845–16849.
- [11] C. Kong, L. Tang, X. Zhang, S. Sun, S. Yang, X. Song, Z. Yang, Templating synthesis of hollow CuO polyhedron and its application for nonenzymatic glucose detection, *J. Mater. Chem. A.* 2 (2014) 7306–7312.

- [12] C. Li, Y. Su, S. Zhang, X. Lv, H. Xia, Y. Wang, An improved sensitivity nonenzymatic glucose biosensor based on a Cu_xO modified electrode, *Biosens. Bioelectron.* 26 (2010) 903–907.
- [13] H. Yin, Z. Cui, L. Wang, Q. Nie, In situ reduction of the $\text{Cu}/\text{Cu}_2\text{O}/\text{carbon}$ spheres composite for enzymaticless glucose sensors, *Sens. Actuators B Chem.* 222 (2016) 1018–1023.
- [14] N. Lu, C. Shao, X. Li, T. Shen, M. Zhang, F. Miao, P. Zhang, X. Zhang, K. Wang, Y. Zhang, Y. Liu, $\text{CuO}/\text{Cu}_2\text{O}$ nanofibers as electrode materials for non-enzymatic glucose sensors with improved sensitivity, *RSC Adv.* 4 (2014) 31056–31061.
- [15] H. Huo, C. Guo, G. Li, X. Han, C. Xu, Reticular-vein-like $\text{Cu}@\text{Cu}_2\text{O}/\text{reduced}$ graphene oxide nanocomposites for a non-enzymatic glucose sensor, *RSC Adv.* 4 (2014) 20459–20465.
- [16] G. Wang, Y. Wei, W. Zhang, X. Zhang, B. Fang, L. Wang, Enzyme-free amperometric sensing of glucose using $\text{Cu}-\text{CuO}$ nanowire composites, *Microchim. Acta.* 168 (2010) 87–92.
- [17] Q. Yang, M. Long, L. Tan, Y. Zhang, J. Ouyang, P. Liu, A. Tang, Helical TiO_2 Nanotube Arrays Modified by $\text{Cu}-\text{Cu}_2\text{O}$ with Ultrahigh Sensitivity for the Nonenzymatic Electro-oxidation of Glucose, *ACS Appl. Mater. Interfaces.* 7 (2015) 12719–12730.
- [18] X. Cheng, J. Zhang, H. Chang, L. Luo, F. Nie, X. Feng, High performance $\text{Cu}/\text{Cu}_2\text{O}$ nanohybrid electrocatalyst for nonenzymatic glucose detection, *J. Mater. Chem. B.* 4 (2016) 4652–4656.
- [19] F. Meng, W. Shi, Y. Sun, X. Zhu, G. Wu, C. Ruan, X. Liu, D. Ge, Nonenzymatic biosensor based on Cu_xO nanoparticles deposited on polypyrrole nanowires for improving detection range, *Biosens. Bioelectron.* 42 (2013) 141–147.
- [20] X. Li, C. Wei, J. Fu, L. Wang, S. Chen, P. Li, H. Li, Y. Song, Electrolyte-controllable synthesis of Cu_xO with novel morphology and their application in glucose sensors, *RSC Adv.* 4 (2014) 52067–52073.
- [21] Y. Zhao, Y. Zhang, H. Zhao, X. Li, Y. Li, L. Wen, Z. Yan, Z. Huo, Epitaxial growth of hyperbranched $\text{Cu}/\text{Cu}_2\text{O}/\text{CuO}$ core-shell nanowire heterostructures for lithium-ion batteries, *Nano Res.* 8 (2015) 2763–2776.
- [22] Blood Test Results with Normal Range Reference Chart - BloodBook, Blood Information for Life, <http://www.bloodbook.com/ranges.html>, 2013.

- [23] UK Prospective Diabetes Study (UKPDS) Group, Effect of Intensive Blood-Glucose Control with Metformin on Complications in Overweight Patients with Type 2 Diabetes. *The Lancet* 1998, 352 (9131), 854–865.
- [24] L. Luo, L. Zhu, Z. Wang, Nonenzymatic amperometric determination of glucose by CuO nanocubes–graphene nanocomposite modified electrode, *Bioelectrochemistry*. 88 (2012) 156–163.
- [25] J.M. Marioli, T. Kuwana, Electrochemical characterization of carbohydrate oxidation at copper electrodes, *Electrochimica Acta*. 37 (1992) 1187–1197.
- [26] R. Ortiz, O.P. Márquez, J. Márquez, C. Gutiérrez, Necessity of Oxygenated Surface Species for the Electrooxidation of Methanol on Iridium, *J. Phys. Chem.* 100 (1996) 8389–8396.
- [27] Q. Yang, M. Long, L. Tan, Y. Zhang, J. Ouyang, P. Liu, A. Tang, Helical TiO₂ Nanotube Arrays Modified by Cu-Cu₂O with Ultrahigh Sensitivity for the Nonenzymatic Electro-oxidation of Glucose, *ACS Appl. Mater. Interfaces*. 7 (2015) 12719–12730.
- [28] H. Li, C.-Y. Guo, C.-L. Xu, A highly sensitive non-enzymatic glucose sensor based on bimetallic Cu–Ag superstructures, *Biosens. Bioelectron.* 63 (2015) 339–346.
- [29] Hassan, H. B.; Hamid, Z. A. Electrodeposited Cu–CuO Composite Films for Electrochemical Detection of Glucose. *Int. J. Electrochem. Sci.* 2011, 6 (11) 5741-5758.
- [30] X. Zhang, G. Wang, W. Zhang, N. Hu, H. Wu, B. Fang, Seed-mediated growth method for epitaxial array of CuO nanowires on surface of Cu nanostructures and its application as a glucose sensor, *J. Phys. Chem. C*. 112 (2008) 8856–8862.
- [31] J. van der Valk, D. Brunner, K. De Smet, Å. Fex Svenningsen, P. Honegger, L.E. Knudsen, T. Lindl, J. Noraberg, A. Price, M.L. Scarino, G. Gstraunthaler, Optimization of chemically defined cell culture media – Replacing fetal bovine serum in mammalian in vitro methods, *Toxicol. In Vitro*. 24 (2010) 1053–1063.
- [32] S. Sun, X. Zhang, Y. Sun, S. Yang, X. Song, Z. Yang, Facile water-assisted synthesis of cupric oxide nanourchins and their application as nonenzymatic glucose biosensor, *ACS Appl. Mater. Interfaces*. 5 (2013) 4429–4437.
- [33] W. Lu, Y. Sun, H. Dai, P. Ni, S. Jiang, Y. Wang, Z. Li, Z. Li, Direct growth of pod-like Cu₂O nanowire arrays on copper foam: Highly sensitive and efficient nonenzymatic glucose and H₂O₂ biosensor, *Sens. Actuators B Chem.* 231 (2016) 860–866.

- [34] P. Ni, Y. Sun, Y. Shi, H. Dai, J. Hu, Y. Wang, Z. Li, Facile fabrication of CuO nanowire modified Cu electrode for non-enzymatic glucose detection with enhanced sensitivity, *RSC Adv.* 4 (2014) 28842–28847.
- [35] Y. Zhong, T. Shi, Z. Liu, S. Cheng, Y. Huang, X. Tao, G. Liao, Z. Tang, Ultrasensitive non-enzymatic glucose sensors based on different copper oxide nanostructures by in-situ growth, *Sens. Actuators B Chem.* 236 (2016) 326–333.
- [36] S.K. Meher, G.R. Rao, Archetypal sandwich-structured CuO for high performance non-enzymatic sensing of glucose, *Nanoscale.* 5 (2013) 2089–2099.
- [37] A.A. Ensafi, N. Zandi-Atashbar, B. Rezaei, M. Ghiaci, M. Taghizadeh, Silver nanoparticles decorated carboxylate functionalized SiO₂, New nanocomposites for non-enzymatic detection of glucose and hydrogen peroxide, *Electrochimica Acta.* 214 (2016) 208–216.
- [38] Q. Yi, W. Huang, W. Yu, L. Li, X. Liu, Hydrothermal Synthesis of Titanium-Supported Nickel Nanoflakes for Electrochemical Oxidation of Glucose, *Electroanalysis.* 20 (2008) 2016–2022.
- [39] X.-C. Dong, H. Xu, X.-W. Wang, Y.-X. Huang, M.B. Chan-Park, H. Zhang, L.-H. Wang, W. Huang, P. Chen, 3D Graphene–Cobalt Oxide Electrode for High-Performance Supercapacitor and Enzymeless Glucose Detection, *ACS Nano.* 6 (2012) 3206–3213.
- [40] K. Dhara, R. Thiagarajan, B.G. Nair, G.S.B. Thekkedath, Highly sensitive and wide-range nonenzymatic disposable glucose sensor based on a screen printed carbon electrode modified with reduced graphene oxide and Pd-CuO nanoparticles, *Microchim. Acta.* 182 (2015) 2183–2192.
- [41] J. Nai, S. Wang, Y. Bai, L. Guo, Amorphous Ni(OH)₂ nanoboxes: Fast fabrication and enhanced sensing for glucose, *Small.* 9 (2013) 3147–3152.

Supporting Information

for

A highly sensitive non-enzymatic glucose sensor based on Cu/Cu₂O/CuO ternary composite hollow spheres prepared in a furnace aerosol reactor

Experimental

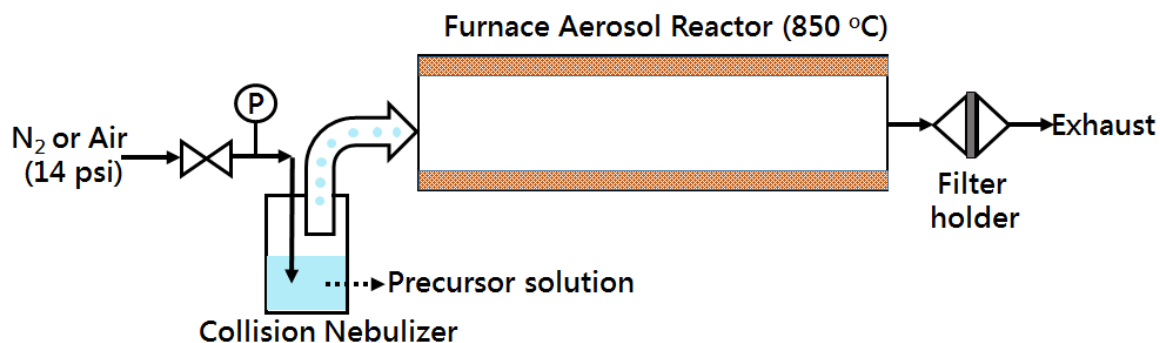


Fig. S1. The furnace aerosol reactor (FuAR) experimental setup. The setup consists of a controlled gas supply, a precursor solution, a collision nebulizer, an electric furnace, and a membrane filter for particle collection.

SI-1. Preparation of Cu/Cu₂O HSs and CuO HSs

Cu/Cu₂O HSs were synthesized using copper nitrate and citric acid (dissolved in DI water) as the precursors using nitrogen (14 psi) as the carrier gas. The preparation of CuO HSs was performed using copper nitrate, citric acid and ammonia (dissolved in DI water) as the precursors, while compressed air (14 psi) was the carrier gas in the FuAR process. The subsequent aerosol process for the preparations of Cu/Cu₂O HSs and CuO HSs was the same as that for Cu/Cu₂O/CuO HSs. Detailed synthetic parameters of the aerosol-made materials are summarized in **Table S1**.

Table S1. Detailed synthetic parameters of Cu/Cu₂O/CuO, Cu/Cu₂O, and CuO.

Sample	Precursor	Carrier gas (14 psi)
Cu/Cu ₂ O/CuO	Copper nitrate, citric acid and ammonia	Nitrogen
Cu/Cu ₂ O	Copper nitrate and citric acid	Nitrogen
CuO	Copper nitrate, citric acid and ammonia	Air

Results and Discussion

SI-2. Formation mechanism of Cu/Cu₂O/CuO HSs

The formation of mixed-phased copper oxide HSs is based on an *in situ* gas release mechanism in a single aerosol droplet, where citric acid acts as a blowing agent [1]. As the droplet containing the precursors enters the heated zone, the rapid water evaporation results in a temperature gradient within the aerosol droplet. The surface of the aerosol droplets is heated first, and then heat is transferred to the core. Further, the decomposition of citric acid results into hot gasses including CH₄, H₂, CO, CO₂, NH₃, NO₂, and H₂O[2,3], which then creates an outward “blowing force,” leading to the formation of a hollow sphere. The gasses heating of the droplet proceeds, a CuO shell forms as a result of supersaturation, precipitation, and decomposition of copper nitrate at the droplet surface. It is important to note that the hollow sphere formation does not occur with only copper nitrate precursor (**Fig. S2**), but with the presence of citric acid.

Recently, Trusov et al. [4] demonstrated the synthesis of metallic Cu and Cu/Cu₂O hollow microspheres, using copper nitrate and glycine as precursors in a spray solution combustion method under an argon atmosphere. Their study showed that at a high temperature (600-750 °C), the decomposition of glycine resulted in the evolution of NH₃ gas that further

reduced the pre-formed CuO nano-grains to produce metallic Cu and Cu/Cu₂O particles. We believe the formation of Cu/Cu₂O HSs in our work occurred by a similar mechanism where pre-formed CuO is reduced to Cu/Cu₂O from the decomposition of citric acid. The decomposition of citric acid produced a large amount of gas including CH₄, H₂, CO, CO₂, NH₃, NO₂, and H₂O [2,3], which acted as *in situ* gas releasing agents inside the particles. These agents induced a high pressure inside the particles and promoted the formation of hollow structures. Therefore, the *in-situ* reduction of CuO particles by strong reducing gasses (e.g., CH₄ and H₂) under a nitrogen atmosphere led to the formation of Cu/Cu₂O HSs.

Interestingly, we found that the addition of ammonia in the precursor solution facilitated the formation of a Cu/Cu₂O/CuO system under a nitrogen atmosphere. During the preparation of the precursor solution of copper nitrate, citric acid, and ammonia, soluble NH₄NO₃ crystallites formed, as revealed by the XRD results (**Fig. S3**). NH₄NO₃ is a strong oxidizer [5], and the decomposition products from NH₄NO₃, including O₂, N₂O, and NO₂, are also strong oxidizers. In the presence of these strong gaseous oxidizers, the reduction of CuO by the decomposition products of citric acid may, therefore, be hindered. As a result, not all CuO is reduced, and this can lead to the formation of Cu/Cu₂O/CuO composite during the FuAR process. Overall, the formation of Cu/Cu₂O/CuO ternary composite is a result of a trade-off between reduction and oxidation reactions involving copper nitrate, citric acid, and ammonia. On the basis of the above formation mechanism, the phase composition of Cu, Cu₂O, and CuO in the Cu/Cu₂O/CuO ternary composite can, therefore, be controlled by tuning the following parameters: (i) furnace temperature, (ii) citric acid/Cu ratio, and (iii) the concentration of ammonia in the precursor mixture.

Crystalline CuO was also identified in the copper nitrate–citric acid–ammonia precursor in a strong oxidizing atmosphere (air and NH_4NO_3) during the FuAR process. To the best of our knowledge, this is the first study demonstrating the preparation of Cu/Cu₂O/CuO composite HSs using an aerosol-based synthesis method.

Previous studies on preparing Cu-based electrode materials were typically performed in an aqueous batch system (e.g., a hydrothermal method, electrospinning, and electrodeposition) in which multiple synthetic steps and tens of hours of processing time are required [6–9]. In contrast, the FuAR is a scalable method which ensures an easy, rapid and highly reproducible synthesis; more importantly, it can be operated continuously, with a residence time of only several seconds [10,11]. Also, the Cu/Cu₂O/CuO composite HSs were produced from an aqueous solution of copper nitrate, citric acid, and ammonia, all of which are low-cost and readily available for mass production of HSs.

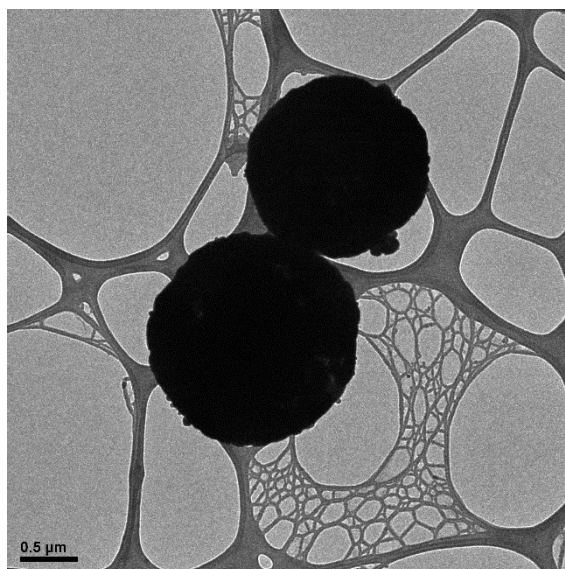


Fig. S2. TEM image of CuO microspheres synthesized with copper nitrate only through FuAR.

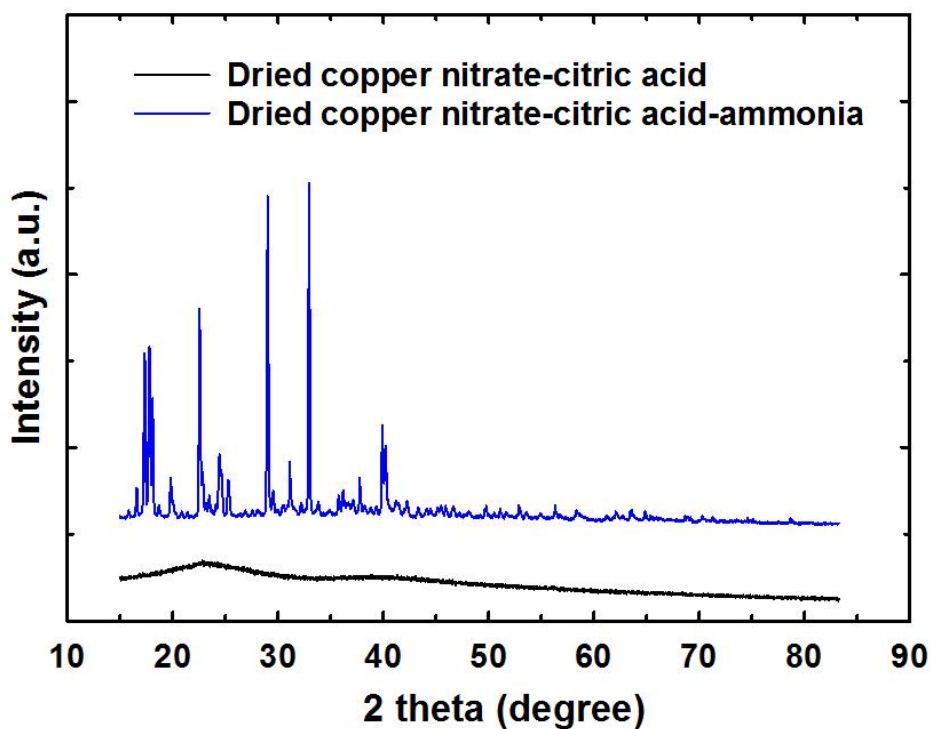


Fig. S3. XRD patterns of dried copper nitrate-citric acid and copper nitrate-citric acid-ammonia precursors.

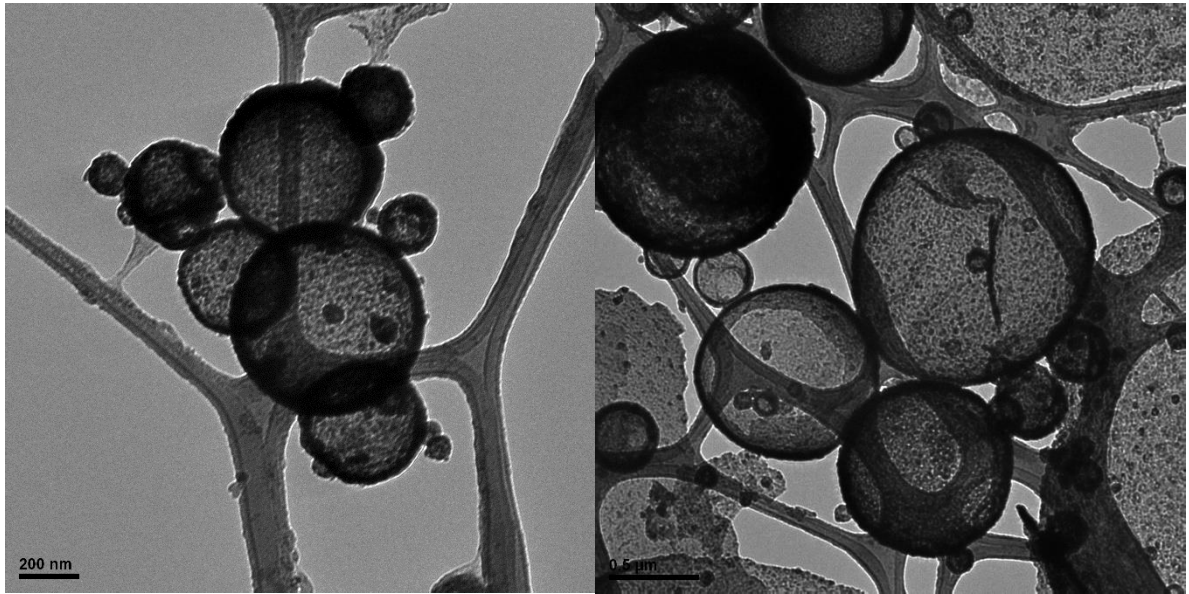


Fig. S4. TEM images of (a) Cu/Cu₂O HSs and (b) CuO HS

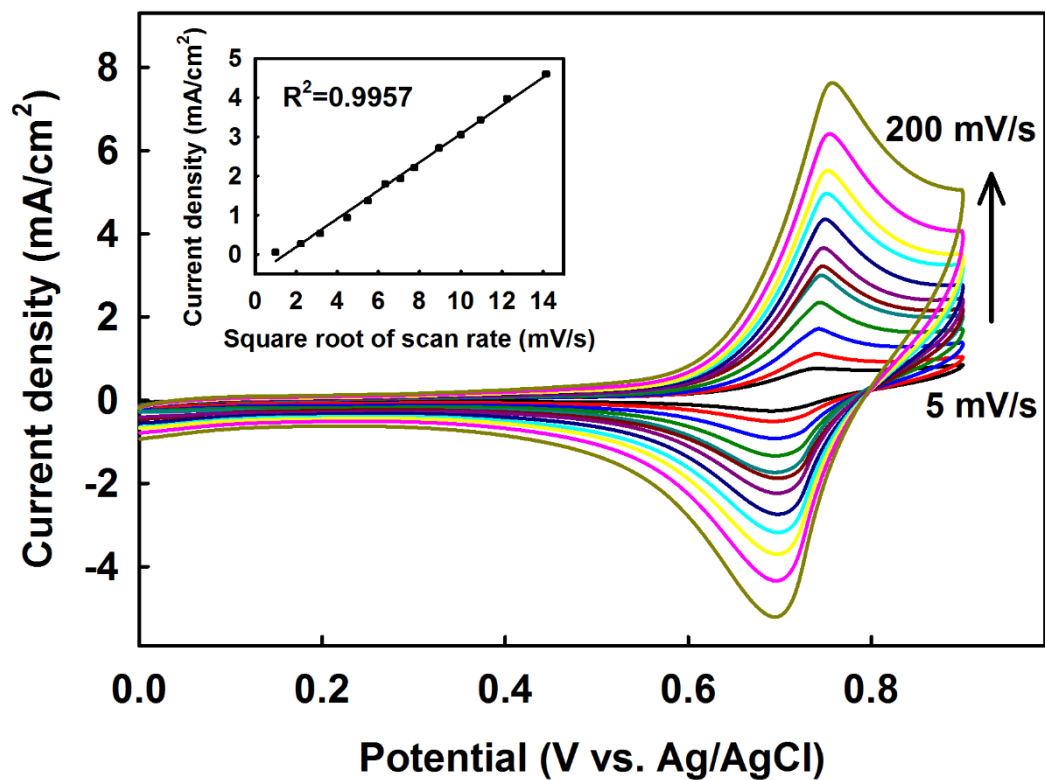


Fig. S5. CV curves of Cu/Cu₂O/CuO-modified electrode in 0.1 mM glucose and 100 mM KCl electrolyte solution containing equimolar (0.01 M/0.01 M) [Fe(CN)₆]^{4-/3-} solution at different scan rates. The inset is the corresponding calibration curve.

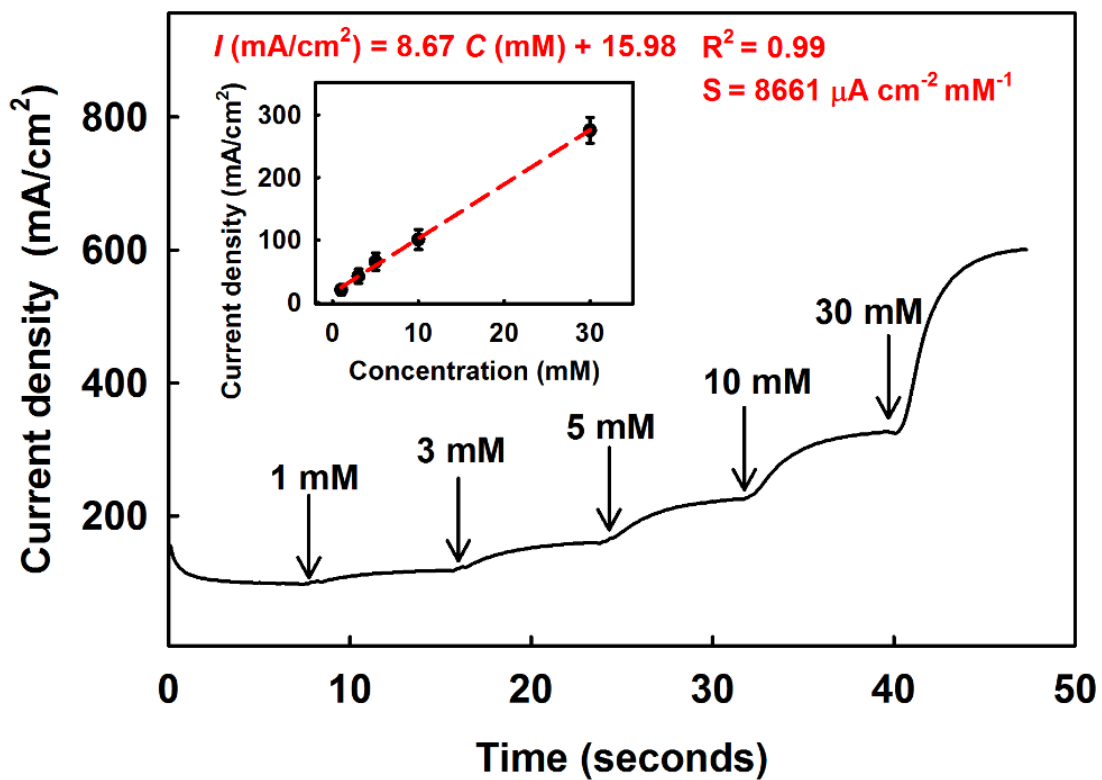


Fig. S6. Amperometric response at 0.55 V of the Cu/Cu₂O/CuO modified GCE to successive ~10 s additions of different concentrations of glucose to 0.1 M NaOH.

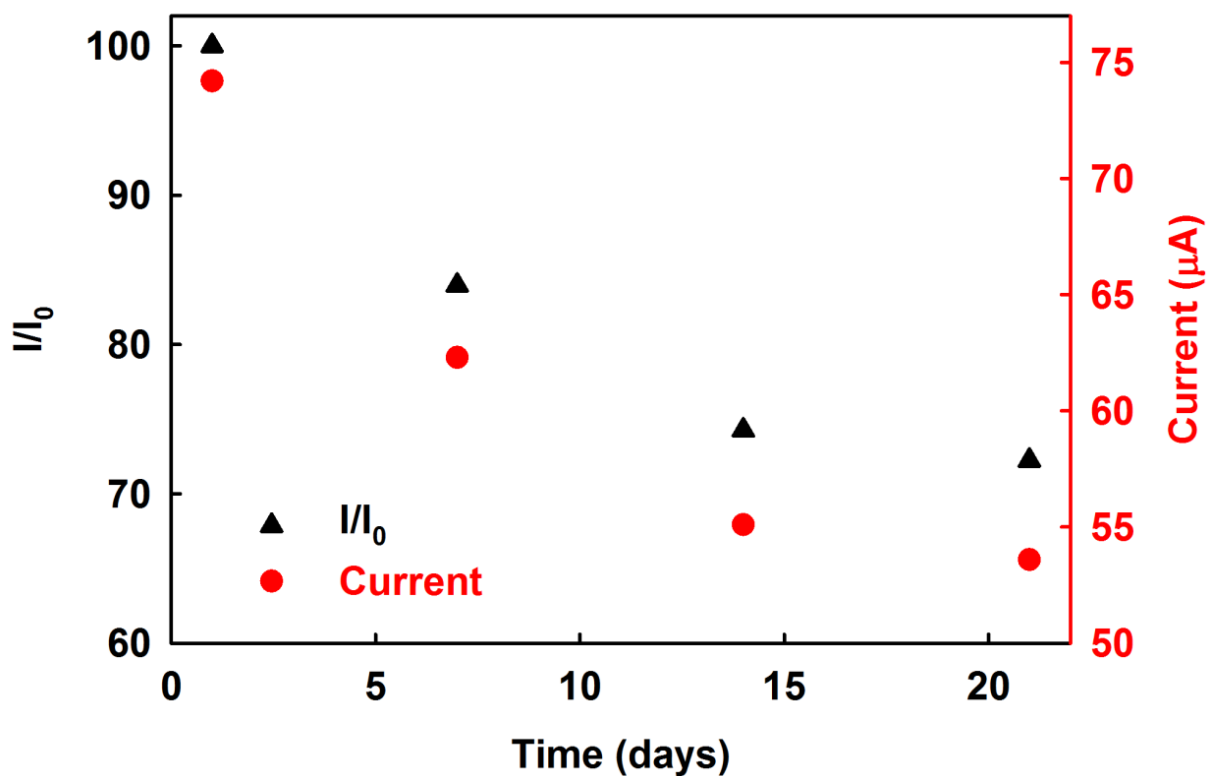


Fig. S7. The long-term stability of the hollow Cu/Cu₂O/CuO-modified GCE, measured by its current response to 50 μM glucose. The measurements were taken at Day 1, 7, 14, and 21. The left y-axis denotes the percentage of the measured current response to the initial current at Day 1. The right y-axis displays the value of the measured current.

Table S2. The current responses to 50 μM glucose at 0.55V of Cu/Cu₂O/CuO-modified GCE on day 1, 7, 14 and 21.

Day	Current (μA)	I/I_0
1	74.2	100.0
7	62.3	83.9
14	55.1	74.2
21	55.0	74.2

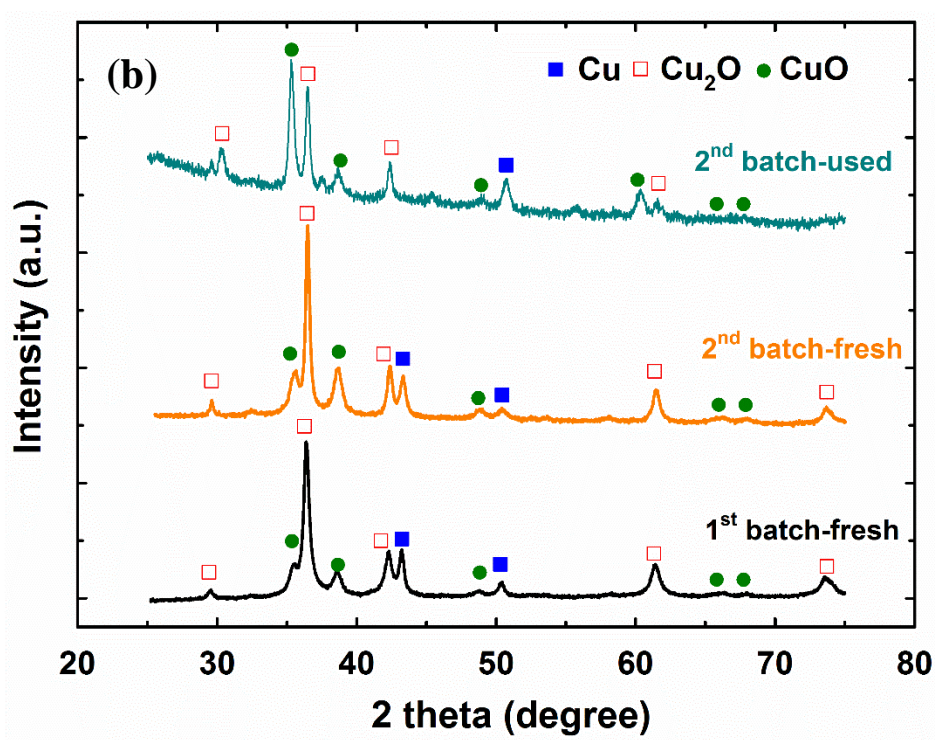
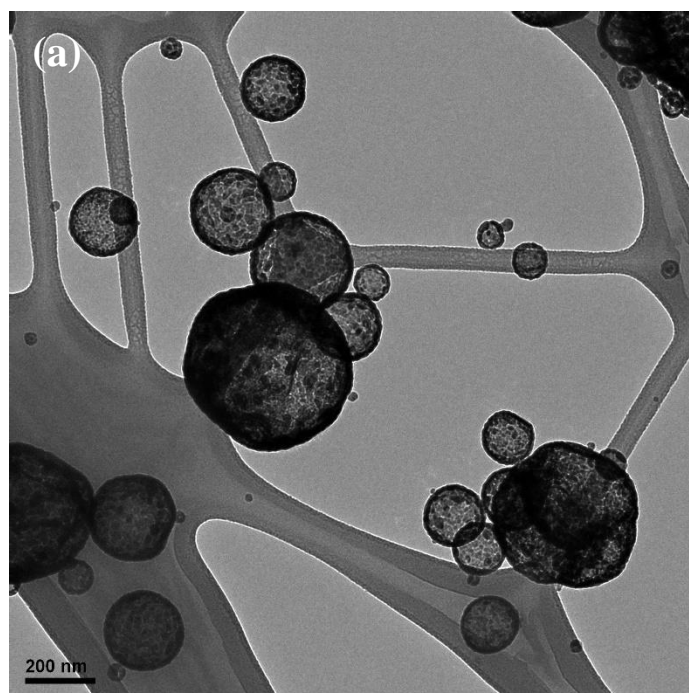


Fig. S8. (a) TEM image of the Cu/Cu₂O/CuO sample after glucose detection. (b) Comparative XRD patterns of Cu/Cu₂O/CuO composite samples before and after reactions.

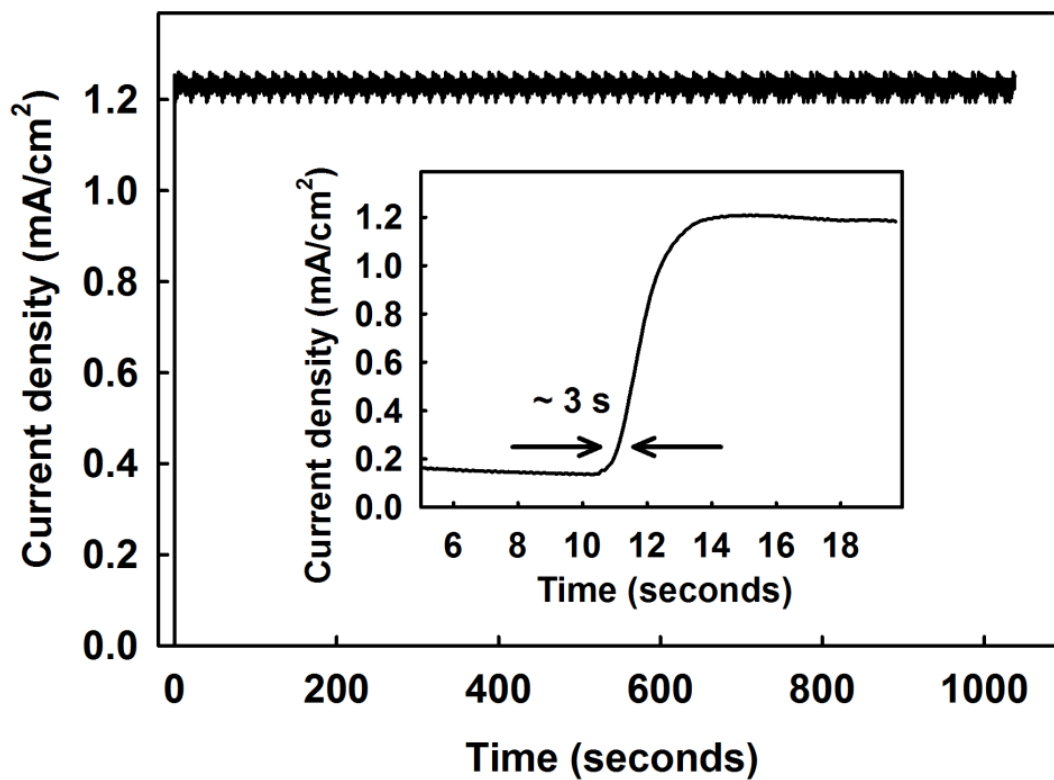


Fig. S9. The short-term stability of the hollow Cu/Cu₂O/CuO-modified GC electrode, measured by its amperometric response 0.55 V to 100 μ M glucose for more than 1000 seconds. The inset shows the response time of the electrode to reach a steady-state current. It takes approximately 3 seconds for the electrode to respond to glucose addition.

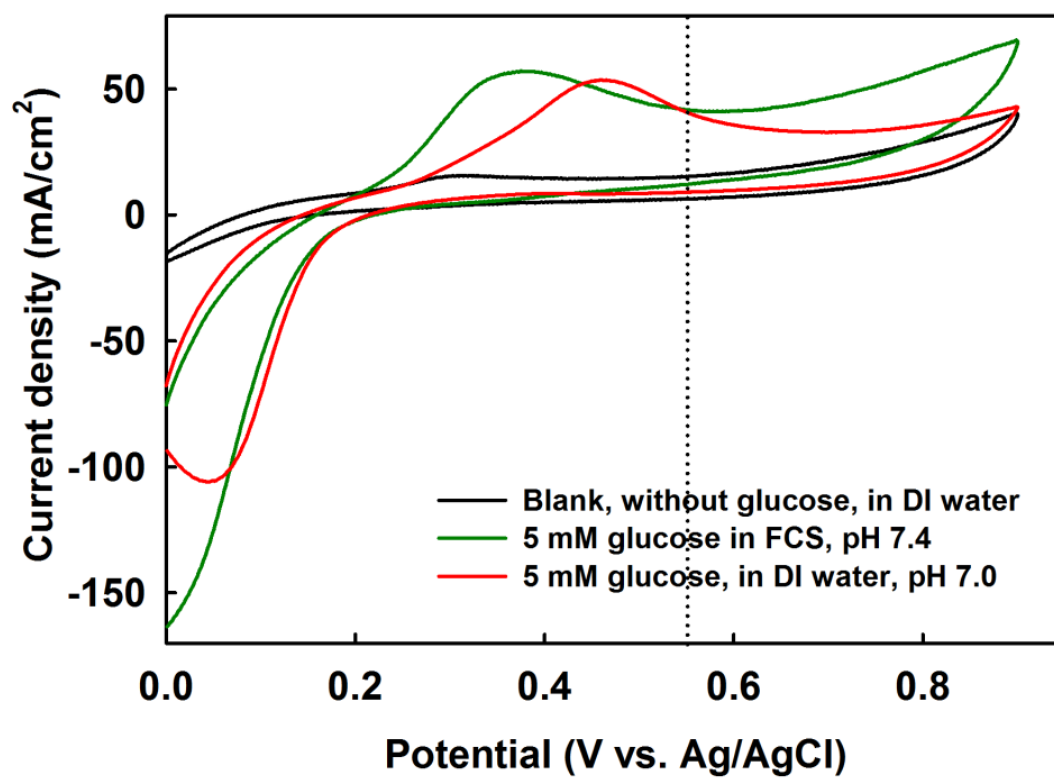


Fig. S10. CV curves at 50 mV/s of Cu/Cu₂O/CuO modified GCE with glucose concentrations of 5 mM in fetal calf serum (FCS), pH 7.4 and DI water, pH 7.0. The blank represents the CV curve without the addition of glucose.

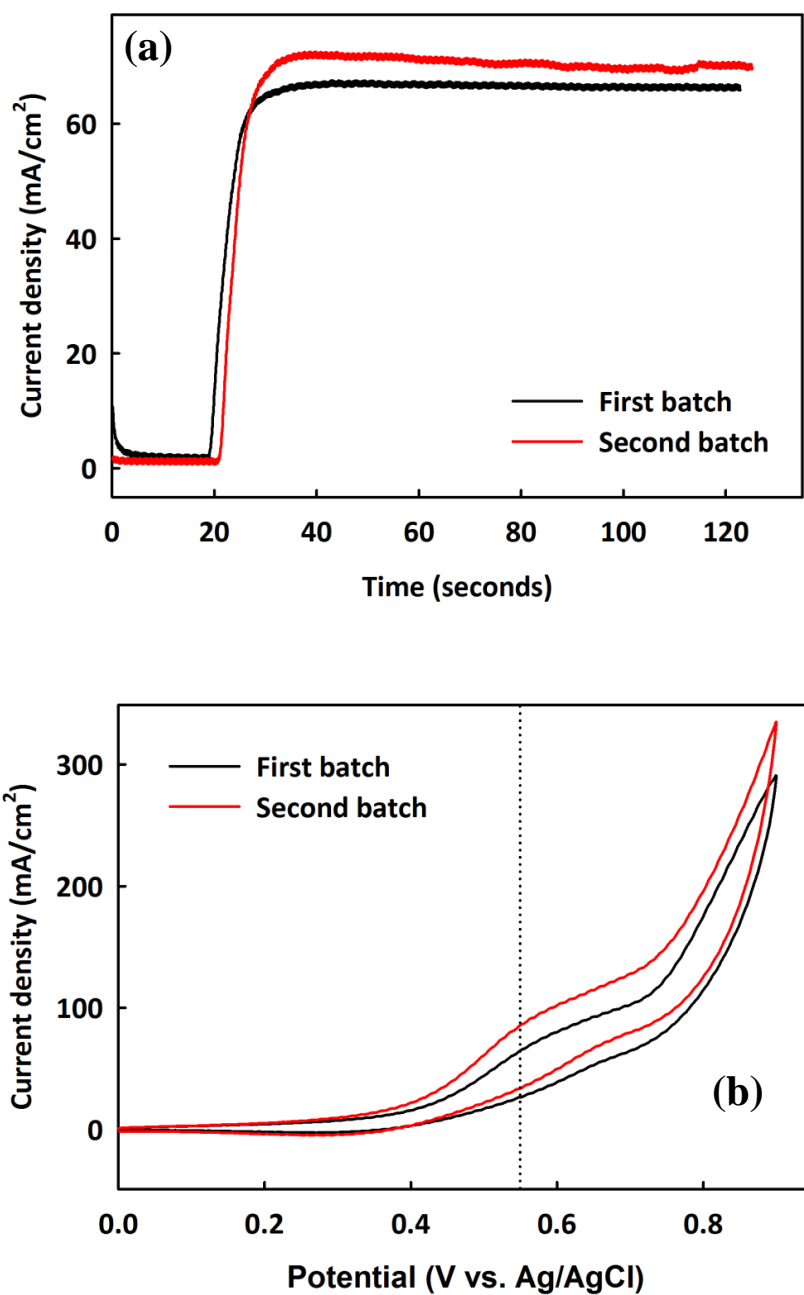


Fig. S11. Two different batches of Cu/Cu₂O/CuO HSs were synthesized, and the performance of Cu/Cu₂O/CuO-modified GC electrodes were compared. **(a)** Amperometric responses measured at 0.55 V to 5 mM glucose for more than 120 seconds. **(b)** CV curves at 50 mV/s of two different batches of synthesized Cu/Cu₂O/CuO modified GCE with glucose concentrations of 5 mM in 0.1 M NaOH.

References

- [1] G. Jian, L. Liu, M.R. Zachariah, Facile Aerosol Route to Hollow CuO Spheres and its Superior Performance as an Oxidizer in Nanoenergetic Gas Generators, *Adv. Funct. Mater.* 23 (2013) 1341–1346.
- [2] Y. Jiang, S. Yang, Z. Hua, H. Huang, Sol–Gel Autocombustion Synthesis of Metals and Metal Alloys, *Angew. Chem. Int. Ed.* 48 (2009) 8529–8531.
- [3] L. Shi, K. Tao, R. Yang, F. Meng, C. Xing, N. Tsubaki, Study on the preparation of Cu/ZnO catalyst by sol–gel auto-combustion method and its application for low-temperature methanol synthesis, *Appl. Catal. Gen.* 401 (2011) 46–55.
- [4] G.V. Trusov, A.B. Tarasov, E.A. Goodilin, A.S. Rogachev, S.I. Roslyakov, S. Rouvimov, K.B. Podbolotov, A.S. Mukasyan, Spray Solution Combustion Synthesis of Metallic Hollow Microspheres, *J. Phys. Chem. C* 120 (2016) 7165–7171.
- [5] J.C. Oxley, S.M. Kaushik, N.S. Gilson, Thermal decomposition of ammonium nitrate-based composites, *Thermochim. Acta.* 153 (1989) 269–286.
- [6] M. Long, L. Tan, H. Liu, Z. He, A. Tang, Novel helical TiO₂ nanotube arrays modified by Cu₂O for enzyme-free glucose oxidation, *Biosens. Bioelectron.* 59 (2014) 243–250.
- [7] Q. Yang, M. Long, L. Tan, Y. Zhang, J. Ouyang, P. Liu, A. Tang, Helical TiO₂ Nanotube Arrays Modified by Cu-Cu₂O with Ultrahigh Sensitivity for the Nonenzymatic Electro-oxidation of Glucose, *ACS Appl. Mater. Interfaces.* 7 (2015) 12719–12730.
- [8] Y. Zhong, T. Shi, Z. Liu, S. Cheng, Y. Huang, X. Tao, G. Liao, Z. Tang, Ultrasensitive non-enzymatic glucose sensors based on different copper oxide nanostructures by in-situ growth, *Sens. Actuators B Chem.* 236 (2016) 326–333.
- [9] S. Sun, X. Zhang, Y. Sun, S. Yang, X. Song, Z. Yang, Facile water-assisted synthesis of cupric oxide nanourchins and their application as nonenzymatic glucose biosensor, *ACS Appl. Mater. Interfaces.* 5 (2013) 4429–4437.
- [10] K. Okuyama, I. Wuled Lenggoro, Preparation of nanoparticles via spray route, *Chem. Eng. Sci.* 58 (2003) 537–547.
- [11] W.-N. Wang, J. Park, P. Biswas, Rapid synthesis of nanostructured Cu–TiO₂–SiO₂ composites for CO₂ photoreduction by evaporation driven self-assembly, *Catal Sci Technol.* 1 (2011) 593–600.

Appendix VI.

Investigating the Effects of Stove Emissions on Ocular and Cancer Cells

The results of this appendix have been compiled as a full paper and submitted to Scientific Reports. Karakoçak B. B., Patel S., Ravi N., Biswas P. Investigating the Effects of Cookstove Emissions on Ocular Cells. 2018.

Abstract

More than a third of world's population relies on solid fuels for cooking and heating, with major health consequences. Although solid fuel combustion emissions are known to increase the prevalence of illnesses such as chronic obstructive pulmonary disease and lung cancer, however, their effect on the eyes is underexplored. This study assesses the acute toxicity of solid fuel combustion emissions on healthy ocular cells and a cancer cell line. Three healthy ocular cell lines (corneal, lens, and retinal epithelial cells) and a cancer cell line (Chinese hamster ovary cells) were exposed to liquid and gas phase emissions from applewood and coal combustion. Following the exposure, real-time cell attachment behavior was monitored for at least 120 hours with electrical cell impedance spectroscopy. The viability of the cells, amount of apoptotic cells, and generation of reactive oxygen species (ROS) were quantified with MTT, ApoTox-Glo™, and ROS-Glo™ H₂O₂ assays, respectively. The results showed that coal emissions compromised the viability of ocular cells more than applewood emissions. Interestingly, the cancer cells, although their viability was not compromised, generated 1.7 to 2.7 times more ROS than healthy cells. This acute exposure study provides compelling proof that biomass combustion emissions compromise the viability of ocular cells and increase ROS generation. The increased ROS generation was fatal for ocular cells, but it promoted the growth of cancer cells.

3. Introduction

Nearly three billion people still use solid fuels, such as biomass, coal, and cow dung cakes, in inefficient stoves for cooking and heating. These stoves generate pollutants such as particulate matter (PM), CO, and CH₄. The resultant exposure to household air pollution (HAP) has been associated with respiratory (Noonan et al. 2010) and cardiovascular diseases (Pena et al. 2017), as well as formation of cataracts (Pokhrel et al. 2005, Pokhrel et al. 2013). The World Health Organization (WHO) recognizes HAP as the single most significant health risk, accounting for 4.3 million premature deaths in 2012 (World Health 2015).

Epidemiological studies have investigated associations between stove emissions and different health indicators, such as cardiovascular risk, hypertension, and lung function (Pokhrel et al. 2005, Silva et al. 2009, Dutta et al. 2013, Pokhrel et al. 2013, Dutta and Ray 2014). However, epidemiological associations between indoor air pollutants and morbidity and mortality are often hindered by relatively small sample sizes, which are frequently not considered representative, and by the logistical difficulties of fieldwork in developing countries. A truly fundamental approach to understand and characterize the human health burden related to indoor stove exposure would be to investigate effects both *in-vitro* and *in-vivo*.

Both *in-vitro* and *in-vivo* studies centered on the respiratory system have shown that emissions from biomass fuels have carcinogenic and mutagenic properties (Danielsen et al. 2011, Mauderly et al. 2011, Corsini et al. 2013, Liberda and Chen 2013, Muala et al. 2015, Dilger et al. 2016). However, on the cellular level, no study has investigated the possible adverse effects of exposure to solid fuel combustion emissions on the eye, a part of the central nervous system (Figure 1). Only a few *in-vivo* studies have explored the effects of combustion smoke on the eye (Zou et al. 2009, Kunchithapautham et al. 2014). One *in-vivo* study showed that combustion smoke inhalation injury is caused by hypoxia and particulate

matter acting alone or in combination (Zou et al. 2009). How inhaling stove emissions causes secondary injury to the eye has not been fully explored; however, there is evidence that in response to smoke exposure from cotton burning, the permeability of the ocular blood vessels increased, which resulted in edema in the retina (Zou et al. 2009).

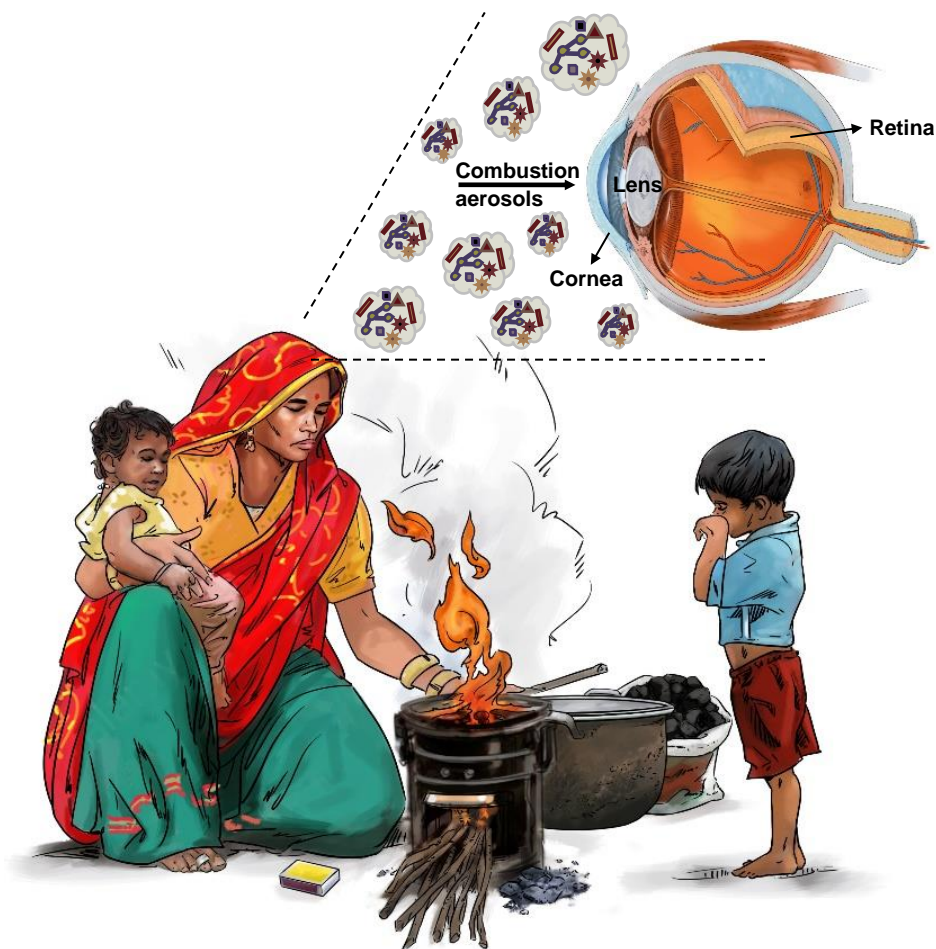


Figure. 1. Daily activities like cooking and heating pose a threat, especially to women and children whose eyes are in direct contact with combustion smoke

Exposure to stove emissions can induce oxidative stress because it depletes the antioxidant protection against cataract formation (Pokhrel et al. 2013). On the cellular level, oxidative stress can lead to the subsequent release of reactive oxygen species (ROS), which damages both nuclear DNA and mitochondrial DNA (Barrett et al. 1999, Elder et al. 2000, Guo et al.

2013). Thus, biochemical and molecular changes occur which may lead to apoptosis (cell death) or tumor initiation (Galadari et al. 2017). The ROS handling capacities of healthy cells and cancer cells are different, and cancer cells are known to adapt well to oxidative stress (Liou and Storz 2010). On the other hand, healthy ocular cells handle oxidative stress differently. For example, unlike corneal and lens epithelial cells, retinal cells can cope well with oxidative stress due to their unique ROS handling capacity, an evolutionary mechanism for tolerating light exposure (Zou et al. 2009). In view of this information, and because biomass and coal combustion is a repetitive daily activity for women, especially in developing countries (Joshi et al. 2010, Hosgood et al. 2011, Anenberg 2012, Kumar 2012, Hodnebrog et al. 2016), there are clear motives to investigate the effect of biomass and coal combustion smoke at the cellular level first. The present study sought to determine whether ocular cells, as well as cancer cells, would be affected by exposure to emissions from applewood and coal combustion in a stove. To our knowledge, this is the first evaluation of the *in-vitro* toxicity of biomass and coal combustion emissions on the eye.

Experimental Methods

Particulate matter collection and characterization. An improved gasifier cookstove, described in a previous study (Patel et al. 2016), was used to burn applewood and coal. Detailed physical and chemical characteristics of the cookstove emissions from applewood and coal have also been reported in previous work (Patel et al. 2016), and therefore are not repeated here. A forced-draft gasifier cookstove (Phillips, Model HD4012 LS) was used. Applewood chips with no additives were purchased locally (St. Louis, MO) and bituminous coal was procured from Brilliant, Alabama.

For gas phase exposure, cell culture plates were placed inside a chamber as illustrated in Figure 2A. A minimum amount of medium was left in the wells to prevent the cells from drying out and to create an air-liquid interface for the exposure experiment (inset of Figure

2A). The humidity of the chamber was maintained at 67% by placing wet towels inside the box. Air, either alone (as the control) or containing cookstove emissions, was passed through the chamber for one hour at the same flow rate of 3 LPM as used for PM collection via a filter (Figure 2). At the end of the exposure, the cell plates were removed from the chamber, and the cell culture medium was replenished.

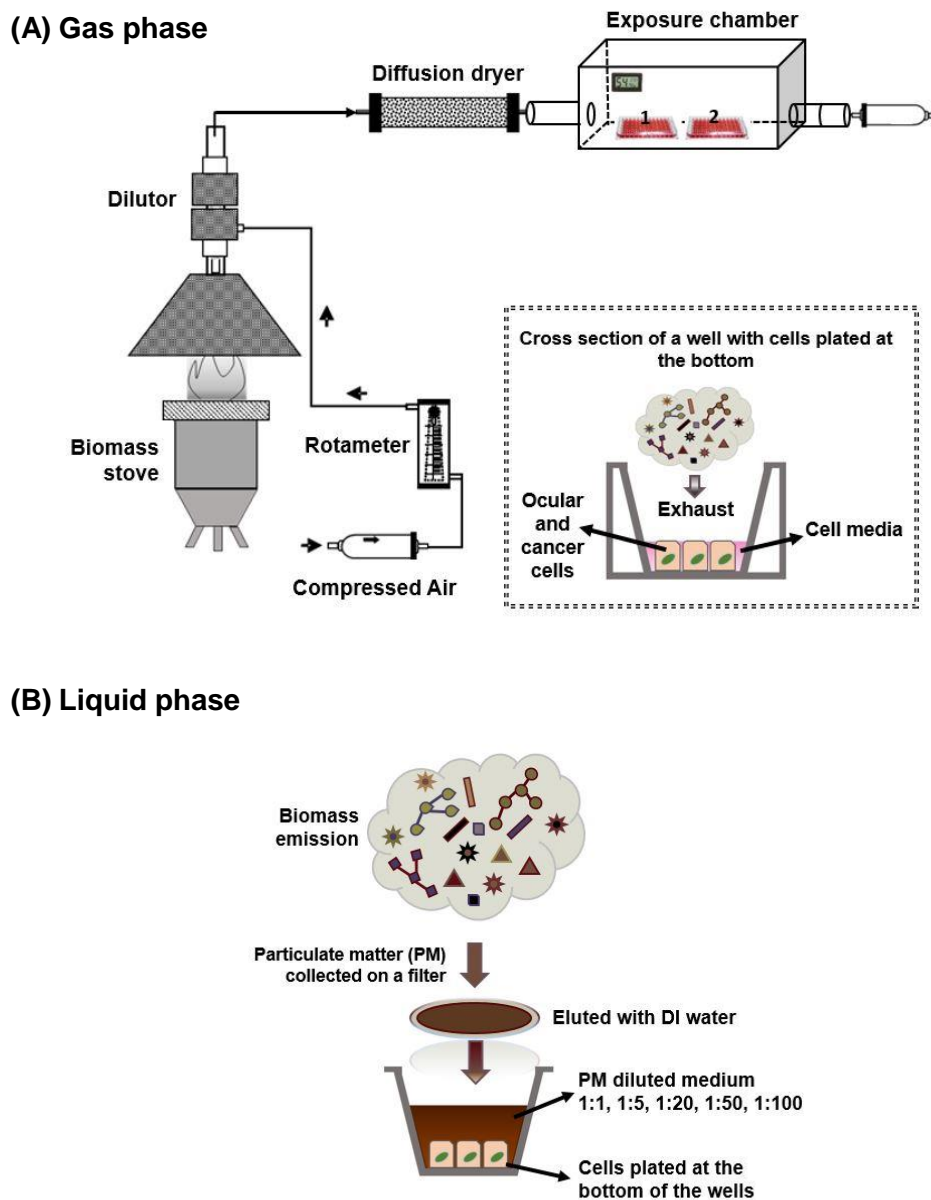


Figure. 2. Schematic illustration of the experimental setup (A) Gas phase exposure. The inset represents the air-liquid interface created for the gas phase exposure. (B) Liquid phase exposure.

For liquid phase exposure, the particulate matter (PM) emissions were first collected on a 47 mm Teflon filter (Sigma-Aldrich, St. Louis, MO) as illustrated in Figure 2B. To extract the collected PM, the filter was submerged in 100 ml of deionized water and sonicated for 30 minutes. This extract was then further diluted to different strengths with Dulbecco's modified Eagle's medium (DMEM F-12) (Sigma-Aldrich, St. Louis, MO) with 10% fetal calf serum (Sigma-Aldrich, St. Louis, MO) and 1% antibiotic-antimitotic solution (Sigma-Aldrich, St. Louis, MO). Particle suspensions (1000-200-50-20-10 $\mu\text{g/ml}$, denoted in the rest of the study as dilution ratios of 1:1, 1:5, 1:20, 1:50, 1:100, respectively) were sonicated with a Branson sonicator bath (Hach, Loveland, CO) for 30 seconds immediately before being added to cell cultures. The cell media was removed prior to the applewood extract exposure in the liquid phase. The volume of applewood extracts was verified to be 150 μl in each well.

Cell models. The selection criterion for cell lines was the likelihood of the cells being in direct environmental contact with the biomass emission. As illustrated in Figure 1, biomass smoke is expected to hit the cornea first. Epidemiological studies have reported a direct correlation between cataract formation and biomass smoke exposure (Shalini et al. 1994, Pokhrel et al. 2005, Pokhrel et al. 2013, Ravilla et al. 2016), so lens epithelial cells were also included in this study. Further, retinal pigment epithelial cells have been reported to be adversely affected by cigarette smoke exposure (Alcazar et al. 2007, Jia et al. 2007, Bertram et al. 2009), so they were included in this study as the last healthy ocular cell line. On the other hand, the *in-vitro* toxicity of biomass smoke to lung cancer cell lines is well documented (Dogan et al. 2011, Dilger et al. 2016); therefore, lung cancer cells were not assessed in this study. Instead, we chose an ovarian cancer cell line which has been shown to have a high mitotic index (Tobey et al. 1967, Harada and Morris 1981) and also has not been studied before for *in-vitro* toxicity assessment of biomass smoke emissions.

Corneal epithelial cells (ATCC® PCS-700-010™), lens epithelial cells (ATCC® CRL-11421™), retinal pigment epithelial cells (ATCC® CRL-2302™), and Chinese hamster ovary (CCL-61™) cells were purchased from American Type Culture Collection (Manassas, VA).

Cell culture conditions. In flat-bottom 96-well plates, 150 µl volumes of cells (2.0×10^4 cells per well) were incubated at 37 °C in 5% CO₂ until confluent, then exposed to biomass emissions. For gas phase experiments, a minimum amount of cell medium was kept in each well to prevent cells from drying, while also ensuring direct contact with the biomass emission. For liquid phase experiments, biomass emission extracts were dispersed in cell culture medium (DMEM/F12) to be used for cell exposure.

Assessment of cytotoxicity measurements with MTT, ApoTox-Glo™, and ROS-Glo™H₂O₂ assays. Cell metabolic activity, and hence the viability of cells in the presence of biomass smoke, was assessed with MTT (3-[4, 5 dimethyl-thiazoly-2-yl] 2-5 diphenyl tetrazolium bromide).

The apoptotic cell amount and ROS generation, respectively, were measured by ApoTox-Glo™ and ROS Glo™ H₂O₂ assays. In all biological and imaging tests, cells exposed to filtered air alone served as a negative control. For the MTT assay, following the gas and liquid phase exposures, 100 µL of MTT (1 mg/l in growth media) was added to each well, and the plate was incubated for an additional 5 h at 37 °C in 5% CO₂. The resulting blue component, produced by the reduction of the tetrazolium salt of MTT by mitochondrial dehydrogenase enzyme, was dissolved in 100 µL dimethyl sulfoxide (DMSO). The optical density of the colored product was read photometrically, using a spectrophotometer at 540 nm with a microplate reader (Molecular Devices Spectra Max 190). The absorbance of untreated cells was used as the negative control. The percentage viability of the cells was calculated

from the ratio of the mean optical density of the sample to the optical density of the negative control (Karakocak et al. 2016).

For the apoptosis and ROS detection experiments, the cells were cultured and exposed to liquid and gas phase biomass emissions in 96-well, clear-bottomed white plates. Caspase 3/7 activity, the key indicator for apoptosis, was evaluated using the ApoTox-Glo™ Triplex assay according to the manufacturer's protocol (Promega Biosciences San Luis Obispo, CA). The light output, measured with a luminometer, correlates with Caspase-3/7 activation, and luminescence was measured using a microplate reader (Molecular Devices SpectraMax 190).

ROS generation was evaluated with the ROS-Glo™ H₂O₂ assay according to the manufacturer's protocol (Promega Biosciences San Luis Obispo, CA). The light signal produced by recombinant Luciferase enzyme is proportional to the level of H₂O₂ in the cells. The luminescence was measured using a microplate reader (Molecular Devices SpectraMax 190).

Electrical Impedance Spectroscopy. The cell attachment behavior of the cells was analyzed real-time using electrical impedance spectroscopy (ECIS), a noninvasive technique that measures the impedance across gold electrodes at the bottom of tissue culture wells, using frequencies of alternating current (Wegener et al. 2000, Arndt et al. 2004). Cells were plated in a 96-well ECIS array (Applied Biophysics, 96W20idf PET, Troy, NY) similar to those plated for the endpoint toxicity assays. The change in resistance at frequencies ranging from 400 to 64,000 Hz was measured over time. Low-frequency impedance can be used to monitor the solution paths around the cells, and hence the layer's cell-to-cell barrier functions (Wegener et al. 2000). The addition of particles may complicate the impedance of the system. However, at a frequency of 4,000 Hz, the contribution to resistance from cells was dominant over the contribution to resistance from biomass extracts with the medium (Kandasamy et al.

2010). Therefore, we chose a frequency of 4,000 Hz to monitor cell growth and biocompatibility.

Statistical Analysis. Analysis of variance (ANOVA) was used to statistically compare ECIS results with the negative control (untreated cells) and positive control (medium only). A significance level of $**P < 0.001$ was deemed statistically acceptable.

ANOVA was also used to statistically evaluate endpoint biocompatibility testing results with a negative control. A significance level of $*P < 0.05$ was deemed statistically acceptable. All tissue culture data (MTT, ApoTox-Glo™, and ROS-Glo™ H₂O₂) were expressed as the mean \pm standard error of the mean (SEM) values of at least three independent culture experiments. Eight replicates were performed for each separate cell culture experiment.

Data Availability

All data generated or analyzed during this study are included in this article.

Results

We conducted laboratory experiments to investigate the effects of stove emissions on ocular and cancer cells exposed via two pathways: (1) gas phase and (2) liquid phase. *In-vitro* models can be designed to closely mimic real exposure conditions; i.e., creating an air-liquid interface (Mulhopt et al. 2016). When used with a direct particle-to-cell deposition system, *in-vitro* models provide more physiologically relevant conditions for evaluating the cellular reactions, i.e., apoptosis initiation and ROS generation, in response to environmental pollutants (Seagrave et al. 2005, Hawley and Volckens 2013, Mulhopt et al. 2016). In the first part of our study, to closely simulate ocular cell exposure to air pollutants, we performed gas phase exposure to cells maintained in “air-liquid interface” conditions, where only a thin layer of fluid separates the cells from the aerosols (Figure 2A). Unlike the liquid phase exposure experiments, these conditions expose the target cells to both particulate and non-particulate constituents of the exhaust in naturally occurring proportions. In the second part of

the study, liquid phase exposure experiments were conducted where particulate matter extracts were exposed to submerged cell cultures (Figure 2B).

Coal and applewood were the two fuels used in this study. A laboratory hood setup (Figure 2) with an aspiration-based dilution system was used to capture the emissions from fuel burned in a micro-gasifier stove. Comprehensive details about the stove, fuel properties, and their combustion and emissions characteristics were reported in previous studies (Patel et al. 2016, Leavey et al. 2017).

Acute toxicity: Gas phase exposure

To assess the cellular responses to gas phase exposure, at approximately the 47th hour of cell growth the viability, apoptotic cell amount, and ROS production were measured before and after exposing the cells to applewood and coal combustion emissions for one hour. The cell attachment behavior, however, was monitored in real time for more than 120 hours.

Figure 3A compares the viability, amount of apoptotic cells, and the amount of ROS generation for the four cells types exposed (gas phase) to emissions from applewood and coal combustion. No significant difference was observed for the biocompatibility of corneal and lens epithelial cells exposed to the emissions from the two fuels (Figure 3A). Both retinal and CHO cells were more biocompatible with applewood emissions than coal emissions. The viability of the CHO cells was not compromised; instead, when exposed to applewood emissions, their biocompatibility was measured to be greater than 100%. However, coal emissions adversely affected the CHO cells' viability (89%). The apoptotic cell measurements showed statistically significant differences in the responses to applewood and coal combustion emissions (Figure 3B). Lens epithelial cells showed the highest apoptosis signal, followed by corneal and retinal cells. The apoptotic signals recorded from retinal and CHO cells were significantly less strong than the signals from corneal and lens epithelial

cells. Similar to the apoptotic signal results, corneal and lens epithelial cells produced significantly higher amounts of ROS (Figure 3C) than retinal and CHO cells.

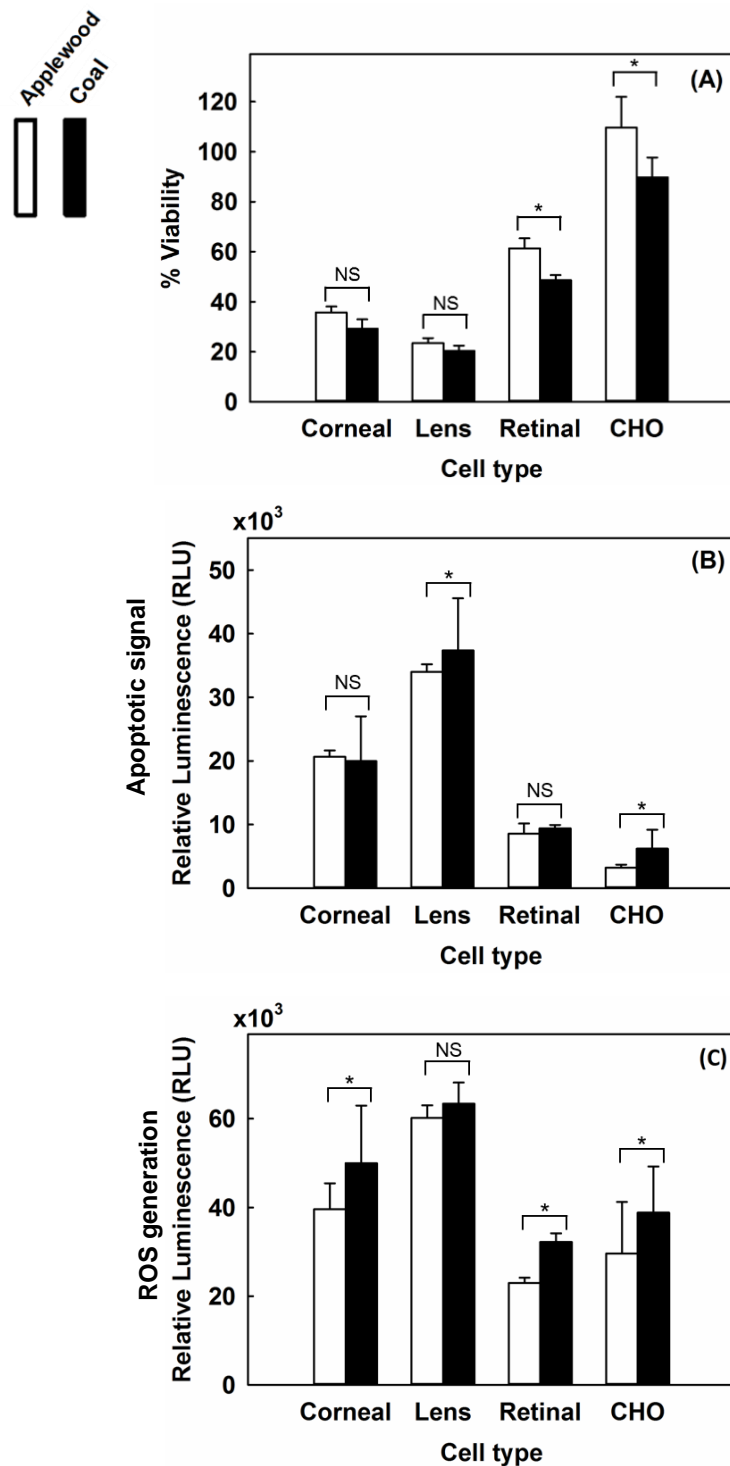


Figure 3. Comparative biocompatibility of applewood and biomass combustion emissions with corneal epithelial cells, lens epithelial cells, retinal pigment epithelial (RPE-19) cells,

and Chinese hamster ovary (CHO) cells. (A) Viability results. (B) Amount of apoptotic cells. (C) ROS. Values are expressed in mean \pm SEM, with each condition tested (n = 4). * $P < 0.05$

ECIS allows monitoring the changes in cell morphology that are essentially evoked by alterations in the architecture of the cell's structural components, such as the cytoskeleton and cell-cell and cell-substrate junctions (Stolwijk et al. 2015). Figure 4 illustrates the real-time (120 hours) impedance measurements of all cell lines tested. Figure 4A shows the results for the negative control group, the cells exposed to air only. All the cell types grew and reached confluency without showing any disruption in the impedance measures. Figure 4B demonstrates the cells' response to applewood combustion emissions. Except for the cancer cells, all the ocular cells were adversely affected by the exposure. Similarly, all the ocular cell lines exposed to coal combustion emissions detached from the plate, resulting in a decrease in impedance. On the other hand, CHO cells maintained their confluency, although their growth rate was significantly less than that of the negative control group.

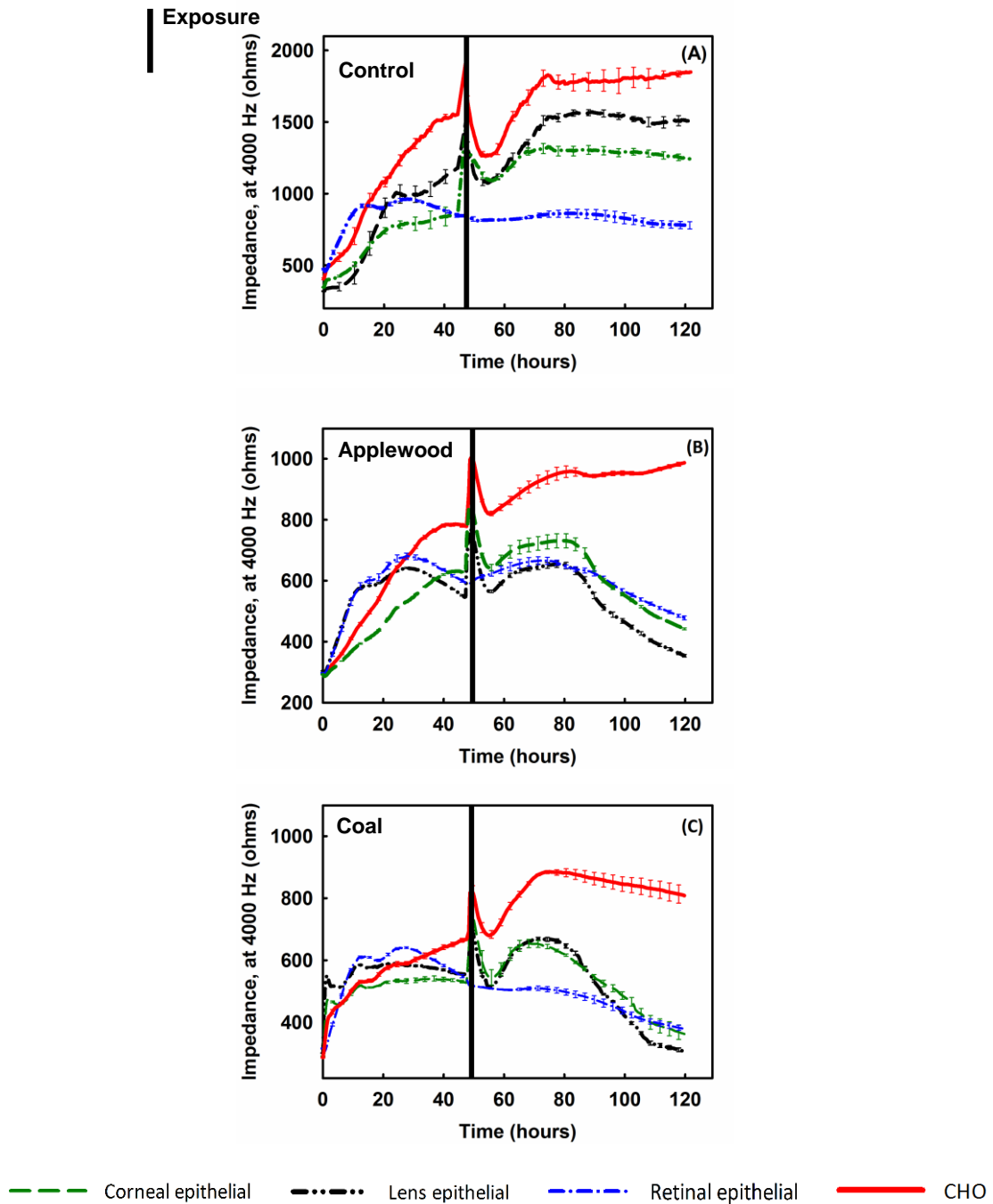


Figure 4. Real-time impedance measurements of corneal epithelial cells, lens epithelial cells, retinal pigment epithelial cells, and Chinese hamster ovary (CHO) cells. Cells were plated at 20,000 cells/well and exposed to stove emissions for one hour. (A) Control (B) Cells exposed to applewood combustion emissions. (C) Cells exposed to coal combustion emissions. Values are expressed in mean \pm SEM, with each condition tested ($n = 8$). Black vertical lines represent the timing and the duration of exposure $**P < 0.001$.

Acute toxicity: Liquid phase exposure

Our previous study showed that emissions from coal combustion exceeded those from applewood on almost all characterization metrics, such as mass concentration, number concentration, particle size, surface area concentration, organics concentration, and carcinogenic polycyclic aromatic hydrocarbons (PAH) concentration (Patel et al. 2016).

Consistent with the above-mentioned results, the gas phase exposure study revealed that coal combustion emissions were more toxic to all cell lines tested. Therefore, for the liquid phase exposure study, only the effect of applewood combustion emission was investigated.

As shown in Figure 5A, overall viability declined with increasing emission exposure levels (decreasing dilution ratio) for all healthy ocular cell types, but the viability of retinal epithelial cells demonstrated the least sensitivity to the exposure levels. Conversely, cancer cells were not affected until the exposure concentration was increased to a dilution of 1:1. Interestingly, except for the 1:1 dilution, the cancer cells showed more than 100% viability, i.e., their growth was promoted. Unlike the overall viability results, retinal cells sent the strongest signals of impeding apoptosis until the exposure concentration was increased to a dilution of 1:20 (Figure 5B). On the other hand, the amount of ROS generation in healthy ocular cells increased with increasing exposure concentration (until a dilution of 1:20), and similar to the apoptosis signaling results, retinal cells generated relatively more ROS than corneal and lens epithelial cells (Figure 5C).

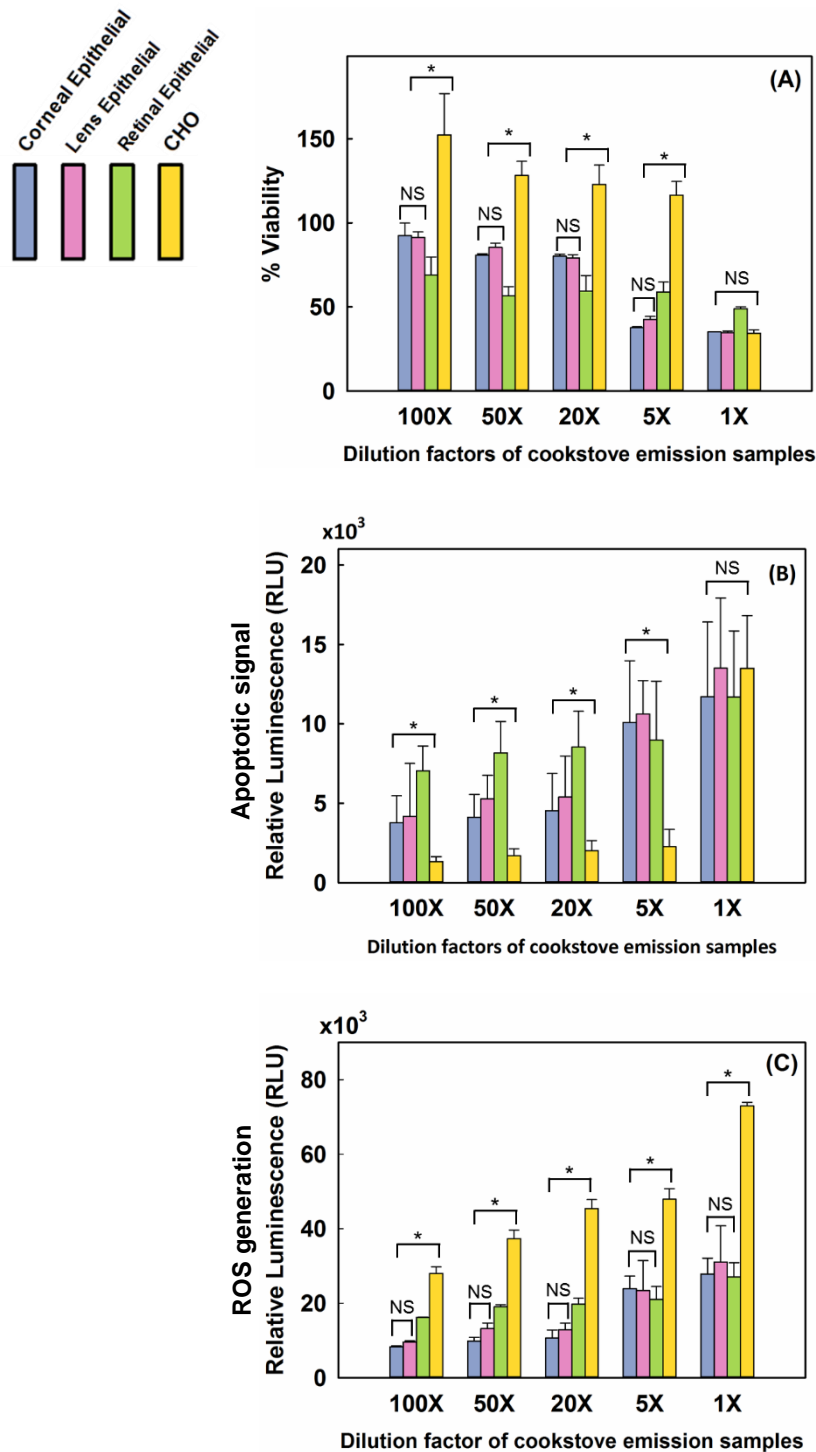


Figure 5. Biocompatibility measures of applewood emission extracts in contact with corneal epithelial cells, lens epithelial cells, retinal pigment epithelial (RPE) cells, and Chinese hamster ovary (CHO) cells. (A) Viability results. (B) Amount of apoptotic cells. (C) ROS generation. Values are expressed in mean \pm SEM, with each condition tested ($n = 8$). $*P < 0.05$.

In addition to the experimental endpoint toxicity evaluations of viability, apoptosis, and ROS generation, electrical impedance spectroscopy (ECIS), a sensing technique for monitoring cell motion and morphological changes real-time, was also used (Xiao et al. 2002, Karakocak et al. 2018). Upon plating, cells start to attach to and spread out over the gold electrodes. As a result, the impedance increases because the insulating cell membranes form tight junctions that block the electrical current's flow. Conversely, when cells are stressed and dying, cell-to-cell junctions are disrupted. Moreover, changes in cell morphology, such as contractile rounding of membranes and detachment of cells from the gold electrode, result in higher electrical current passage, which leads to a decrease in impedance over time (Pennington and Van de Walle 2017).

Figure 6 presents electrical impedance measurements for all cell types tested. Cells were allowed to reach confluency (~97 hr) and then exposed to emission extracts twice, once at the 97th hour and again at 168th hour, when they had recovered and again reached confluency. The real-time response behavior for corneal epithelial (Figure 6A) and lens epithelial cells (Figure 6B) was similar. For both cell types, after the initial response to exposure, a sharp decline was recorded in impedance during the first 20 hours post-exposure for all exposure levels tested. The impedance level recovered following both the first and second exposures; however, eventually, it dropped gradually. After the second exposure, the decline was irreversible. The impedance levels of both cell types (Figures 6A and 6B) continuously declined irreversibly below the initial impedance level, based on the data collected up to the 265th hour, the end of the experiment. It was also observed that the rate of the final decline in impedance was higher for higher exposure levels. With higher exposure concentrations, it is likely that the cells reacted more drastically. In what follows, it is evident that there is a complex pattern of growth followed by retardation and resumption as a result of exposure to biomass smoke. Most notably, however, the retinal cells were markedly less affected (Figure

6C). The growth rate of the retinal cells was significantly affected; however, the cells still maintained a confluent layer by the end of the experiment. Finally, for the cancer cells, except at the highest exposure concentration, the impedance levels were higher than for the control cells (Figure 6D). Interestingly, when the cells were exposed to the extracts with the lowest dilution ratio, the impedance level of the cells was recorded to be 53% more than the impedance level of the unexposed cells (the negative control) by the end of the experiment (265th hour).

Exposure

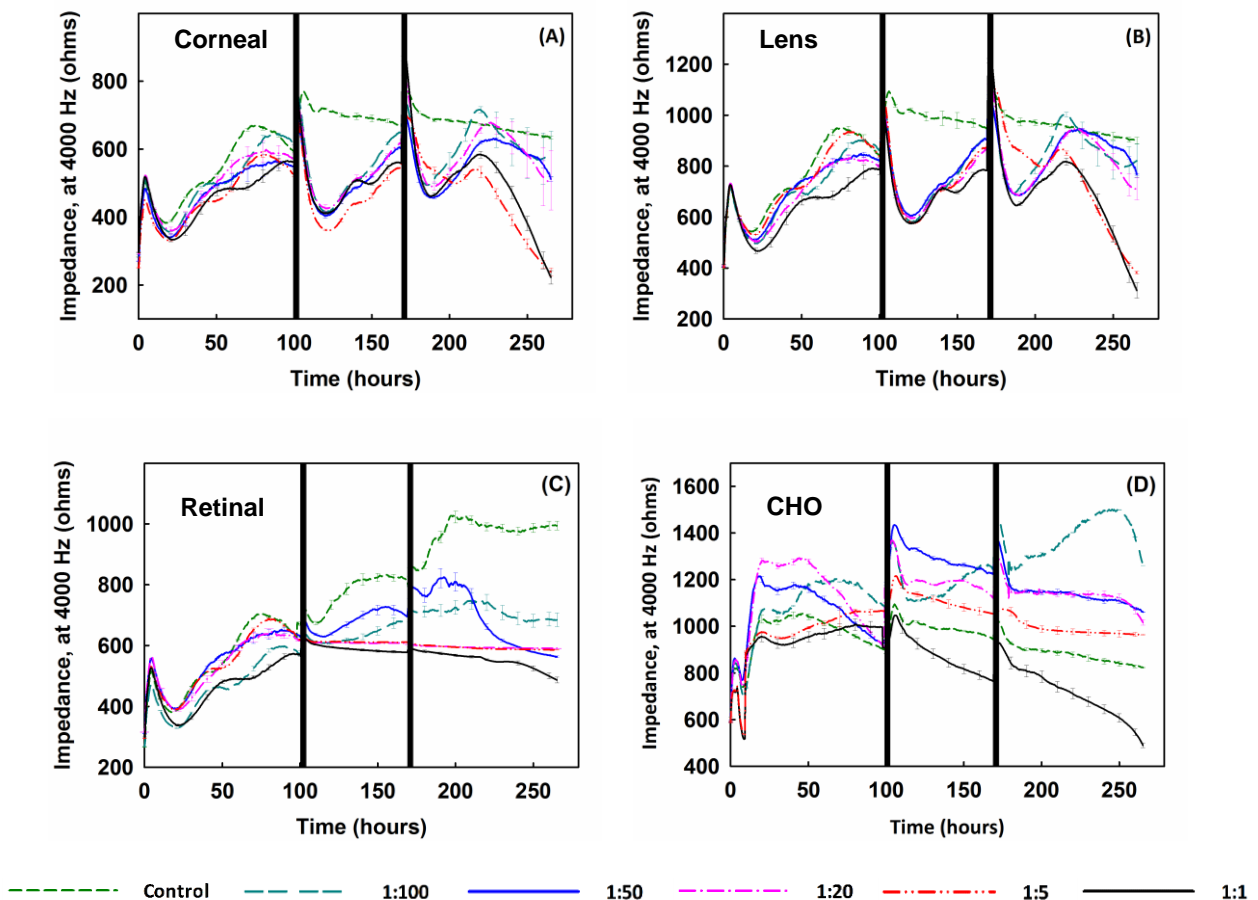


Figure 6. Impedance measurements of (A) corneal, (B) lens, (C) retinal epithelial, and (D) CHO cells plated at 20,000 cells/well, exposed to applewood emission extracts with different dilution rates. Note that after the cells become confluent, the medium was changed only once throughout the rest of the lengthy exposure period. As compared to the control cells, the healthy cells, which were exposed to the extracts, could not recover, except at the highest dilution rate (1:100). Overall, the applewood emission extract did show a toxic effect on ocular cells; however, the same concentrations that were toxic to healthy cells accelerated the growth of CHO cells. Values are expressed in mean \pm SEM, with each condition tested (n = 8). ** $P < 0.001$.

Discussion

In short, biomass smoke generated ROS that retarded the growth of healthy ocular cells and eventually killed them. Among the non-cancerous healthy cell lines tested, retinal cells showed the greatest resistance to bio-induced ROS generation. In fact, the CHO cancer cells stood out in their resistance: For both gas and liquid phase exposures, biomass smoke promoted their growth. The specifics are discussed below.

Acute toxicity: Gas phase exposure

In-vitro studies with biomass and coal smoke can potentially generate toxic products from reactions between the smoke components and cell media (Lee et al. 2015, Capistrano et al. 2017). Nevertheless, for both practical and ethical reasons, evaluating emissions on cells is a logical precursor to *in-vivo* tests. In conformance with strict animal protocols, animals, unlike cells, cannot be exposed to biomass and coal emissions for extended periods (Capistrano et al. 2017). Furthermore, the specific way a cell reacts to its environment varies with the set of receptor proteins on its cell membrane and according to their primary role in the body (Epanand and Ruyschaert 2017). Cell types have evolved to perform different roles, and thus their responses to the same stimuli can be dissimilar (Hanley et al. 2009). *In-vitro* models can advantageously provide results for longer exposure periods and multiple types of cells.

In Figure 3A, we compare the viability, amount of apoptotic cells, and the amount of ROS generation for the four cell types exposed (gas phase) to emissions from applewood and coal combustion. Corneal and lens epithelial cells exposed to the emissions from the two fuels showed similar viability results, and the type of fuel did not show a statistically significant difference (Figure 3A). On the other hand, both retinal and CHO cells were more tolerant of applewood emissions than coal emissions. Surprisingly, when exposed to applewood emissions, CHO cells actually grew, their viability was recorded as 109%

(Figure 3A). Unlike applewood emissions, coal emissions did adversely affect the CHO cells' viability (89%). The apoptotic cell measurements showed statistically significant differences in response to applewood and coal combustion emissions for lens epithelial and CHO cells only (Figure 3B). The amount of apoptotic cells was highest among the lens epithelial cells, followed by corneal and retinal cells. Simply put, cells succumb to environmental stress differently (Reed 2000, Hanley et al. 2009). The concentration of applewood and coal smoke that led to apoptosis in corneal and lens epithelial cells did not result in the same level of apoptotic response in retinal and CHO cells. Our results also showed that retinal pigment epithelial (RPE) cells can cope well with oxidative stress (Figure 3C). This result may be attributed to their unique ROS handling capacity, an evolutionary mechanism for tolerating light exposure (Qin and Rodrigues 2008). Similar to the apoptotic signal results, corneal and lens epithelial cells produced significantly higher amounts of ROS (Figure 3C). On the other hand, retinal and CHO cells showed relatively less ROS generation as a result of gas phase exposure to biomass and coal emissions. As expected, since the ROS generation was higher in corneal and lens epithelial cells, apoptosis signal initiation was higher in those cells and evidently was reflected in the eventual viability results (Figure 3). Overall, based on viability, apoptosis, and ROS generation results, coal appears to show more adverse effects than applewood combustion emissions on all cell lines tested.

Smoke from solid-fuel combustion is a complex mixture of hundreds of organic and inorganic chemical species in both gaseous and particulate phases, making it very difficult to associate health effects with a single component. More details on smoke constituents and their associated health effects can be found in (Zhang and Smith 2007), where the authors reviewed relevant studies from 1980 to 2016, with a focus on China. Detailed physical and chemical characterizations of the PM emissions from the two fuels tested in this study have

been published in our previous studies (Patel et al. 2016, Leavey et al. 2017), and therefore are not included here. Emissions from coal combustion exceeded those from applewood on almost all characterization metrics, such as mass concentration, number concentration, particle size, surface area concentration, organics concentration, and polycyclic aromatic hydrocarbons (PAH) concentration (Patel et al. 2016). Therefore, it is not possible to comment on the role of any single metric in the trends observed in Figure 3. Systematic and controlled laboratory studies are required to associate different specific emission components and metrics with their health effects.

Figure 4A shows real-time cell attachment impedance measurements for all four cell types when removed from incubation conditions and exposed to filtered air (negative control). For all cell types except retinal cells, impedance levels decline sharply just after exposure to filtered air, but eventually recover to their original value. The variations in the initial drop in the impedance might be due to the cells' varied abilities to compensate for and adapt to the changes in the extracellular environment (Berg et al. 2002, Brooks et al. 2011). It is clear that retinal cells are least affected by changes in, for example, the amount of carbon dioxide and the temperature, and therefore their impedance level is least altered (Figure 4A).

Figures 4B and 4C show the responses of all cell types to applewood and coal emissions, respectively. The initial post-exposure responses of cells were similar to those for the control, i.e., a decline in impedance, followed by recovery. Again, this decline may be due to the cells' varied abilities to adapt to the extracellular environment. Unlike the control experiments, the impedance dropped for retinal, lens, and corneal epithelial cells, starting at the 73rd, 78th, and 81st hours, respectively. However, the impedance level of CHO cells continued to rise until the end of the experiment (~120 hours) (Figure 4C). This increase is a result of cell proliferation, triggered by the increased amount of intracellular ROS (Figure

5C), as reported previously (Liou and Storz 2010, Sullivan and Chandel 2014, Galadari et al. 2017). It can, therefore, be concluded that for CHO cells, the increased ROS caused more cell proliferation (Zamkova et al. 2013).

Acute toxicity: Liquid phase exposure

The retinal cells withstood increased oxidative stress better than the corneal and lens epithelial cells (Figures 5A and 5C). ROS production in cells is a double-edged sword (Martin and Barrett 2002). ROS are created mainly as host defenses against infectious agents; however, when a threshold is exceeded, increased ROS can lead to apoptosis (Sullivan and Chandel 2014). We measured both the apoptotic cell amount as well as ROS generation and found a direct correlation for healthy ocular cells (Figures 5B and 5C). When the amount of ROS production exceeded the cells' capacity to repair oxidative damage, the cells initiated apoptosis, as was also reported in previous studies (Fiers et al. 1999, Lemarie et al. 2011). On the other hand, cancer cells adapted to oxidative stress. Their viability results were significantly higher than for the healthy ocular cells (Figure 5A). Comparing the apoptosis onset values measured in RLU (Figure 5B) with the ROS values in Figure 5C, it can be seen that cancer cells tolerate 1.7-2.7 times greater concentration of ROS than healthy ocular cells. This finding is consistent with previous studies that reported significantly higher ROS generation in cancer cells than healthy cells (Fiers et al. 1999, Sullivan and Chandel 2014). Notably, our apoptosis measurement technique is based on Caspase 3/7 activity measurement, which is detectable only during apoptosis, not during necrosis (Denecker et al. 2001). Apoptotic cell death is a programmed cell death as a result of increased oxidative stress (ROS generation); therefore, there is a strong correlation between ROS generation and the apoptotic cell amount (Figure 5).

Unlike the corneal and lens cells (Figures 6A and 6B), the real-time impedance results for retinal epithelial cells did not show a sharp decline following the exposure events (Figure

6C). The first exposure did not affect the impedance; however, after the second exposure, the impedance decreased slightly. The cells did not crash by the end of the experiment because, as explained previously, retinal cells can cope with oxidative stress better than other ocular cell types. Interestingly, the impedance measurements of the cancer cells revealed an unexpected behavior. The CHO cells which were exposed to cookstove emissions extracts grew more than the control cells, displaying the same unexpected behavior found with gas phase exposure, which suggests that exposure to biomass exhaust can promote tumor growth.

Although we do not fully understand exactly how inhaling stove emissions causes secondary injury to the eye and other organs (Zou et al. 2009, Hawley and Volckens 2013), extended exposure to smoke efficiently transfers environmental pollutants to the bloodstream (Pappas 2011, Schulze et al. 2017). Due to their high metabolic activity, tumor cells need more oxygen and nutrients than normal cells (Amoêdo et al. 2013). It has been shown that tumor cells can grow their own blood vessels (Jain 2005), and as a result, tumors receive more blood than normal cells (Carmeliet and Jain 2000, Chambers et al. 2002). Once environmental pollutants enter the bloodstream, their constituents inevitably reach tumor cells. Our *in-vitro* study demonstrates that once tumor cells are in direct contact with biomass emissions, their growth is promoted. Based on our findings, it is reasonable to hypothesize that daily exposure to biomass smoke from stoves poses a risk for cancer patients.

Conclusions

Our *in-vitro* study found a significant disturbance in healthy ocular cells' attachment, indicative of death, as a result of both liquid and gas phase biomass smoke exposure. On the other hand, the growth of cancer cells was significantly promoted. The ROS amount that led to ocular cell death did not destroy the cancer cells, but instead accelerated their

growth. Our *in-vitro* study connects cellular responses with epidemiological disease findings, clearly underscoring the troubling implication that people exposed daily to biomass-fueled stove smoke are at risk, especially considering that our findings were for a limited exposure time. People who are regularly exposed to biomass combustion smoke are more prone to developing eye diseases, either from direct exposure or secondary exposure by inhalation. More importantly, everyday activities like cooking and heating using stoves with biomass fuels may accelerate the growth of tumors. These findings emphasize that we should pay added attention to the environment of the person living with cancer, not only to their genetic predisposition.

References

1. C. W. Noonan, J. R. Balmes and W. Hlth Outcomes, *Inhalation Toxicology*, 2010, **22**, 108-112.
2. M. S. B. Pena, E. J. Velazquez, J. D. Rivera, F. Alenezi, C. Wong, M. Grigsby, V. G. Davila-Roman, R. H. Gilman, J. J. Miranda and W. Checkley, *Indoor Air*, 2017, **27**, 737-745.
3. A. K. Pokhrel, K. R. Smith, A. Khalakdina, A. Deuja and M. N. Bates, *International Journal of Epidemiology*, 2005, **34**, 702-708.
4. A. K. Pokhrel, M. N. Bates, S. P. Shrestha, I. L. Bailey, R. B. DiMartino, K. R. Smith and N. Joshi, *Optometry and vision science: official publication of the American Academy of Optometry*, 2013, **90**, 257.
5. O. World Health, *WHO guidelines for indoor air quality: household fuel combustion*, World Health Organization, 2015.
6. A. Dutta and M. R. Ray, *Air Quality, Atmosphere & Health*, 2014, **7**, 229-238.
7. A. Dutta, M. R. Ray, B. Mukherjee and S. Chowdhury, *Air Quality, Atmosphere & Health*, 2013, **6**, 307-315.
8. L. Silva, P. Saldiva, T. Mauad, S. Saldiva and M. Dolhnikoff, *Am J Respir Crit Care Med*, 2009, **179**, A4743.
9. P. H. Danielsen, P. Moller, K. A. Jensen, A. K. Sharma, H. Wallin, R. Bossi, H. Autrup, L. Molhave, J. L. Ravanat, J. J. Briede, T. M. de Kok and S. Loft, *Chemical Research in Toxicology*, 2011, **24**, 168-184.
10. M. Dilger, J. Orasche, R. Zimmermann, H. R. Paur, S. Diabate and C. Weiss, *Archives of Toxicology*, 2016, **90**, 3029-3044.
11. E. Corsini, S. Budello, L. Marabini, V. Galbiati, A. Piazzalunga, P. Barbieri, S. Cozzutto, M. Marinovich, D. Pitea and C. L. Galli, *Archives of Toxicology*, 2013, **87**, 2187-2199.
12. J. L. Mauderly, E. G. Barrett, A. P. Gigliotti, J. D. McDonald, M. D. Reed, J. Seagrave, L. A. Mitchell and S. K. Seilkop, *Inhalation Toxicology*, 2011, **23**, 349-362.
13. E. N. Liberda and L. C. Chen, *Journal of the Air & Waste Management Association*, 2013, **63**, 671-680.
14. A. Muala, G. Rankin, M. Sehlstedt, J. Unosson, J. A. Bosson, A. Behndig, J. Pourazar, R. Nystrom, E. Pettersson, C. Bergvall, R. Westerholm, P. I. Jalava, M. S. Happonen, O. Uski, M. R. Hirvonen, F. J. Kelly, I. S. Mudway, A. Blomberg, C. Boman and T. Sandstrom, *Particle and Fibre Toxicology*, 2015, **12**, 14.
15. K. Kunchithapautham, C. Atkinson and B. Rohrer, *Journal of Biological Chemistry*, 2014, **289**, 14534-14546.
16. Y. Y. Zou, J. Lu, D. J. F. Poon, C. Kaur, Q. Cao, A. L. Teo and E. A. Ling, *Neuroscience*, 2009, **160**, 698-709.
17. C. Y. Guo, L. Sun, X. P. Chen and D. S. Zhang, *Neural Regeneration Research*, 2013, **8**, 2003-2014.
18. A. C. P. Elder, R. Gelein, J. N. Finkelstein, C. Cox and G. Oberdorster, *Inhalation Toxicology*, 2000, **12**, 227-246.
19. E. G. Barrett, C. Johnston, G. Oberdorster and J. N. Finkelstein, *American Journal of Physiology-Lung Cellular and Molecular Physiology*, 1999, **276**, L979-L988.
20. S. Galadari, A. Rahman, S. Pallichankandy and F. Thayyullathil, *Free Radical Biology and Medicine*, 2017, **104**, 144-164.
21. G. Y. Liou and P. Storz, *Free Radical Research*, 2010, **44**, 479-496.

22. S. K. Joshi, A. Dahl, T. Kristensen and P. Roldin, *Kathmandu University medical journal (KUMJ)*, 2010, **8**, 276-280.
23. H. D. Hosgood, III, H. Wei, A. Sapkota, I. Choudhury, N. Bruce, K. R. Smith, N. Rothman and Q. Lan, *International Journal of Epidemiology*, 2011, **40**, 719-728.
24. S. Anenberg, *Nature*, 2012, **490**, 343-343.
25. S. Kumar, *Nature*, 2012, **491**, 333-333.
26. O. Hodnebrog, G. Myhre, P. M. Forster, J. Sillmann and B. H. Samset, *Nature Communications*, 2016, **7**, 8.
27. S. Patel, A. Leavey, S. He, J. Fang, K. O'Malley and P. Biswas, *Energy for Sustainable Development*, 2016, **32**, 130-139.
28. T. D. Ravilla, S. Gupta, R. D. Ravindran, P. Vashist, T. Krishnan, G. Maraini, U. Chakravarthy and A. E. Fletcher, *Environmental Health Perspectives*, 2016, **124**, 1857-1862.
29. V. K. Shalini, M. Luthra, L. Srinivas, S. H. Rao, S. Basti, M. Reddy and D. Balasubramanian, *Indian Journal of Biochemistry & Biophysics*, 1994, **31**, 261-266.
30. O. Alcazar, S. W. Cousins and M. E. Marin-Castano, *Investigative Ophthalmology & Visual Science*, 2007, **48**, 5662-5670.
31. L. Jia, Z. Liu, L. Sun, S. S. Miller, B. N. Ames, C. W. Cotman and J. Liu, *Investigative Ophthalmology & Visual Science*, 2007, **48**, 339-348.
32. K. M. Bertram, C. J. Baglole, R. P. Phipps and R. T. Libby, *American Journal of Physiology-Cell Physiology*, 2009, **297**, C1200-C1210.
33. O. T. Dogan, S. Elagoz, S. L. Ozsahin, K. Epozturk, E. Tuncer and I. Akkurt, *Clinics*, 2011, **66**, 1081-1087.
34. R. A. Tobey, E. C. Anderson and D. F. Petersen, *Journal of Cellular Physiology*, 1967, **70**, 63-&.
35. J. J. Harada and D. R. Morris, *Molecular and Cellular Biology*, 1981, **1**, 594-599.
36. B. B. Karakocak, R. Raliya, J. T. Davis, S. Chavalmane, W.-N. Wang, N. Ravi and P. Biswas, *Toxicology in Vitro*, 2016, **37**, 61-69.
37. S. Arndt, J. Seebach, K. Psathaki, H. J. Galla and J. Wegener, *Biosensors & Bioelectronics*, 2004, **19**, 583-594.
38. J. Wegener, C. R. Keese and I. Giaever, *Experimental Cell Research*, 2000, **259**, 158-166.
39. K. Kandasamy, C. S. Choi and S. Kim, *Nanotechnology*, 2010, **21**, 10.
40. S. Mulhopt, M. Dilger, S. Diabate, C. Schlager, T. Krebs, R. Zimmermann, J. Buters, S. Oeder, T. Wascher, C. Weiss and H. R. Paur, *Journal of Aerosol Science*, 2016, **96**, 38-55.
41. J. Seagrave, J. D. McDonald and J. L. Mauderly, *Experimental and Toxicologic Pathology*, 2005, **57**, 233-238.
42. B. Hawley and J. Volckens, *Indoor Air*, 2013, **23**, 4-13.
43. A. Leavey, S. Patel, R. Martinez, D. Mitroo, C. Fortenberry, M. Walker, B. Williams and P. Biswas, *Environmental Research*, 2017, **158**, 33-42.
44. J. A. Stolwijk, K. Matrougui, C. W. Renken and M. Trebak, *Pflügers Archiv-European Journal of Physiology*, 2015, **467**, 2193-2218.
45. C. Xiao, B. Lachance, G. Sunahara and J. H. T. Luong, *Analytical Chemistry*, 2002, **74**, 1333-1339.
46. B. B. Karakocak, J. Liang, P. Biswas and N. Ravi, *Carbohydrate Polymers*, 2018, **186**, 243-251.
47. M. R. Pennington and G. R. Van de Walle, *mSphere*, 2017, **2**, e00039-00017.
48. S. J. Capistrano, D. van Reyk, H. Chen and B. G. Oliver, *Toxics*, 2017, **5**, 36.

49. A. Lee, P. Kinney, S. Chillrud and D. Jack, *Annals of global health*, 2015, **81**, 368-374.
50. R. M. Epanand and J.-M. Ruysschaert, *The Biophysics of Cell Membranes: Biological Consequences*, Springer, 2017.
51. C. Hanley, A. Thurber, C. Hanna, A. Punnoose, J. Zhang and D. G. Wingett, *Nanoscale Research Letters*, 2009, **4**, 1409-1420.
52. J. C. Reed, *The American journal of pathology*, 2000, **157**, 1415-1430.
53. S. Qin and G. A. Rodrigues, *Journal of inflammation research*, 2008, **1**, 49.
54. J. Zhang and K. R. Smith, *Environmental health perspectives*, 2007, **115**, 848-855.
55. A. N. Brooks, S. Turkarslan, K. D. Beer, F. Yin Lo and N. S. Baliga, *Wiley Interdisciplinary Reviews: Systems Biology and Medicine*, 2011, **3**, 544-561.
56. J. M. Berg, J. L. Tymoczko and L. Stryer, *Journal*, 2002.
57. L. B. Sullivan and N. S. Chandel, *Cancer & metabolism*, 2014, **2**, 17.
58. M. Zamkova, N. Khromova, B. P. Kopnin and P. Kopnin, *Cell Cycle*, 2013, **12**, 826-836.
59. K. R. Martin and J. C. Barrett, *Human & experimental toxicology*, 2002, **21**, 71-75.
60. A. Lemarie, L. Huc, E. Pazarentzos, A.-L. Mahul-Mellier and S. Grimm, *Cell Death & Differentiation*, 2011, **18**, 338-349.
61. W. Fiers, R. Beyaert, W. Declercq and P. Vandenabeele, *Oncogene*, 1999, **18**.
62. G. Denecker, D. Vercammen, M. Steemans, T. V. Berghe, G. Brouckaert, G. Van Loo, B. Zhivotovsky, W. Fiers, J. Grooten and W. Declercq, *Cell death and differentiation*, 2001, **8**, 829.
63. R. S. Pappas, *Metallomics*, 2011, **3**, 1181-1198.
64. F. Schulze, X. Gao, D. Virzonis, S. Damiani, M. R. Schneider and R. Kodzius, *Genes*, 2017, **8**, 244.
65. N. D. Amoêdo, J. P. Valencia, M. F. Rodrigues, A. Galina and F. D. Rumjanek, *Bioscience reports*, 2013, **33**, e00080.
66. R. K. Jain, *Science*, 2005, **307**, 58-62.
67. P. Carmeliet and R. K. Jain, *Nature*, 2000, **407**, 249.
68. A. F. Chambers, A. C. Groom and I. C. MacDonald, *Nature Reviews Cancer*, 2002, **2**, 563.

Appendix VII. Curriculum Vitae

Education

Ph.D., Energy, Environmental & Chemical Engineering, (August, 2013 – August, 2018 (expected))

Washington University in St. Louis, MO, USA.

M.S., Energy, Environmental & Chemical Engineering, 2016

Washington University in St. Louis, MO, USA.

M.S., Environmental Technology, 2011

Boğaziçi University, Institute of Environmental Sciences, Istanbul, Turkey.

B.S., Environmental Engineering, 2008

Istanbul Technical University, Faculty of Civil Engineering, Department of Environmental Engineering, Istanbul, Turkey.

Professional and Academic Experience

2013.08 - present

Graduate Research Assistant

Energy, Environmental & Chemical Engineering Department,
Washington University in St. Louis, MO, USA.

Advisors: Drs. Nathan Ravi and Pratim Biswas

2016.11 - present

Course Developer/Technical Assistant

McDonnell Energy & Environment Partnership Education Network
<https://education.mageep.net>

2012.05 - 2012.11

Visiting Scholar

Energy, Environmental & Chemical Engineering Department,
Washington University in St. Louis, MO, USA.

Advisors: Drs. John D. Fortner and Daniel E. Giammar

2010.06 - 2013.07

Graduate Research Assistant

Institute of Environmental Sciences, Boğaziçi University, Istanbul,
Turkey.

Advisor: Dr. Orhan Yenigün

2010.01 - 2013.07

Air Quality Monitoring Group, Measurement Surveyor

Institute of Environmental Sciences, Boğaziçi University, Istanbul,
Turkey.

Research Interests

Synthesis, characterization, and applications of engineered nanoparticles

- *Designing and synthesizing engineered nanoparticles for ocular targeted drug delivery*
- *In-vitro and in-vivo bioimaging of engineered nanoparticles*

Toxicology

- *In-vitro and in-vivo toxicity assessment of engineered nanoparticles*
- *Health risk assessment of indoor air quality*

Electrochemical sensor analysis

- *Designing and assessing the performance of highly sensitive sensors for biomedical applications*

Publications

Peer-reviewed publications

1. **Karakoçak B. B.***, Liang J*, Biswas P., Ravi N. Optimization of Red-Emitting Nitrogen-doped Carbon Dots for Use in Bioimaging. **2018**. *ACS Appl. Nano Mater.* DOI: 10.1021/acsnm.8b00799.
2. **Karakoçak B. B.**, Liang J., Biswas P., Ravi N. Hyaluronate Coating Enhances the Delivery and Biocompatibility of Gold Nanoparticles. **2018**. *Carbohydr. Polym.* 189:243-251.
3. Lin L. Y*, **Karakoçak B. B.***, Kavadiya S., Biswas P. A Highly Sensitive Non-enzymatic Glucose Sensor Based on Cu/Cu₂O/CuO Ternary Composite Hollow Spheres Prepared in a Furnace Aerosol Reactor. **2018**. *Sens. Actuators B. Chem.* 259: 745-752.
4. Lin L. Y, Kavadiya S., **Karakoçak B. B.**, Nie Y., Biswas P. Band Gap Engineered ZnO_{1-x} Hollow Particles Synthesized Using Single Step Tubular Aerosol Reactor with Enhanced Visible-Light-Induced Photoreduction of CO₂. **2018**. *Appl. Catal. B. Environ.* 230:36-48.
5. Liang J., **Karakoçak B. B.**, Struckhoff J., Ravi N. Synthesis and Characterization of Injectable Sulfonate-Containing Hydrogels. **2016**, *Biomacromolecules.* 17(12): 4064-4074.
6. **Karakoçak B. B.**, Raliya R, Davis J, Chavalmane S, Wang W, Ravi N, Biswas P. Biocompatibility of Gold Nanoparticles in Retinal Pigment Epithelial Cell Line. **2016**, *Toxicol. In Vitro.* 37:61-69.
7. **Karakoçak B. B.**, Yenigün O., Taşlı R.T. An Integrated Approach to Water Management in Kayseri: Rain Water Collection and Use in an Amusement Park. **2013**, *Water Sci. Tech.* 67(5):1137-1143.

Under review publications

8. **Karakoçak B. B.**, Patel S., Ravi N., Biswas P. Investigating the Effects of Cookstove Emissions on Ocular Cells. Submitted to *Sci. Rep.*
9. Santhanam S., Shui Y., Struckhoff J., **Karakoçak B. B.**, Hamilton P. D., Harocopos G. J., Ravi N. Bioinspired Fibrillary Hydrogel with Controlled Swelling Behavior: Applicability as an Artificial Vitreous. Submitted to *ACS Appl. Bio Mater.*

In preparation publications

10. **Karakoçak, B. B.**, Biswas, P., and Ravi N. Applications of Gold Nanoparticles in Ophthalmology. In preparation for *Prog. Retin. Eye Res.*
11. **Karakoçak B. B.**, Santeford A., Lee T. J., Biswas P., Apte R. S., Ravi, N. Crossing the Blood-Retinal Barrier: A Quantitative Study on Targeted Delivery of Gold Nanoparticles. In preparation for *Biomaterials*.
12. Raliya R., Reed N., **Karakoçak B. B.**, Ravi N., Biswas P. Brain Delivery of Engineered Nanoparticles: Current Status and Future Perspectives. In preparation for *Curr. Pharm. Des.*
13. **Karakoçak B. B.**, Liang J., Biswas P., Ravi N. Hyaluronate-coated Nitrogen-doped Carbon Quantum Dots for Bioimaging and Targeted Drug Delivery in Ophthalmology. In preparation for *ACS Appl. Nano Mater.*
14. **Karakoçak B. B.**, Soundappan T., Nie Y., Ravi N., Biswas P. Aerosol Assisted Fabrication of a Crumpled Graphene Oxide Sensor for Detection of Endocrine Disrupter Bisphenol-A. In preparation for *Biosens. Bioelectron.*
15. Lin L. Y., Kavadiya S., **Karakoçak B. B.**, Nie Y., Biswas P. TiO₂/Pt Composite Materials Prepared in a Furnace Aerosol Reactor for CO₂ Photoreduction. In preparation for *Appl. Catal. B. Environ.*
16. Lin L. Y., **Karakoçak B. B.**, Sharma G., Ravi N., Biswas P. Highly Fluorescent Carbon Quantum Dots Prepared in a Furnace Aerosol Reactor for Bioimaging Applications. In preparation for *ACS Nano*.

Patents

17. **Karakoçak B. B.***, Liang J*., and Ravi N.*. Fluorescent Carbon Quantum Dots for Bioimaging and Targeted Drug Delivery in Ophthalmology. US 016997. Provisional Patent Application Submitted.

Skills & Certifications

Ph.D. Training in Ophthalmology (September 2013 - September 2017)

Department of Ophthalmology & Visual Sciences, School of Medicine, Washington University in St. Louis

Programming Languages and Design Software

Matlab 2014, Autocad 2007, Adobe Photoshop® CC, ePath 3D Biological Network Design.

Modeling Software

EPA SWMM 5.0., Simulation Environment (Stella 9.0.1), EPA BREEZE AERMOD Pro.

Instrument Experience

Electrical Impedance Spectroscopy (ECIS), Single Particle Inductively Coupled Plasma Mass Spectrometer (SP ICP-MS), Transmission Electron Microscopy (TEM), X-Ray/Ultraviolet Photoelectron Spectrometer (XPS), Total Organic Carbon (TOC) Analysis, Thermal Gravimetric Analysis (TGA), Cyclic Voltammetry Analysis.

Tissue Culture Experience & Toxicology Assays

Establishing and growing human, mouse, and pig cell lines. Development and applications of viability, apoptosis, and reactive oxygen species assays such as: MTT, MTS, LDH, Apo-TOX-GLO™, ROS-Glo™ H₂O₂ assays.

In-vitro and In-vivo Imaging Modalities

LEICA TC8 SPF8 Confocal microscopy (2D and 3D), Bright&dark field microscopy, Pearl Small Animal NIR fluorescence imaging system (LI-COR Biosciences, NE). *In-vivo* Multispectral Pro System (Bruker, Billerica, MA).

Statistical Analysis

Stat-Ease Design Expert (DOE) software (version 10.0), one-two-three-way ANOVA analysis.

Honors & Awards

- Graduate Student Teaching Assistant Award, Washington University in St. Louis, April, 2016.
- Travel grant award by TUBITAK (The Scientific & Technological Council of Turkey) for IWA International Conference on Cities of the Future, Xi'an, China, 15-19 September, 2011.
- Best presentation award, RENET Summer School on Renewable Energy, Boğaziçi University, July, 2009.

Presentations

Oral Conference Presentations

1. 253rd American Chemical Society Meeting, San Francisco, CA, April, 2017.
Hyaluronic Acid Conjugated Carbon Quantum Dots for Bioimaging and Targeted Drug Delivery Applications in Ophthalmology.
2. 245th American Chemical Society National Meeting, New Orleans, LA, April, 2013.
The Effect of Competing Anions on Arsenic Removal via Magnetite Nanoparticles.
3. 4th International Symposium on Energy & Environment: ACESS, Mumbai, India, December, 2012. *The Effect of Competing Anions on Arsenic Removal via Magnetite Nanoparticles.*
4. International Water Association, Cities of the Future Xi'an, China, September, 2011.
An Integrated Approach to Water Management in Kayseri: Rain Water Collection and Use in an Amusement Park.

Poster Conference Presentations

5. The Association for Research in Vision and Ophthalmology, Seattle, WA, May, 2016.
Biocompatibility Assessment of End-thiolated Hyaluronate Coated Gold Nanoparticles on Retinal Pigment Epithelial (ARPE-19) cells.
6. The Association for Research in Vision and Ophthalmology, Orlando, FL, May, 2014. *Effects of Nanoparticle Exposure on the Growth of Retinal Pigment Epithelial Cells.*
7. 4th International Symposium on Energy&Environment: ACESS, Mumbai, India, December 2012. *Impacts of Fracturing Fluids Chemistry on Trace Element Mobilization from Shales.*

Teaching Experience

Teaching Assistant (3)

1. Engineering Analysis of Chemical Systems (E44.EECE.201, Fall 2015)
Washington University UG course, Instructors: Drs. Pratim Biswas and Fuzhong Zhang
2. Transport Phenomena II: Mass Transfer (E63.ChE.368.01, Spring 2015)
Washington University UG course, Instructor: Dr. Phalghat Ramachandran
3. Introduction to Energy, Environ. & Chem. Eng. (E63.ChE.146A, Fall 2014)
Washington University UG course, Instructors: Drs. Daniel Giammar and Jay Turner

Professional Affiliations

Member,	American Chemical Society	2012 - present
Member,	Association for Research in Vision and Ophthalmology	2014 - present

Journal Reviewer Activity

Journal of Hazardous Materials	2018 - present
Nature Scientific Reports	2017 - present
Journal of Aerosol Science	2017 - present
Water Science and Technology	2013 - present